Chemical Composition Measurements of Cloud Condensation Nuclei and Ice Nuclei by Aerosol Mass Spectrometry

Dissertation
zur Erlangung des Grades
"Doktor der Naturwissenschaften"
am Fachbereich Physik, Mathematik und
informatik
der Johannes Gutenberg-Universität
in Mainz

vorgelegt von

Paul Reitz
geboren in Ettelbruck, Luxemburg

Mainz, den 4. Juli 2011

b

Tag der Prüfung: 29. August 2011

Abstract

In this study the Aerodyne Aerosol Mass Spectrometer (AMS) was used during three laboratory measurement campaigns, FROST1, FROST2 and ACI-03. The FROST campaigns took place at the Leipzig Aerosol Cloud Interaction Simulator (LACIS) at the IfT in Leipzig and the ACI-03 campaign was conducted at the AIDA facility at the Karlsruhe Institute of Technology (KIT). In all three campaigns, the effect of coatings on mineral dust ice nuclei (IN) was investigated.

During the FROST campaigns, Arizona Test Dust (ATD) particles of 200, 300 and 400 nm diameter were coated with thin coatings ($<$7 nm) of sulphuric acid. At these very thin coatings, the AMS was operated close to its detection limits. Up to now it was not possible to accurately determine AMS detection limits during regular measurements. Therefore, the mathematical tools to analyse the detection limits of the AMS have been improved in this work. It is now possible to calculate detection limits of the AMS under operating conditions, without losing precious time by sampling through a particle filter.

The instrument was characterised in more detail to enable correct quantification of the sulphate loadings on the ATD particle surfaces. Correction factors for the instrument inlet transmission, the collection efficiency, and the relative ionisation efficiency have been determined. With these corrections it was possible to quantify the sulphate mass per particle on the ATD after the condensation of sulphuric acid on its surface.

The AMS results have been combined with the ice nucleus counter results. This revealed that the IN-efficiency of ATD is reduced when it is coated with sulphuric acid. The reason for this reduction is a chemical reaction of sulphuric acid with the particle's surface. These reactions are increasingly taking place when the aerosol is humidified or heated after the coating with sulphuric acid. A detailed analysis of the solubility and the evaporation temperature of the surface reaction products revealed that most likely $Al_2(SO_4)_3$ is produced in these reactions.

Contents

1

Introduction

1.1 Motivation

Clouds cover approximately 52 % of the sky over land and 65 % over ocean (Warren et al., 1986) and (Warren et al., 1988), which corresponds to an average cloud coverage of 60 %. This cloud coverage influences the earth radiation budget by reflecting sunlight to space and trapping infrared radiation emitted by the earth (Seinfeld and Pandis, 1998). Precipitating clouds transport water from the atmosphere to the ground. However, 90 % of the clouds evaporate before precipitation occurs and even when it occurs, some droplets evaporate prior to reaching the ground. Aerosol particles interact with the clouds and influence their effect on the radiation budget (Albrecht, 1989, DeMott et al., 2010, Lohmann and Feichter, 2005, Solomon et al., 2007, Twomey, 1977). Furthermore chemical reactions in the aqueous phase take place in cloud droplets, forming new compounds in the gas, the liquid and solid phase (Seinfeld and Pandis, 1998, chapter 6).

Cloud drops do not form in particle free air but through condensation of water on aerosol particles called cloud condensation nuclei (CCN). Whether a particle is able to act as a CCN under the supersaturations found in the atmosphere depends on its hygroscopicity and its size: larger particles and more hygroscopic particles act more efficiently as CCN. If more CCN are present in a cloud, more droplets form and compete for the available water in the cloud. This results in an increase of the droplet number concentration and a decrease of their size. In these clouds the light from the sun is more efficiently scattered back to space resulting in a higher cooling effect. This is known as the first aerosol indirect effect (Twomey, 1977). A second effect, referred to as the second aerosol indirect effect, is that by reducing the size of the cloud droplets, it takes more time for the cloud to form drops which are big enough to fall to the ground. High CCN concentrations thus result in a longer life time of the clouds, enlarging the cloud coverage of the earth (Albrecht, 1989, Pincus and Baker, 1994). In contrast under conditions with very low amounts of CCN, the

amount of CCN can become a limiting factor for the formation of clouds, as was reported by Mauritsen et al. (2011) for the Arctic.

Clouds can be composed of liquid water or ice or both phases. Below 0 °C, the thermodynamicly stable phase of pure water is ice. However, water can be supercooled down to approximately −38 °C without freezing, as an energy barrier needs to be overcome for the formation of an ice crystal to start. Some solid surfaces, so called ice nuclei (IN), show properties which lower the activation energy of the freezing process. In the atmosphere these are often mineral dust particles as was reported by Cziczo et al. (2004), DeMott et al. (2003), Kamphus et al. (2010), Mertes et al. (2007) and Richardson et al. (2007) from the analysis of snow crystal residuals. Additionally some authors state that biological particles like pollen (Diehl et al., 2001, 2002, von Blohn et al., 2005), fungal spores and bacteria might be important IN as some of them already induce freezing at temperature close to 0 °C (Möhler et al., 2007, Morris et al., 2004, Szyrmer and Zawadzki, 1997). Christner et al. (2008) state that biological IN are ubiquitous in snow but Hoose et al. (2010) found that the concentration of biological IN is too low to be important on a global scale but nevertheless they might be important on a local scale. Soot particles and metallic particles were found to act as IN under cirrus cloud conditions (Chen et al., 1998, DeMott et al., 1999). Cziczo et al. (2009) found that anthropogenic lead might be an important constituent of IN. The exact properties responsible for a particle incorporated in a droplet to act as an IN are still unknown for most systems.

The effect on the cloud albedo of aerosol particles acting as IN has been investigated by DeMott et al. (2010), and Storelvmo et al. (2011) on a global scale using models. Both state that the increase of IN in the atmosphere has a net warming effect, however Storelvmo et al. (2011) obtain a smaller effect, as their model includes not only the cloud lifetime effect but also the cloud albedo effect of an increased IN population. The albedo effect is similar to the one of CCN and increases the cloud albedo when the IN concentration is higher. However, the life time effect is opposite to the CCN effect, as the freezing of clouds promote the formation of precipitation (Roedel, 2000). Lohmann and Diehl (2006) showed that not only the number concentration but also the chemical nature of IN is important for the effect on the earth radiation budget.

In mid latitudes the formation of precipitation typically involves the ice phase (Roedel, 2000). Cloud droplets start to sediment after their formation and evaporate at the cloud base where the saturation ratio drops below 100 %. For precipitation to form, the droplets must grow to a size which allows them to reach the ground prior to their evaporation. In a liquid but supercooled cloud, a few droplets which

incorporate IN freeze at temperatures well above −38 °C. The saturation vapour pressure over ice is lower than over water due to the increased evaporation enthalpy of ice compared to water. In the liquid cloud, the air is slightly supersaturated with respect to water, which is a huge supersaturation with respect to ice. The ice crystals can thus grow much faster than water droplets and form crytals with sufficient settling velocities to reach the ground prior to evaporation within a few minutes. While falling through the cloud, ice particles efficiently scavenge additional supercooled droplets on their way. If the ice melts before reaching the ground, it rains, otherwise the ice reaches the ground as snow or hail (Pruppacher and Klett, 1997, chapter 13.3.1).

The preceding paragraphs show that ice nuclei play an important role in cloud physics. Nevertheless, it was up to now not possible to determine the properties of an IN responsible for its IN ability. In this thesis the nature of mineral dust ice nuclei is analysed using Arizona Test Dust (ATD) as a model substance. In the atmosphere mineral dust is often internally mixed with organic and inorganic material due to particle ageing processes in the atmosphere (Falkovich et al., 2001, Hinz et al., 2005, Sullivan and Prather, 2007, Sullivan et al., 2007, Wiacek and Peter, 2009). Such additions potentially influence the efficiency of mineral dust particles to act as ice nuclei (Gallavardin et al., 2008, Möhler et al., 2005, 2008, Niedermeier et al., 2010, Sullivan et al., 2010a,b). In this thesis the effect of sulphuric acid on the IN ability of ATD is studied. In Niedermeier et al. (2010) we showed that the IN-ability of ATD is reduced by the sulphuric acid coating and in Sullivan et al. (2010b) we demonstrated further that this loss is irreversible. The main goal of this thesis was to determine why the sulphuric acid reduces the IN-ability of ATD, with the objective to better understand the properties of the ATD that make it behave as an IN.

1.2 Hygroscopic Growth, Droplets and Ice Formation

1.2.1 Köhler Theory

The interaction of aerosol particles with elevated relative humidities is described by the Köhler theory. It links the water saturation vapour pressure over a flat water surface (p°) to saturation water vapour pressure ($p_w(D_p)$) over a solution surface with curvature radius $D_p/2$. This relation is expressed by the Köhler equation Eq. (1.1) (Köhler, 1936, Seinfeld and Pandis, 1998).

$$\ln \frac{p_w(D_p)}{p^\circ} = \frac{A}{D_p} - \frac{B}{D_p^3} \tag{1.1}$$

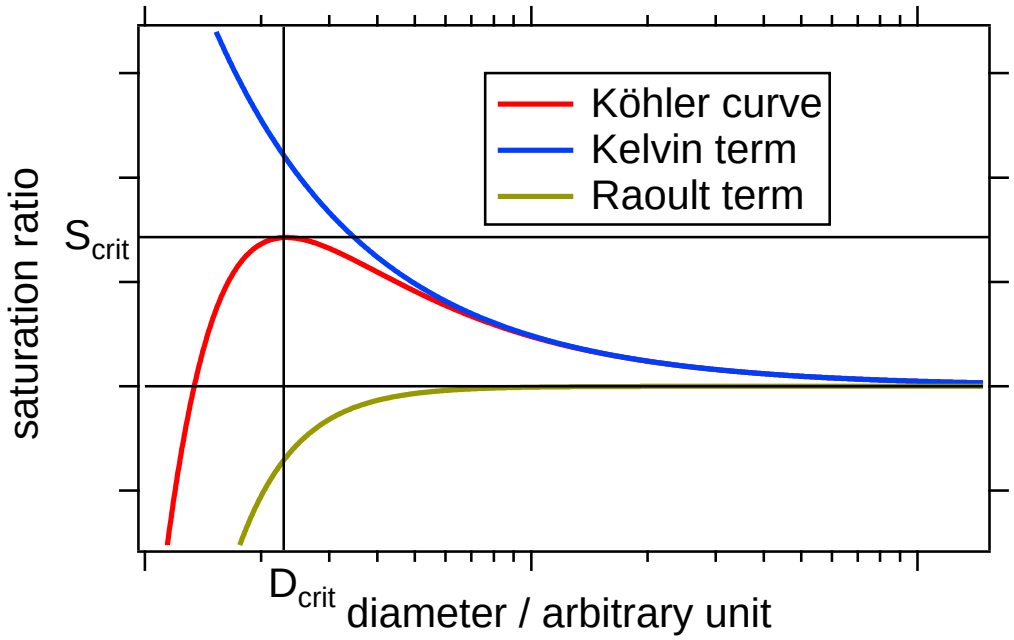

Fig. 1.1: Köhler equation with Kelvin and Raoult term.

$$A = \frac{4M_w\sigma_w}{RT\rho_w} \qquad B = \frac{6n_sM_w}{\pi\rho_w}$$

The term $\frac{A}{D_p}$ describes the so-called Kelvin effect which is responsible for the effect of the surface curvature. The smaller the surface curvature and thus the droplet size, the higher the vapour pressure over this surface. In A, M_w is the molecular weight of water, σ_w the surface tension of water, ρ_w the density of water, R the universal gas constant and T the temperature. The term $\frac{B}{D_p^3}$ is the so-called Raoult term which describes the effect of a solute in the water. The more hygroscopic material is dissolved in the water, the lower its saturation vapour pressure. In B, n_s is the number of solute moles. For small droplet radii the Raoult term is dominant and for high radii the Kelvin term is dominant. Figure 1.1 shows the Köhler curve together with the Raoult and the Kelvin term. The branch of the Köhler curve left of the critical diameter D_{crit} shows a stable behaviour, meaning that if the saturation ratio is changed below the critical saturation ratio S_{crit} the droplet size will always adapt until an equilibrium is established. This behaviour is called hygroscopic growth or evaporation. If the saturation ratio surpasses S_{crit}, the droplet can grow to a diameter higher than D_{crit} and reach the unstable branch of the Köhler curve. The droplet can now grow until the supersaturation is depleted and form a cloud droplet. Droplets which grow above the critical diameter are called activated.

Several modifications of the Köhler equation have been developed to take into account different effects like insoluble or partially soluble material as well as water soluble gases in the surrounding air. In case of an insoluble core, as is the case for an immersed mineral dust particle, the diameter in the Raoult term in Eq. (1.1) is replaced by $D_p^3 - d_{ic}^3$ with d_{ic}^3 being the effective diameter of the insoluble core.

Both forms of the Köhler equation described above are approximations of the real physics for droplets with highly diluted solutes. If the solute is highly concentrated as is the case for low saturation ratios, e.g. under smog conditions, the Köhler equation can no longer be applied. Additional effects like efflorescence and deliquescence become relevant (Seinfeld and Pandis, 1998). At low relative humidities salts are dry and do not take up water. When the relative humidity is increased, the salts take up water and are transformed to a highly concentrated solution at the deliquescence relative humidity. If the relative humidity is again decreased, the salt recrystallises at the efflorescence relative humidity, which is lower than the deliquescence relative humidity. However, in this study, the measurements were conducted at humidities close to and above water saturation and therefore the Köhler equation is a suitable model.

1.2.2 Ice Formation in the Atmosphere

Homogeneous Freezing

Homogeneous freezing takes place at low temperatures in the absence of ice nuclei. It is thought to be important for the formation of cirrus clouds (Heymsfield and Miloshevich, 1993, Jensen et al., 1998) and polar stratospheric clouds (Carslaw et al., 1998, Jensen et al., 1991, Peter, 1997, Tabazadeh et al., 1997). However, more recent publications also propose different heterogeneous mechanism for the formation of cirrus clouds (Abbatt et al., 2006, Murray et al., 2010). For the freezing of a water droplet or solute to start in the absence of an heterogeneous ice nucleus a critical ice embryo must form in the droplet. Simulations by Matsumoto et al. (2002) indicate that this can happen when an ice like structure forms by statistical fluctuations and at the same time the density of the droplet is slightly reduced due to local density fluctuations. Temperatures below -35 °C are necessary for the formation of a critical embryo to become likely in pure water. Solution droplets show even lower temperatures for the onset of homogeneous ice nucleation.

Heterogeneous Freezing

Heterogeneous freezing can take place in four different ways (Pruppacher and Klett, 1997, chapter 9.2). If the air is subsaturated with respect to water but supersatu-

rated with respect to ice, water molecules can deposit on the ice nuclei and directly form ice without the intermediate of the liquid phase. This process is called deposition freezing. If the air is supersaturated with respect to water, water droplets can form prior to freezing. If the droplets formed on the IN at temperatures above 0 °C and freeze when the temperature is lower, the freezing mode is called immersion freezing. If the droplets formed on the IN at temperatures already below 0 °C and the freezing occurs during the condensation, the freezing mode is referred to as condensation freezing. If the droplets formed without including an IN and the ice nucleus gets into contact to the droplets from the outside, contact freezing takes place.

There are two main theories to explain heterogeneous freezing. The first one is a stochastic approach assuming that the freezing is of statistic nature with the surface of the IN reducing the energy barrier for the critical ice embryo to form and thus increasing the probability of ice formation at higher temperatures. The freezing rate j_{het} for the stochastic approach is given in Eq. (1.2) (Pruppacher and Klett, 1997, chapter 9.2). The presented form is shown in Niedermeier et al. (2010):

$$j_{het}(T) = \frac{kT}{h} \exp\left(-\frac{\Delta F(T)}{kT}\right) \times n_s \exp\left(-\frac{\Delta G_{het}(T)}{kT}\right) \tag{1.2}$$

T is the temperature, h the Planck and k the Boltzmann constant, and n_s is the number density of water molecules at the ice nucleus/water interface. $\Delta F(T)$ describes the activation energy for crossing the liquid water/ice boundary. It represents a kinetic term for the growth of ice embryos. $\Delta G_{het}(T)$ is the Gibbs free energy for the formation of a critical ice embryo in the presence of the respective IN.

A second theory involves the hypothesis of ice active sites on the IN surface, which trigger ice formation at a critical temperature as soon as this temperature is reached. This theory was named singularity approach. The surface density $n_a(T)$ of ice active sites which are active at a temperature T is given by (Pruppacher and Klett, 1997, chapter 9.2):

$$n_a(T) = -\int_{0°C}^{T} k(\theta) d\theta \tag{1.3}$$

where $k(\theta)d\theta$ represents the number of sites per surface that become active in the interval $d\theta$.

The major difference between these two models is that in the stochastic approach, the freezing can start at any temperature if the aerosol has enough time. The presence of an IN is only increasing the probability that a particle freezes at higher

temperatures and thus reduces the time necessary for the freezing. The singularity approach assumes that the active sites on the particle surface trigger ice formation, as soon as a certain temperature is reached. In Niedermeier et al. (2010), two models have been derived from Eq. (1.2) and Eq. (1.3) to fit the number fraction of particles that acted as IN in the immersion freezing mode at different temperatures. Both models fit the data well and thus no model could be discarded.

1.3 Measurements under Extreme Instrumental Conditions

The main instrument used in this thesis is the Aerodyne Aerosol Mass Spectrometer (AMS) (Canagaratna et al., 2007, DeCarlo et al., 2006, Drewnick et al., 2005, Jayne et al., 2000). It was used to chemically characterise sulphuric acid coatings on Arizona Test Dust (ATD) which was used as model mineral dust ice nuclei. The ATD itself cannot be evaporated in the AMS and therefore does not produce any signal. Beside the disadvantage, that the AMS could not collect chemical information from the ATD particles, the advantage was that small signals from coatings were not disturbed by high signals from the particle core. After the characterisation, the AMS was therefore suitable to chemically analyse coatings of a few nanometres, which are relevant in the atmosphere, as well as their reactions with the ATD surface. These reactions prooved to be the key reason for the reduction of the ATD IN efficiency when coated with sulphuric acid.

The particle size analysed in this thesis is in the range of a few 100 nm. This size range is known as the accumulation mode. The particles in this mode have the longest residence time in the atmosphere, which is typically around 10 days (Pruppacher and Klett, 1997). Due to their long residence time, these particle are omnipresent in the atmosphere and thus of highest importance for the interaction with clouds.

Coatings of a few nm produce only low signals on the AMS detector. To avoid interpreting data which is below the detection limit, it was necessary to develop a method to determine detection limits under measurement conditions, which include all factors involved. For this purpose an experimental method to determine AMS detection limits as described by Drewnick et al. (2009) was improved to be applicable under most experimental conditions. Furthermore, AMS measurements are subject to several systematic errors linked to the collection efficiency, the particle size transmission range and more. In typical ambient experiments, these errors can only be estimated or are completely inaccessible. However, under controlled laboratory conditions, the instrument can be characterised to correct for these errors, making quantitative measurements possible.

Most of the data presented in this thesis was collected during the measurement campaigns FROST1 and FROST2 (FReezing Of duST) at the institute for tropospheric reasearch in Leipzig. The AMS sampled the ATD aerosol in parallel to the Leipzig Aerosol Cloud Interaction Simulator (LACIS), to characterise the aerosol which was introduced into LACIS. Further characterisation of the aerosol was performed with additional instrumentation, whose data was combined with the AMS data to complete the chemical charaterisation of the aerosol during the FROST campaigns. The results of the FROST campaigns are presented in Chap. 5. In addition to the FROST campaigns, the AMS participated at the ACI-03 (Aerosol Cloud Interaction) campaign at the AIDA (Aerosol Interaction and Dynamics in the Atmosphere) facility at the Karlsruhe Institute of Technology (KIT). These measurements are dicussed in Chapt. 6.

2

Experimental Methods

2.1 Aerosol Mass Spectrometer (AMS)

2.1.1 Instrument Description

The Aerodyne Aerosol Mass Spectrometer (AMS) (Fig. 2.1) was first introduced by Jayne et al. (2000) with a quadrupole detector (Q-AMS). The modification of the instrument used for this thesis was introduced by Drewnick et al. (2005). In this improved version of the instrument the quadrupole mass spectrometer was exchanged by a compact time of flight mass spectrometer (C-TOF-AMS). A similar instrument type was presented by DeCarlo et al. (2006), with a high resolution time of flight mass spectrometer (HR-TOF-AMS). The AMS measures mass spectra of aerosol particles in the vacuum aerodynamic diameter (d_{va}) range from 40 to 1000 nm, with 100 % inlet transmission efficiency in the range of 60 to 600 nm. The vacuum aerodynamic diameter is the aerodynamic diameter of a particle in the free molecular regime, meaning that the size of the particles is much smaller than the mean free path of the air the particles are suspended in inside the instrument. It is an equivalent diameter which corresponds to the diameter of a sphere of density 1 g/cm^3 which experiences the same drag force in the the air as the probed particle. The aerosol is introduced into the instrument via an aerodynamic lens which focuses the aerosol particles on a thermal vaporiser, typically set to a temperature of 600 °C. Particles which do not evaporate at the temperature the vaporiser is set to are refered to as refractory throughout this work. The vaporised particle compounds are ionised by 70 eV electron impact and the resulting ions are introduced into a time of flight mass spectrometer via ion optics. After the time of flight region, the ions are detected by a multi channel plate (MCP) detector. As the air molecules are not focused by the aerodynamic lens, the particles are enriched by a factor of 10^7 by mass relative to gas molecules.

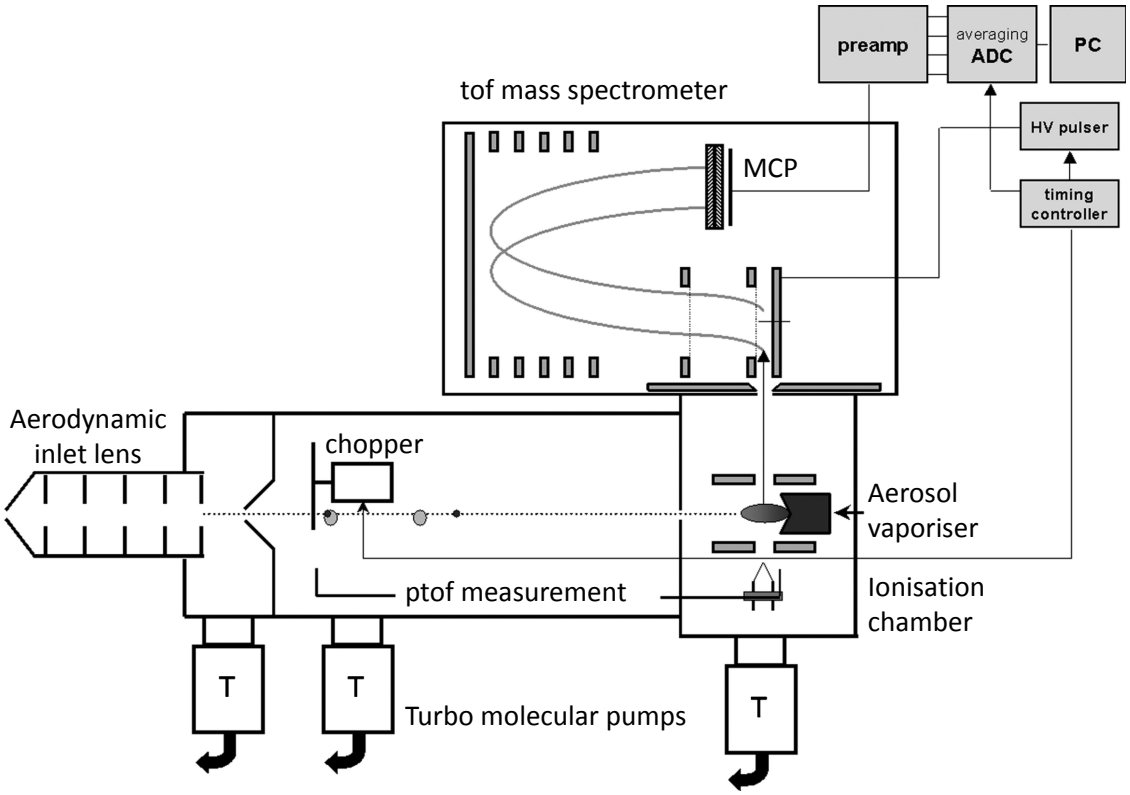

Fig. 2.1: Schematics of the AMS modified after Drewnick et al. (2005). ptof: particle time of flight, MCP: multi channel plate, preamp: preamplifier, ADC: analog digital converter.

2.1.2 Modes of Operation

The first mode of operation is the mass spectra mode (MS-mode). To separate the particle signal from the background signal, the instrument is alternating between the measurement of the background together with the particle signal (open) and the measurement of the background alone with the particle beam blocked (closed). In the open mode, the particle beam and the airbeam are measured by the instrument. In the closed mode the aerosol is blocked and cannot reach the ioniser. The closed signal is subtracted from the open signal, yielding mass spectra of the particles together with the remaining air ions which reached the vaporiser together with the particle beam. The signal originating from the air can be separated from the particle signal using a fragmentation table under the assumption that the ratios of the concentrations of nitrogen, oxygen and argon are constant. The fragmentation table is described in Allan et al. (2004). The factors in the fragmentation table are determined by blank measurements using a particle filter in front of the instrument. A further important use of the fragmentation table is to attribute the signals of the different mass to charge ratios m/z to the corresponding chemical species, as different chemical substances often show signals on the same mass to charge ratios. The

main species distinguished by the AMS are nitrate, sulphate, ammonium, chloride and organics. Molecules which are evaporated and ionised decompose into different fragments. Thus one molecule e.g. N_2 produces signals on different m/z. In the case of N_2 the main fragments are N_2^+ on $m/z = 28$ and N^+ on $m/z = 14$. Additionally to the fragmentation, most molecules can include different isotopes of their composing elements. In case of N_2 these are ^{14}N and ^{15}N resulting in additional signals on $m/z = 15, 29, 30$. These signals interfere with other substances producing signals on the same m/z e.g. C_2H5^+ on $m/z = 29$. As the ratios between different isotopes of most atoms in the atmosphere are known and rather stable, the strong signals on $m/z = 14$ and $m/z = 28$ can be used to calculate the expected fractions of $m/z = 15, 29, 30$ which belong to N_2 and thus correct the intensities of other substances which show a signal on these m/z. Similar to the isotopic ratios, the fragmentation patterns for different molecules are stable and can be corrected via the table. Practically, the information used by the fragmentation table was gathered in numerous laboratory studies (Allan et al., 2004) and as far as possible, the ratio between different fragments are determined for each instrument.

Beside the mass spectra, the AMS is able to determine the d_{va}-distribution of the aerosol particles. At the outlet nozzle of the aerodynamic lens the particles are accelerated and reach different terminal velocities depending on their d_{va}. A chopper with an opening time fraction of 2 % is used between the aerodynamic lens and the vaporiser. During each cycle of the chopper, approximately 200 mass spectra are recorded. The opening time of the chopper is recorded and thus the time when particles can pass the chopper is known. The particles with lower d_{va} have higher velocities and arrive first at the ioniser and thus their mass spectra are recorded first. The particle-time-of-flight (PTOF) between the opening of the chopper and the recording of the mass spectrum is converted into the d_{va} using a calibration. The calibration is performed using polystyrol latex size standards (PSL) and size selected ammonium nitrate particles. An examplary size calibration curve is shown in Fig. 2.2. As the size of the particles is determined by the particle time of flight, this mode is referred to as PTOF-mode.

2.1.3 Electronic Baseline

The signal of the AMS typically has an offset which is blocking the lowest bits of the anolog to digital conversion and reducing the dynamic range of the hardware. To avoid this loss of dynamic range, the average voltage of the electronic noise, the so called baseline, is determined and subtracted from the signal prior to recording. The area below a signal is calculated for the signal above this systematic off-set,

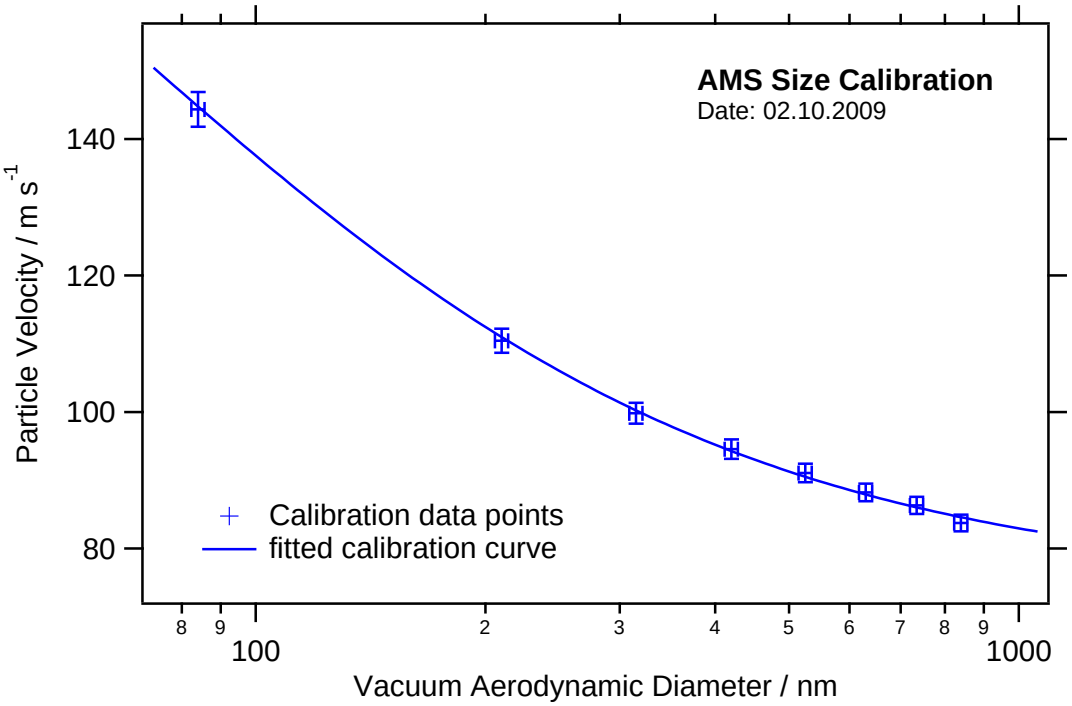

Fig. 2.2: Exemplary size calibration recorded during the measurement campaign ACI-03 by measuring PSL size standards. The error bars are calculated from the estimated uncertainties of the particle time of flight (34 µs), the uncertainty of the flight distance in the AMS vacuum chamber (5 mm) and a 2 % error in the calibration particle mobility diameter.

avoiding recording a constant baseline without signal information. To make sure no signal is disturbing the baseline measurements but nevertheless the electronic noise is visible, the MCP voltage is reduced from the typical operation value of $\sim$ 2000 V to 1000 V, which is low enough to avoid ions from being detected. Figure 2.3 shows a screenshot of the baseline recording window from the data acquisition software. The baseline was found to be approximately 0.7 mV.

2.1.4 AMS Detection Limits

The detection limits (DL) of the AMS correspond to the minimum signal which can clearly be distinguished from the noise level of the background. The background noise is mainly composed of the electronic noise of the detector and the counting statistics of the residual gas in the AMS vacuum chamber. In addition, slowly evaporating compounds which accumulated on the vaporiser can increase the DL. In addition to these physical sources of noise, the data processing adds additional random variations to the signal, which also have to be considered in the final determination of the detection limits. These errors originate from the digitisation of

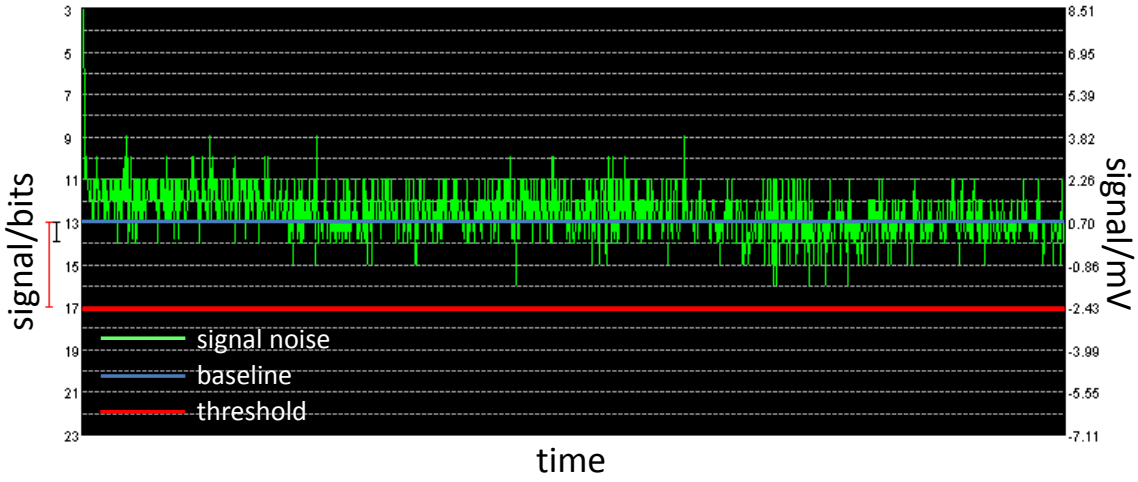

Fig. 2.3: Screen shot of the AMS baseline determination window. The y-axis is inverted. The green line is the signal as recorded with the MCP at low voltage. The blue line is the baseline and the red line is the baseline plus the threshold.

the analogue signal as well as from later off-line corrections like the determination of baselines.

To reduce the AMS detection limit, the data is filtered prior to the averaging to reject signals which only contain noise. Data is only recorded if it is above a threshold value, which is set in a way that it suppresses most of the noise but not the smallest signals. In Fig. 2.4 the effect of thresholding is depicted on a generated signal. Figure 2.3 shows the threshold set for the first week of the ACI-03 campaign at the AIDA. Note that in the depicted signal no peak is above the threshold level. To determine the highest level the threshold can be set to without loosing small signals, the ratio of the ions resulting from nitrogen and argon is compared for different thresholds. In ambient air this ratio is constant. The signal from the nitrogen is always clearly above the threshold, while argon often produces signals composed of a single ion. If the value of the threshold becomes too high, the single ion signals of the argon tend to be below the threshold, causing the ratio of argon to nitrogen to drop. The threshold must not be set higher than the highest value which does not yet cause small signals to be lost.

2.1.5 Mass to Charge Calibration

In the time of flight mass spectrometer the ions are accelerated by a pulser electrode. As all ions get approximately the same energy per charge, those ions with the lowest mass to charge ratio (m/z) attain the highest velocity and arrive first at the detector. The ion time of flight is proportional to the square root of the m/z. The proportionality factor is determined via the calibration with prominent m/z in

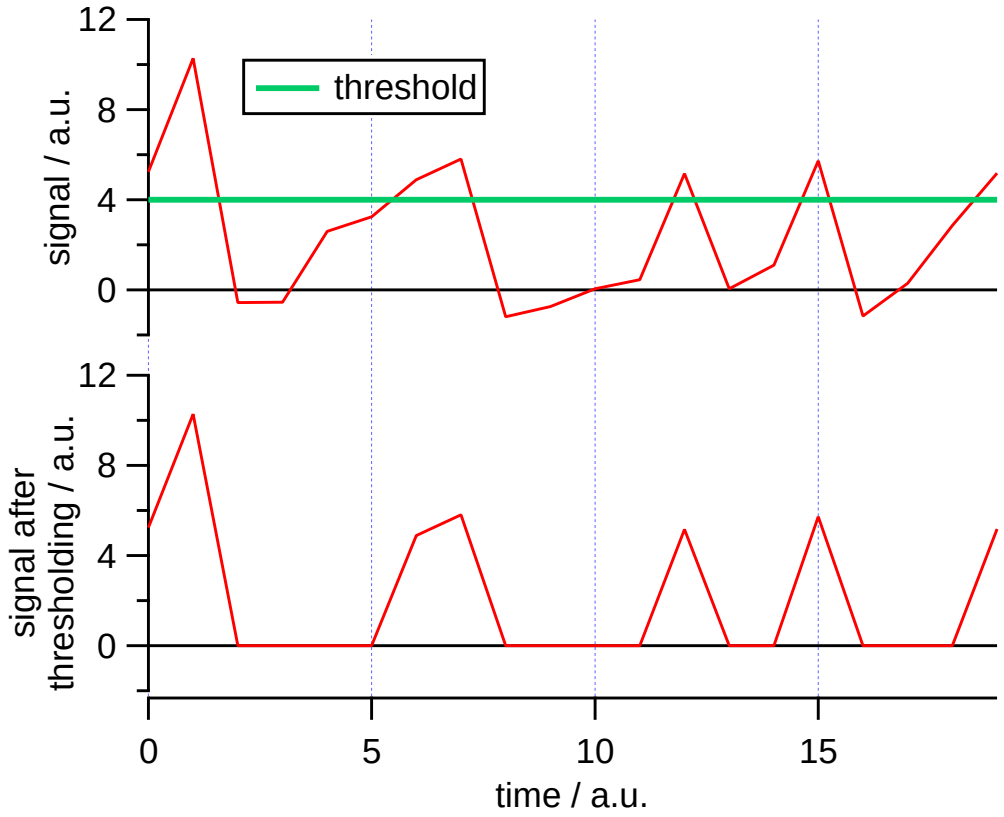

Fig. 2.4: Effect of thresholding on a signal. The upper graph shows the signal with the threshold level marked in green and the lower graph depicts the signal after the threshold was applied.

the mass spectrum like H_2O^+, HO^+, and O^+ from water, and the tungsten isotopes $^{182}W^+$, $^{183}W^+$, $^{184}W^+$,and $^{186}W^+$. These originate from the filament and can be easily identified by their pattern in the mass spectrum. After the calibration, the time-of-flight intervals attributed to one m/z can be integrated to provide unit mass resolution mass spectra ("sticks spectra") (Hings, 2007, pp. 42-44).

2.1.6 Calculation of Aerosol Mass Concentration

To convert the count rates I_S of the detector to mass concentration C_S, the count rates are divided by the ionisation efficiency (IE), the inlet flow rate Q_{in} and the Avogadro number N_A and multiplied by the molecular weight (MW_{NO_3}) of nitrate. The IE is determined via a calibration with ammonium nitrate using the nitrate m/z 30 and 46. As the ionisation efficiencies of other compounds differ from the ionisation efficiency of nitrate, their relative ionisation efficiencies (RIE) need to be determined (Allan et al., 2003). The flow rate is calculated from the pressure in the instrument inlet using a calibration with a flow meter. As some particles bounce off

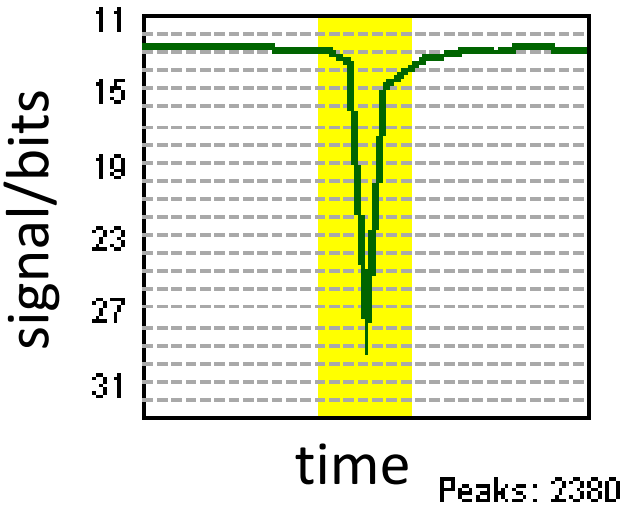

Fig. 2.5: Screen shot of the AMS SI calibration window. The peak shown is the averaged signal of 2380 single ion events.

the vaporiser before evaporation, the mass concentration needs to be divided by the reduced collection efficiency (CE) due to this effect (Huffman et al., 2005, Matthew et al., 2008). The calculation of the mass concentration of a given species C_S is summarised in Eq. (2.1).

$$C_S = \frac{1}{RIE_S\, CE_S} \cdot \frac{I_S\, MW_{NO_3}}{N_A\, Q_{in} IE_{NO_3}} \tag{2.1}$$

The output voltage of the AMS detector after digitisation is in bits. The signal of a certain m/z corresponds to the integrated signal in bits over the time bins attributed to the m/z of interest. This yields a signal in $bits \cdot s$ which is converted into ion counts by dividing it by the intensity of the signal of a single ion (SI). The SI is recorded by measuring very low concentrations, as for example the residual gas of the instrument without the typical air ions but with active thresholding in order to avoid noise to be considered a small real signal. At mass to charge ratios with very low signal, most of the signals originate from single ion events. These signals are averaged to determine the single ion area. Figure 2.5 shows the averaged signal of 2380 single ion peaks.

To calibrate the IE of the AMS, an ammonium nitrate solution is atomised and the droplets are dried in two diffusion dryers. The dry particles are size selected in a differential mobility analyser and the size selected particles are measured by the AMS in the so called brute force single particle (BFSP) mode. In this mode the signals of single particles is recorded by triggering the recording only when a certain threshold is reached by the signal of the m/z the filter is applied to. The chopper

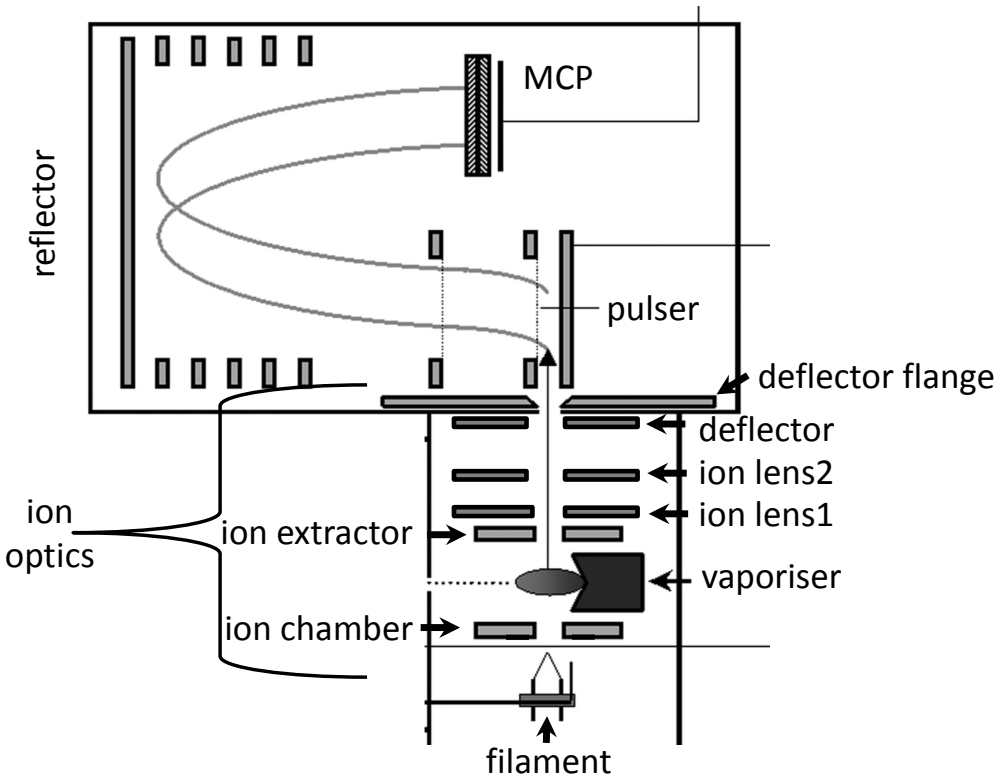

Fig. 2.6: AMS ion optics introducing the ions created in the ioniser into the mass spectrometer.

is operated as in the PTOF-mode, enabling the recording of the particle size. As the size of the ammonium particles is known as well as the ratio between their size and their mass, the signal of a single particle can be compared to the mass of a single particle and the number of ions detected by number of molecules sampled can be calculated. To avoid including multiply charged particles in the calibration, the recorded particle time of flights should be analysed for doubly charged particles. To avoid multiple particles to be recorded at the same time, the number concentration of the particles should not exceed 1000 particles/cm^3.

2.1.7 Overshooting Duty Cycle Correction

The duty cycle of an instrument is the time the instrument is really measuring a certain quantity. It is composed of different limiting factors. In the AMS these are the open time of the particle beam, which reduces the duty cycle by a factor of 2 in the MS-mode and by a factor of 50 in the PTOF-mode. In addition the switching between open and closed reduces the time that is spent recording signals. These factors are independent of the mass to charge ratio and are logged by the data acquisition software. In addition the so called overshooting duty cycle is m/z

dependent. The ions are introduced into the mass spectrometer by the ion optics which are shown in Fig. 2.6. The ions are accelerated into the mass spectrometer by the voltage of the ion optics, mainly the voltage between the ion chamber and the ion extractor. Depending on their m/z, the ions get different velocities. After passing the ion optics, the ions pass the pulser and are accelerated into the time of flight region. However, a fraction of the ions passes the pulser prior to the acceleration pulse. These ions are lost for the final signal and thus the signal must be corrected for this factor. The factor is proportional to the ion velocity and thereby to the square root of the mass to charge ratio.

2.1.8 Tuning of the Ion Optics and Mass Spectrometer Electrodes

The voltages of the ion optics shown in Fig. 2.6, as well as those of the electrodes inside the mass spectrometer need to be adjusted to obtain the optimal transmission and resolution of the instrument. Primary, maximum signal intensity must be achieved. This is important, as only when the signal is maximised, the transmission function of the ion optics introducing the ions into the mass spectrometer is independent of the m/z of the ions. If the signal is not maximised, the ion transmission becomes m/z dependent. Only after maximising the signal, the resolution can be optimised (Trimborn, 2009). Because up to now their is no standardised way to determine the ion transmission function, an m/z dependent ion transmission reduces the quantification ability of the AMS. The voltages of the mass spectrometer itself can be tuned to get a good resolution without loosing "too much" signal. Adjusting the voltage of the electrodes is achieved by scanning through the different voltages, starting with the ion optics. There is no standarised procedure to do this meaning that the optimal tuning is achieved by trial and error.

2.1.9 Detection Efficiency Correction: Airbeam Correction

The detection efficiency of the MCP detector of the AMS is decreasing with aging time on scales of hours to days. To account for this effect, it is necessary to continuously measure a constant quantity to monitor this loss in signal intensity. In the AMS m/z 28, which corresponds to N_2^+ from the gas phase, is used for this purpose as it always has a very high and constant signal which is only weakly influenced by other ions. A reference value of the intensity of m/z 28 is recorded on calibration. During the data evaluation process the ratio of the reference value and the measured intensity on m/z 28 can be used to correct the measured mass concentrations for the reduction of the efficiency of the MCP. This effect is referred to as airbeam correction. When analysing closed or open data alone, the airbeam correction adds to

the noise of the signal. However, as the same factor is applied to both the closed and the open signal, the noise introduced by the airbeam correction is mostly removed when analysing the difference signal. This effect is important in Sect. 3.2.7 when calculating AMS detection limits using the closed signal only.

2.1.10 Data Evaluation

The raw data of the AMS is typically evaluated using the software environment Igor (WaveMetrics, Inc. Lake Oswego, Oregon, USA). The different data evaluation steps have been implemented as Igor procedures. These procedures, together with a graphical user interface form the Igor software package SQUIRREL (http://cires.colorado.edu/jimenez-group/ToFAMSResources/ToFSoftware/index.html). Nowadays SQUIRREL is used by basically the whole AMS community to perform the standard data processing steps. This software also implements the fragmentation table (see: Sect. 2.1.2) with default values, which can be adapted to the particular experiments.

2.2 Additional Instruments and Methods

2.2.1 Cloud Condensation Nuclei Measurements

The cloud condensation nucleus properties of the aerosol during the FROST campaigns were determined using a cloud condensation nucleus counter (CCNC) of the type described in Roberts and Nenes (2005). The instrument was operated by Heike Wex, IfT Leipzig. In this instrument, the supersaturation of the aerosol is scanned in the range of 0.07 to 0.6 % at a controlled temperature. Those particles that activate as CCN grow to a size at which they can be counted optically. The number of activated particles is then compared to the total number of aerosol particles yielding the activated fraction at a given supersaturation.

Using single parameter Köhler theory (Petters and Kreidenweis, 2007, Wex et al., 2007), the CCNC data can be translated into soluble mass per particle loadings if the material of the soluble mass is known. Eq. (2.2) shows the single parameter Köhler equation linking the size of the wet particle D to the saturation ratio S. D_{dry} represents the dry diameter of the particle and A is a parameter depending on the temperature and the surface tension at the solute/air interface.

$$S(D) = \frac{D^3 - D_{dry}^3}{D^3 - D_{dry}^3(1-\kappa_{app})} \exp\frac{A}{D} \tag{2.2}$$

The parameter κ_{app} is the apparent hygroscopicity parameter of the particle material. It is composed of the sum of the apparent hygroscopicity parameters κ_i of the different compounds of the particle multiplied by their volume fraction ϵ_i (Eq. (2.3)). The term "apparent" is used, as the hygroscopicity determined from the CCNC measurements can be biased towards lower values if a fraction of the particle material is only partially soluble. Material which is not soluble does not contribute to the particle hygroscopicity and affects the CCN behaviour of the particles only by increasing the particle dry diameter.

$$\kappa_{app} = \sum_i \epsilon_i \kappa_i \tag{2.3}$$

In case of a nearly insoluble particle core with a known soluble coating, Eq. (2.3) simplifies to Eq. (2.4) with the indices "coat" and "core" referring to the coating and the particle core respectively.

$$\kappa_{app} = \epsilon_{coat}\kappa_{coat} + \epsilon_{core}\kappa_{core} \tag{2.4}$$

The sum of the volume fractions must be equal to 1. If the apparent κ-value from the particle core and the coating are known from preceding reference measurements (Sullivan et al., 2009), Eq. (2.4) can be rearranged to determine the volume fraction of the coating. The volume fraction is then multiplied by the total volume of the particle (V_{total}) and multiplied by the density of the coating (ρ_{coat}). This yields a soluble coating mass per particle loading ($m_{soluble}$), which can be compared to AMS mass per particle loadings (Eq. (2.5)).

$$\begin{aligned} m_{soluble} &= \rho_{coat} \times V_{coat} \\ &= \rho_{coat} \times V_{total} \times \epsilon_{coat} \\ &= \rho_{coat} \times V_{total} \times \frac{\kappa_{app} - \kappa_{core}}{\kappa_{coat} - \kappa_{core}} \end{aligned} \tag{2.5}$$

The above technique works best if the particle core does not chemically react with the coating on its surface. For the quartz particles coated with sulphuric acid, which were used for reference experiments in these studies this was the case. If the coating material reacts with the particle surface and the reaction products can not be completely identified and quantified, the determination of the coating mass fraction is restricted to an estimation assuming a probable surface material composition.

2.2.2 Continuous Flow Diffusion Chamber

The Continuous Flow Diffusion Chamber (CFDC) originally described by Rogers et al. (2001) and modified as described in Sullivan et al. (2010b), was operated by Ryan Sullivan and Markus Petters (Colorado State University). It was used to determine the number fraction of aerosol particles which nucleated ice at a set temperature and water saturation ratio. The measurements and results were published in Sullivan et al. (2010b). After cooling, the dry aerosol enters a region between two concentric cylinders which are coated with ice. The cylinder walls are set to different temperatures in order to produce a supersaturated region with respect to ice between the walls. The supersaturation is controlled via the temperatures and can reach values above water saturation. If the aerosol is in a subsaturated regime with respect to water, the freezing mechanism is deposition freezing (water molecules deposit on the particle and form ice without passing the liquid phase). If the aerosol gets supersaturated with respect to water, the freezing regime is either immersion or condensation freezing (water passes the liquid phase prior to freezing). The different freezing mechanisms are described in (Pruppacher and Klett, 1997, chapter 9.2). The ice crystals are detected at the end of the chamber with an optical particle counter. In order to prevent droplets from being detected together with ice, a water subsaturated but ice saturated region follows the activation region. In this region, the water droplets evaporate due to the Bergeron-Findeisen process (Findeisen, 1938).

2.2.3 Leipzig Aerosol Cloud Interaction Simulator

The Leipzig Aerosol Cloud Interaction Simulator (LACIS) is a continuous flow tube which can be used to study both CCN and IN abilities of aerosols. However, in this work only the IN-measurements of LACIS are used. It was operated by scientists of the IfT in Leipzig and results have been published in Hartmann et al. (2011), Niedermeier et al. (2010, 2011). The facility was introduced by Stratmann et al. (2004) and its use for IN-studies is described in Hartmann et al. (2011). It consists of a tube of seven metre length whose wall segments are temperature controlled. The humidity of the aerosol is set to a controlled value at the beginning of the tube. While passing the tube, the aerosol beam is surrounded by sheath air. Through the lowering of the wall temperature, the aerosol is cooled down and thus its relative humidity increases until particles activate as cloud droplets. By further lowering the temperature, particles including an IN can freeze. At the outlet of the tube, the particle size distribution is measured with an optical particle counter, which can

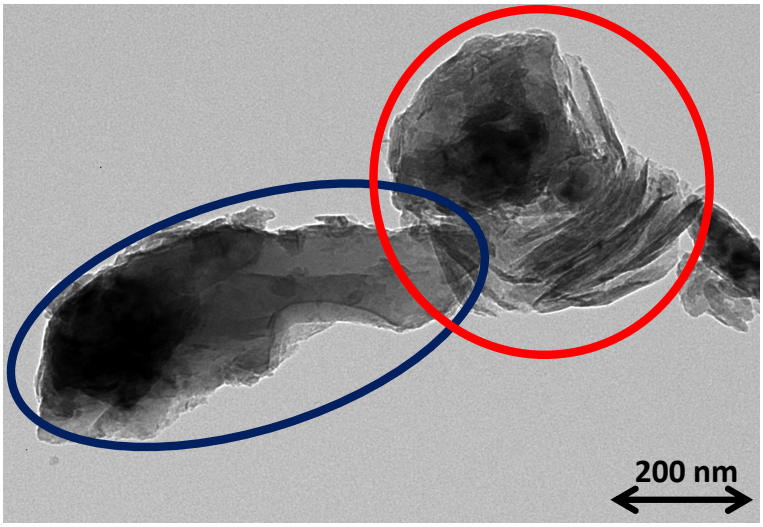

Fig. 2.7: TEM picture of two ATD particles. Note the difference in the aspect ratio between the two particles indicated by the red circle and the blue oval. (TEM picture by A. Kiselev, Institute for Tropospheric Research, Leipzig and I. Lieberwirth, MPI-P, Mainz)

detect droplets and ice crystals. The retrieval of the ice and the droplet fraction from the size distributions is described in Niedermeier et al. (2010).

2.2.4 The Atmospheric Simulation Chamber AIDA

The atmospheric simulation chamber AIDA (Aerosol Interaction and Dynamics in the Atmosphere) (Möhler et al., 2001, Nink et al., 2000) at the Karlsruhe Institute of Technology (KIT) consists of a vessel with a size of 84 m^3. To simulate ascending air parcels, so called expansion experiments can be performed in the chamber. The chamber pressure is quickly reduced via pumping which provokes adiabatic cooling of the air parcel. As in real atmospheric air parcels at a certain temperature the water vapour pressure reaches supersaturation over ice and/or water. This way cloud processing of aerosols and aerosol cloud interactions can be simulated. The facility can be equipped with various instruments to characterise the air and the particles in the chamber.

2.3 Arizona Test Dust

Arizona Test Dust is a mineral dust which is industrially produced from natural sand collected in the desert of Arizona by Powder Technology Inc. (Burnsville, MN 55306). It is milled and size selected and is available in different standardised size ranges. The dust used in this study belongs to the lowest available size range (A1 Ultrafine Tests Dust; ISO 12103-1) containing 1 to 3 % by volume of particles smaller

than 1 µm in aerodynamic diameter according to the manufacturer, which was the particle size range of interest. The main reason for using the industrial dust in these study was to get good comparability to other studies using the same dust. The industrially treated ATD was expected to show a lower variability between different samples than dust collected in the atmosphere. Figure 2.7 shows a transmission electron microscope (TEM) picture of ATD, which was sampled during the FROST1 campaign. Note the difference in the aspect ratios of the two particle visible in this picture. Theses variabilities in shape also cause variabilities in the aerodynamic shape factors of the particles (see Sect. 4.1.1).

2.4 BCR-66 Size Standards

The BCR-66 quartz size standards (European commission, Institute for Reference Materials and Measurements) (BCR) were used in this study as a model dust for silicates. Their aerodynamic size range is 0.35 to 2.5 µm and they are, according to the manufacturer, composed of quartz. The particles were used as a model mineral dust which does not react with sulphuric acid coatings, is completely insoluble and refractory at the temperatures the AMS is used at.

2.5 Sulphuric Acid Coating Unit

During the FROST campaigns, the ATD was coated with sulphuric acid by passing the aerosol over a heated sulphuric acid bath. The temperature of the bath is stabilised by a water bath which surrounds the sulphuric acid bath. The temperature of the surrounding water bath and thus the temperature of the sulphuric acid was controlled by a thermostat. The thermostat was coupled to a heater to maintain the temperature at a set value. Figure 2.8 shows a picture of the sulphuric acid coating unit. It was designed at the IfT. The residence time of the aerosol within the heated section is ~ 5 s. To ensure reproducibility of the coatings, great care was taken to have a constant flow and thus a constant residence time in the coating unit for all experiments.

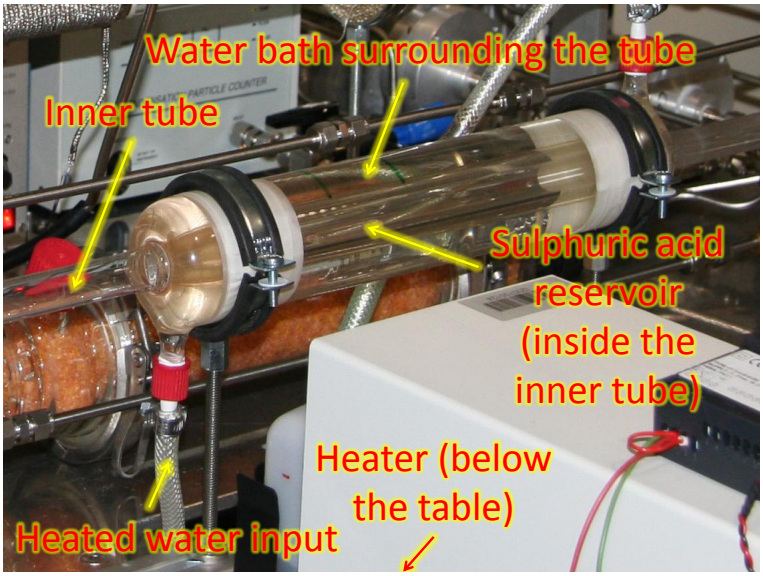

Fig. 2.8: Sulphuric acid coating unit used during the FROST campaigns. The aerosol enters the coating unit in a glass tube and passes over a small heated sulphuric acid bath. To control the temperature, the sulphuric acid bath section is surrounded by a water bath. The temperature of the water is maintained by a heating unit below the table.)

3

Continuous Determination of AMS Detection Limits

The measurement of thin coatings on refractory particles as performed in this study implies the necessity of detecting very small amounts of material. It is therefore important to determine the smallest amount of material that can be reliably attributed to the real signal. This amount is typically referred to as detection limit (DL). It is commonly defined as three times the standard deviation of the signal noise distribution σ_{noise} plus a possible offset μ of a blank measurement (Kellner et al., 2004).

$$DL = 3 \times \sigma_{noise} + \mu \tag{3.1}$$

This chapter gives an overview of methods used in the past to determine AMS detetction limits and presents two new methods, whose applicability are tested. The first method (Sect. 3.2.2) involves Bezier-smoothing-spline and is therefore referred to as Bezier-method. It suffers from some critical drawbacks which will be overcome in the second, improved method presented in Sect. 3.2.3. The second new method is based on local cubic interpolations and will be referred to as *DL-cubic* .

3.1 Classical Methods

In the recent AMS literature different methods with different strengths and weaknesses have been described to determine the limits of detection. The most commonly used ones are summarised in the following sections.

3.1.1 Counting Statistics

A mathematically straight forward approach is to use the ion counting statistics of the signal of a measurement through a particle filter, thus only probing particle free

air. In the case of the AMS, this corresponds to the counting statistics error ΔI_{diff} of the difference of the open I_{open} and the closed I_{closed} signal, as shown in Eq. (3.2).

$$\Delta I_{diff} = \sqrt{I_{open} + I_{closed}} \tag{3.2}$$

A typical value of ΔI_{diff} for organics (recorded during the FROST1 campaign in spring 2008 at the IfT in Leipzig) would be $\sqrt{3,517,000 + 3,520,000}/\sqrt{132} = 231$ This corresponds to a mass concentration DL of 0.14 µg/m^3. The division by $\sqrt{132}$ is necessary to scale the counting statistics error for the whole measurement period, which were 132 min, to a time resolution of 1 min. More values are shown in Tab. 3.8 in Sect. 3.2.8. The disadvantages of this method is that it wastes precious measurement time while sampling through a particle filter. Furthermore, it does not take into account the electronic noise of the instrument. To get correct results, the electronic noise needs to be determined separately. This proves difficult in the case of the AMS (see Sect. 3.2.8). Additional effects resulting from the processing of the data, like baseline shifts, are not covered by this method as they add random noise to the signal which is not directly linked to counting statistics.

3.1.2 Standard Deviation of Filter Measurements

Bahreini et al. (2003), Salcedo et al. (2006), Takegawa et al. (2005), Zhang et al. (2005) and DeCarlo et al. (2006) used filtered air measurements to determine the detection limits of the AMS. The DL is estimated as three times the standard deviation of a filter measurement ($3 \times \sigma_{filter}$). The advantage of this method is that the detection limits are determined experimentally and thus take into account all effects which might be ignored when only taking into account the ion counting statistics. A disadvantage is the need of filter periods, which do not represent the varying state of the instrument during regular measurements, where the closed loadings can be increased due to the sampled aerosol (Drewnick et al., 2009).

3.1.3 Frequency Space Closed Signal Analysis

Crosier et al. (2007) avoid the need of filter period measurements by using only the closed signal of the instrument to determine the detection limits. They apply a Fast Fourier Transformation (FFT) to the closed signal time series and use the relation in Eq. (3.3) to determine the standard deviation of the noise σ. N and N' are the number of points in the time and the frequency space[1], respectively, and I_{closed} is the

[1]The FFT decomposes a time series into periodic functions $C_j \exp -2\pi i\omega_j t$ whose sum corresponds to the original signal. The complex intensities C_j for every constituent frequency ω_j yield a spectrum in the frequency space.

closed signal of the AMS. Note that the Fourier transformed spectrum is in complex number space.

$$\sigma^2 = \frac{2}{N^2} \sum_{n=1}^{N'-1} |[FFT(I_{closed})]_n|^2 \tag{3.3}$$

Figure 3.1a shows the closed signal of the organic species, recorded during one flight of the POLARCAT campaign over Greenland[2]. The data is an example of a real closed signal recorded during aircraft measurements. Figure 3.1b shows the squared amplitudes of the Fourier Transformation of the signal in Fig. 3.1a. The separation of random noise from frequencies originating from slower variations in the closed signal is performed by using the property of the random noise signal to produce a constant level in the frequency space (Stull, 1988). The region of the constant signal in the frequency space is marked as "flat" in Fig. 3.1b. Those frequency regions which are not "flat" are ignored in the sum of Eq. (3.3). The noise level in the "non-flat" regions must be the same as for the "flat" region, as the random noise has the same intensity over the whole frequency range. To get the noise from all frequencies, the sum of the squared amplitudes from the "flat" region is multiplied by the ratio of the total number of frequency bins minus one to the number of bins in the flat region. An example should clarify this method:

The sum of the squared amplitudes of the "flat" region in Fig. 3.1b is 63159 $(\mu g/m^3)^2$. The signal has a length of 196 points resulting in a length in the Fourier space of 99 complex points. The length of the flat region in the Fourier space is 33 points. The sum of the squared amplitudes thus needs to be scaled by a factor of $(99-1)/33$ to estimate the contribution to the noise from all frequencies. Following Eq. (3.3) the extrapolated sum of the squares is now multiplied by $2/N^2$. The square root of the resulting number corresponds to the standard deviation of the noise which in this example is equal to 3.12 $\mu g/m^3$. The confidence interval of this value could not be determined. The new algorithm, *DL-cubic* , to calculate the standard deviation of the noise, which is presented in Sect. 3.2.3, yields a standard deviation of 0.79 ± 0.07 $\mu g/m^3$. As the *DL-cubic* algorithm is never biased to low standard deviations, 3.12 $\mu g/m^3$ must be a strong overestimation of the noise level. The reason for this overestimation is that the FFT assumes that the signal can be periodically prolonged to an infinite time. In the example shown in Fig. 3.1c, the periodical continuation of the signal effectively means that the first point of the signal is connected to the last point. This introduces strong discontinuities in the

[2]Data from Julia Schmale, Max Planck Institute for Chemistry, Mainz

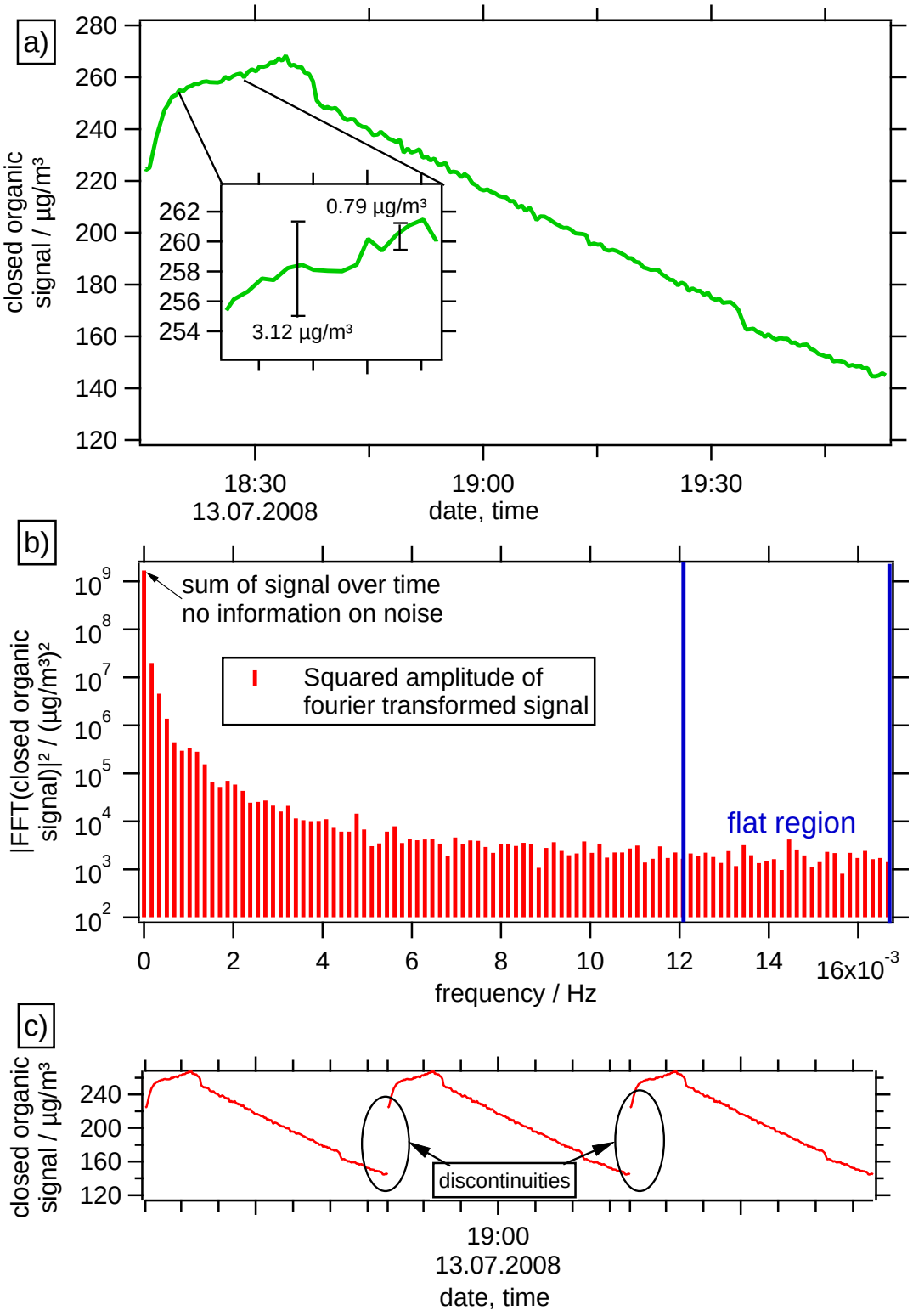

Fig. 3.1: a) Organic closed signal recorded during one flight of the measurement campaign POLARCAT. The noise standard deviations for of the FFT b) Squared amplitudes of the Fast Fourier Transformation of the signal shown in a). c) Illustation of the periodic continuation of the signal for the FFT with discontinuities at the matching points.

time series. These discontinuities contribute to the signal at every frequency in the Fourier spectrum and thus artificially increases the estimated noise level.

As a typical AMS closed signal is not periodic, the possible applications of the FFT-method to determine AMS detection limits is very limited. Crosier et al. (2007) did not use the FFT-method to calculate absolute values of the detection limits but only showed relative changes in the sum over the squares of the amplitudes of the flat region in the frequency space. The authors do not explain how they dealt with the non-periodicity of signals, but as the noise reduction method described in Crosier et al. (2007) showed a very clear effect, the FFT-method showed a meaningfull qualitative reduction of the noise.

3.1.4 Time Space Closed Signal Analysis

Drewnick et al. (2009) similar to Crosier et al. (2007) used the closed signal of the AMS to determine the detection limits experimentally during regular instrument operation. They directly calculated the standard deviation of the closed time series. To avoid disturbances from long term variations in the AMS closed signal, only periods during which the closed signal was constant were used to determine the detection limits. This restricts the method to special situations for which the closed signal is not disturbed and also limits the number of points that can be used for the calculation. However, unlike the method described by Crosier, this method allows for the calculation of absolute values of the DL.

An example for a signal region to which this method could be applied is shown in Fig. 3.2. The red curve is the closed signal which can be attributed to methyl silicone. At the beginning of the curve the signal is flat and the standard deviation of the signal in the flat region is equal to 0.85 ng/m^3. The rest of the curve is not suitable for this method to be applied, as the signal is not constant and thus the signal itself would contribute to the standard deviation in addition to the noise.

In the next section, a method is presented which removes the trend of the signal, ideally only leaving the random noise. In Fig. 3.2 this method is indicated by the green curve which corresponds to the trend of the signal and the blue curve which is the detrended signal.

3.2 Noise Retrieval in Time Space

3.2.1 Detrending of Closed Signals by Subtraction of a Running Mean

The major problem of the retrieval of detection limits from the noise level of the closed signal are long term variations in this signal. The easiest way to eliminate

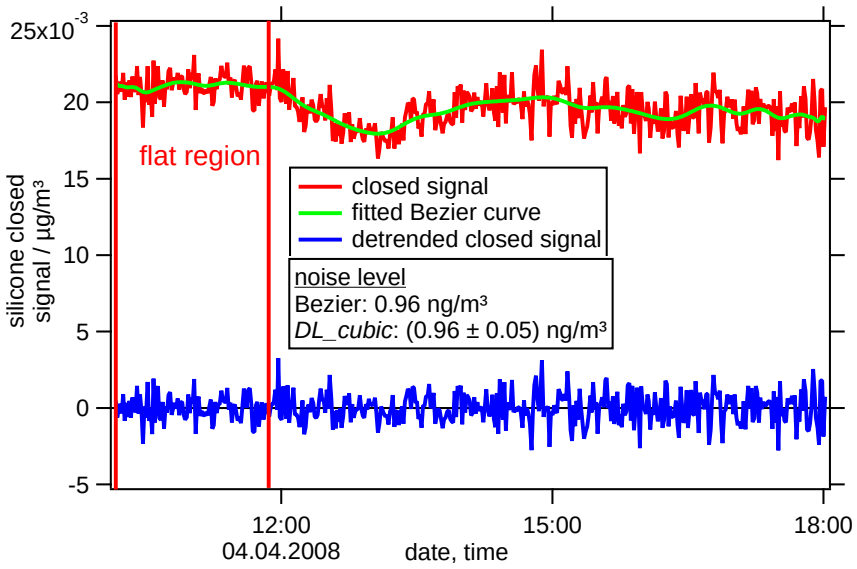

Fig. 3.2: Closed signal (red) with a Bezier curve (green, explained in Sect. 3.2.2) using the signal points as vertices for the calculation of the curve. The Bezier curve was subtracted from the closed signal resulting in a detrended curve (blue) which can be used to calculate the standard deviation of the noise of the closed time series. The region named "flat region" can be used to directly estimate the closed signal noise level by calculating the standard deviation of the closed signal. The noise level calculated by the Bezier curve detrending and the *DL-cubic* algorithm are shown on the graph. They agree perfectly.

these variation is to subtract a running mean from the signal and thus detrending it. Figure 3.2 shows the principle of the detrending. The red curve is the closed signal including long term variations and the green curve is a detrending curve. The blue line shows the signal after removing the long term variations by subtracting the green curve which only includes the long term trend. The calculation of the green curve, a Bezier spline, is explained in detail in the following. After the detrending, the standard deviation of the detrended curve can be calculated, as ideally only the noise is left and no additional apparent noise amplitude is included into the calculation of the standard deviation due to the long term variations. Several moving average window functions (box and binomial of different widths) have been tested in order to find an optimal detrending curve, but none of them seemed to perform well for all situations. An example is given in Fig. 3.3. The same window function is used on a sine of one period (upper graph) and a sine of two periods (lower graph). In the situation of the upper graph, the estimated noise after the detrending is close to the standard deviation of the input noise. In the lower graph, the noise level is overestimated. The major challenge is to find a detrending function which is sensitive to the trend of the signal but does not lead to a subtraction of parts of the

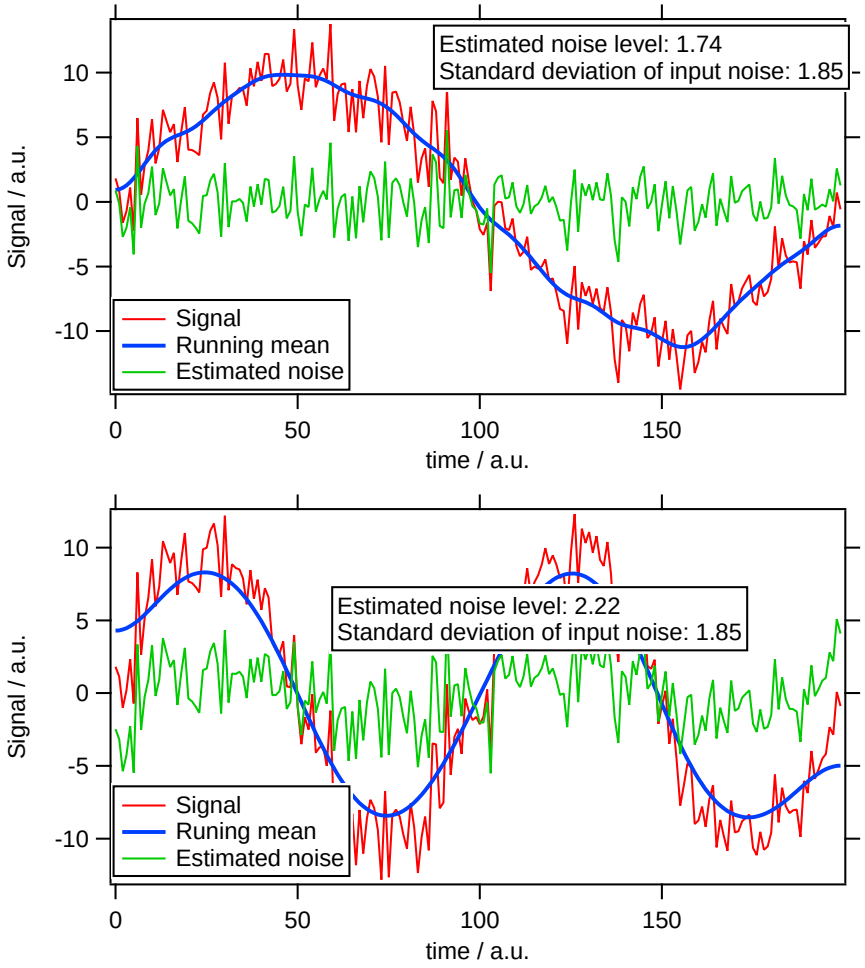

Fig. 3.3: Illustration of the problem to find a running mean which detrends a curve well in all situations. Upper graph: Using a binomial running mean window with a width of 50 points detrends the curve well. Lower graph: The same running mean window used in this curve results in an overestimation of the noise level.

noise. When using running means, a compromise between these to objectives has to be found, by adjusting the number of points averaged into a running mean bin.

3.2.2 Detrending of Closed Signals Using Bezier Splines

In random checks, it was not possible to find a running mean window which performed well in most situations. However, tests with Bezier splines as detrending function seemed to yield good results for many of the first exploratory tests. Bezier splines are a standard tool in computer graphics. They have originally been developed for Computer-Aided Design (CAD) to design car models. In the example of Fig. 3.3, the detrending using a Bezier spline results in a estimated noise level of 1.74 for the upper graph, which is identical to the result of the running mean that

worked fine. For the lower graph, the detrending with the Bezier curve resulted in an estmated noise level of 1.80. This is even closer to the standard deviation of the input signal as for the running mean example. The Bezier splines were calculated using the points of the signal as the vertices of the defining pologonal line. Normal splines interpolate vertices, meaning that they create a smooth curve which passes through all of its defining points. Bezier splines do not interpolate the vertices, whcih in this thesis correspond to the signal points. They form curves which lie in between the vertices and are only attracted towards these points. The major difference between this method and a least square regression is that no model function of the data is needed to obtain the curve. Figure 3.2 shows a closed signal with the corresponding Bezier curve and the detrended closed noise signal. Mathematically a Bezier curve or Bernstein-Bezier-curve $\vec{r}$ is defined as (see Bronstein et al., 2008, p. 1007):

$$\vec{r}(z) = \sum_{i=0}^{n} B_{i,n}(z)\vec{P}_i, \quad 0 \leq z \leq 1 \tag{3.4}$$

with $\vec{P}_i$ being the polygon defining the curve, which in our case is the closed signal. z is a parameter referring to the position on the curve with $z = 0$ being the starting point and $z = 1$ the end point of the curve. The parameter z is not the x position on a graph. $B_{i,n}(z)$ are the Bernstein polynomials defined as:

$$B_{i,n}(z) = \binom{n}{i} z^i (1-z)^{n-i}, \quad 0 \leq z \leq 1 \quad (i = 0, 1, \ldots, n) \tag{3.5}$$

Calculating Bezier Curves: The de Casteljau Algorithm

The defining equation of the Bezier curves are shown for completeness. Calculating Bezier curves by directly using Eq. (3.4) is unusual. Typically special algorithms are used to determine Bezier splines. In this work, the calculation of the Bezier curves is performed using the de-Casteljau-algorithm, developed by Paul de Faget de Casteljau in the early 1960's at Citroën. A description of the de-Casteljau-algorithm is given at Schwarz and Köckler (2006). An very comprehensive description is given at Wikipedia (2011). The text of the original patent (de Casteljau, 1959) was not available. As the de-Casteljau-algorithm is not commonly applied in the field of aerosol science, it is described here in more details referring to Fig. 3.4.

The figure shows the construction of one single point of a Bezier curve. In a), the blue polygonal line $\vec{P}_i$ from Eq. (3.4) corresponds to the signal to be detrended. It is used to define the Bezier curve. The first step of the construction is to determine the red points which are situated half way between the blue vertices $\vec{P}_i$. These points

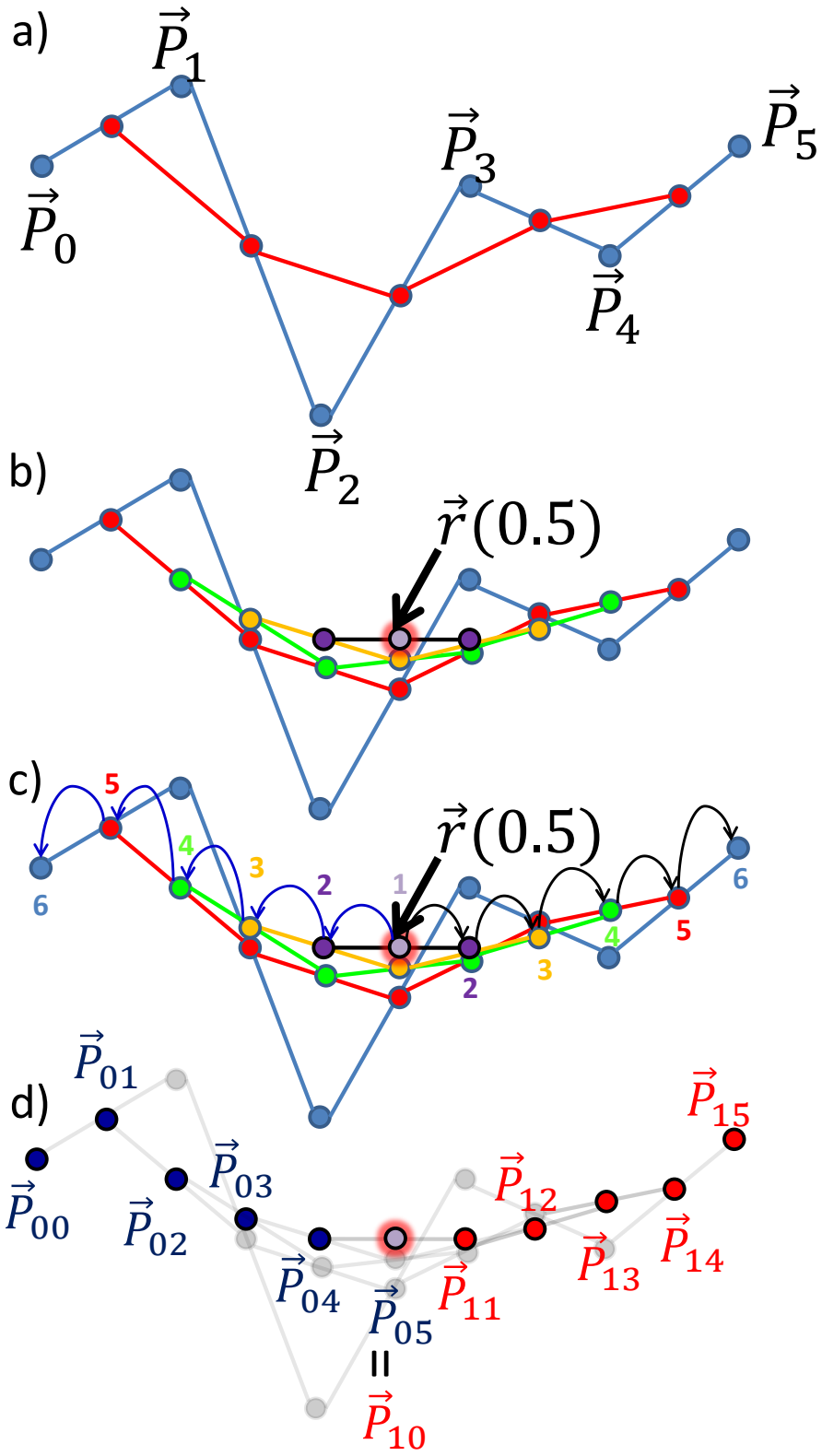

Fig. 3.4: Schematics of the construction of one point of a Bezier curve. The blue points represent the signal which is smoothed.

form a new polygonal line which has one point less than the original polygonal line $\vec{P}_i$. Similar to the constrauction of the red polygonal, again, the points situated half way between the points can be used to construct a new polygonal. This polygonal has one point less than the red polygonal. It is marked in green in Fig. 3.4b. By iterating the procedure, the degree of the polygonal lines is reduced by one in every iteration step until only one single point is left. This is the first point $\vec{r}(0.5)$ of the Bezier curve.

Using points which were determined during the calculation of the first point, two additional points on each side of the first point can be calculated. The procedure to find these points is illustrated in Fig. 3.4c. The first vortex defining the new point on each side of $\vec{r}(0.5)$ is $\vec{r}(0.5)$ itself. The second defining vortex is the purple point to left of $\vec{r}(0.5)$. It is the closest point on the left of $\vec{r}(0.5)$ which is connected to this point by a line. The third vortex is obtained by again moving to the left of the second vortex allong the yellow connecting line to the yellow point. By moving to the left allong the connecting lines, all the new vertices defining the point on the left are determined. The last vortex is the first point of the signal (blue point on the left). The same procedure can be used on the left of $\vec{r}(0.5)$ to obtain the defining vertices for the new point on the right. In Fig. 3.4d, the two new polygonal lines are marked in blue and red, respectively and share the point $\vec{r}(0.5)$. These two polygonal lines can be used to calculate two further points $\vec{r}(0.25)$ and $\vec{r}(0.75)$ on each side of $\vec{r}(0.5)$ using the same procedure that was used to determine $\vec{r}(0.5)$. By further iterating this procedure, additional points of the Bezier spline can be calculated, until the desired precision is reached. In every iteration step k, 2^k new points are obtaned. In this work the desired number of points was the lowest possible number which was higher than the number of signal points which were smoothed. Before subtraction from the signal, the Bezier curve needs to be calculated at the positions of the points of the signal. This was done using linear interpolation.

Test of the Bezier Detrending Method

Prior to its application to determine detection limits, the Bezier detrending method was validated for a set of realistic signals. These tests showed that the simple Bezier curves do often not properly detrend the noise and some modifications are proposed to improve the detrending. However, the Bezier curves, although being an improvement compared to simple moving averages, proved to be inappropriate for a reproducible detrending. Hence a different method is developed in Sect. 3.2.3.

To test if a signal detrended with a Bezier curve does really correspond to the noise of the curve, this method was tested on artificial, generated signals with Gaussian

Table 3.1: Test functions used for the evaluation of the performance of the Bezier detrending method. The first five curves are signals which produce visually good detrending (EXP, 2EXP, EXPX2, GAUSS, QUAD) while the following three functions are visually badly detrended. The last function is a simple constant signal with noise, representing the extreme case of no variation of the signal. l is the length of the signal.

function name	equation
EXP	$y = \exp(-0.005x)$
2EXP	$y = 0.5\,(\exp(-0.005x) + \exp(-0.0025x))$
EXPX2	$y = \exp(-0.01x^2)$
GAUSS	$y = 0.5 + 0.25\exp(-0.0005\,(x - l/2)^2)$
QUAD	$y = 2 \times 10^{-5}\,(x - l/2)^2 + 0.5$
SIN2EXP	$y = \left(1 + 0.2\sin(2\pi\frac{x}{l})\right)\exp(-0.0025x)$
SSINEXP	$y = 0.5\left(1 + 0.2\sin(2\pi\frac{x}{l}\sin(2\pi\frac{x}{l}))\right)\exp(-0.0025x)$
SINEXP	$y = \left(1 + 0.2\sin(2\pi\frac{x}{l})\right)\exp(-0.0025x)$
FLAT	$y = 0.5$

noise added. Figure 3.5 shows a schematic of the test for the detrending method. In a first step, a signal without noise was generated (Fig. 3.5a). In the second step, a set of random numbers from a Gaussian distribution was generated (Fig. 3.5b). These random numbers simulate random noise and were added to the signal from step one (Fig. 3.5c) (third step). In the fourth step, the signal with the noise is used as polygonal line for the calculation of a Bezier curve (Fig. 3.5d). This Bezier curve is subtracted from the signal with the random numbers to get an estimation of the noise added to the signal in the fifth step (Fig. 3.5e). The standard deviation of the estimated noise (σ_{est}) is calculated and compared to the standard deviation of the noise (σ_{input}) from step two (Fig. 3.5b). Step two to five are iterated several times for the same signal. Every time, a new set of random numbers with the same amplitude is generated using a set of random numbers generated by the the IGOR function gnoise(). The relative difference ($\Delta\sigma_{rel}$) between σ_{input} and σ_{est} after the detrending is calculated using Eq. (3.6):

$$\Delta\sigma_{rel} = \frac{\sigma_{est} - \sigma_{input}}{\sigma_{input}} \tag{3.6}$$

The signals used for the tests are shown in Tab. 3.1 and in Fig. 3.6, together with the detrending functions. The first five signals (EXP, 2EXP, EXPX2, GAUSS, and QUAD) represent situations in which the detrending was expected to work well. These signals do not have any points of inflexion[3]. Points of inflexion showed to be

[3]Point of inflexion: Locations at which the second derivative is zero.

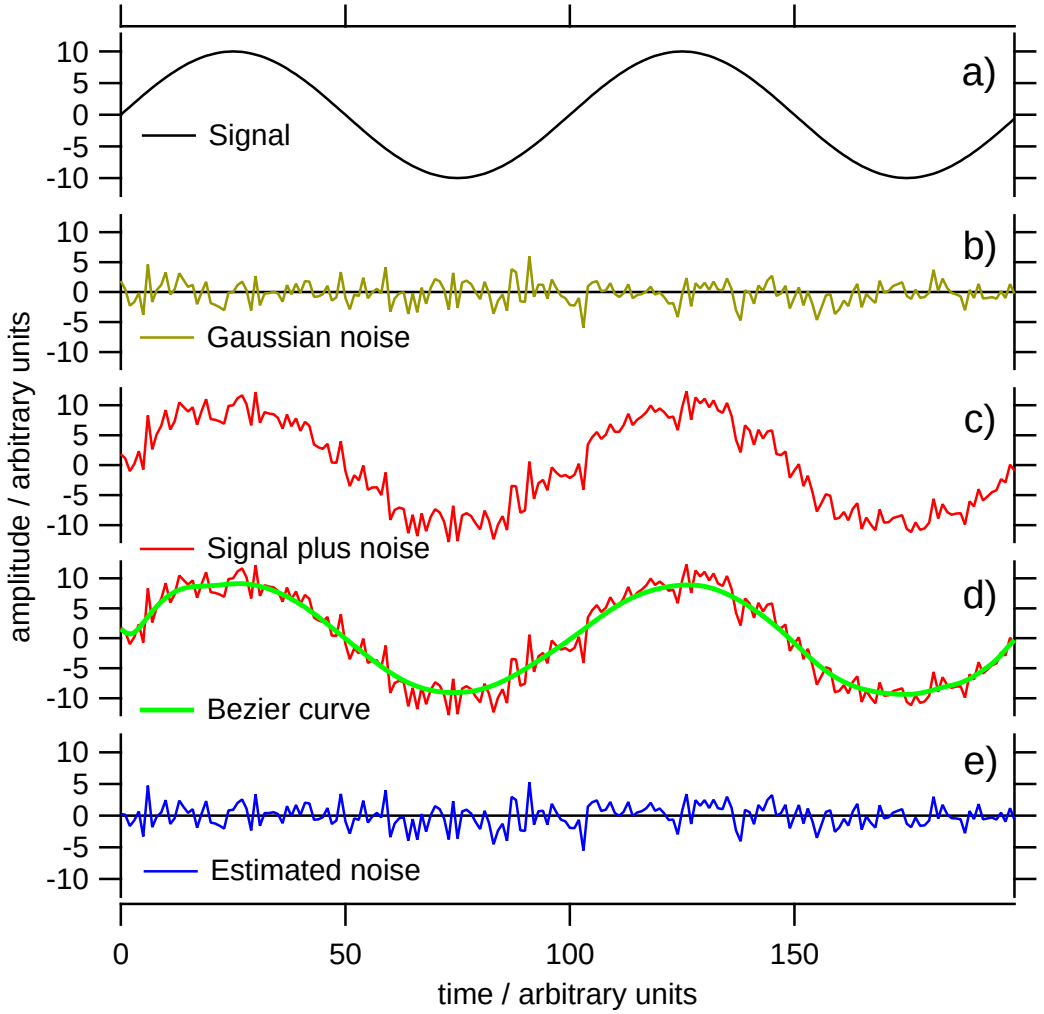

Fig. 3.5: a) Generated signal. b) Generated Gaussian noise. c) Generated signal with generated nosie added. d) Curve from "c)" with Bezier curve. e) Estimated noise after the detrending using the Bezier curve.

the most difficult feature to detrend in the first tests, especially in situations when only few signal points were available per inflexion point. An example of a curve including inflexion points for which the detrending works fine is the curve in Fig. 3.5. In this case, 50 signal points were available for every inflexion point. On each of the graphs $\Delta\sigma_{rel}$ is indicated for the special set of random numbers added to the function shown in the graph. For all of these "simple" cases, the noise level was underestimated.

Each test function from Tab. 3.1 was used 20 times with different sets of random numbers. The estimated noise levels were compared to the input noise levels. For each function, $\Delta\sigma_{rel}$ was calculated for every set of random numbers. Figure 3.7 summarises the averages of the relative deviations $\Delta\sigma_{rel}$ together with the standard

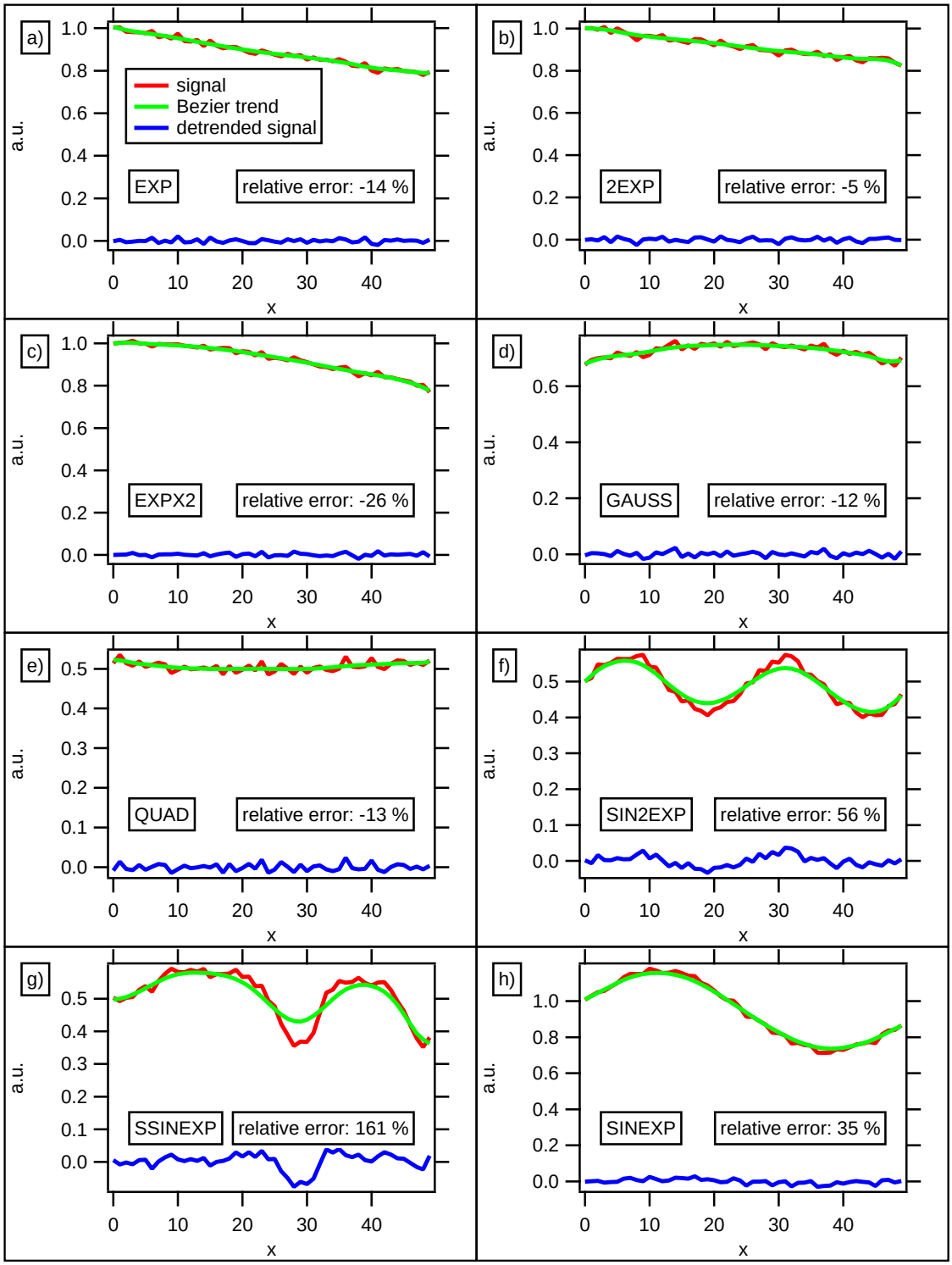

Fig. 3.6: Generated signals with normal noise with a standard deviation of 0.01. Each figure shows the signal together with an attempted detrending with a Bezier curve calculated directly using the signal points as vertices. The signal equations are listed in Tab. 3.1. The relative errors were calculated using Eq. (3.6)

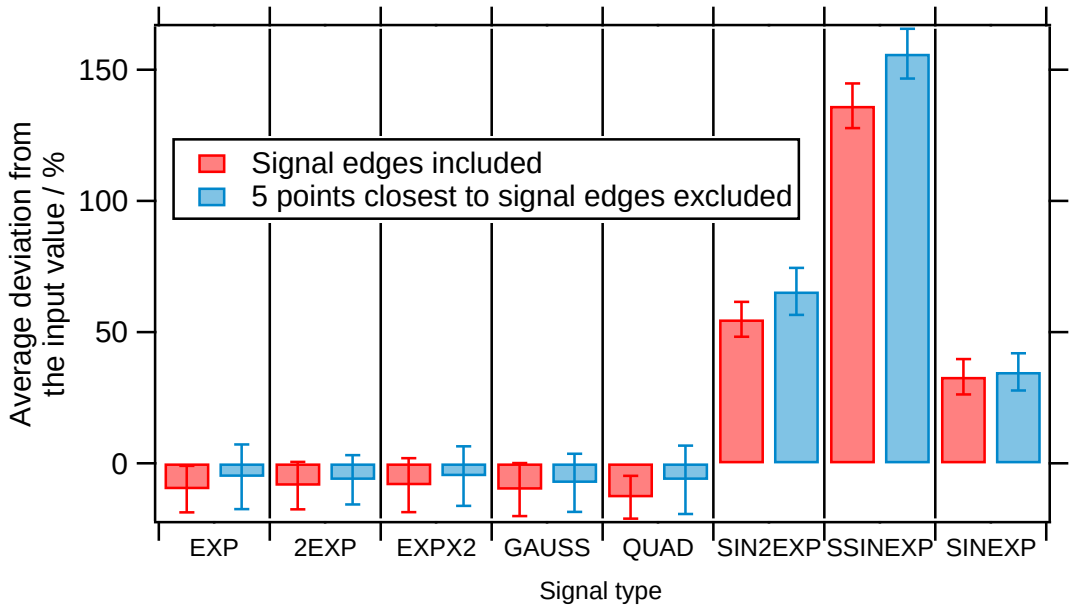

Fig. 3.7: Summary of the results from the tests of the noise level determination using Bezier curves to detrend the signal. For each function from Tab. 3.1 the average relative deviation of the estimated noise from the input noise (Eq. (3.6)) is presented. The red bars were obtained when the whole detrended signal was used to estimate the standard deviation. The blue bars refer to the situation that the 5 points closest to the signal edge were omitted in the calculation of the estimated noise. This way, disturbances from the signal edges were avoided.

deviation for each test function (error bars). The red bars in Fig. 3.7 refer to signals detrended with a Bezier curve where the whole signal interval was used to estimate the noise level. In addition, the blue bars corresppond to the average relative deviations, if the 5 point closest to the edge of the signal were excluded in the calculation of σ_{est}. This is dicussed later. The standard deviation of the mean of the $\Delta\sigma_{rel}$ would be smaller by $\sqrt{20}$ than the error bars shown in Fig. 3.7. This shows that the estimated noise for the first five signals is biased to low values in average.

In a realistic signal, inflexion points are present and thus a good detrending method must be able to catch these features correctly. Using the functions SIN2EXP, SSINEXP, and SINEXP the effect of inflexion points is analysed. Fig. 3.6 shows that in these test cases the detrending has major problems to catch all the features of the trend. The detrended curves still include part of the signal and thus the noise level is overestimated. This behaviour is also confirmed by the test summary in Fig. 3.7, where the functions SIN2EXP, SSINEXP, and SINEXP show a large overestimation of the noise level.

Attempts to Optimise the Bezier Detrending Method

Reduction of disturbances from the signal edges

The first test series show that the straightforward calculation of the Bezier curves suffers from two issues. First, for signals without any inflexion points (Fig. 3.6a-e) the method results in an underestimation of the noise level. Second, for signals with inflexion points of a few signal points (Fig. 3.6f-h) the noise is overestimated. The underestimation can partially be explained by the property of the Bezier curves to extrapolate the vertices at the edge of the curve. Furthermore, vertices close to the edge attract the curve much stronger than those in the middle of the signal. To reduce this effect, the noise level of the 8 signals introduced above was calculated without using the five points closest to the signal edges on each side of the signal, respectively. The blue bars in Fig. 3.7 show the average results of this modified method. For all signals which underestimated the noise level, this method results in an improvement. However, as expected, those signals that tend to overestimate the noise level become even worse.

A drawback of ignoring the points at the edge of the signal is that the information of these points is lost. Therefore, as an alternative method, the signal was extrapolated linearly on each side prior to the calculation of the Bezier curve. However, the standard deviation was only calculated for the part of the detrended curve which originates from the signal. The extrapolation was done by calculating a linear fitting curve through the 10 points closest to the signal edges. The number of extrapolated points was 20. This extrapolation prevents the edges of the signal to be the edges of the Bezier curve, reducing the effect of the underestimation similarly to ignoring the edges. Fig. 3.8 shows an example of a prolonged signal with the corresponding detrending. In this specific case, the underestimation was reduced from $-28\,\%$ to $-24\,\%$.

Optimisation of the locations of the vertices

Despite the elimination of the boundary effects, the noise level is still systematically underestimated for the five first test cases. Furthermore, the existance of inflexion points in the functions SIN2EXP, SSIN2EXP, and SINEXP resulted in drastic overestimations. The underestimation can be lowered by decreasing the number of vertices used for the Bezier curve. This effectively reduces the degree n (Eq. (3.4)) of the polynomial used to interpolate the curve an thus it is less sensitive to the short variations of the curve. However, with the reduction of the number of vertices, the signal points can no longer be used as vertices. It is thus necessary to determine new vertices which can afterwards be fitted by using standard fitting routines. The

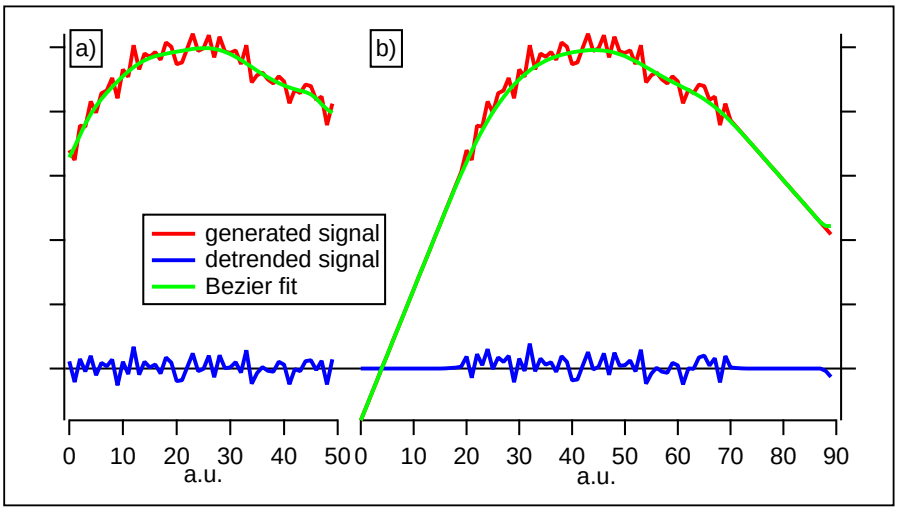

Fig. 3.8: a) Generated signal with Bezier detrending. The standard deviation is underestimated by 28 % b) Generated signal with linearly extrapolated edges which reduce the underestimation of the noise standard deviation to 24 %.

objective is to improve the detrending of signals with inflexion points along with reducing the degree of freedom of the curve. Therefore, the vertices must be set at those x-values at which the major changes of the signal take place. These are the locations of the roots[4] of the derivatives of the signal.

In practice, the calculation was done as follows: In the first step a Bezier curve was calculated from the signal as described above to get a rough estimation of the real signal. This Bezier curve was used to calculate the roots of the first, the second, and the third derivative. These roots were used as the x-positions of the new vertices. The y-values of the vertices were initialised with the first value of the signal. The fitting algorithm of Igor (WaveMetrics, Inc. Lake Oswego, Oregon, USA) quickly converges to a good approximation of the curve. Nevertheless, the Bezier curve needs to be calculated several times, which causes the fitting to take up to two minutes for a signal of only 50 points on an Intel® Core™ 2 Duo CPU with two 2 MHz processor cores. If the signal is composed of 400 points, the computation time expense is raised to up to a quarter of an hour on the used computer.

The method using a Bezier fitting function was tested using optionally the x-locations of the first three derivatives, the first two derivatives or the second and the third derivative. For all three choices of the vertices's x-coordinates the signal edges were used with and without a linear extrapolation of the signal edges. Table 3.2 shows a compilation of the effects of the combination of different optimisation attempts. Only the functions FLAT, as the extreme case for underestimation effects,

[4]Roots of a function: Positions where the function is zero.

Table 3.2: Relative errors (Eq. (3.6)) of a subset of the Bezier fitting tests in %. "der..." refers to the derivatives used for the determination of the locations of the vertices. "long" means that the signal was extrapolated by 20 points to either side and short means that no extrapolation was done.

	der1-3		der1-2		der2-3	
function name	long	short	long	short	long	short
FLAT	-21	-32	-19	-28	-17	-29
SINEXP	1	-10	76	12	6	-6
SSINEXP	86	-12	231	154	217	26

as well as SINEXP and SSINEXP representing functions which typically produce a large overestimation were evaluated.

The use of the second and third derivative without shortening of the signal seems to work best on average. However, the FLAT signal noise is still underestimated by -29 %. As expected, the use of more derivative roots reduces the estimated noise level. As the number of vertices determined this way can vary strongly from signal to signal, the results of the test cases show a large scatter. The results shown in Tab. 3.2 originate from only one test run each. Only a short set of tests was performed, as the results of the few initial test cases were not satisfactory enough to justify the high amount of processing time larger tests would cost.

Test of the Reliability of the Determined Noise Levels

The preceding tests show that it is very difficult, if not impossible, to find parameters for the detrending curves that perform well in all realistic cases. Nevertheless, on many of the tested artificial signals, like the signal in Fig. 3.4, the method the method worked fine. If it were possible to determine which detrended signals represent good estimations of the noise, the results of the detrending could at least be used for these situations. As the noise of the signal is distributed normally (this is certainly the case for the test signals and it should be a good assumption for the real AMS signals), the detrended signals should also be distributed normally. To test if the normality of the signal is a good proxy for the quality of the detrended signal, the χ^2-test was applied to the detrended signal. When the signal was strongly overestimated, the normality hypothesis did only reach a significance level below 0.05, which is the typical rejection condition. However, in these situations the detrended signal was visually contaminated by long term variations and thus it was obvious that the detrending failed even without the test. In those cases where the signal was underestimated, the χ^2-test still yielded significance levels of more than

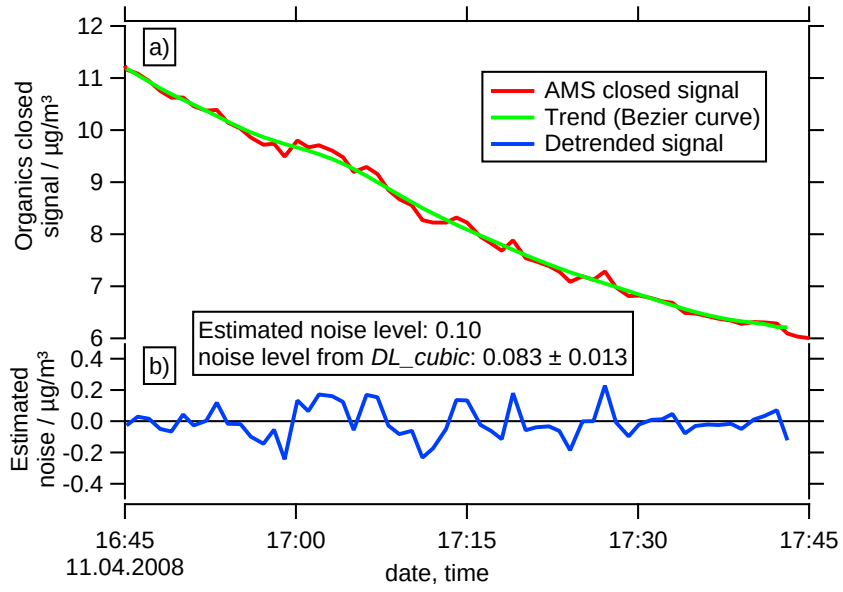

Fig. 3.9: Example of a situation in which the Bezier method worked fine. a): Signal (red) with a Bezier curve. Middle graph: Good detrended signal.

0.95. From these findings, the test for normality cannot be considered to be a useful proxy for bad detrending.

Limits of the Bezier Detrending Method

All detrending methods discussed above have the disadvantage that they result in large underestimations or overestimations in cases where the detrended signal looks fine. "Fine" means that the detrended signal does not show any features of the long trend signal and the χ^2-test did not reject the hypothesis that the detrended signal belongs to a Gaussian distribution. In order to overcome these problems, a new detrending method called *DL-cubic* was developed. The detrended signal calculated by the *DL-cubic* method is analytically linked to the standard deviation of the noise of the signal. However, it no longer generates an estimation of the signal without noise. A comparison of the Bezier detrending method to the *DL-cubic* method shows that in some cases the Bezier method resulted in good estimation of the noise levels, even on real signals. An example is presented in Fig. 3.9. It shows an AMS organics closed signal (red line) recorded during the FROST1 measurement campaign at the IfT in Leipzig in Spring 2008. In addition, the detrending Bezier curve is shown in this graph (green line), as well as the detrended signal (blue line). The standard deviation of the blue line is equal to 0.10 µg/m^3. This is a slight but acceptable overestimation compared to the noise level calculated with the

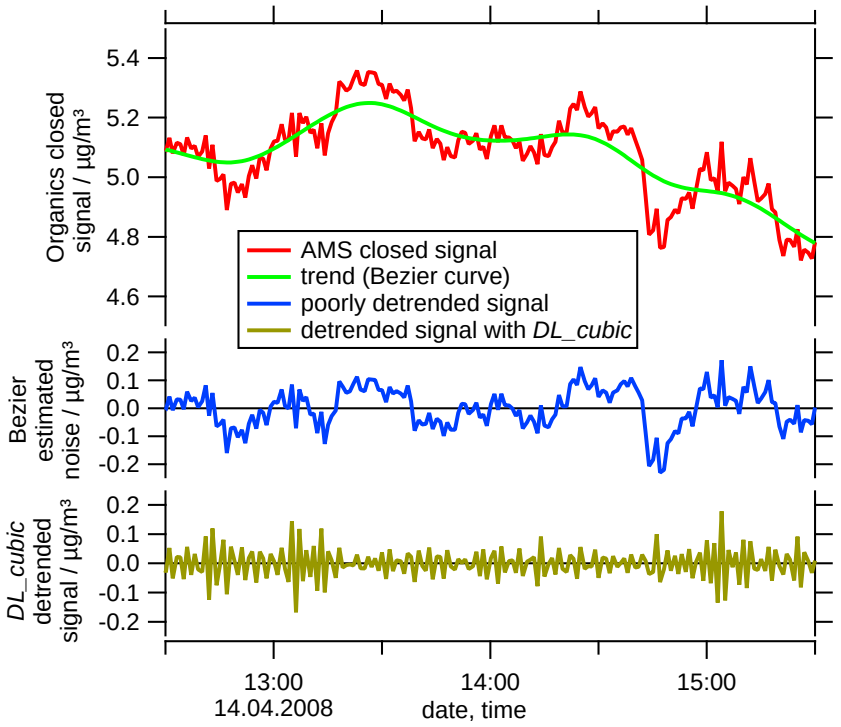

Fig. 3.10: Example of a situation in which the Bezier method worked bad. Upper graph: Signal (red) with a Bezier curve. Middle graph: Badly detrended signal. Lower Graph: Alternative detreding using the *DL-cubic* .

DL-cubic-method (0.083 ± 0.013 µg/m^3). However, Fig. 3.10 shows the organics closed signal of the AMS, recorded three days later during the same campaign. For this curve, the Bezier detrending fails. The noise level is estimated to 0.071 µg/m^3 while the *DL-cubic* yields a noise level of 0.035 ± 0.003 µg/m^3. In addition to the Bezier detrending, the detrended signal using the *DL-cubic* method is shown in the lower graph. In contrast to the detrended signals of the Bezier method, it does not correspond to the noise of the curve. However, it does not show the long term trends of the signal, which are visible for the Bezier detrended signal.

In favourable situations, the Bezier detrending method can thus give good approximations of the noise and in addition yield an approximation of the signal without noise. The drawback of the method is the inability to determine when the Bezier method worked fine and when it failed. Nevertheless, the trends of the Bezier curve can be used as good approximations of the real signals, if the noise level was correctly determined. If this is the case needs to be determined using an independent method to determine the noise level. However, finding the signal without noise was not the goal of this work. If the noise level is already known, mathematically more powerful methods to determine the trend of a signal exist, without knowing the exact fitting

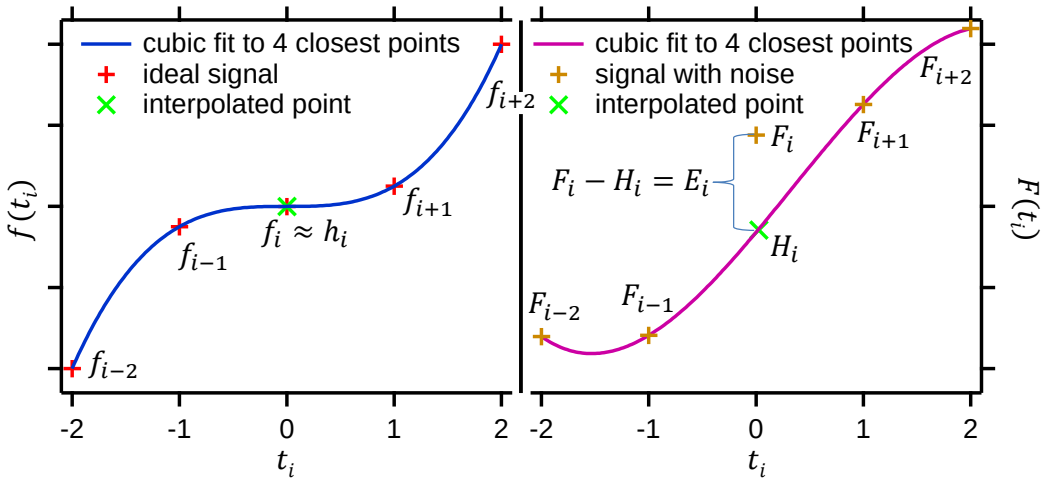

Fig. 3.11: Local fit of a signal by a third order polynomial with the centre point omitted. The green points h_i and H_i mark the interpolated central points. For the ideal signal f (left graph) it is approximately equal to the central point of the curve. In the case of a real signal with noise F, F_i and H_i differ by E_i.

function. An example would be Generalised Additive Models Wood (2006). For the needs of this thesis, the Bezier detrending method is thus not an optimal choice and therefore the new method *DL-cubic* was developed and is presented in the following section.

3.2.3 Derivation of a Cubic Detrending Algorithm

In the following sections an algorithm for the determination of the noise level of a curve is presented and its application to AMS detection limits is demonstrated. The algorithm was named *DL-cubic* as it is mainly used to calculate detection limits of the AMS using a detrending of the AMS closed signal by a local signal interpolation with a cubic function. Originally, the algorithm was designed to automatically find locations of curves, which cause problems to the Bezier algorithm, because the signal abruptly changes its direction. For this purpose, the local deviation of the curve from a cubic function was probed. The derivation from a cubic function was used as a cubic function is the first polynomial which includes an inflexion point. After a mathematical analysis, it was possible to determine an analytical relation between the probed value and the noise level itself.

The main condition for the application of the *DL-cubic* algorithm is that the time scale of variation of the signal is clearly longer than the time scale of the noise. The time scale of the noise is equal to the sampling interval. Furthermore, it must be possible to locally approximate the signal by a polynomial of the third order. In the AMS the long term variations of the signal are mainly caused by substances accu-

mulating in the instrument residual gas as well as by slowly evaporating substances, which accumulate on the vaporiser. Additionally, the detector ages on time scales of hours to days. Fig. 3.11 illustrates the local fitting of an ideal signal f without noise (left) and a real signal F with noise (right). In the situation without noise, the fit is calculated without using the point f_i at location $t_i = 0$. The fit is nearly perfectly interpolating the point f_i at location 0 by the point h_i, while for the real signal the interpolated point H_i and F_i differ by the quantity E_i.

The quantities used in the derivation are defined as follows. The function $f(t)$ represents an ideal signal without noise and $F(t)$ is the sum of the function $f(t)$ and the Gaussian noise function $\epsilon(t)$.

$$F(t) = f(t) + \epsilon(t) \tag{3.7}$$

The third order local polynomial fitting functions to $f(t)$ and $F(t)$ are $h(t)$ and $H(t)$, respectively. The signal is recorded at discrete time steps t_i. The values of the functions f,F,h, and H at the time t_i are abbreviated as f_i,F_i,h_i, and H_i respectively and the time steps of the signal are assumed to be equidistant with $t_j - t_i = j - i$. Without limitation of generality, it ca be assumed that all time steps have a length of unity. However, the assumption of equidistant time steps is a constraint to the applicability of the algorithm. The fitting parameter a_i, b_i, c_i, and d_i of the local polynomial $h_i = a_i t_i^3 + b_i t_i^2 + c_i t_i + d_i$ are unambiguously determined by the following system of equations (four equations in short notation using the symbol $\mp$):

$$\begin{cases} f_{i\pm1} = a_i(t_i \pm 1)^3 + b_i(t_i \pm 1)^2 + c_i(t_i \pm 1) + d_i \\ f_{i\pm2} = a_i(t_i \pm 2)^3 + b_i(t_i \pm 2)^2 + c_i(t_i \pm 2) + d_i \end{cases} \tag{3.8}$$

The equations above must be true for any value of t_i, thus it can also be evaluated for the simple case of $t_i = 0$:

$$\Rightarrow \begin{cases} f_{i\pm1} = \pm a_i + b_i \pm c_i + d_i \\ f_{i\pm2} = \pm 8a_i + 4b_i \pm 2c_i + d_i \end{cases} \tag{3.9}$$

If the assumption that the signal can be locally approximated by a cubic curve is fulfilled, it is obvious that $f_i - h_i \cong 0$. Equation (3.9) can be rewritten for $F(t)$ and $H_i = A_i t_i^3 + B_i t_i^2 + C_i t_i + D_i$:

$$\begin{cases} F_{i\pm1} = \pm A_i + B_i \pm C_i + D_i \\ F_{i\pm2} = \pm 8A_i + 4B_i \pm 2C_i + D_i \end{cases} \tag{3.10}$$

For $t_i = 0$ the local fitting functions h and H at the location i simplify to $h_i = d_i$ and $H_i = D_i$. Solving the system of equations (3.9) yields the values of the fitting parameters as a function of f and F respectively and thus h_i and H_i are determined:

$$H_i = D_i = \frac{2}{3}F_{i-1} - \frac{1}{6}F_{i-2} + \frac{2}{3}F_{i+1} - \frac{1}{6}F_{i+2} \tag{3.11}$$

$$h_i = d_i = \frac{2}{3}f_{i-1} - \frac{1}{6}f_{i-2} + \frac{2}{3}f_{i+1} - \frac{1}{6}f_{i+2} \tag{3.12}$$

The difference E_i between F_i and H_i can now be expressed as a function of the signal F:

$$E_i = F_i - H_i = F_i - \left(\frac{2}{3}F_{i-1} - \frac{1}{6}F_{i-2} + \frac{2}{3}F_{i+1} - \frac{1}{6}F_{i+2}\right) \tag{3.13}$$

$$\overset{(3.7)}{=} f_i + \epsilon_i - \frac{2}{3}f_{i-1} + \frac{1}{6}f_{i-2} - \frac{2}{3}f_{i+1} + \frac{1}{6}f_{i+2} - \frac{2}{3}\epsilon_{i-1} + \frac{1}{6}\epsilon_{i-2} - \frac{2}{3}\epsilon_{i+1} + \frac{1}{6}\epsilon_{i+2} \tag{3.14}$$

The bottom graph in Fig. 3.10 shows the E_i values determined for the signal presented in the top graph of this figure.

From Eq. (3.12) it follows that:

$$-\frac{2}{3}f_{i-1} + \frac{1}{6}f_{i-2} - \frac{2}{3}f_{i+1} + \frac{1}{6}f_{i+2} = -h_i \tag{3.15}$$

and thus Eq. (3.14) can be rewritten as:

$$E_i = f_i + \epsilon_i - h_i - \frac{2}{3}\epsilon_{i-1} + \frac{1}{6}\epsilon_{i-2} - \frac{2}{3}\epsilon_{i+1} + \frac{1}{6}\epsilon_{i+2} \tag{3.16}$$

With the requirement that $f_i = h_i$ in very good approximation we get:

$$E_i \cong \epsilon_i - \frac{2}{3}\epsilon_{i-1} + \frac{1}{6}\epsilon_{i-2} - \frac{2}{3}\epsilon_{i+1} + \frac{1}{6}\epsilon_{i+2} \tag{3.17}$$

This expression depends only on the noise of the signal.

Similar to the definition of the standard deviation σ: $\sigma = \sqrt{\frac{1}{n-1}\sum_{i=0}^{n-1}\epsilon_i^2}$ a quantity R (Eq. (3.18)) can be calculated using E_i. H_i (Eq. (3.11)) cannot be determined for the first two and the last two points of a signal segment used for their calculation, as two neighbouring points are necessary on each side of every F_i. Thus E has four points less than the signal segment:

$$R^2 = \frac{1}{((N-4)-1)} \sum_{i=2}^{N-3} E_i^2 \quad \text{with N: number of points of the signal} \tag{3.18}$$

$$\begin{aligned} =& \frac{1}{N-5} \sum_{i=1}^{N-3} \left(\epsilon_i^2 - \frac{4}{3}\epsilon_i\epsilon_{i-1} + \frac{1}{3}\epsilon_i\epsilon_{i-2} - \frac{4}{3}\epsilon_i\epsilon_{i+1} + \frac{1}{3}\epsilon_i\epsilon_{i+2} + \frac{4}{9}\epsilon_{i-1}^2 - \frac{2}{9}\epsilon_{i-1}\epsilon_{i-2} \right. \\ & + \frac{8}{9}\epsilon_{i-1}\epsilon_{i+1} - \frac{2}{9}\epsilon_{i-1}\epsilon_{i+2} + \frac{1}{36}\epsilon_{i-2}^2 - \frac{2}{9}\epsilon_{i-2}\epsilon_{i+1} + \frac{1}{18}\epsilon_{i-2}\epsilon_{i+2} + \frac{4}{9}\epsilon_{i+1}^2 \\ & \left. - \frac{2}{9}\epsilon_{i+1}\epsilon_{i+2} + \frac{1}{36}\epsilon_{i+2}^2 \right) \end{aligned} \tag{3.19}$$

$$\begin{aligned} =& \frac{1}{N-5} \sum_{i=1}^{N-3} \left(\epsilon_i^2 + \frac{4}{9}\epsilon_{i-1}^2 + \frac{1}{36}\epsilon_{i-2}^2 + \frac{4}{9}\epsilon_{i+1}^2 + \frac{1}{36}\epsilon_{i+2}^2 \right) \\ & + \frac{1}{N-5} \sum_{i=1}^{N-3} \left(-\frac{4}{3}\epsilon_i\epsilon_{i-1} + \frac{1}{3}\epsilon_i\epsilon_{i-2} - \frac{4}{3}\epsilon_i\epsilon_{i+1} + \frac{1}{3}\epsilon_i\epsilon_{i+2} - \frac{2}{9}\epsilon_{i-1}\epsilon_{i-2} \right. \\ & \left. + \frac{8}{9}\epsilon_{i-1}\epsilon_{i+1} - \frac{2}{9}\epsilon_{i-1}\epsilon_{i+2} - \frac{2}{9}\epsilon_{i-2}\epsilon_{i+1} + \frac{1}{18}\epsilon_{i-2}\epsilon_{i+2} - \frac{2}{9}\epsilon_{i+1}\epsilon_{i+2} \right) \end{aligned} \tag{3.20}$$

The first sum of Eq. (3.20) can be split into five sums, e.g.: $\frac{1}{N-5}\sum_{i=1}^{N-3}\epsilon_i^2$, $\frac{1}{N-5}\sum_{i=1}^{N-3}\frac{4}{9}\epsilon_i^2$, ...etc. They all correspond to the definition of the square of the standard deviation reduced to segments shorter by four points than the signal and multiplied by different factors. For example the sum of the first term yields σ^2 and the second term yields $\frac{4}{9}\sigma^2$. Summing up all terms of the first sum yields approximately $\frac{35}{18}\sigma^2$ and for $N \to \infty$ it is exactly equal to $\frac{35}{18}\sigma^2$.

In the second sum, the sum of every term tends to zero, as the distribution of the product of the ϵ_i is a normal product distribution with a mean value of zero and a standard deviation of σ^2 times the respective factor. This means that the second sum approaches zero with a standard deviation proportional to $\frac{1}{\sqrt{N-4}}\sigma^2$. The exact proportionality factor is determined numerically in Sec. 3.2.5.

The above calculations show, that $R^2 \cong \frac{35}{18}\sigma^2$ which can be rearranged using the definition of R^2 in Eq. (3.18) together with the definition of E_i in Eq. (3.13) and H_i in Eq. (3.11) to form:

$$\begin{aligned}\sigma &\cong \sqrt{\frac{18}{35}}R \\ &= \sqrt{\frac{18}{35}\frac{1}{N-5}\sum_{i=2}^{N-3}E_i^2} \\ &= \sqrt{\frac{18}{35}\frac{1}{N-5}\sum_{i=2}^{N-3}\left(F_i - H_i\right)^2} \\ &= \sqrt{\frac{18}{35}\frac{1}{N-5}\sum_{i=2}^{N-3}\left(F_i - \frac{2}{3}F_{i-1} + \frac{1}{6}F_{i-2} - \frac{2}{3}F_{i+1} + \frac{1}{6}F_{i+2}\right)^2}\end{aligned} \tag{3.21}$$

It is thus possible to approach the standard deviation of the noise of the real signal f for any interval by Eq. (3.21). This equation is only a function of the F_i values of the measured signal in the interval.

3.2.4 Computational complexity of the *DL-cubic* compared to the Bezier method

The computation time of the *DL-cubic*-algorithm scales linearly with the number of points N in the signal. For every E_i^2 (Eq. (3.14) and (3.21)) four additions and one multiplication need to be performed. The computational complexity for one E_i^2 is thus independent of the number of points $(O(1))$[5]. E_i^2 is calculated for all points of the signal except for the two first and the two last points of the signal. Thies yields a total of $N-4$ E_i^2 which are added (Eq. (3.21)). Accordingly, the number of additions is proportinal to $N-4$ $(O(N))$. The multiplication by $\frac{18}{35}\frac{1}{N-5}$ and the calculation of the square root are performed only once and are again independent of N with respect to computational time $(O(1))$. The total complexity $C_{DL\text{-}cubic}(N)$ of the *DL-cubic*-algorithm is thus:

$$C_{DL\text{-}cubic}(N) = O(1)\cdot O(N)\cdot O(1) = O(N) \tag{3.22}$$

The Bezier detrending method has a complexity of $O(N^3)$, which is shown in the following. The Casteljau algorithm has a complexity of $O(N^2)$ (Schwarz and Köckler, 2006), for the calculation of one point of the curve. The number of points

[5] $O(N^p)$ means that the time needed to compute the result of a function scales with the number of input values N to the power of p for "big" N. "Big" N means that N is big enough that lower powers on N can be ignored. Other functions of N, like $\log N$ are also possible. In the special case of $p = 0$ $(O(1))$ the computational time is independent of the number of input points N.

of the Bezier curve caluculated is proportional to the number of points of the signal ($O(N)$). The total complexity $C_{Bezier}(N)$ is thus:

$$C_{Bezier}(N) = O(N^2) \cdot O(N) = O(N^3) \tag{3.23}$$

This result shows the big improvement of the *DL-cubic*-algorithm compared to the Bezier detrending method with respect to computation time. The time to estimate the standard deviation using the Bezier method for $N = 100$, which is a typical length for AMS measurements, is thus 10^6 times the time to perform the calculation for $N = 1$. In contrast, the *DL-cubic* method only needs 100 times more time for $N = 100$ than for $N = 1$. These considerations are important for the testing of the *DL-cubic* method in the next section. Because the *DL-cubic* algorithm is very fast, it can be tested with millions of generated signals without consuming much time.

3.2.5 Test of the *DL-cubic*-Algorithm

The evaluation of the *DL-cubic*-algorithm was performed similarly to the evaluation of the Bezier detrending method. Artificial test functions were created and different sets of random numbers were added to these functions to simulate signals with noise. The algorithm was then applied to these signals to remove the trend and to calculate the standard deviation of the noise. The noise was generated using the IGOR-function gnoise() which performs a Box-Müller transformation of uniform random numbers created by the Linear Congruential generator by L'Evuyer with added Bayes-Durham shuffle (Press, 1992). As the calculation time of the new algorithm scales only linearly with the number of points used, it was possible to perform tests with a high number of test signals. Like in Sect. 3.2.2, Fig. 3.5, every test function was used multiple times. Every time a different set of random numbers of the same standard deviation was added to the function and the algorithm was applied to the resulting signal with noise.

The *DL-cubic* does not try to reproduce the set of random numbers added to the signal. Its objective is to determine the standard deviation σ_{base} of the basic population of the random numbers. In the tests it is therefore compared to σ_{base} of the random numbers, which is the input of the IGOR-function gnoise(). In contrast, the Bezier method was always compared to the standard deviation of the set of random numbers (Eq. (3.6)) which is only an estimator of σ_{base}. For every signal, the distribution of the *DL-cubic*-outputs for different sets of random numbers added to a function was calculated. If the *DL-cubic* output was accurate, the center of the distribution corresponded to σ_{base}. The standard deviation of the calculated distribution corresponds to the precision of the *DL-cubic*-results. An example of a

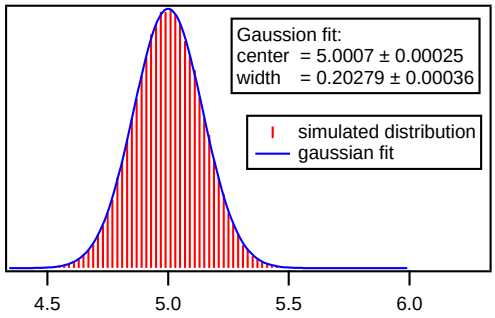

Fig. 3.12: Distribution of the result of *DL-cubic* for 100,000 signals with a length of 1000 points. The standard noise level of these signals was 5.0.

distribution is presented in Fig. 3.12. Due to the high number of sets of random numbers used with every signal function, this method yielded statistically precise statements on the accuracy and the precision of the algorithm output.

The first tests were performed using a constant zero signal-function in order to check if the algorithm works correctly if there is no disturbance from a real signal. In the following sections, *DL-cubic* is tested with different non-constant signal-functions to systematically test the influence of different types of signal-function on the accuracy of the *DL-cubic*-output. Figure 3.12 shows the distribution of the output of the algorithm for a test of 10^5 runs with a length of 1000 points. In every run, the noise was different, but it was always part of a population with a standard deviation of 5.0. The output of the algorithm statistically varies for every set of noise. A Gaussian fit to the algorithm output distribution is shown. It fits the data very well, showing that the results are distributed normally. As the maximum of the distribution is at 5.0, the *DL-cubic*-outputs are thus accurate for the test function used. The widths of the distribution of the *DL-cubic*-outputs corresponds to the standard deviation of the outputs. It is a measure for the precision of *DL-cubic* . In the following the widths is used to calculate confidence interval for the *DL-cubic*-outputs.

Figure 3.13 shows the ratio $\Delta\sigma_{base,rel}$ of the standard deviation of the algorithm outputs $\Delta\sigma_{base}$ (the width of the distribution) to the real standard deviation of the input noise σ_{base} (Eq. (3.24)) as a function of $\frac{1}{\sqrt{N-4}}$. For every point 10^5 signals of the respective length have been evaluated. The slope of the fitting curve gives the proportionality factor between $\frac{1}{\sqrt{N-4}}$ and the relative error of the algorithm results $\Delta\sigma_{base,rel}$. The proportionality of the standard deviation of the algorithm outputs $\Delta\sigma_{base}$ to $\frac{1}{\sqrt{N-4}}\sigma_{base}$ was deduced from the fact that the uncertainty of the mean of a Gaussian distribution is reduced with the square root of the number of data points used for its calculation. Furthermore, it scales with the mean value. The number of

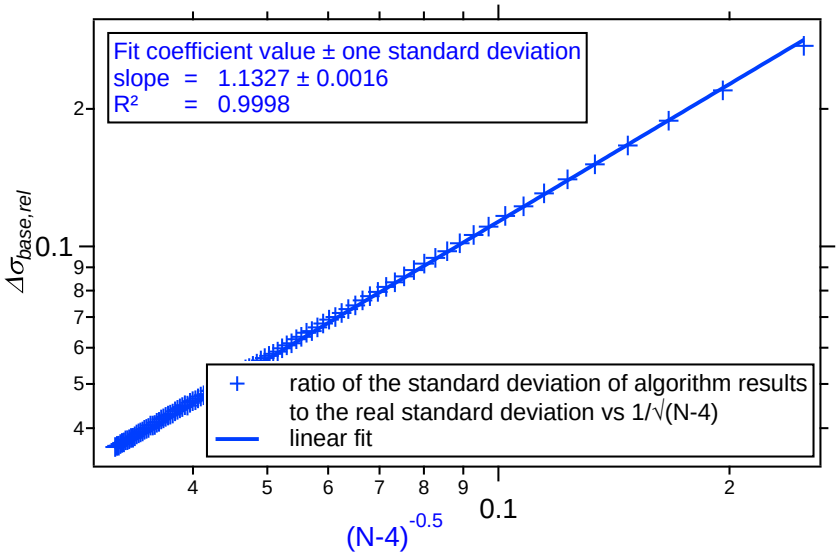

Fig. 3.13: Relative deviation $\Delta\sigma_{base,rel}$ of the *DL-cubic* output distribution (Eq. (3.24)) vs. $\frac{1}{\sqrt{N-4}}$

points that are used to calculate each sum in (3.20) is equal to $N-4$ and thus the error is proportional to $\frac{1}{\sqrt{N-4}}$.

$$\Delta\sigma_{base,rel} = \frac{\Delta\sigma_{base}}{\sigma_{base}} \tag{3.24}$$

Using the proportional constant from Fig. 3.13 one gets:

$$\sigma_{base} \pm \Delta\sigma_{base} \cong \sqrt{\frac{18}{35}\frac{1}{N-5}\sum_{i=2}^{N-3}\left(F_i - \frac{2}{3}F_{i-1} + \frac{1}{6}F_{i-2} - \frac{2}{3}F_{i+1} + \frac{1}{6}F_{i+2}\right)^2} \pm 1.1327\frac{1}{\sqrt{N-4}}\sigma_{base} \tag{3.25}$$

$\Delta\sigma_{base}$, as given by Eq. (3.25), can only be estimated by the output of the algorithm, as in the case of an application of the *DL-cubic* to real data, no statistic information is available. Thus, to get a meaningful confidence interval, it is necessary to correct the estimated standard deviations. Table 3.3 gives an overview of the symbols used for the calculation of the confidence intervals. σ_{base} is the real value of the standard deviation of the noise base population of the input signal and $\Delta\sigma_{base}$ is the uncertainty with which *DL-cubic* estimates σ_{base} as given by Eq. (3.25). $\Delta\sigma_{base}$ is thus the correct value of the uncertainty, but it is only available if σ_{base} is known. For a single signal, this is not the case as no statistical information is available. However, $\Delta\sigma_{base}$ can be estimated using σ_{algo}, which is the output of the *DL-cubic*-

Table 3.3: Overview of the symbols used to calculate the uncertainty intervals of the *DL-cubic*-algorithm .

symbol	explanation
σ_{base}	Standard deviation of the base population of the input noise
$\Delta\sigma_{base}$	Real uncertainty in the determination of σ_{algo}, from the evaluation of a high number of signals
σ_{algo}	Estimation of σ_{base} using *DL-cubic*
$\Delta\sigma_{algo}$	Estimation of the uncertainty of σ_{algo} using Eq. (3.25)

algorithm for one signal and thus an estimation of σ_{base}. This yields an estimate of $\Delta\sigma_{base}$ using Eq. (3.25). This estimate is named $\Delta\sigma_{algo}$.

In case σ_{algo} is an overestimation of σ_{base}, $\Delta\sigma_{algo}$ is also an overestimation of $\Delta\sigma_{base}$. The other way round, if σ_{algo} is an underestimation, $\Delta\sigma_{algo}$ is underestimated too. The goal of the following consideration is to find the correction factor for $\Delta\sigma_{algo}$ as a function of the desired probability that the value of σ_{algo} lies within the confidence interval. To do so, two extreme cases were considered: one case with σ_{algo} being too low by j times $\Delta\sigma_{base}$ and one case with σ_{algo} being to high by j times $\Delta\sigma_{base}$. Both cases are summarised in Eq. (3.26).

$$\sigma_{base} = \sigma_{algo} \pm j\Delta\sigma_{base} \tag{3.26}$$

$\Delta\sigma_{...}$ is proportional to $\sigma_{...}$:

$$\frac{\Delta\sigma_{base}}{\sigma_{base}} = const. \tag{3.27}$$

$$\frac{\Delta\sigma_{algo}}{\sigma_{algo}} = const. \tag{3.28}$$

As in both equations, Eq. (3.27) and Eq. (3.28), the proportionality constant is the same, the combination of these equations yields:

$$\begin{aligned} \Delta\sigma_{base} =& \frac{\sigma_{base}}{\sigma_{algo}}\Delta\sigma_{algo} \\ \overset{(3.26)}{\Longrightarrow} \Delta\sigma_{base} =& \frac{\sigma_{algo} \pm j\Delta\sigma_{base}}{\sigma_{algo}}\Delta\sigma_{algo} \\ =& \Delta\sigma_{algo} \pm \frac{j\Delta\sigma_{base}\Delta\sigma_{algo}}{\sigma_{algo}} \end{aligned} \tag{3.29}$$

Solving for $\Delta\sigma_{base}$ results in:

$$\Delta\sigma_{base} = \frac{\Delta\sigma_{algo}}{1 \mp \frac{j\Delta\sigma_{algo}}{\sigma_{algo}}} \tag{3.30}$$

or

$$j\Delta\sigma_{base} = \frac{j\Delta\sigma_{algo}}{1 \mp \frac{j\Delta\sigma_{algo}}{\sigma_{algo}}} \overset{(3.25)}{=} \frac{\sigma_{algo}}{\frac{\sqrt{N-4}}{j1.1327} \mp 1} \tag{3.31}$$

Merging the results with $j = 1$ yields:

$$= \sqrt{\frac{18}{35}\frac{1}{N-5}\sum_{i=2}^{N-3}\left(F_i - \frac{2}{3}F_{i-1} + \frac{1}{6}F_{i-2} - \frac{2}{3}F_{i+1} + \frac{1}{6}F_{i+2}\right)^2} \pm \frac{\sigma_{algo}}{\frac{\sqrt{N-4}}{1.1327} \mp 1} \tag{3.32}$$

$$\sigma_{algo} \pm \Delta\sigma_{base}$$

If $j = 1$ is chosen, this estimation does no longer give any meaningful results for the upper limit when N becomes lower than 5, because of a singularity at $N \cong 4.80$. Below this singularity the values become negative. For $j = 2$ the critical value of N is equal to 7.2 and for $j = 3$, $N_{crit} = 11.2$. Thus for values close to the respective N_{crit}, the results of the algorithm become useless.

Evaluation of the Algorithm Using Non-Constant Signals without Noise

When introducing the new method, it was stated that the time-scale of variations of the signal has to be longer than the time scale of the noise. More precisely, it must be possible to fit the signal locally with a polynomial of the third order. In the following it is shown to what extend the algorithm is able to separate the noise and the signal. As a first example, a sine wave of amplitude 1 without noise was created and the number of periods n was increased step by step to determine at which number of periods the signal was considered to be part of the noise by the algorithm (see Eq. (3.33)). The test functions had a length of 201 points.

$$f(x) = \sin\left(\frac{2\pi x}{200} \bullet n\right) \tag{3.33}$$

Figure 3.14a shows that the output of the *DL-cubic*-algorithm is clearly below 1 % of the amplitude of the sine function, down to about 6.25 signal points per inflection point. This is close to the 5 points that are used to calculate a single E_i (see Eq. (3.14)). Figure 3.14b shows a sine signal with a sample rate that is at the lower limit of the applicability of the algorithm. As a rule of thumb, the curve should have about 10 signal points per inflection point to ensure that the algorithm can be applied. These values were estimated considering the use of the *DL-cubic* algorithm

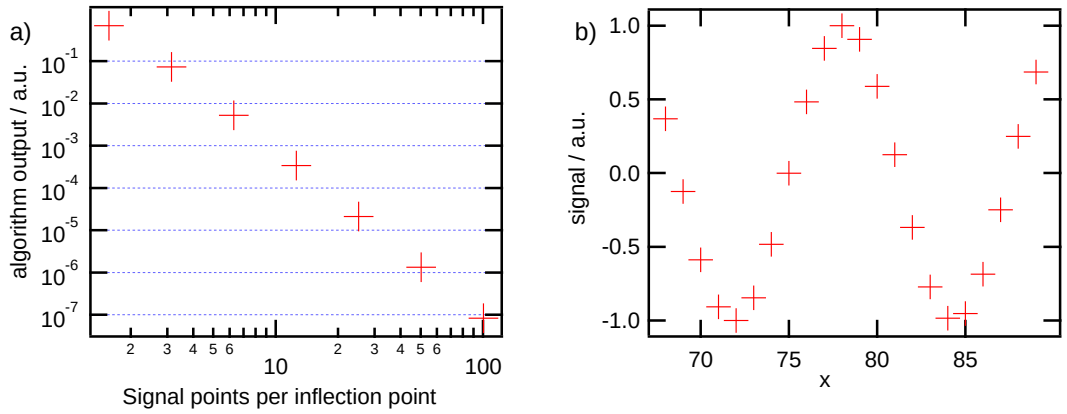

Fig. 3.14: a) Evolution of the algorithm output with increasing number of signal points per inflection point for a sine function without noise.
b) Sine function with 6.25 signal points per inflection point as an example for the lower limit of the sample rate for the algorithm to work properly.

for the calculation of AMS detection limits. An AMS closed signals, which varies as fast as the sine wave shown in Fig. 3.14b and which has an amplitude of more than ten times the noise level, is an extreme case. If *DL-cubic* is used to determine very low noise levels, one must check if the zero outputs (output on functions without noise) described in this section are not perturbing the output of the *DL-cubic* .

For the next test, some combinations of different functions have been used in order to cover realistic situations. The exact functions and scaling factors ar not important. The choice of the functions was done empirically to approximated the shape of closed signals measured by the AMS. No noise was added to these functions. The functions used were:

$$
\begin{aligned}
divers1(x) &= \exp\left(\frac{-x}{100}\right) \\
divers2(x) &= \frac{2\,(x-30)^2 + 3\,(x-50)^2 - 2.5\,(x-90)^2 - \exp\left(\frac{x}{18}\right)}{54178.2} + 0.5\sin\left(\frac{x}{10}\right) \\
divers3(x) &= divers2(x) - \sqrt{\frac{x}{200}} \\
divers4(x) &= divers3(x) - \arctan\left(\frac{x}{100}\right) \\
divers5(x) &= \frac{divers3(x) - \sinh\left(\frac{x}{100}\right)}{3.49786} \\
divers6(x) &= divers5(x) + \frac{\sin\left(\frac{2\pi}{20}x\right)}{2}
\end{aligned}
$$

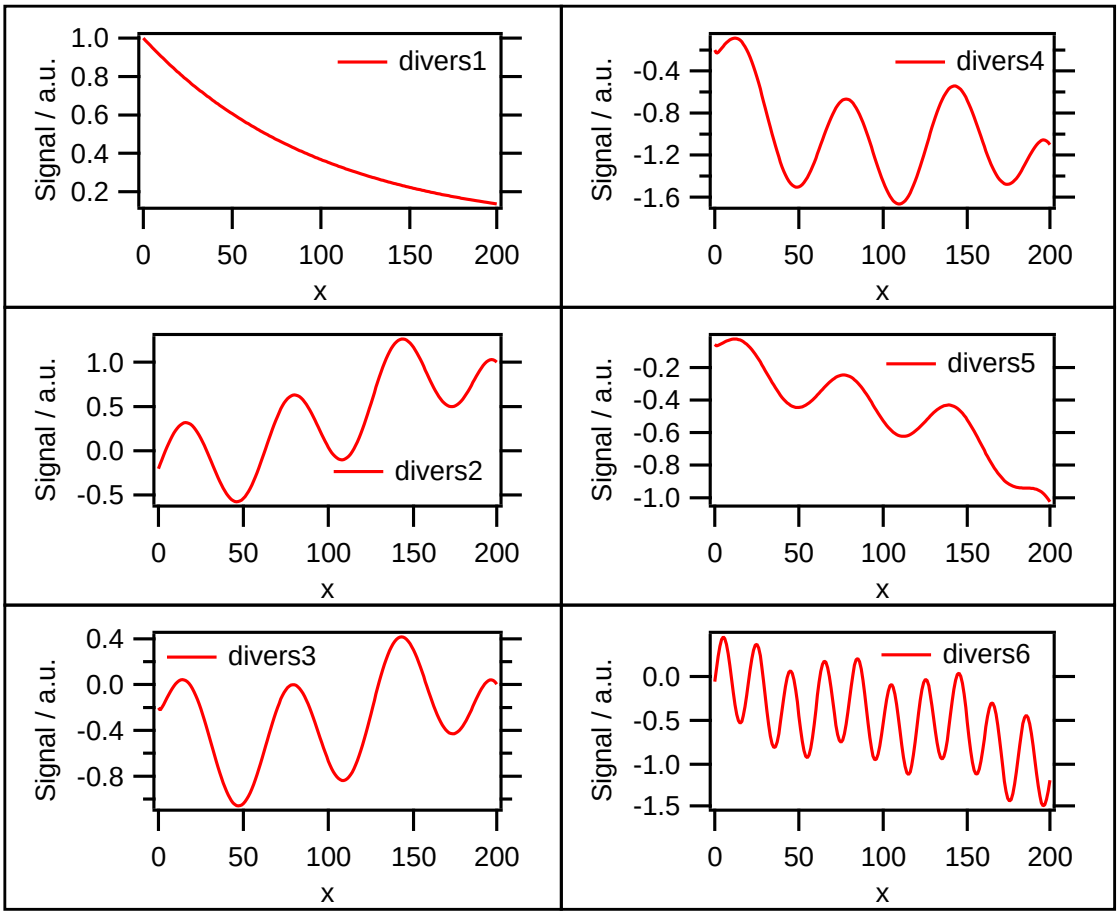

Fig. 3.15: Plots of the test functions *divers*1 to *divers*6. The output of the *DL-cubic* for these functions is shown in Tab. 3.4.

The graphs of the functions are shown in Fig. 3.15 and the outputs of the algorithm in Table 3.4. For these signals the algorithm produced the desired outputs close to zero. For example the simple exponential decay of *divers*1 is the typical behaviour of the AMS closed signal after a restart of the instrument after a vacuum failure. Adding a sine function with a relatively high frequency clearly alters the algorithm result. However it is still too low to affect the result when applying the algorithm to a realistic AMS closed signals.

As a final test of the zero output of the algorithm, some non-continuous functions were tested. The step functions in Fig. 3.16 were used to simulate discontinuities. These functions drastically violate the constraint that it has to be possible to locally interpolate the curves by a cubic function. The results of tested step functions are presented in Tab. 3.5. They show that it is important to make sure that the analysed signal has no strong discontinuities. A simple step function that is -1 for

Table 3.4: "Zero"-values of the algorithm for the six test functions *divers*1 to *divers*6 where no noise was added.

function	Calculated standard deviation (see Eq. (3.21))
*divers*1	5.90×10^{-10}
*divers*2	4.21×10^{-6}
*divers*3	2.69×10^{-4}
*divers*4	2.69×10^{-4}
*divers*5	7.69×10^{-5}
*divers*6	4.21×10^{-4}

Table 3.5: "Zero"-values of the algorithm for the five step functions

function	standard deviation estimation
$step1(x) = \Theta(x - 100)$	0.0766
$step2(x) = \frac{1-\exp(-3(x-100))}{1+\exp(-3(x-100))}$	0.02031
$step3(x) = \frac{1-\exp(-2(x-100))}{1+\exp(-2(x-100))}$	0.011927
$step4(x) = \frac{1-\exp(-(x-100))}{1+\exp(-(x-100))}$	0.0022421
$step5(x) = \frac{1-\exp(-0.8(x-100))}{1+\exp(-0.8(x-100))}$	0.0011462

the first 100 points and then changes to 1 for the next 100 points yields an estimated standard deviation of the signal noise of 0.0766 without any noise added. As soon as the step becomes smoother the algorithm result decreases and approaches zero. By comparing the number of points of the signal describing the point of inflection of the different step functions, it can be seen that for the function *step*5 there are nine points describing the step before the function becomes nearly constant. This is in accordance to the results of the sine test curves, where it is shown that ten points are a good estimation for the minimum number of points per inflection point that are necessary for the algorithm to work properly.

Evaluation of the Algorithm Using Non-Constant Signals with Noise

For this series of tests the functions *divers*1 to *divers*6 and *step*5 were used. Different sets of random numbers with a standard deviation of 0.05 were added to the functions to create different test signals from every function. A noise level of 0.05 yields a typical signal-to-noise ratio as it can be found in realistic experimental set-ups. As an example Fig. 3.17a shows the function *divers*2 with added noise. Every set of random numbers used for the test was added to all of the seven test functions and

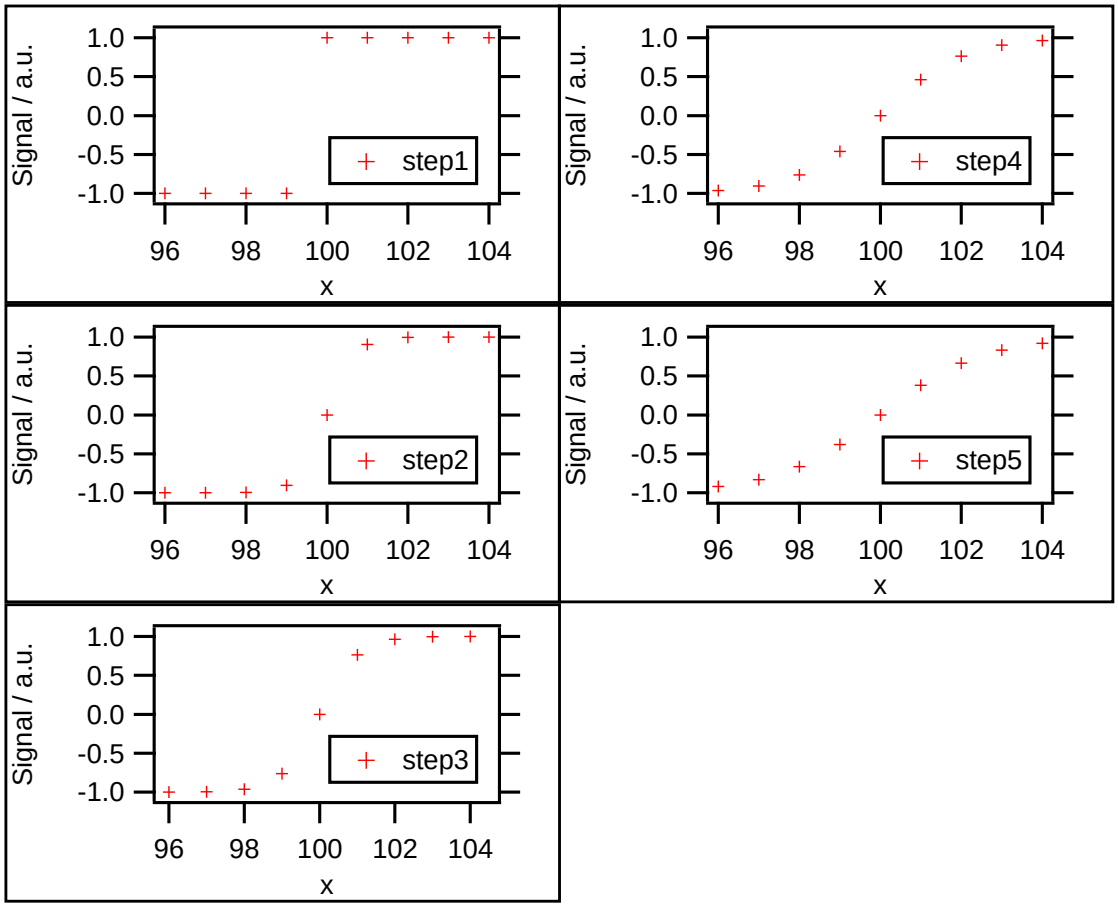

Fig. 3.16: Plots of the test functions *step*1 to *step*5

the algorithm was used to retrieve the standard deviation of the random numbers. This procedure was repeated one million times. Fig. 3.17b shows the histogram of the results of the algorithm used on the *divers*2 function with noise. A Gaussian curve has been fitted to the histogram and the centre of the distribution is 0.050026, which is in excellent aggrement with the real value of 0.05. The standard deviation is equal to 0.004 which is equal to the values determined using Eq. (3.21). When *DL-cubic* was applied to the other test functions, the distributions of the outputs had the same centre values and the same relative error as for the *divers*2 function.

With the new algorithm it is now possible to recalculate the standard deviations of the test functions used to test the Bezier detrending method. As an example, the functions considered in Tab. 3.2 are used with the new algorithm. The noise added to all of these functions had a standard deviation of 0.01. The output of *DL-cubic* is summarised in Tab. 3.6. All of the new results are within the 1σ-confidence interval. This does not only show the enhanced performance of the new algorithm compared

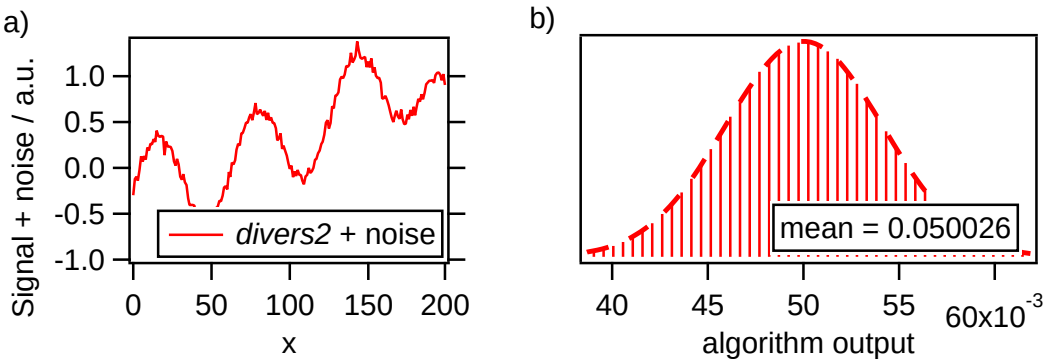

Fig. 3.17: Function *divers*2 with noise and a histogram of the results of the algorithm used with this function. The standard deviation of the noise was 0.05.

Table 3.6: Results of the application of the *DL-cubic* algorithm on the function used to test the Bezier detrending method showed in Tab. 3.2.

function	*DL-cubic* -result	up-error	down-error
FLAT	0.0087528	0.0017549	0.0012526
SINEXP	0.0090203	0.0018085	0.0012909
SSINEXP	0.0095738	0.0019195	0.0013701

to the Bezier method or any other running mean method but in addition, the results can be calculated with a confidence interval which makes them much more reliable.

3.2.6 Detection of Points Not Fulfilling the *DL-cubic* Prerequisites

Sometimes it is difficult to judge if a signal fulfils the the requirement that it can be locally approximated by a cubic function. Therefore, a test was included in the *DL-cubic* procedure to detect outlier of the E_i-values which have been defined in Eq. (3.14). If for a given index $i = a$, E_a is significantly higher than the average level of the E_i-values this value can be considered as an outlier and the point F_a should be excluded from the calculation. As the value of F_a also interferes with the values of $E_{a\pm1}$ and $E_{a\pm2}$, these values will be lost too for the estimation of the standard deviation. To detect the outliers, a test described in Barnett and Lewis (1994) under the name Nμ6 is used. Accordingly this so called discordancy test is the best test to detect one or more outliers in a normally distributed sample if its mean value μ is known and the variance σ^2 is unknown. In the present case the

samples are the E_i-values with $\mu = 0$. The test statistic ($T_{N\mu 6}$) is the kurtosis[6] of the sample based on the deviations from its mean, which is zero in this case:

$$T_{N\mu 6} = \frac{\sum_{i=2}^{N-3} E_i^4}{n s^4} \quad \text{with} \quad s^2 = \frac{1}{n} \sum_{i=2}^{N-3} E_i^2 \tag{3.34}$$

The outliers are considered to belong to so called location-slippage distributions. These distributions have the same width than the sample distribution, but their mean values are shifted by different values. These shifts result from short term variations in the closed signal, which do not originate from the noise level. Such short term variations cannot be approximated by a polynomial of the third grade and thus the *DL-cubic* prerequisites are no longer fulfilled. Therefore these short term variations erroneously increase the E_i. The test intrinsically has a certain probability to interpret non-outlier values as outliers, depending on a set threshold. The values for the thresholds are tabulated and can be calculated numerically for the desired probability. A probability of 5 % turned out to be a reasonable value and will be used in the following section discussing the practical use of the algorithm. It should be mentioned that if a signal does not fulfil the algorithm prerequisites on more than 1/3 of the interval, this method will be unable to detect the outliers. It is the user's responsibility to ensure that most of the signal fulfils the requirements of the algorithm.

As an example, the algorithm with implemented outlier detection was applied to the step functions used to determine the effect of discontinuities. A set of random numbers with a standard deviatio of 0.01 was added to these functions and the outputs of the algorithm with and without outlier detection were compared. The procedure was iterated 1000 times with different sets of random numbers to obtain statistically relevant results. In Tab. 3.7 the average outputs of the 1000 runs for each step function are compared. The column named "unfiltered" shows the results of the algorithm without filtering for outliers, while the column "filtered" shows the noise levels determined after removal of the outliers. The confidence intervals in the table are the standard deviations of the distributions of the *DL-cubic* outputs. They match very well the error calculated from Eq. (3.25) which is 0.00081, if all 200 points were used in the calculation.

The ability of the algorithm to detect outliers is important when applied to large data sets. Without the automated detection of outliers, much time would be lost to manually scan for bad regions in the closed signal. With the use of the outlier

[6]The kurtosis is the fourth moment of a distribution. It is high if many extremely high values, compared to a normal distribution, are present in a set of numbers.

Table 3.7: Comparison of the algorithm outputs for the step functions described in Tab. 3.5 without outlier detection (unfiltered) to the results when the filtering for outliers was applied (filtered). For these tests normal noise with an amplitude of 0.01 was added to the signal. The table shows the average output for 1000 different noise functions together with the estimated standard deviations.

function	unfiltered	filtered
*step*1	0.0772±0.0011	0.00991±0.00087
*step*2	0.02262±0.00074	0.00991±0.00088
*step*3	0.01555±0.00071	0.01010±0.00087
*step*4	0.01022±0.00081	0.01012±0.00086
*step*5	0.01004±0.00082	0.00999±0.00085

detection it is sufficient to ensure that the data is not violating the *DL-cubic* - prerequisites for more than 1/3 of the signal interval used to determine the noise level. This can be achieved by a quick investigation of the time series of the signal.

3.2.7 Application to Retrieve AMS Detection Limits

The goal of the development of the *DL-cubic*-algorithm was to determine AMS detection limits based on the continuous method introduced by Drewnick et al. (2009). Drewnick et al. (2009) calculated the detection limits directly from the closed signal after conversion to mass concentrations. Thus their results already had the dimension of a mass concentration. However, a closed signal which was converted to mass concentrations, includes the random variations of the inlet flow and the airbeam correction (see Sect. 2.1.9). These additional random variations are multiplied by the closed signal intensity. If the closed signal is high, the airbeam correction and the inlet flow thus introduce large random variations, which are attributed to the detection limit by the *DL-cubic* . This is not correct because this apparent noise is mostly removed in the calculation of the difference signal as the inlet flow and the airbeam correction are multiplied to both, the closed and the open signal (see Sec. 2.1). The algorithm must thus be applied directly to the counts time series prior to the conversion to mass concentrations. This results is a counts noise level σ_{cnt}, which needs to be converted to a mass concentration noise level σ_{mc} using Eq. (2.1). The flow rate Q_{in} and the airbeam correction factor f_{AB} are substituted by their respective average values $\overline{Q_{in}}$ and $\overline{f_{AB}}$ for the interval the detection limit is calculated for. This introduces only a very small error as long as the flow rate and the airbeam do not drastically change during the period for which the DL is calculated. This is normally fulfilled. Typically the time periods spent

measuring the open and the closed signal are equal. In this case, σ_{mc} needs to be multiplied by a factor of $\sqrt{2}$ to estimate the noise level of the difference signal. If the time spent recording the open and the closed signal differs, the factor changes to $\sqrt{\frac{T_{closed}}{T_{open}}+1}$, with T_{closed} and T_{open} being the time periods spent in closed or open mode, respectively. Finally, the estimated noise level of the difference signal is multiplied by 3, as by convention the detection limit (DL) is defined as three times the standard deviation of the difference signal when sampling particle free air (Bahreini et al., 2003, DeCarlo et al., 2006, Salcedo et al., 2006, Takegawa et al., 2005, Zhang et al., 2005). Equation (3.35) summarises the conversion of the counts closed noise level to a mass concentration detection limit.

$$\begin{aligned} DL =& 3\sqrt{\frac{T_{closed}}{T_{open}}+1}\cdot\sigma_{mc} \\ =& 3\sqrt{\frac{T_{closed}}{T_{open}}+1}\cdot\frac{1}{RIE_S\,CE_S}\cdot\frac{\sigma_{cnt}\,MW_{NO_3}\,\overline{f_{AB}}}{N_A\,\overline{Q_{in}}IE_{NO_3}} \end{aligned} \tag{3.35}$$

Similar to Eq. (2.1) RIE_S is the relative ionisation efficiency of the species, the mass concentration is calculated for and CE is its collection efficiency. MW_{NO_3} is the molecular weight of nitrate, N_A the Avogadro number and IE_{NO_3} is the ionisation efficiency for nitrate determined from calibration.

3.2.8 Application and Limits of the Algorithm

When applying the new algorithm, one has to keep in mind the assumptions made for its derivation. The main assumption is that the random variations in the closed signal can be separated from the non-random variations by the time scale on which they occur. If the time scale of the non-random variations in the closed signal is close to the sampling rate of the instrument, the algorithm can no longer be applied accurately. The following example demonstrates a situation using real data, which contains a region in which the algorithm fails and demonstrates how this region was identified.

Evolution of the Detection Limits after Vacuum Failure

In Fig. 3.18 the evolution of the detection limits of the main species measured by the AMS after a pump exchange are plotted. The measurement starts about 20 hours after the pump exchange. After this time, the detection limits of the organics species as well as of ammonium were still improving and reached their final

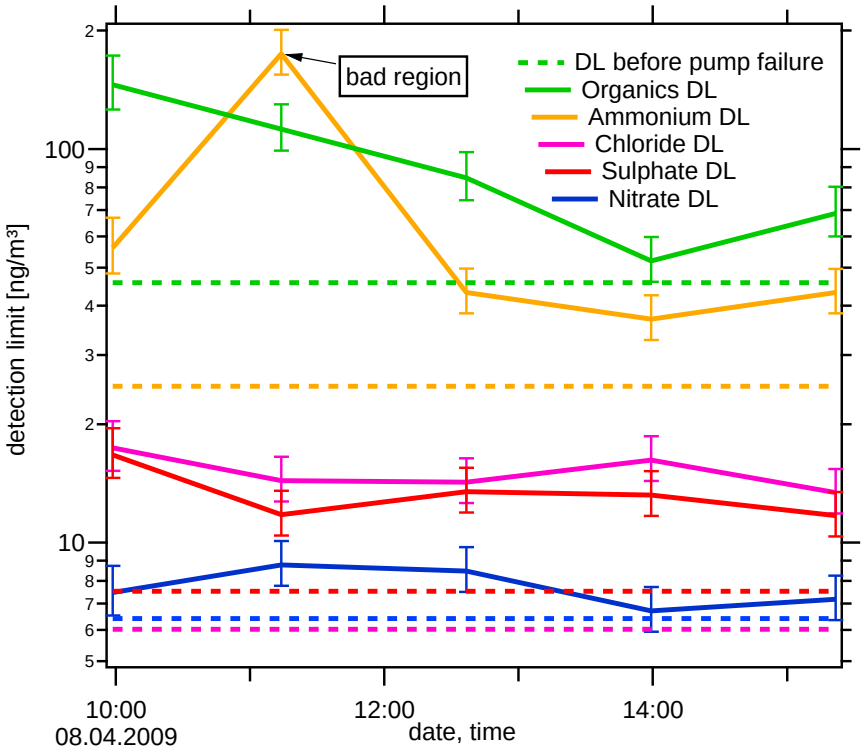

Fig. 3.18: Decay of the detection limits of different species after a pump exchange. The detection limits were determined for 30 s averaging time.

values after about 24 hours. These data show that after one day of pumping, the detection limits were no longer decreasing significantly. The apparent increase of the detection limit for ammonium around 11:00 is due to a period during which the algorithm prerequisites were not fulfilled. In Fig. 3.19 the roughly detrended beam closed and beam open signals are shown. The red region corresponds to the apparent higher detection limit. The short term variations are a lot higher in this interval than for the rest of the signal, which causes the algorithm to calculate a high detection limit. However, the strong short term variations show the same shape in the closed and in the open signal. This means that they were not of random origin but have a systematic although unknown reason. This statement is supported by the linear correlation coefficient R^2 between the open and the closed signal, which is significantly higher during this period. When calculating the difference between the beam open and beam closed signal, these systematic variations disappear. If such a situation occurs, it is not possible to retrieve the detection limit from the closed signal.

The levels of detection before the pump failure correspond to the typical values for the C-ToF-AMS that has been used in this study. These values are summarised

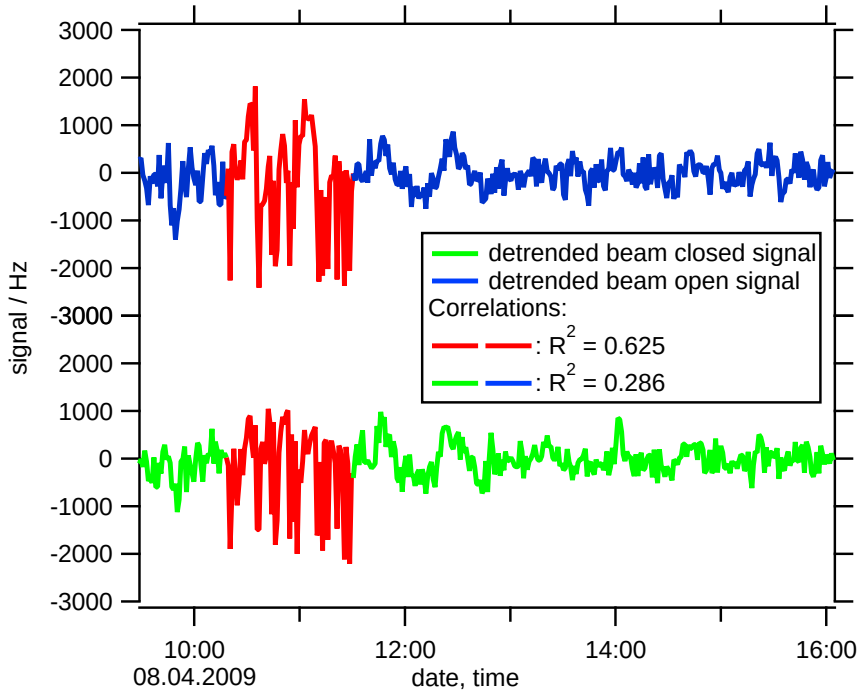

Fig. 3.19: Roughly detrended beam open and beam closed signals of the period after the pump exchange shown in Fig. 3.18. The correlation coefficient R^2 is clearly increased in the red period, indicating that the variations of the signal are not of random nature.

in Tab. 3.8 and compared to values reported in literature. The values calculated using *DL-cubic* are higher than those reported by DeCarlo et al. (2006). This is probably due to higher instrument residual gas pressure and because they have been determined during regular measurements. During measurements, some substances become enriched in the instrumental residual gas and/or stick to the vaporiser where they evaporate slowly. The values of DeCarlo have been determined using filter periods as described in Sect. 3.1.2. A non-optimal tuning of the instrument could also lead to an increase of the detection limits as will be discussed in detail in Sec. 4.1.3. Compared to the values calculated by Drewnick et al. (2009), the values are higher for nitrate, sulphate and organics, but lower for chloride and similar for ammonium. The values from Drewnick et al. (2009) were also calculated from the closed signal, but without detrending. Nevertheless, the values in this study are often substantially higher than the values from Drewnick et al. (2009). These differences show the high variability of the DL between different instruments and different measurement situations and emphasise the necessity to monitor the DL.

Table 3.8: Comparison of the detection limits calculated with *DL-cubic* to the detection limits found by Drewnick et al. (2009) and DeCarlo et al. (2006). The values shown always refer to an averaging time of 30 s. The DeCarlo et al. (2006) values have been multiplied by $\sqrt{2}$ to be comparable.

Citation	t_a (recorded)	Nitrate	Sulphate	Ammonium	Chloride	Organics
DeCarlo et al. (2006)	60 s	1.7	3.1	23	5.6	27
Drewnick et al. (2009)	30 s	3	3	30	20	25
This study	30 s	6.4	7.5	25	6.0	46

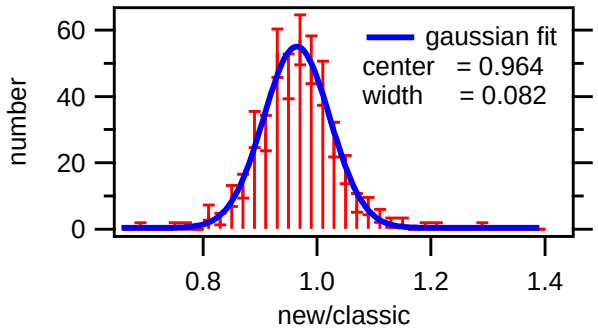

Fig. 3.20: Distribution of the ratio of the output of the *DL-cubic* to the classic method.

Comparison of the Classic to the Continuous Experimental Method

As the *DL-cubic*-algorithm is the only experimental method to retrieve detection limits during regular measurements, it is not possible to validate its output with a second method. However, during filter periods, the classic method to retrieve the detection limits from the difference signal can be applied and compared to the output of the algorithm. The filter periods were recorded in our laboratory with an averaging time of 10 s and lasted 64 min. Figure 3.20 shows the distribution of the ratio of the *DL-cubic*-outputs and the classic method for all m/z values recorded during the measurement shown. The centre of the Gaussian fit to the distribution is slightly shifted to values below 1. This behaviour can be explained by the higher number of ions in the spectrometer when the air beam is not blocked (open), causing the noise level to increase relatively to the periods during which the air beam is blocked (closed) (Drewnick et al., 2009). A measurement with a closed inlet no longer showed the above discrepancy. A detailed analysis of the difference of the noise between closed and open periods revealed that the higher the ion masses, the lower the difference in noise level. This again confirms the assumption that the reason for the higher noise in the beam open periods is due to air ions, which

Table 3.9: Comparison of the DL calculated by the classic method compared to the *DL-cubic* based method. The averaging interval was 10 s.

Species	*DL-cubic* [ng/m^3]	classic [ng/m^3]	relative error
Nitrate	15 ± 0.9	18	−17 %
Sulphate	21 ± 1.3	21	0 %
Ammonium	66 ± 4	66	0 %
Chloride	22 ± 1.4	24	−6 %
Organics	56 ± 3	62	−11 %

correspond to low m/z, that are still entering the instrument when a particle filter is used. This means that the detection limits as given by the continuous method are slightly lower than those from the classic method, depending on the m/z values the algorithm is applied to.

In Tab. 3.9 the DL calculated using the classic method and the *DL-cubic* based method are compared for main species of the AMS. Nitrate shows the highest discrepancy with −17 %. This was expected as nitrate is calculated using m/z 30 and 46. m/z 30 is measured immediately after the very high air ion loadings originating from nitrogen (m/z 28 and 29) entering the mass spectrometer and is therefore influenced most strongly by the effect described above. The organic signal is influenced by the same effect as it includes different m/z close to the air ions. The other species are within the expected range of the *DL-cubic* output. Ammonium is probably also influenced by the air ions measured at m/z 14 and 16 (N^+ and O^+), but these are lower than the signal of m/z 28. Because ammonium has a high noise level, the relative effect of the ions in the mass spectrometer is reduced. To make sure that the nitrate DL is not underestimated it might be useful to add 20 % to the DL calculated using the closed signal only. It should be noted, that the descrepancies are not an error of the *DL-cubic*, but an intrinsic problem of the calculation of the DL using the closed signal only as described in Drewnick et al. (2009).

Comparison of the *DL-cubic*-results to Noise Levels Calculated from Counting Statistics

A second possibility to validate the *DL-cubic*-algorithm is to compare its results to calculated noise levels using ion counting statistics. For those regions in which the counting statistics dominate the noise, one would expect the *DL-cubic* results and the counting statistics error to agree. In the electronic noise dominated region, the counting statistics noise alone should underestimate the real noise level. Figure 3.21

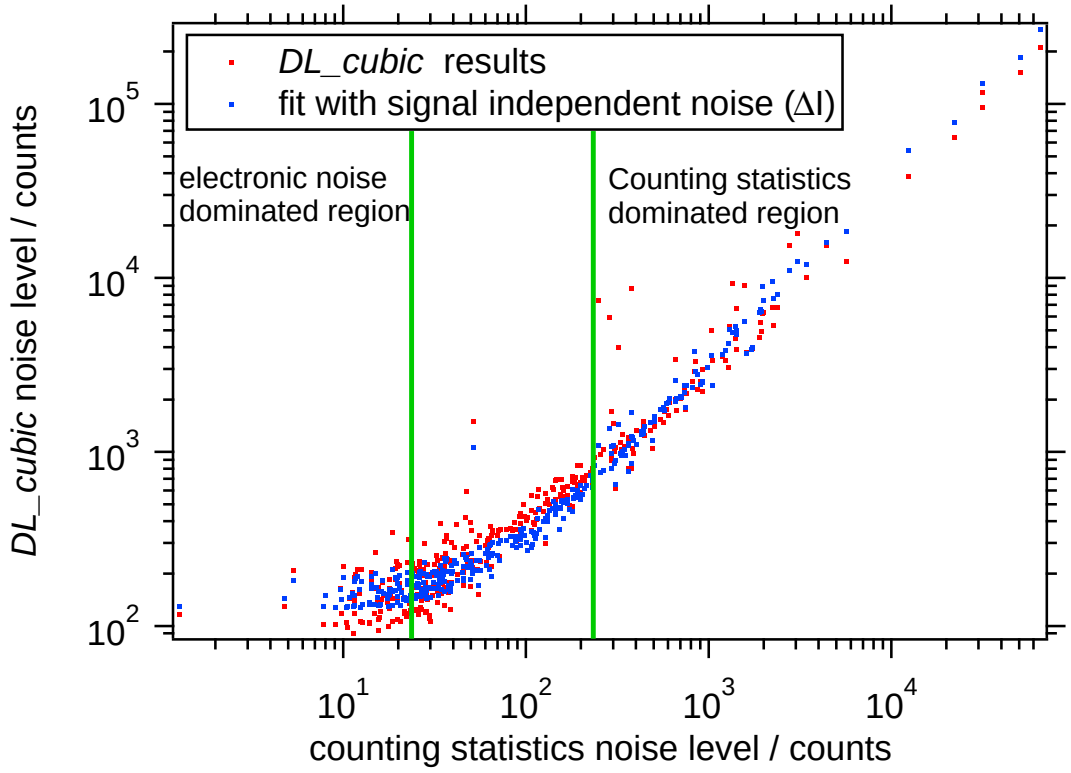

Fig. 3.21: Comparison of the results of the continuous method to the counting statistics. The noise level was estimated for every m/z using the new method and by calculating counting statistics. The data was fitted using Eq. (3.36).

shows the comparison of the output of the *DL-cubic*-tool to the noise level calculated from counting statistics alone (red dots). The data was recorded during the laboratory measurement campaign ACI-03 at the AIDA facility. The counting statistics noise level was calculated from the output of the evaluation tool SQUIRREL (Sect. 2.1.10) and summed for a whole day. As the signal of a single ion event (Sect. 2.1.6) is varying from ion to ion, the counting statistic distribution is convoluted with the distribution of a single ion signal. Therefore the width of the counts distribution is increased by a factor $\sigma = 1.2$. The counts from SQUIRREL included the correction of the overshooting duty cycle (Sect. 2.1.7). This correction could not be undone, as the necessary parameters were not accessible. Due to all these factors, no one to one relation can be expected in Fig. 3.21, even in the counting statistics dominated region with high signal.

To be able to compare the experimental noise level with the noise level estimated from the counting statistics, a model accounting for random noise α was fitted to the data using Eq. (3.36) (blue points in Fig. 3.21):

$$\Delta I = \sqrt{\frac{T_{int} F_{puls} t_{meas}}{V_{SI}} \frac{(A_{duty})^2}{m/z} \alpha^2 + \sigma I \frac{A_{duty}}{\sqrt{m/z}}} \tag{3.36}$$

I is the counts signal as given by SQUIRREL and ΔI is the modelled noise level. T_{int} is the time integrating the signal which is attributed to one m/z during one pulse of the mass spectrometer. F_{puls} is the number of pulses of the mass spectrometer per second and t_{meas} is the total time spend measuring. $T = T_{int} \times F_{puls} \times t_{meas}$ is thus the time spend averaging one m/z during the measurement. V_{SI} is a unit conversion factor equal to the area below a single ion signal. All these values are accessible in SQUIRREL. A_{duty} is a fitting parameter scaling the duty cycle correction effect which is proportional to $\sqrt{m/z}$ (Sect. 2.1.7). This parameter was fitted as the value used by SQUIRREL was not accessible. It was also not possible to calculate the value as the exact quantities necessary could not be accessed. The fit using this model function looks fine, but a more detailed analysis reveals some weaknesses. Both, the *DL-cubic*-results and the fit seem to have a high noise level. However, the apparent random variations of the curve are not only due to noise. Part of them are due to the duty cycle correction. The duty cycle correction continuously varies with $\sqrt{m/z}$. As the signal corresponding to the different m/z is spread over the whole signal intensity range, the duty cycle correction is varying between neighbouring points. These variations appear to be a random variation although they are systematic. To optically improve the comparison between the fit and the experimental values, the noise level determined by the fitted model function can be directly plotted versus the *DL-cubic*-outputs. The data should now be situated on the one-to-one-line. This graph is presented in Fig. 3.22. It shows that the model function overestimates the noise when the *DL-cubic*-output is high and very low. Furthermore, the noise is systematically underestimated when it is between 200 and 1000 counts. To account for this effect, the source of the random noise needs to be examined in detail.

Analysis of the recording of noise in the AMS

To improve the AMS signal to noise ratio, only signals that exceed a certain threshold value are recorded (Sect. 2.1.4). This produces a term, which is up to now not considered in the AMS standard evaluation procedures and which is signal dependent. It is mathematically deduced in the following.

Figure 3.23 shows the effect of thresholding on the recorded noise. In the upper panel pure noise is shown and in the middle panel this noise was added to a signal. This signal is now subject to thresholding with a threshold of 4. Only those points with the signal above the threshold are recorded and thus only the noise coinciding with these points above the threshold is recorded. The noise which passes the

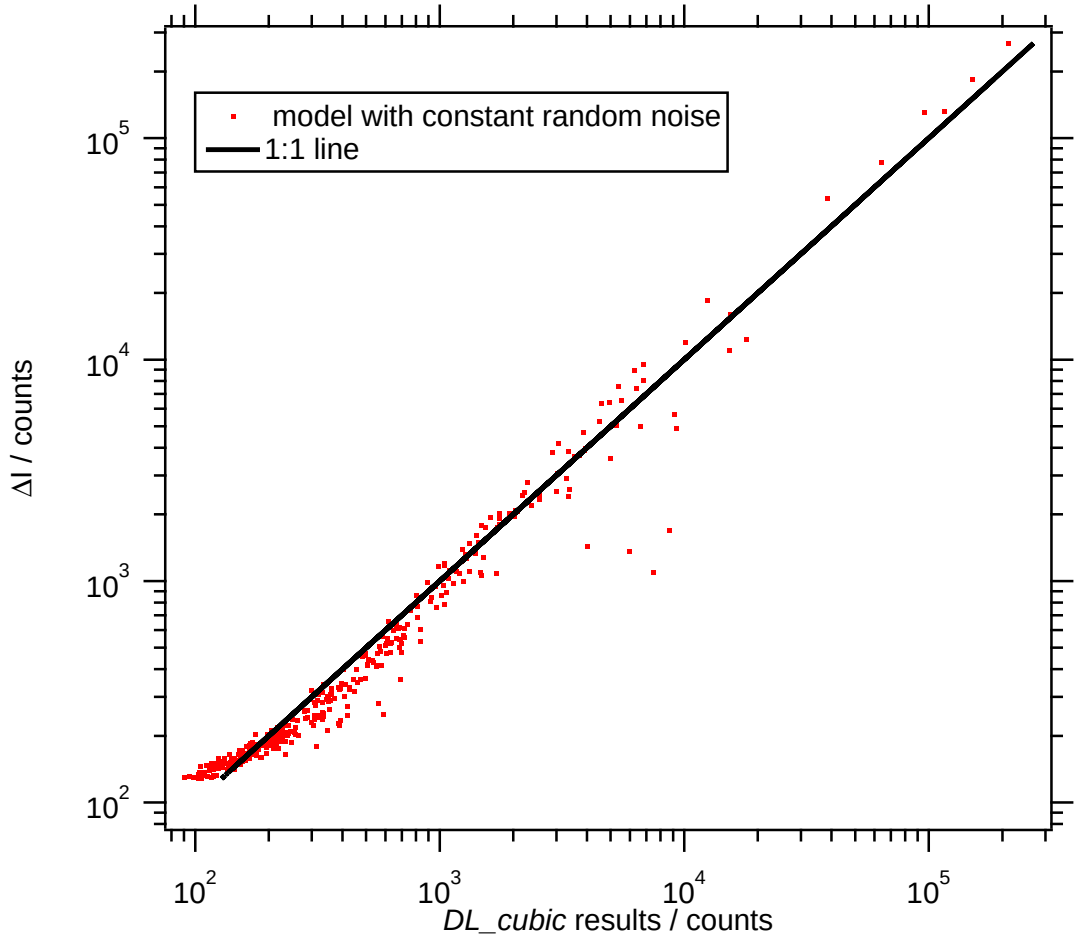

Fig. 3.22: Comparison of the model using constant random noise to the output of the *DL-cubic*-algorithm .

thresholding filter is shown in the lower panel of Fig. 3.23. When the signal is above the threshold, the noise is recorded completely, independent from the intensity of the signal of the respective time bin. There must therefore be a signal dependent electronic noise term for the part of the noise which is added to the signal prior to thresholding.

For the derivation of the fraction of the noise recorded at a certain signal intensity, it is assumed that the width in time of a single ion signal (SIS) is constant. This means that in the AMS detector every ion produces a signal of the same length in time. Furthermore it is assumed that the SISs are distributed equally in time. The goal is to find an equation which yields the average fraction of points contributing to the noise as a function of the number of time bins N and the number of SIS k. It is thus the situation of taking k times an object (a time bin) from a set of objects. Each time an object was taken, it is put back to the set and can thus be chosen

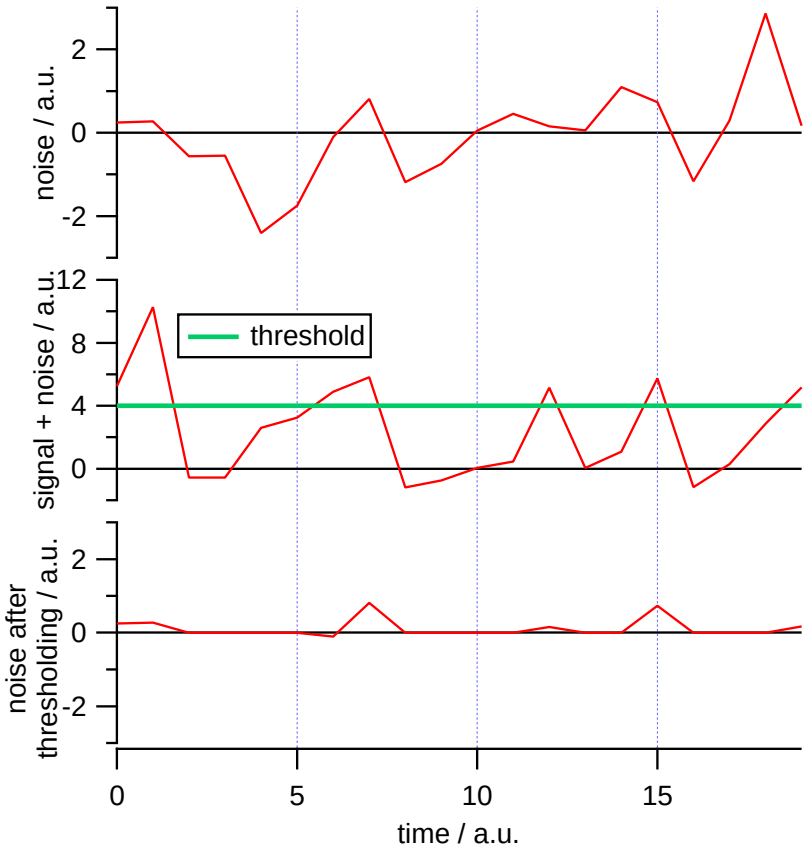

Fig. 3.23: Comparison of the electronic noise (upper panel) to the recorded electronic noise after thresholding (lower panel). The panel in the middle shows a signal with noise added and the threshold is marked in green.

multiple times. The question is, how many objects have been taken at least one time in average. Figure 3.24 illustrates the situation. The x-axis corresponds to the time bins. In this case the number of time bins N is equal to 10. On the left axis, the number of SISs k is located. If a SIS is detected in a time bin (thus this time bin was chosen from the set of time bins), the noise term belonging to this time bin is recorded as depicted in Fig. 3.23. If two SISs are recorded, only 9 free time bins are left for the second SIS. In Fig. 3.24 the second SIS is again recorded in a time bin which was not yet used previously. Thus the noise of the fourth time bin adds to the noise of the first time bin. For the third SISs, only 8 empty time bins are available. This time it is assumed that the SIS is recorded in the first time bin, which already contains the signal of the first SIS. In this case, no additional noise is added to the signal, as the noise present in time bin number 1 was already added after the first SIS hit. The fourth SIS is again assumed to be recorded in a free time bin and thus the recorded noise is increased. Of course in a real measurement situation, the time

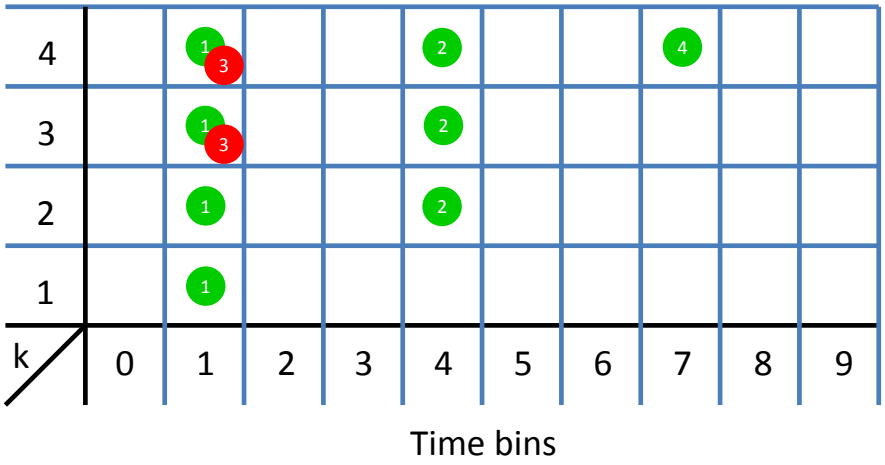

Fig. 3.24: Illustration of the signal dependent noise. The left axis is equal to the number k of SISs and the x-axis are the time bins. The dots represent SISs which are recorded in the time bins and the numbers on the dots are referred to in the text.

bins are filled chronologically and all SIS which are recorded in one time bin are recorded simultaniously as one big peak. However, for the mathematical derivation, the order of the events is not relevant.

$p(k, N)$ is defined as the probability that in a time series with N time bins, the k^{th} SIS is recorded in a time bin which did not include an SIS before. The distribution of the SIS to the time bins is done with equal probability for every time bin. The recorded fraction of the noise is equal to $1 - p(k, N)$.

In the trivial case of only one SIS, the probability that this signal is detected in a signal-free bin is equal to 1.

$$p(1, N) = 1 \tag{3.37}$$

The chance that a second SIS falls into a signal free time bin is equal to:

$$p(2, N) = 1 - \frac{p(1, N)}{N} \tag{3.38}$$

The second SIS can thus fall in all bins but one to hit a free bin. For a third SIS, the probability of falling into a signal free time bin is 1 minus the expectation of the number of bins hit by the first two SIS. This expectation is $\frac{1}{N}$ for the first SIS and $\frac{p(2,N)}{N}$ for the second SIS. The probability of the third SIS to fall into a free bin is thus: $p(3, N) = 1 - \frac{1}{N} - \frac{p(2,N)}{N}$. Generally speaking, the probability for a new SIS to fall into a free time bin is equal to 1 minus the sum of the expectations of the number of free bins hit by the preceding SISs (Eq. (3.39)).

$$p(k,N) = 1 - \sum_{i=1}^{k-1} \frac{p(i,N)}{N} \tag{3.39}$$

The calculation of $p(k,N)$ defined recursively is very expensive with respect to computation time. It is thus preferable to have an explicit form of $p(k,N)$. The explicit form of $p(k,N)$ is:

$$p(k,N) = \left(1 - \frac{1}{N}\right)^{k-1} \tag{3.40}$$

This can be proven by mathematical induction.

Base case:

$$p(1,N) = \left(1 - \frac{1}{N}\right)^{1-1} = 1 \tag{3.41}$$

The proposed equation is thus true for the base case. The inductive hypothesis is given by Eq. (3.40) and the inductive step is:

$$\begin{aligned}
p(k+1,N) &= 1 - \sum_{i=1}^{k-1} \frac{p(i,N)}{N} && (3.42)\\
&= 1 - \frac{\sum_{i=1}^{k} p(i,N)}{N} && (3.43)\\
&= 1 - \frac{\sum_{i=1}^{k-1} p(i,N) + p(k,N)}{N} && (3.44)\\
&= 1 - \frac{\sum_{i=1}^{k-1} p(i,N)}{N} - \frac{p(k,N)}{N} && (3.45)\\
&= p(k,N) - \frac{p(k,N)}{N} && (3.46)\\
&= \left(1 - \frac{1}{N}\right)^{k-1} - \frac{\left(1 - \frac{1}{N}\right)^{k-1}}{N} \qquad \text{by Eq. (3.40)} && (3.47)\\
&= \left(1 - \frac{1}{N}\right)^{k-1} \left(1 - \frac{1}{N}\right) && (3.48)\\
&= \left(1 - \frac{1}{N}\right)^{k} \quad \text{q.e.d.} && (3.49)
\end{aligned}$$

It has been proven that if the assumed explicit form of $p(k,N)$ is correct for k SIS, it is also correct for $k+1$ SIS. This means that if it was correct for $k=1$, it is also correct for $k=2$. This also means that it must be correct for $k=3$ and so on. With this new term, the equation describing the noise ΔI of the AMS reads:

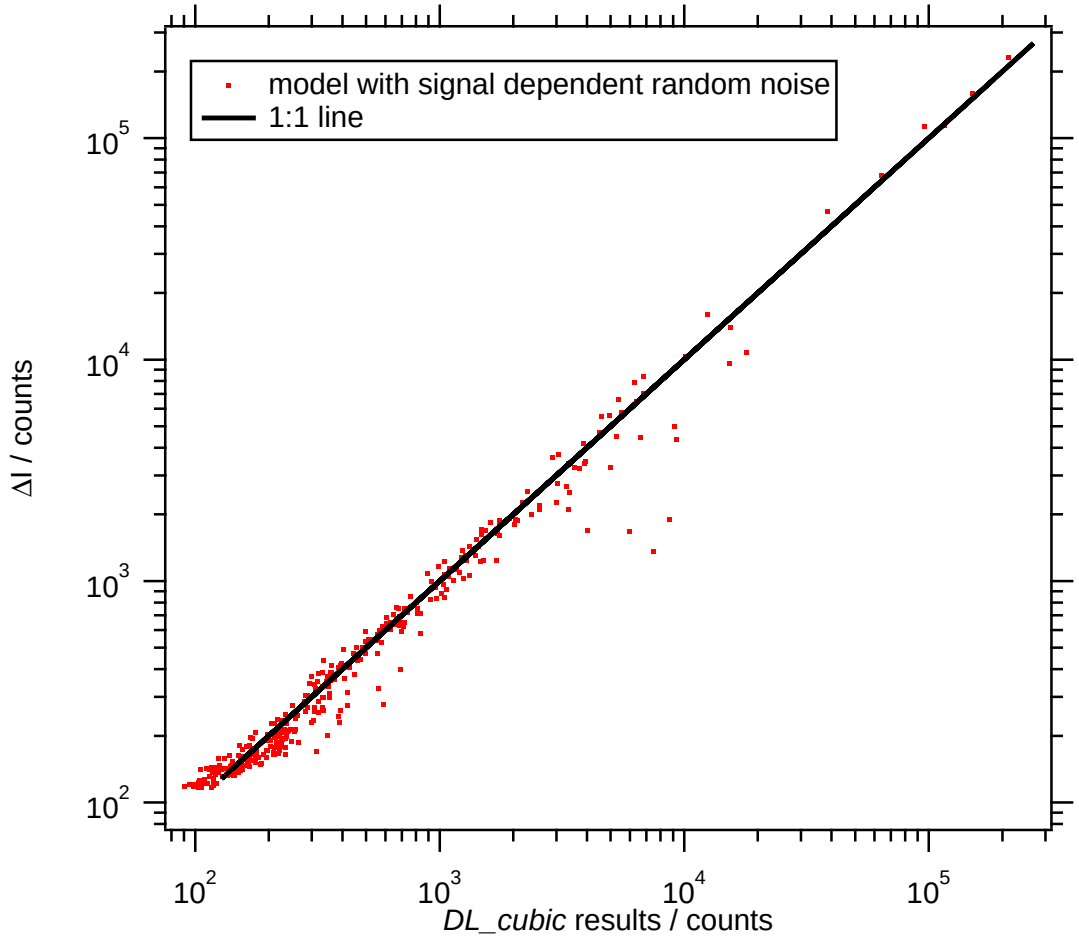

Fig. 3.25: Comparison of the model using signal dependent random noise to the output of the *DL-cubic* .

$$\Delta I = \sqrt{T\left\{\alpha^2 + \gamma^2\left[1 - \left(1 - \frac{1}{N}\right)^{k-1}\right]\right\} + \sigma I} \tag{3.50}$$

α is the constant part of the random noise. Its origin is not completely clear. It includes effects like random threshold breakers originating from electronic noise as well as accumulated errors during data processing. γ is expected to mainly describe the amplitude of the electronic noise. It is only partially recorded due to the thresholding and only fully visible for high signal intensities I. The factor σ originates from the broadening of the counting statistics error due to variations of the intensity between different SISs. T is the integration time of the AMS for a single m/z. To fit the data, Eq. (3.50) was related to the available parameters as shown in Eq. (3.51), which is an extension of Eq. (3.36) which includes the signal dependent random noise term.

Table 3.10: Overview of the parameters in the fitting equation (3.51)

Parameter	Description	fitted?
α	constant random noise	yes
γ	signal dependent random noise	yes
T_{int}	time integrated for one m/z per spectra	no
F_{puls}	number of spectra recorded per second	no
t_{meas}	number of seconds averaged	no
V_{SI}	area of a single ion signal	no
m/z	mass to charge ratio	no
S	scaling factor for the signal dependent noise term. See text.	yes
A_{duty}	factor for the duty cycle correction. See text.	yes

$$\Delta I = \sqrt{\frac{T_{int}F_{puls}t_{meas}}{V_{SI}}\frac{(A_{duty})^2}{m/z}\left(\alpha^2+\gamma^2\left(1-\left(1-\frac{1}{t_{meas}F_{puls}S}\right)^{\left(I\frac{A_{duty}}{\sqrt{m/z}}-1\right)}\right)\right)} + \sigma I\frac{A_{duty}}{\sqrt{m/z}} \tag{3.51}$$

Figure 3.25 shows the comparison of the new model function to the *DL-cubic* data. The discrepancies have nearly completely vanished. Only for very low noise levels, the model seems to overpredict the noise. Nevertheless, some distinct points are underestimated close to one order of magnitude. The parameters in Eq. (3.51) are summarized in Tab. 3.10. The parameters S and A_{duty} were used as additional fitting parameters as their values were not accessible. A_{duty} is the factor of the duty cycle correction. Its theoretical value is 38.7, calculated using equation (3.12) of Hings (2007):

$$A_{duty} = \left(x_{pulser}F_{puls}\sqrt{\frac{1}{2U_{ion}}}\frac{1}{9824\ \frac{\mathrm{kg\,C}}{\mathrm{u\,eV}}}\right)^{-1} \tag{3.52}$$

with the open length of the pulser electrode $x_{pulser} = 46$ mm (Drewnick et al., 2005), $F_{puls} = 50$ kHz, and the voltage in the ion chamber $U_{ion} = 41$ V. Except for x_{pulser} the values were retrieved from the recorded AMS data files. The exact values used by SQUIRREL were unknown. The fit using Eq. (3.51) yielded a value of 44.2 when σ was set to 1.2, which is an experimental value described in Allan (2010). When setting A_{duty} to 38.7, σ is found to be 1.39. The values found are thus reasonably close to the theoretical value and the value from literature, respectively. A summary

Table 3.11: Fitting values corresponding to the curve in Fig. 3.25 with $\sigma = 1.2$

fitting parameter	value
α	$(6.74 \pm 0.12) \times 10^{-7}$
γ	$(1.103 \pm 0.035) \times 10^{-6}$
S	$(1.289 \pm 0.094) \times 10^{-4}$
A_{duty}	44.17 ± 0.72

of the fitting parameters as determined for Fig. 3.25 is shown in Tab. 3.11. The values of α and γ are relatively close to each other. This means that they must have different origins. If both originated from electronic noise, the value of the constant noise α should be lower than γ by several orders of magnitude. The thresholding would block most of the noise which is not accompanied by signal and only purely random threshold breakers would be recorded. Usually the AMS threshold is set in a way that nearly no electronic noise is transmitted when no signal is recorded.

The product $t_{meas}F_{puls}$ in Eq. (3.51) corresponds to the total number of recorded mass spectra. It was expected to be approximately equal to the number of time bins N in Eq. (3.50). T_{int} is not included in this product, as the width of one time bin is approximately equal to T_{int}. In the factor $\frac{1}{t_{meas}F_{puls}S}$ in Eq. (3.51), S is a scaling factor which was introduced to account for the difference between T_{int} and the real width of a time bin. S was expected to be close to 1. However, the fitted S was much lower. The reason for this high discrepancy could not be determined. A straightforward interpretation would be that the signals are broader than expected. However, this interpretation does not make physically sense as the peaks cannot be broader than the ion time of flight range attributed to one m/z (Sect. 2.1.5). This range corresponds to the maximum time integrated for one peak. A signal outside of this range is not added to the signal of an m/z. A second possibility would be that the signal dependent noise term is not relevant to the overall noise and the effect seen in the fit has a different physical reason than thresholding. This would mean that it matches the shape of the curve derived for the thresholding effect only by coincidence. Nevertheless it can be expected that the thresholding effect is present in the data as it is based on the physics of the data acquisition.

To test the thresholding effect in more details, it would be necessary to use the new algorithm on single time bins and not on the sum of the time of flight bins attributed to a particular m/z. This cannot be done with the standard AMS data evaluation routines and is beyond the scope of this work. The observed effect in

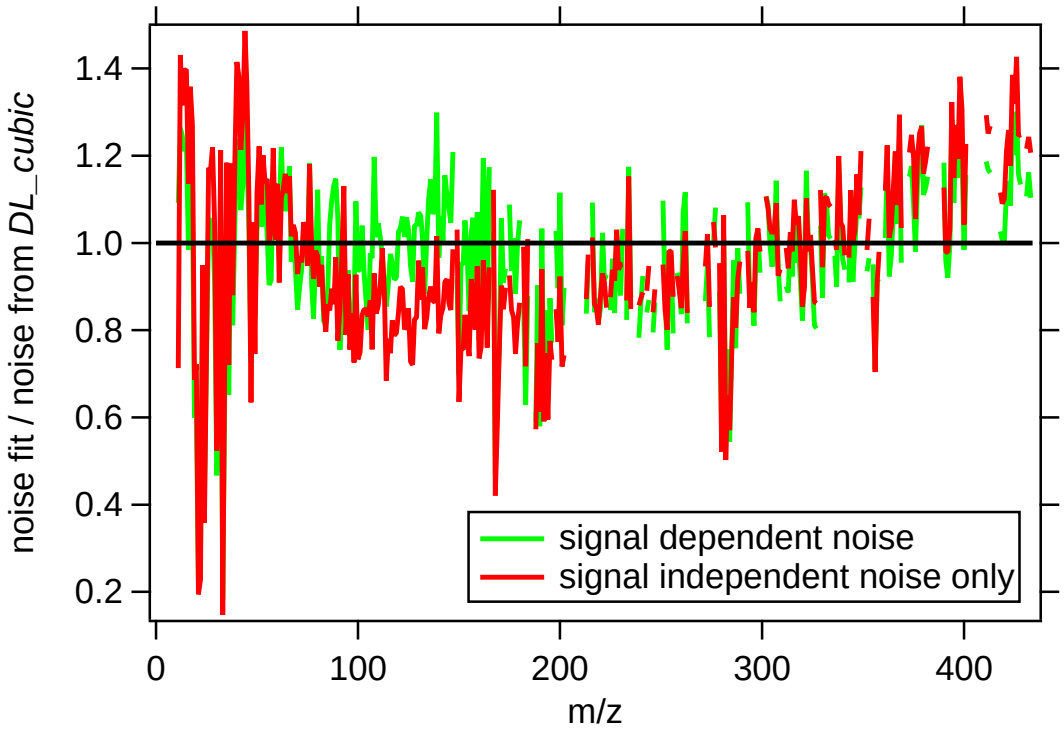

Fig. 3.26: Ratio of the fitted noise levels to the experimentally determined noise levels as calculated with the new algorithm. The green line refers to a fitting with signal dependent noise being taken into account while the red line results from a fit with only assuming a constant random noise level.

the fit might also be due to data processing effects. If this is the case, the error calculation still needs further investigation.

In Fig. 3.26 the fitted data were divided by the experimentally determined noise levels and plotted on a linear scale to improve the visibility of the relative underestimation. In the range of m/z 100 to 200, the noise is underestimated by the constant noise model by approximately 20 %. According to the fitting parameters determined for the improved model function (Fig. 3.25), this corresponds to the signal intensity range in which the signal dependent noise effect is highest.

Figure 3.27 shows a comparison of the ratios between the fit, using Eq. (3.51), and the noise level determined by the new continuous method for two consecutive measurement days during the FROST2 campaign. The points are linearly correlated and the slope of the linear fit is basically equal to one. This shows that the difference between the fitted model function, which takes into account the counting statistics error and the statistic noise terms α and γ, and the *DL-cubic*-results is systematic. If the *DL-cubic*-algorithm would not properly work on the data, e.g. because of regions not fulfilling the algorithm prerequisites, one would expect the *DL-cubic*-

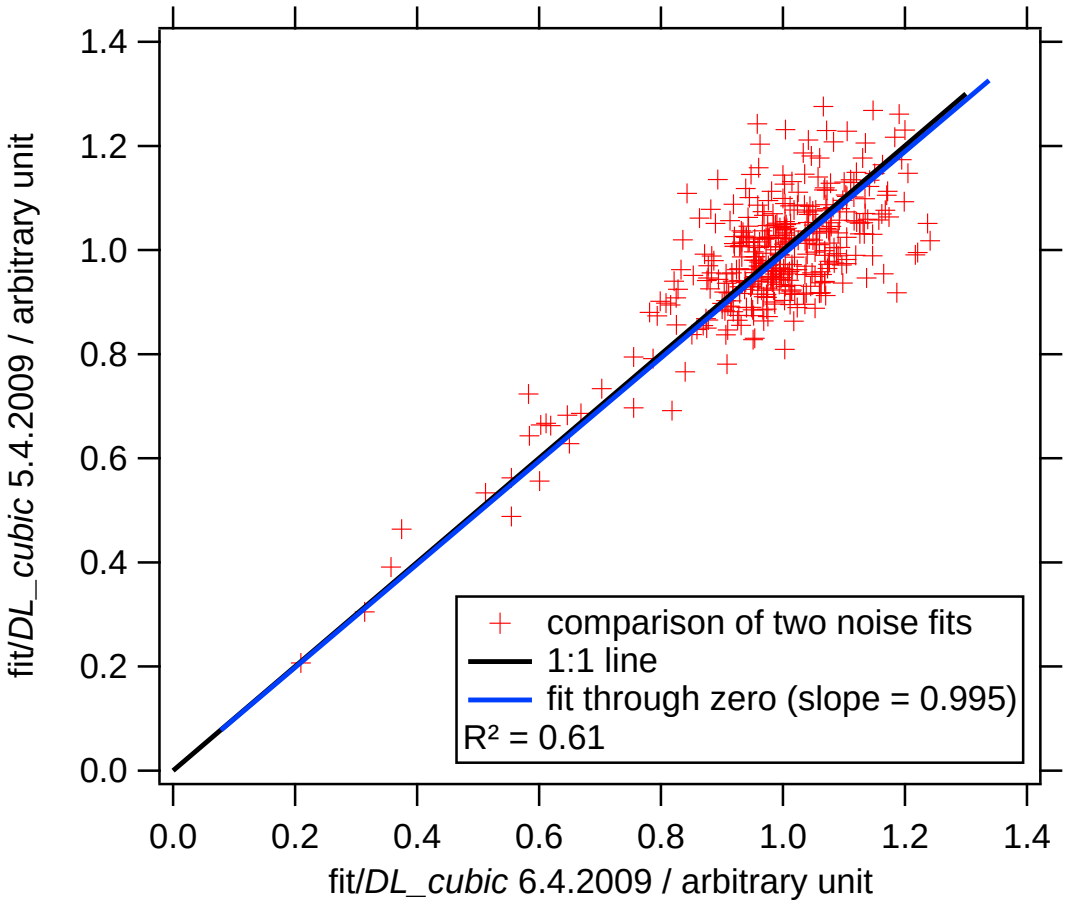

Fig. 3.27: Comparison of the ratios between the fits to the noise using Eq. (3.51) for two different experiments but with similar instrument setting. The graph shows that the discrepancies are of systematic nature and are thus unlikely to be *DL-cubic*-artefacts which would be expected to behave randomly.

algorithm to produce random errors in the noise level determination. In this case it would be very unlikely that the difference between the modelled noise level and the *DL-cubic* noise level would be quantitatively equal for two consecutive days. The systematic difference between these two independent methods to determine AMS DL is therefore a good indication that the *DL-cubic*-algorithm works correctly on real measurement data.

3.3 Importance of the new continuous method

The preceding examples show that the *DL-cubic*-algorithm produces reasonable and realistic noise values when applied to real data. Furthermore, it gives a strong indication that the noise calculation with only taking into account the counting

statistics and a constant random noise term is missing part of the noise. Especially in the transition region from noise to counting statistics dominated signal, this is likely to cause significant errors. As the detection limits are directly proportional to the noise levels, the detection limits are underestimated when calculated using the the model function presented in the preceding section. In the case of low m/z, the algorithm often determines a noise level that is markedly higher than the calculated noise level from the counting statistics model. The m/z in this region, which have low signal intensities, are likely to have much higher DL than the calculated values using the model function would suggest. The DL are not important for some m/z in this region as their difference signals are very high. However, their errors are greatly underestimated if only the counting statistics and a random noise term are considered.

The reasons for these effects are not completely clear. There might be physical reasons in the data acquisition that cause additional noise. However it is likely, that some of the effects are caused by the data evaluation procedures implemented in SQUIRREL (see Sect. 2.1.10). These effects are automatically considered when applying the *DL-cubic*-algorithm to determine the detection limits and errors for the AMS results. As the data evaluation involves many user set parameters which are not handled uniformly in the user community, it is very difficult to consider these effects in an error calculation model.

The use of the closed signal alone for the calculation of detection limits means that potential signal variations which are equal for both open and closed signals are attributed to the noise although they cancel out when calculating the difference of the open and the closed signal. However, the comparison of the filter method to the closed signal method presented in Sect. 3.2.8 showed that these effects are minor. For these reasons, the detection limits in the following chapters were always determined using the method described in Sect. 3.2.7.

The long term variations of the AMS signal need to be clearly longer than the sampling period. The experience with the new algorithm shows that this is typically the case when the sampling period is lower than 2 min. The best performance is reached with sampling periods of 1 min or less. This condition was fulfilled in all experiments conducted in this thesis and thus the calculated detection limits should be reliable.

4

Improvements in Instrument Characterisation

For the correct evaluation of the data, it turned out that several correction factors and instrumental characterisations were necessary which are described in the following.

4.1 Correction Factors

The AMS measures aerosol in the vacuum aerodynamic size range of approximately 40 to 1000 nm. The limitation of the size range is mainly given by the transmission of the aerodynamic lens which is 100 % only between approximately 60 to 600 nm vacuum aerodynamic diameter (d_{va}). The exact transmission varies slightly for every particular aerodynamic lens. Beside the imperfect focussing of the aerodynamic lens, not all of the particles which hit the vaporiser are also evaporated. A fraction of the particles bounce off before evaporation, reducing the detected mass fraction. The last important factor altering the mass quantification of the AMS is the so called relative ionisation efficiency (RIE). Different substances evaporated on the vaporiser are not ionised with the same efficiency. In principle, the RIE values can be determined by laboratory calibration. However, the ions produced in the ioniser show a different transmission to the mass spectrometer depending on their mass to charge ratio. When the instrument is tuned correctly, the ion transmission efficiency ideally is 100 %. Unfortunately, the instrument used in our studies was instable, which means that a tuning which yielded a correct transmission of all ions indepentend from their mass to charge ratio, did no longer work properly one week later. After some days, the ion transmission became stable again and thus it was possible to determine an effective RIE for every compound of interest. In this thesis this were mainly sulphate and ammonium. The determination of correction factors is described in the following section for the three effects mentioned above, with respect to the quantification of sulphuric acid coatings on ATD.

4.1.1 Transmission of the AMS Lens

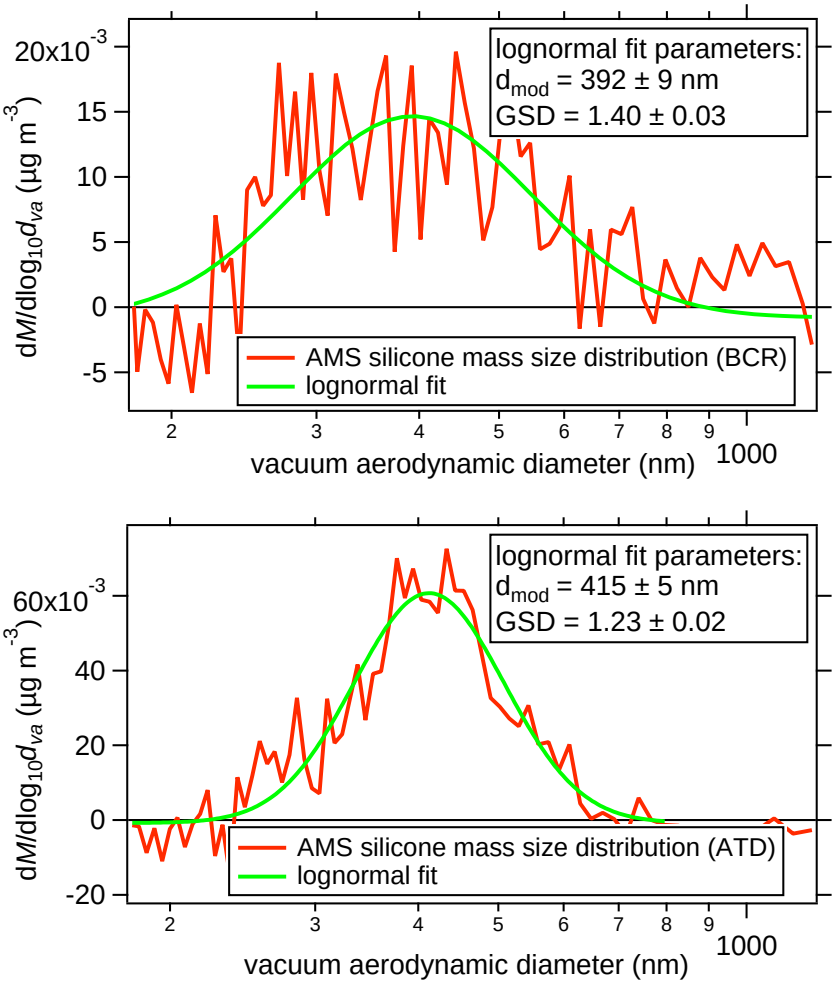

Fig. 4.1: Silicone size distributions for 200 nm mobility diameter particles with log normal fit. Upper graph: BCR, averaged over 1 h 20 min. Lower graph: ATD, averaged over 5 h 39 min. d_{mod} is the modal diamter of the log normal fit and GSD is the geometric standard deviation of the size distribution. The errors correspond to the fitting uncertainties.

During the FROST1 and FROST2 campaigns particles with mobility diameters of 200, 300, and 400 nm have been used. ATD particles with a mobility diameter (d_{mob}) of 300 nm have a vacuum aerodynamic diameter d_{va} of more than 600 nm due to their density ρ_p of 2.6 g/cm^3 (Möhler et al., 2008) and a "Jayne shape factor" S (Jayne et al., 2000) of approximately 0.77 (Eq. (4.1); DeCarlo et al. (2004)). The shape factor varies between different individual particles (see Fig. 2.7) which means that the monodisperse mobility diameter distribution is polydisperse with respect to the vacuum aerodynamic diameter. This causes a fraction of the aerosol to be

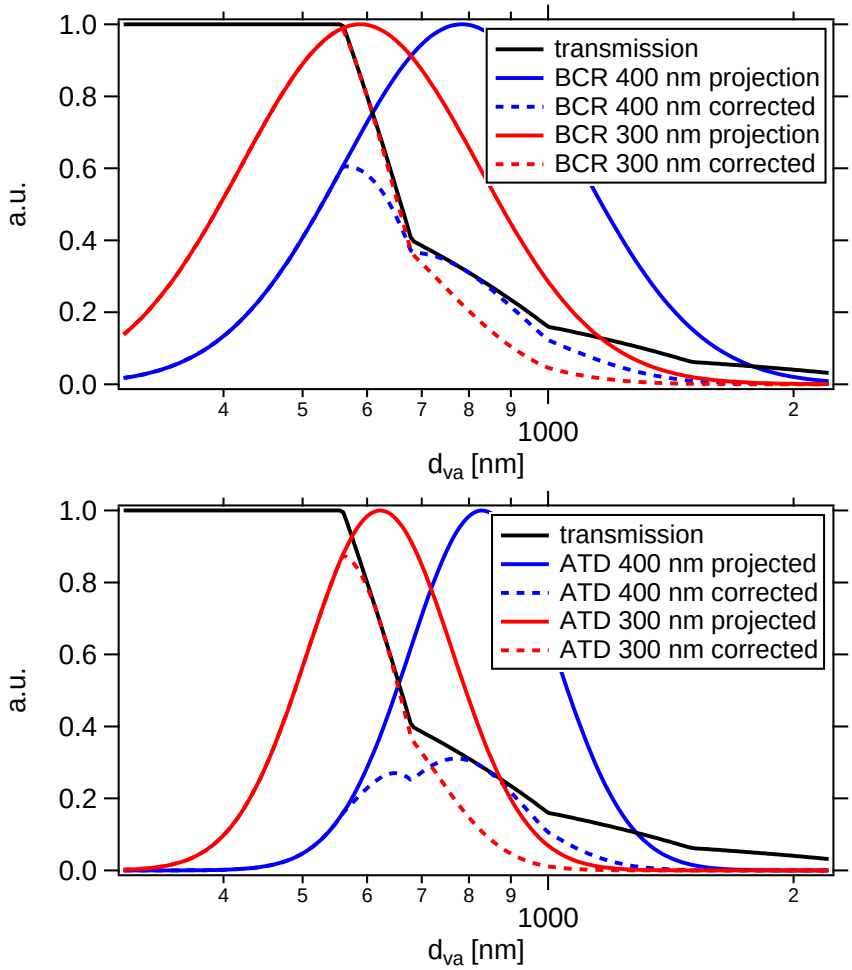

Fig. 4.2: Transmission correction for BCR and ATD particles. The figures show the projected transmission curves as calculated from the fits in Fig. 4.1 as well as the projected size distribution when the transmission of the aerodynamic lens is taken into account.

outside the 100 % transmission range of the AMS inlet. For the 400 nm particles used during FROST1, this effect is even stronger.

$$d_{va} = S\rho_p \cdot d_{mob} \tag{4.1}$$

To get accurate coating thicknesses, this loss factor must be estimated. Due to the thin coatings of the particles the size distributions measured by the AMS were very noisy. Furthermore the size calibration above 600 nm has large uncertainties as it is very flat (see Fig. 2.2). To nevertheless access the size distributions of the 300 and 400 nm particles, some assumptions had to be made: The vacuum aerodynamic mass size distribution of the ATD was assumed to be lognormally distributed with the same geometric width independent of the mode diameter (Fig. 4.1). The lognormal fit to the correctly measured 200 nm particles can be projected to the 300 and

400 nm particles using Eq. 4.1. An independent validation of the projected size distributions was not possible. However, the corrected signal of substances which were expected to be only present on the particle surface, scaled approxmately with the square of the particle diameter after the correction (see Sect. 5.3c).

Table 4.1: Transmission correction factors: The errors have been estimated by varying the mode diameter and the geometric width in the range of the fitting parameter uncertainties of the lognormal distribution.

particle type	correction factor
BCR 300 nm	1.45 ± 0.08
BCR 400 nm	2.31 ± 0.20
ATD 300 nm	1.50 ± 0.041
ATD 400 nm	3.0 ± 0.21

The mass size distributions were calculated from the methyl silicone signal, as this substance showed the best signal to noise ratio. The presence of this substance on the particle surface is discussed in more detail in Sect. 5.2.2. A second assumption was that the transmission function f_{trans} of the aerodynamic lens of ATD and BCR particles is identical to that of polystyrol latex size standards (PSL) which where used to determine the transmission function (Walter, 2008). Finally the integral of the projected mass size distribution D_{ATD} was divided by the integral of the product of the transmission function and the projected mass size distribution resulting in a correction factor k_{trans} for the lens transmission (Eq. (4.2)). The respective projected distributions are shown in Fig. 4.2 and the correction factors are summarised in Table 4.1. The mass per particle of the 300 and 400 nm particles was multiplied by these factors to correct for the reduced signal due to particle transmission losses in the AMS aerodynamic lens.

$$k_{trans} = \frac{\int_0^{+\infty} D_{ATD}(d_{va}) dd_{va}}{\int_0^{+\infty} D_{ATD}\left(d_{va}\right) \cdot f_{trans}(d_{va}) dd_{va}} \tag{4.2}$$

4.1.2 Collection Efficiency of the AMS

Huffman et al. (2005) and Matthew et al. (2008) found that the AMS quantification is altered by bounce-off effects of particles on the instrument vaporiser, reducing the collection efficiency (CE). A quantification of the non-refractory fraction of ATD is only possible if the CE of such particles can be determined. It is possible to calibrate the AMS CE by parallel measurements of coated particles, if the second

instrument is sensitive to the same fraction of the measured coated particles as the AMS. In an ideal case a second instrument with a CE of unity would be used, which measures the same mass fraction of the ATD than the AMS. An instrument that is very close to this prerequisites is a CCNC. If a non-soluble and refractory particle is coated with a thin layer of sulphuric acid, the soluble mass fraction determined with the CCNC as described in Sec. 2.2.1 is identical to the non-refractory mass fraction. In both cases this is the sulphuric acid only. The sulphuric acid can be condensed on the particles from a heated sulphuric acid bath (see Sect. 2.5). ATD itself is not suitable for such a measurement, as it contains a soluble mass fraction and is not completely refractory. It was thus necessary to find a mineral-dust-like material which is expected to behave like ATD. In this study quartz particles (BCR) were used for this purpose. They are expected to have similar bounce-off behaviour than ATD, are completely refractory and insoluble and do not chemically react with sulphuric acid. It is important that the sulphuric acid did not react with the particle surface. If the sulphuric acid reacted with the BCR particles, unknown substances would be produced which could no longer be quantified neither by the AMS nor by the CCNC.

The only commercially available quartz particles that seemed suitable were BCR-66 (European commission, Institute for Reference Materials and Measurements) size standards. The soluble material fraction of these particles is much lower than for ATD particles, even though it was not zero, as could be inferred from the CCNC data. Figure 4.3 shows a compilation of the ratios between AMS and CCNC mass per particle for all experiments conducted in order to determine the CE. Its average value is 0.36 ± 0.02. This value was used in the calculation of the mass concentrations as described in Eq. (2.1). The quality of this value is difficult to quantify. Figure 4.3 shows no trend correlating with the coating thicknesses so it is expected that the same value can be used independently of the coating thickness in the range of the coatings used in this studies. However, if the coating thickness of a mineral dust particle exceeds a few nanometres, it is expected that the particle surface becomes sticky, as it resembles more and more the surface of a sulphuric acid droplet. At the limit of a mineral dust particle immersed in a sulphuric acid droplet, the collection efficiency is expected to reach the value of pure sulphuric acid, which is 1. A further uncertainty is the comparability of ATD bounce-off behaviour and BCR bounce-off behaviour. On the Mohs scale of mineral hardness quartz is the reference mineral for the hardness of 7 (Haynes, 2011). ATD is mostly composed of quartz and aluminium silicates, which are in the same range of hardness as quartz and therefore a similar value for the bounce-off probability is likely.

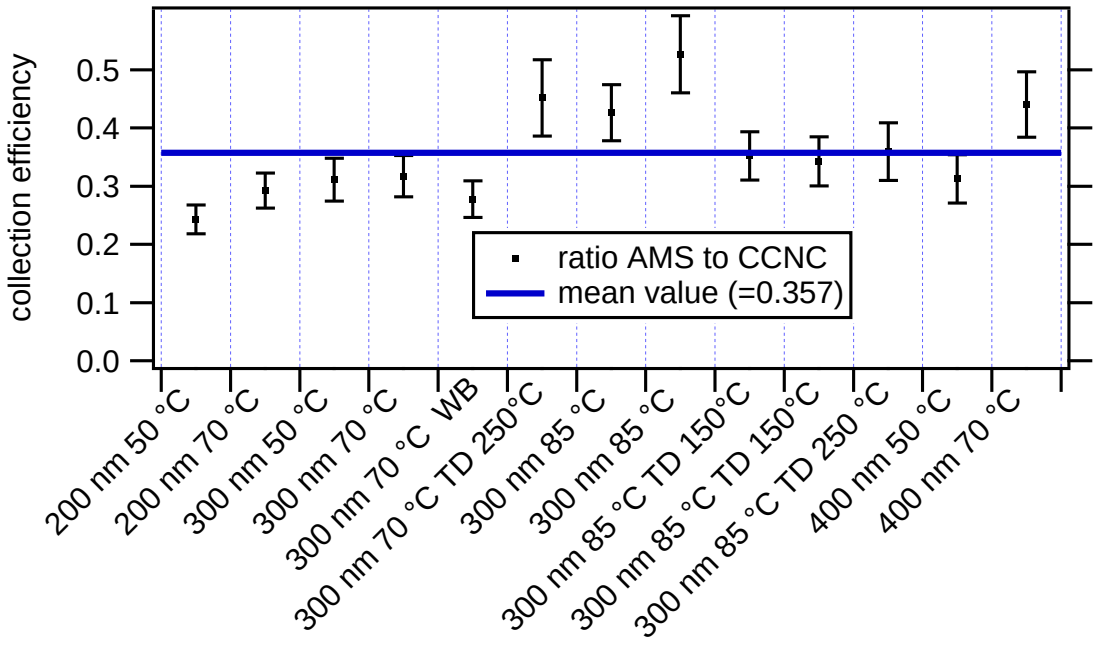

Fig. 4.3: Collection efficiency (CE) for all experiments using coated BCR particles. The categories refer to different experimental conditions. The first number is the d_{mob}, the second the temperature of the sulphuric acid bath used for the coating. WB indicates humidification of the particles with a water bath and TD indicates the use of a thermodenuder at the temperature following TD. Every data point was averaged over $\sim 10^6$ particles. The error bars were calculated from Gaussian error propagation using the standard deviations of the mean values for the time series of the mass per particle corresponding to the data points and the confidence intervals of the soluble mass per particle determined with the CCNC.

A collection efficiency of 0.36 is below the average collection efficiency of 0.5 which is commonly used in the AMS community to correct ambient AMS data, when the exact CE is unknown. However, for pure, dry ammonium sulphate particles, CEs down to 0.2 have been reported (Matthew et al., 2008). The lowest value for the CE of a single experiment in this study was not lower than 0.25. Unfortunately no data for pure ammonium sulphate was collected during the parallel measurements of the AMS and the CCNC. Therefore it is not possible to check if the CE of 0.2 for dry ammonium sulphate could be reproduced with the set-up used during FROST.

Together with the measurements to determine the collection efficiency of the AMS, some experiments of the FROST1 and the FROST2 campaign were repeated. The CCNC reproduced the soluble mass per particle for experiments with the same particle generation settings. However, the AMS did not reproduce the mass load-

ings measured during the FROST campaigns. The mass loadings of the FROST1 campaign were higher by a factor of ~ 2 than the mass per particle for similar experimental settings during the CE determination measurements. In contrast to FROST1, the FROST2 campaign showed mass per particle loadings which were lower by a factor of ~ 2. This effect can partially be explained by accumulated errors of the determination of the mass per particle by normalising the AMS mass concentrations to the CPC particle concentration. According to the manufacturer the CPC has an accuracy of 10 %. The CPC was operated behind a dilution stage, which introduced an additional uncertainty of 10 %. This value was determined from the accuracy with which the flow could be set. As the aerosol was diluted close to a factor of 5, the accuracy of the dilution flow was higly amplified, thus the high value of 10 %. During the CE determination measurements, only the AMS and the CCNC were measuring, which allowed for measurements without a dilution stage in front of the CPC. The AMS calibration accuracy is commonly estimated to be 30 %. These errors can explain an uncertainty of 33 % for one standard deviation. In the less likely case of an error of two standard deviations, this could explain an error of 66 %. Two campaigns could thus be apart by a factor of 2.3 with a probability of ~ 5 % (2σ interval). This is still much less than the observed difference between the FROST1 and the FROST2 campaign. A possible additional reasons could be a misalignment of the aerodynamic lens when finalising the set-up after the lens was adjusted. Furthermore, a slight systematic error in the measurement of the dilution flow could provoke significant errors as the dilution factor was very high. The measured mass per particle loadings within one campaign could be reproduced. This indicates that whatever caused the big difference between the campaigns, was stable within one campaign. Unfortunately, it will never be possible to determine the source of the discrepancies for sure.

To be able to compare the FROST campaigns with each other, the AMS-CPC-dilution-stage-system was recalibrated to the CCNC for both campaigns. With the determination of the collection efficiency by comparison to the CCNC, the AMS-CPC-system is de facto calibrated to the CCNC for these measurements. Those FROST1 experiments, which were reproduced during the CE determination measurements, are all appart by approximately the same factor (Fig. 4.4). Scaling the mass loadings of the FROST1 campaign by this constant factor, corresponds to a recalibration of the FROST1 campaign to the CCNC. The determined recalibration factor k_{comp} for the FROST1 campaign was 0.46 ± 0.02. The comparison to the FROST2 campaign is not trivial, as the vaporiser temperature was higher and thus additional sulphate compounds were evaporated. These formed due to a chemical

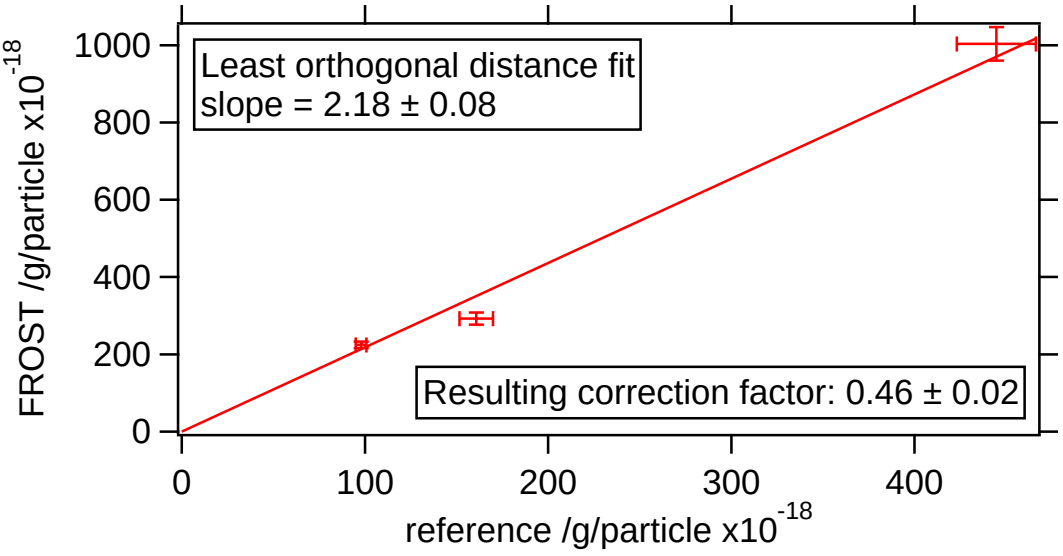

Fig. 4.4: Comparison of the results of the measurements pepeated during the CE determination measurements to the FROST1 campaign.

reaction of the sulphuric acid with the ATD surface (Sect. 5.2.4) and cannot be easily seperated from the sulphuric acid in the mass spectrum. However, for a coating temperature of 85 °C the coating is thick enough for most of the sulphuric acid to remain on the particle surface without chemical reaction and thus this experiment can be used for comparison. This yielded a correction factor of 2.2 ± 0.3 for the FROST2 campaign.

The CE determined in this section is only useful in connection with the factors k_{comp}. Thus it is not clear, how accurate the value of the CE is. It is important to notice that only one correction factor was applied per campaign. It is thus still possible to compare the CCNC measurements to the AMS measurements as the determined quantities were not forced to be equal by the recalibration. Furthermore, the factors applied are real calibration factors with the attempt to yield correct values of the mass per particle determined with the AMS. They are not simple scaling factors ("fudge factors") to force the results of the FROST1 and the FROST2 campaign to agree.

4.1.3 AMS Relative Ionisation Efficiency

Some measurements of pure ammonium sulphate and ammonium nitrate were performed. They revealed that the stoichiometric ratios between ammonium and sulphate and nitrate respectively are not reproduced correctly by the AMS when using values from literature for the relative ionisation efficiencies of sulphate and ammo-

nium (e.g.: Alfarra et al. (2004), and Drewnick et al. (2005)). Alfarra et al. (2004) determined the relative ionisation efficiencies of nitrate, ammonium, sulphate and organics to be equal to 1.1, 3.5, 1.15 and 1.4, respectively. In Drewnick et al. (2005) the RIEs of 1.0, 3.78, 1.2 and 1.4 were reported for the same type of instrument as used during this work.

To get the appropriate values for the instrument used during these studies two methods have been applied to determine the relative ionisation efficiency of sulphate and ammonium. For the first method an internally mixed aerosol of ammonium nitrate and ammonium sulphate was generated by atomising a solution with a known ratio of ammonium sulphate and ammonium nitrate. The ammonium and the sulphate relative ionisation efficiencies could then be determined directly from the ratio to the nitrate signal. A second method was to measure pure ammonium nitrate and pure ammonium sulphate. The RIE for ammonium can be determined from the ammonium nitrate measurement allowing for the correction of the ammonium concentration of the second measurement. The corrected ammonium concentration of the ammonium sulphate measurement can be compared to the sulphate signal. The RIE of sulphate is determined via the expected correct stoichiometric ratio.

The advantage of the first method is that the RIE can be determined directly by comparing to the nitrate concentration without the intermediate of ammonium. This renders the method feasible for the determination of the RIE for substances not containing ammonium, provided that the substances do not chemically react in the atomised solution. However, it is important to very accurately and precisely know the relative concentration of ammonium nitrate to the second compound in the atomised solution. This was achieved by creating parent solutions to avoid weighing of very small quantities. The atomised solutions were created by mixing small quantities of the parent solutions. This resulted in an error of 1 % from the pipette used to prepare the probed solutions. The second method was developed first and used to determine the RIEs of the FROST2 and the ACI-03 campaign. The FROST1 RIEs were calculated using the first method as no other data was available. According to the propagated errors, both methods are approximately equal. However, the first method is more robust as no errors can be introduced by preparing the solutions, which might be relevant when determining RIEs during field campaigns.

For the FROST1, FROST2 and ACI-03 campaigns, the RIE values are shown in Tab. 4.2. The variability of these values is very high, especially for the sulphate RIE, which varies by more than a factor of 3, while the ammonium RIE is within the range which is typically reported in literature (Canagaratna et al., 2007). The

Table 4.2: Relative ionisation efficiencies (RIE) for the species sulphate and ammonium for the FROST1 and FROST2 campaign and the ACI-03 campaign

campaign	sulphate	ammonium
FROST1	0.615 ± 0.011	4.739 ± 0.079
FROST2	0.694 ± 0.026	6.08 ± 0.16
ACI-03	2.06 ± 0.032	5.88 ± 0.092

high variability for sulphate is expected to be due to the different tunings of the ion optics of the instrument. This means that it is not primarily an effect of the ionisation efficiency, but a transmission change of the ion optics introducing the ions into the time-of-flight mass spectrometer and the transmission of the mass spectrometer itself. To avoid this effect, an associate of Aerodyne Inc. retuned the instrument and managed to adjust the RIE values in the range of values reported in literature. However, one week after the retuning, the values were again different. The reproducibility of the mass loadings during the campaigns for similar experimental settings indicate that the RIEs stabilise after some time or vary only slowly. Therefore it was possible to correct for the bad tuning if only known substances were measured.

For laboratory studies as performed in this work it is easy to correct the mass concentrations of ammonium and sulphate while organic species concentrations can only be corrected under favourable conditions. It is necessary to know all individual chemical compounds and it must be possible to separate the mass to charge ratios attributed to the respective substance from the rest of the mass spectrum. Furthermore, as the organic substances mostly do not contain ammonium, it must be possible to create a mixture with known mass ratios of the organic substance to be corrected and a reference substance for which the RIE is known. When sampling ambient air this is nearly impossible except for ammonium and sulphate. Corrections for organics can only be estimated for specific species, which are expected to behave similar as the organic compounds occurring in the ambient air. Schmale et al. (2010) found RIEs of 0.98 for sulphate, 3.11 for ammonium and 1.76 for organics. These values show that it is crucial to determine the RIEs of the different species for every individual AMS to make sure that the mass concentrations are correct.

The ideal way of dealing with the RIE issue would be to analyse the behaviour of the ion transmission of the mass spectrometer with a standard substance. The standard substance must produces known relative ion intensities over a large range of the spectrum to determine if the ion transmission is really responsible for the

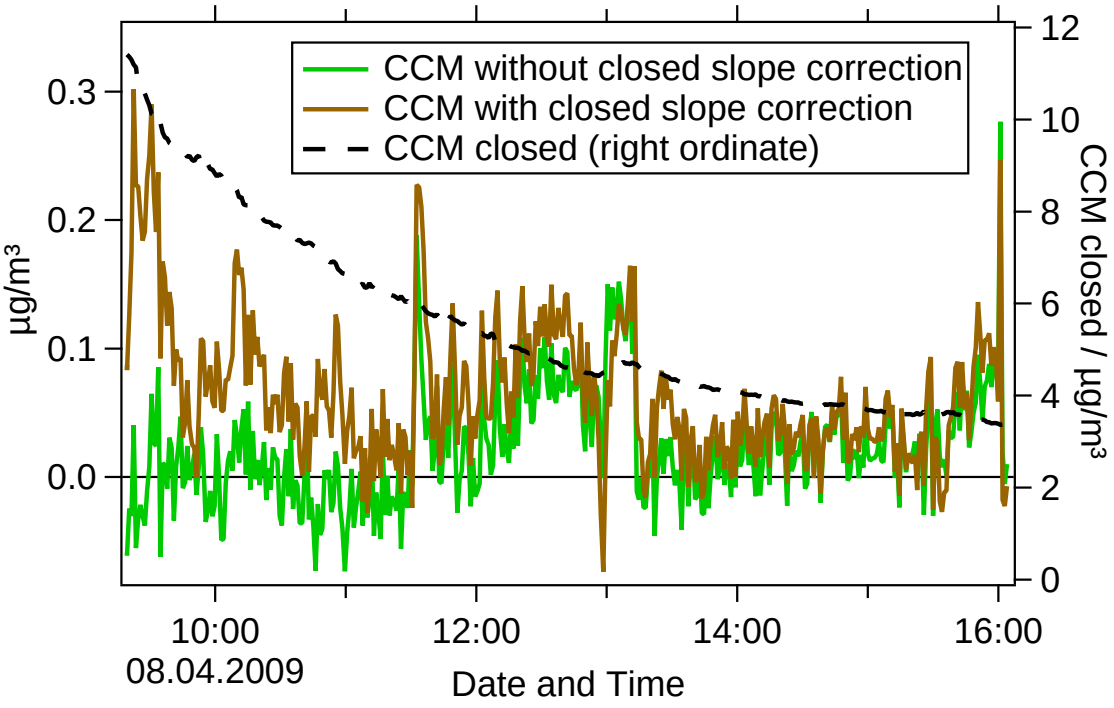

Fig. 4.5: Effect of the correction for high background slope on the CCM signal. Carbon containing material (CCM) is a combination of organics and carbonates.

different RIEs. As the fragmentation is not only determined by the 70 eV impact process but also by the temperature of the vaporiser, the determination of the ion transmission needs an exact control of the vaporiser temperature. This is not provided by the current configuration of the AMS, in which the heating current is set instead of the temperature.

4.2 Signal Correction in the Case of Fast Decreasing AMS Closed Signal

If the particle mass signal in the AMS is low and there is a high and strongly decreasing background signal (closed), the difference signal of the AMS can be significantly biased towards low or even negative apparent mass loadings. This can be the case after a recent vacuum failure or because the instrument was turned off before the measurement, as is often the case during aircraft measurements. This effect is caused by the change of the background between the measurement of the background only and the background plus the particle signal. Figure 4.5 shows the effect of a strongly decreasing background on the signal of carbon containing material. The data was recorded during the FROST2 campaign one day after a vacuum pump exchange.

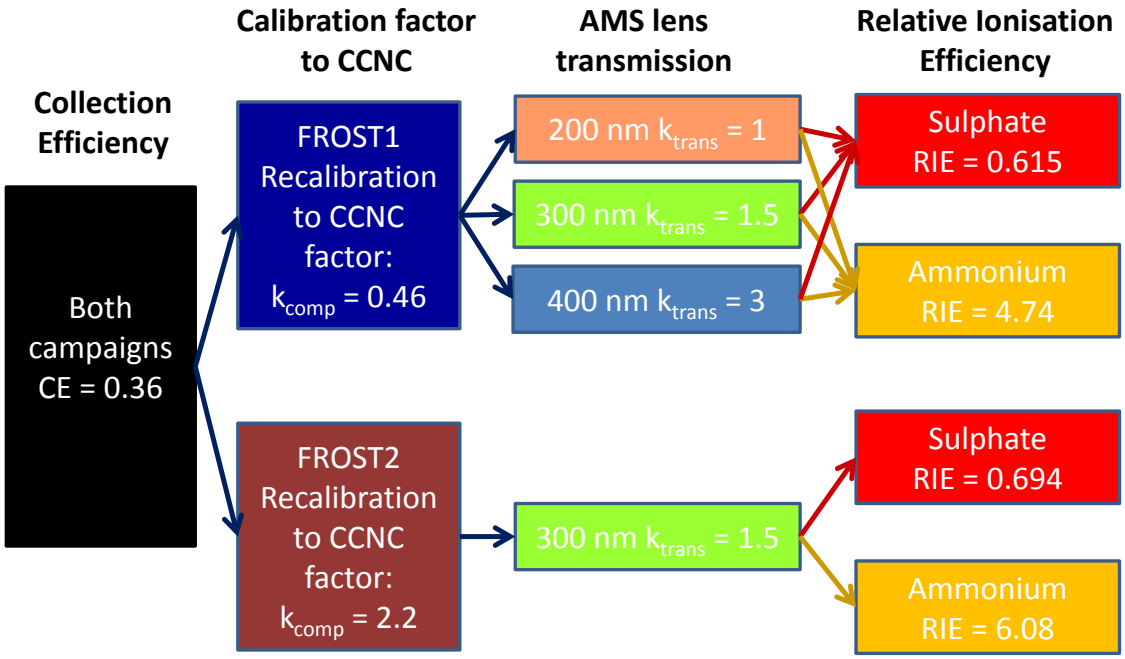

Fig. 4.6: Summary of the correction factors which need to be applied to the different AMS mass loadings to get correct quantitative results.

The black dashed line shows the background signal, which changes between two runs (1 run = 60 s) in the order of magnitude of the real signal. Because of the high change in the background, the real signal is underestimated as shown in the green curve. To correct for this effect, the closed signal was smoothed and the background change between two consecutive sample runs was calculated. As the instrument is switching several times between open and closed during one recording run, the change has to be scaled down to half of one closed-open period before subtraction. For example, if during one recording run three open closed periods are performed, the amount added to the difference signal is equal to 1/6 of the background change between two runs. A drawback of the method is a strong increase of the noise. This technique was applied to those signals which were recorded shortly after a vacuum failure. As shown in Fig. 4.5 the first three hours of this data set are clearly affected by this high background: The uncorrected signal is partly below zero. After about five hours, the instrumental background had markedly decreased, and the difference between the uncorrected and the corrected signal became negligible.

4.3 Summary of the Correction Factors

The correction factors determined in this chapter are summarised in Fig.4.6. To get an accurate determination of the mass per particle for sulphate and ammonium, all the factors shown in Fig. 4.6 must be applied. The collection efficiency for BCR-particles, which is expected to be the same as for ATD, is equal for both FROST campaigns. The recalibration factor to achieve comparability between the measurement campaigns (k_{comp}) differs for both FROST campaigns. The AMS lens transmission correction factors (k_{trans}) are applied to the 300 and 400 nm particle mass loadings. The exact RIE could only be determined for sulphate and ammonium. The correction factors were applied to all measurements of these species. For different species, like organics, the RIE could not be determined and therefore the default values of the fragmentation table were used. It is thus likely that the mass per particle for these substances is not quantitatively correct. However, the conclusions drawn in this thesis do not need a quantification of organics.

For the campaign ACI-03, only the $RIEs$ were determined. The CE and the lens transmission could not be calculated. No recalibration to a CCNC was performed. In Chapt. 6 the attempts to correct the data from the ACI-03 campaign are discussed.

5

Laboratory Studies on the Ice Nucleation Efficiency of ATD

The main goal of this work was to determine the effect of thin coatings on the IN and CCN behaviour of mineral dust particles. During the FROST1 and FROST2 campaigns in Leipzig, ATD was coated with sulphuric acid and optionally humidified and/or heated to determine the effect of these treatments on the IN- and CCN-efficiency of mineral dust particles. In the following it is shown that coating particles with sulphuric acid not only covers the particle surface, but also leads to reactions with the particle surface which irreversibly reduces the IN ability of ATD. The results presented in this chapter have been published in Reitz et al. (2011).

5.1 Experimental Set-up

Figure 5.1 shows the experimental set-up of the FROST campaigns. The left side shows the particle generation section and the right side shows the aerosol characterisation section. The ATD particles are suspended in a fluidized bed generator (TSI 3400A, TSI Inc., St. Paul, Minnesota, USA) which is immediately followed by a multi stage impactor. The impactor removes the large particle fraction of the dispersed aerosol in order to reduce the multiply charged particle fraction when selecting the diameter of the particles with a differential mobility analyser (DMA) at the end of the generation set-up. Mobility diameters of 200 nm, 300 nm, and 400 nm were selected. The 50 % cut-off of the impactor is set to 560 nm aerodynamic diameter when 200 nm or 300 nm mobility diameter particles were selected and to 1 µm when the 400 nm mobility diameter particles were selected. Table 5.1 shows the mobility diameter d_{mob}, the volume equivalent diameter d_{ve} and the aerodynamic diameter d_a of ATD for singly and doubly charged particles for the three diameters used in this study. For $d_{mob} = 300$ nm the doubly charged particles were efficiently suppressed as their aerodynamic size is clearly higher than 560 nm. The size fraction that results in singly charged particles could pass the impactor stages without being reduced. When using particles of 200 nm and 400 nm it is expected

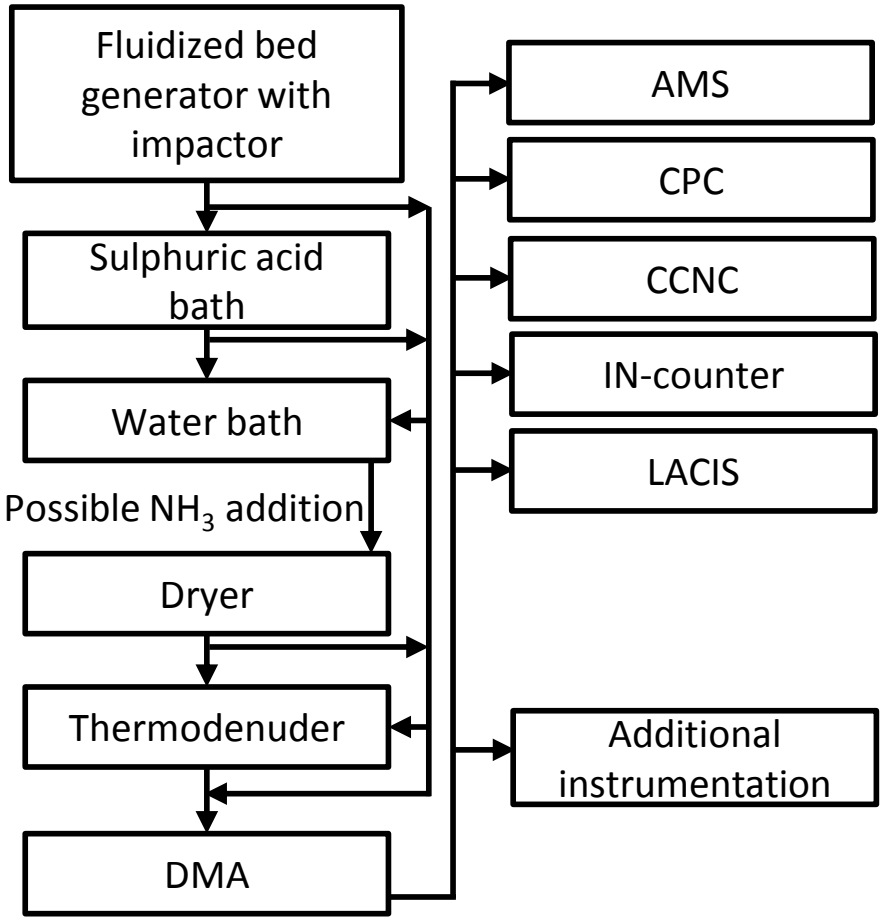

Fig. 5.1: Experimental set-up of the FROST campaigns. The sections between the fluidized bed generator and the DMA can be bypassed.

that some doubly charged particles passed the DMA. Because of this technical reason, the 300 nm mobility diameter particles were studied most extensively and were the only particle size used during FROST2.

Doubly charged particles would have an increased diameter and thus also provide more surface than singly charged particles of the same mobility diameter. The increased diameter would cause the particles to be transmitted less efficiently by the aerodynamic lens of the AMS. Furtehrmore the increased surface would likely cause multiply chared particles to carry more coating material. The CPC however would count the doubly charged particles correctly independent of their size. Whether multiply charged particles cause a bias to higher or lower values depends on the ratio of the additional surface material carried by these particles and the loss due to non-optimal transmission into the AMS. For 200 nm mobility diameter, the doubly charged particles have a size of 323 nm and thus a transmission loss of slightly more

Table 5.1: Mobility, volume equivalent and aerodynamic diameters of the particles used in this study, including the sizes which correspond to doubly charged particles passing the DMA.

d_{mob}		d_{ve}		d_a	
single	double	single	double	single	double
200	323	169	268	268	408
300	508	250	413	383	613
400	697	328	560	493	821

than 33 % as for the 300 nm particles. Assuming a transmission loss of a factor of 0.6 and a coating thickness equal to the 200 nm particles, the doubly charged particles would result in an overestimation of the mass, as the surface increased by a factor of 2.6. How high the overestimation is depends on the number of particles available at a size of 323 nm. For the 400 nm particles, nearly no particles are transmitted into the AMS and thus the mass loadings would be underestimated as the CPC counts all the particles.

The relation between the volume equivalent diameter (d_{ve}) and the mobility diameter (d_{mob}) is given by Eq. (5.1):

$$d_{ve} = d_{mob}\frac{1}{\chi}\frac{C_c(d_{ve})}{C_c(d_{mob})} \tag{5.1}$$

and the relation between the aerodynamic diameter (d_a) and d_{ve} is given by Eq. (5.2):

$$d_a = d_{ve}\sqrt{\frac{1}{\chi}\frac{\rho_{ATD}}{\rho_0}\frac{C_c(d_{ve})}{C_c(d_a)}} \tag{5.2}$$

where $C_c(d) = 1 + \frac{2\lambda}{d}\left[\alpha + \beta\exp(-\frac{\gamma}{2\lambda/d})\right]$ is the Cunningham slip correction factor. α, β, γ are parameter set to 1.142, 0.558 and 0.999 respectively for solid particles according to DeCarlo et al. (2004). λ is the mean free path of air, which is 66.35 nm for atmospheric pressure and 23 °C according to Jennings (1988). The volume equivalent diameters d_{ve} were determined by numerically solving Eq. (5.1) using an dynamic shape factor of $\chi = 1.3$ (Möhler et al., 2008). The determined d_{ve} were used to get numerical solutions for Eq. (5.2). The density of ATD, ρ_{ATD} is equal to 2.6 g/cm^3 (Möhler et al., 2008) and ρ_0 is the unit density. A compilation of different diameter conversion equations is given in DeCarlo et al. (2004).

After the impactor the particles were either directly guided to the DMA and analysed afterwards or the particles were further processed before analysis. The first

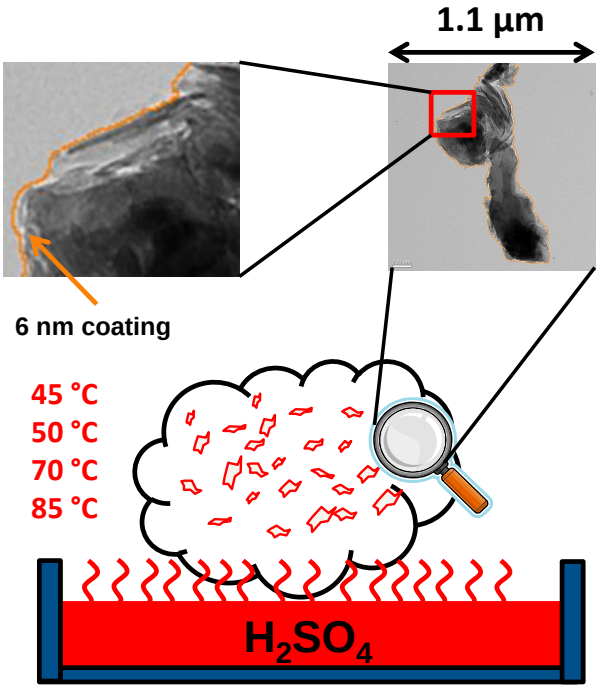

Fig. 5.2: Coating of ATD with sulphuric acid. On the transmission electron microscope picture the thickness of an 6 nm coating is indicated to give an idea of how thin the coatings in this study were. 6 nm is a rather thick coating.

processing unit was a heated sulphuric acid bath over which the particles passed. After the bath, the aerosol cooled down to room temperature and the sulphuric acid vapour condensed on the particle's surface. As the flow through the coating unit was always constant, the amount of sulphuric acid condensed was controlled by the temperature of the sulphuric acid bath. It was set to 45 °C, 50 °C, 70 °C, or 85 °C. Figure 5.2 shows a schematic of this process. As shown later in this chapter, the thickest coating was slightly below 7 nm for a coating temperature of 85 °C on 300 nm particles. The relative humidity in the coating section was always below 10 %.

In the atmosphere particles can be subject to humidity processing. In humid air, hygroscopic particles grow to form small stable droplets with highly concentrated solutions of their soluble material. In the set-up used during FROST, the effect of hygroscopic growth was tested by passing the aerosol over a water bath and thus exposing it to high but subsaturated relative humidity. In some experiments, ammonia was added to the humidified particles to achieve neutralisation. We added the ammonia after the humidification as it turned out that dry particles take up ammonia inefficiently. After this section, the aerosol was dried in a diffusion dryer.

The last processing step was a thermodenuder in order to remove the semi-volatile fraction of the aerosol. It was typically set to 250 °C but in some experiments also 45 °C and 70 °C were used. It turned out that in addition to removing the semi-volatile fraction of the particles, the thermodenuder provoked a heat treatment of the particles. This heat treatment accelerated the reactions taking place on the particles' surface.

After the particles were prepared, they were analysed by a CCNC, an IN counter, LACIS and the AMS. A CPC was operated parallel to the AMS and the AMS mass concentrations were normalised to the particle number concentrations. This was possible as the aerosol was monodisperse and therefore it was expected that all particles have approximately the same surface for the sulphuric acid to condense on. More details on the instruments are provided in Sect. 2.

5.2 Results and Discussion

5.2.1 Uncoated Dust Particles

In a first analysis the AMS mass spectra of pure ATD recorded at 600 °C and 820 °C AMS vaporiser temperature were analysed to obtain information on the non-refractory fraction of the ATD. Afterwards the effect of coating the particles with sulphuric acid is shown. The unit mass resolution spectra shown in Fig. 5.3a to Fig. 5.3c are not corrected for any effects like collection efficiency or inlet transmission. Furthermore, the relative ionisation efficiencies were not applied in these figures. The peak heights shown are thus in nitrate equivalent mass, meaning that they show the concentration the species would have if they had the same ionisation efficiency as the nitrate ions the instrument was calibrated to. However, for the quantification of the coating mass per particle, all correction and conversion factors have to be applied. The calculation of the unit mass resolution spectra is described in Sect. 2.1.5.

Figure 5.3a shows the AMS mass spectrum of uncoated ATD measured with an AMS vaporiser temperature of 600 °C. Except for the grey peaks, which correspond to air compounds, no mass to charge ratios show a high signal. As expected, the core material of the ATD, which has, according to the manufacturer, an evaporation temperature of 1615 ± 75 °C, cannot be detected. The only peaks which are clearly above the surrounding noise are at mass to charge ratios of 55, 56 and 57, which correspond to typical organic fragments, and at 73 and 147, which can be attributed to methyl silicone. The standard species "organics", labelled as "Org" in the AMS user community, was renamed to "carbon containing material" (CCM), as it also covers

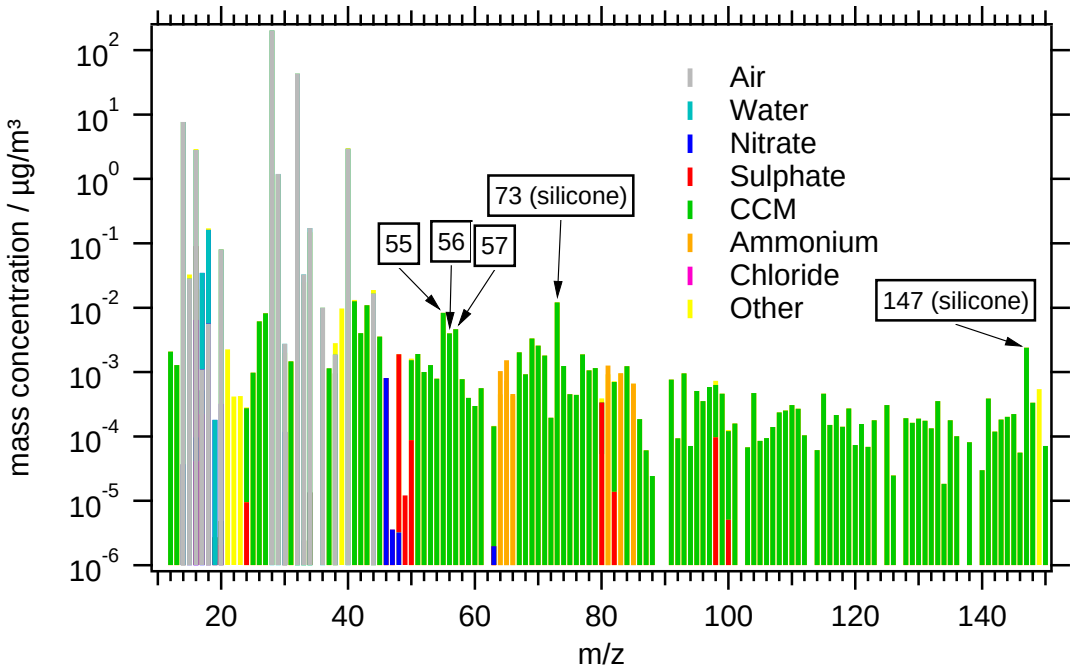

Fig. 5.3a: Average AMS mass spectrum for unprocessed ATD during the FROST1 campaign. Notable are the peaks at m/z 73 and 147 that can be attributed to methyl silicone contaminant.

silicone and carbonates, as shown in the following. The source of the silicone could not be clarified completely. The first possible source that was checked was whether conductive black silicone tubing was used. Timko et al. (2009),Yu et al. (2009), and Schneider et al. (2006) reported this type of tubing to cause these contaminations. However, it turned out that only one very short ($\approx$ 30 cm) connection was made out of silicone. The rest of the set-up only contained stainless steel tubings. Removing this short silicone connection did not reduce the silicone signal. The impactor stages after the suspension of the ATD were covered with silicone grease, but removing the impactor in addition to the silicone tubing did also not remove the silicone signal from the ATD. As a final test, the ATD was directly sampled from a stainless steel bottle which was filled with compressed air. The ATD was introduced into the bottle and the bottle was shaken to mechanically resuspend the particles. Even in this experiment the silicone signal was detected. It can therefore be concluded that the silicone was introduced by the compressed air, which might have used silicone grease in the pumps or it was already present on the ATD after the manufacturing process. For the subsequent analysis it was treated as a known contaminant.

In Fig. 5.3b, the AMS mass spectrum of pure ATD evaporated at 820 °C is presented. The organic peaks at m/z 55, 56, and 57 are lower, probably due to

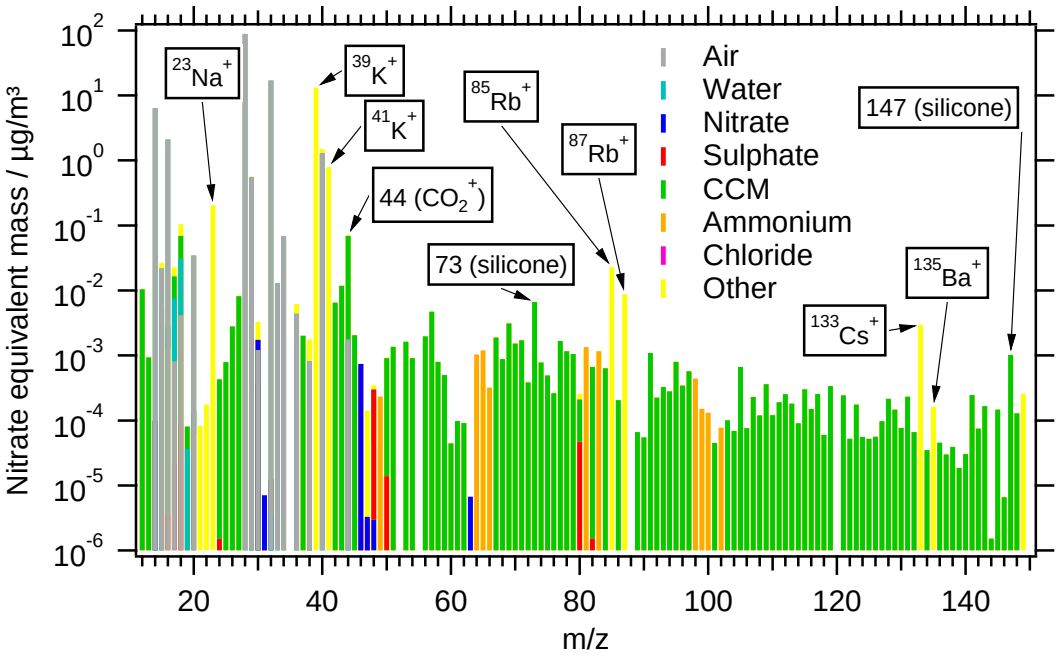

Fig. 5.3b: Average AMS mass spectrum for untreated ATD during the FROST2 campaign. Beside the silicone peaks already visible during FROST1, some new very distinct metal peaks show up in this spectrum, due to the elevated vaporiser temperature of 820 °C: $^{23}Na^+$, $^{39}K^+$, $^{41}K^+$, $^{85}Rb^+$, $^{87}Rb^+$, $^{133}Cs^+$ and $^{135}Ba^+$.

stronger fragmentation because of the higher temperature. In addition some new peaks are visible. In the CCM species, m/z 44, which is the fragment CO_2^+ shows a clear signal. A fraction of this signal can be attributed to strongly fragmented oxygenated organic material. However, some of this signal is expected to originate from decomposing carbonates, as has been shown by Zhao et al. (2010). Beside m/z 44, m/z 23, 39, 41, 85, 87, 133 and 135 show very distinct peaks. These peaks can be attributed to alkali metals and the alkaline earth metal Barium, which all have a very low electronegativity and thus are easily surface ionized (Svane et al., 2004, 2005). As these peaks are not present in the AMS background signal, it can be expected that they really originate from the ATD particles and are not emitted by the AMS vaporiser when it is set to the high temperature. According to analyses by Vlasenko et al. (2005) using X-ray Photoelectron Spectroscopy (XPS) sodium and potassium constitute 2 % and 3 % of the ATD surface metal concentration, respectively. The other alkali metals and Barium were not detected by the XPS, probabely because they were below the detection limit of the method.

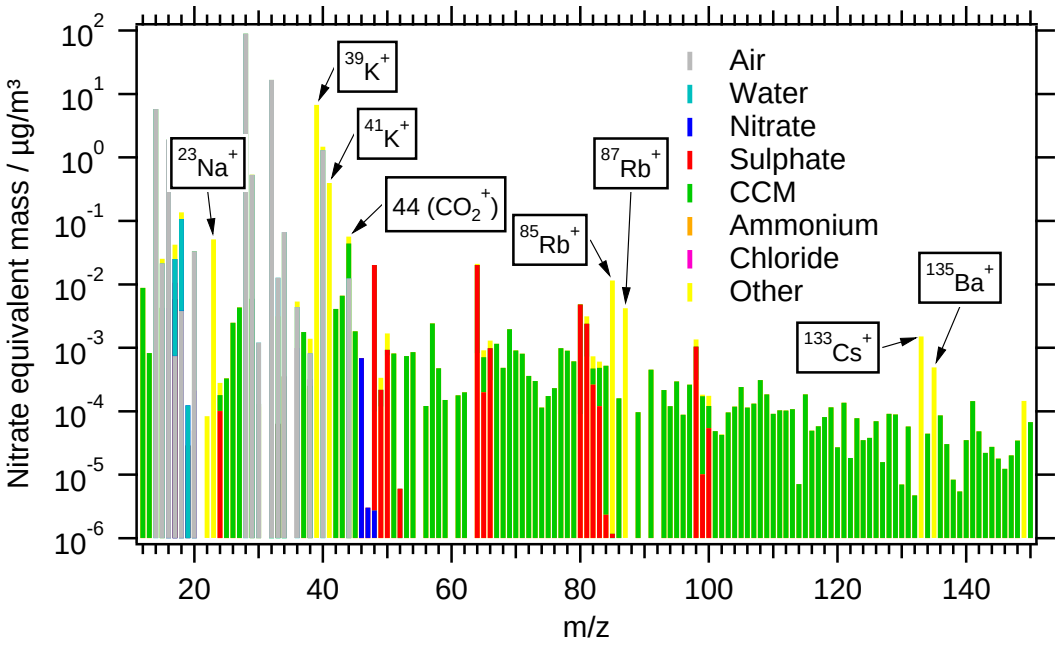

Fig. 5.3c: Average AMS mass spectrum of sulphuric acid processed ATD during the FROST2 campaign. The sulphuric acid bath temperature was 70 °C. Beside the sulphate peaks in red, the metal peaks that were already visible in the unprocessed 820 °C data remain visible. The silicone probably reacted with the sulphuric acid to SiO_2 that is not detected.

5.2.2 Coating Mass per Particle

A mass spectrum of ATD coated with sulphuric acid and evaporated at a temperature of 820 °C in the AMS is shown in Fig. 5.3c. The first thing to notice is the presence of the red peaks belonging to the sulphate species. This species includes sulphuric acid as well as other sulphate compounds like ammonium sulphate or metal sulphates that can form on the particle surface. The peaks attributed to the low-electronegativity metals are still present, but the silicone peaks have disappeared. It is expected that the sulphuric acid oxidised the methyl silicone, leaving gas-phase CO_2, water, and SiO_2. Except for water none of these products can be detected in the AMS. It is likely that the sulphuric acid also etched parts of the surface of the ATD itself. However, the reaction products, which are expected to be mainly metal sulphates, cannot be directly detected by the AMS, as they decompose on heating into sulphur oxides and metal oxides. The sulphur oxides can be detected as part of the sulphate species but metal oxides are mostly refractory and thus invisible to the AMS. To detect the etching it is necessary to combine the results of different instruments which is subject of Sect. 5.2.3 and Sect. 5.2.5.

For the data evaluation, the coating mass per particle measured with the AMS needs to be quantified including all of the correction factors introduced in Sect. 4.1. To determine the mass per particle, the corrected mass concentrations from the AMS data were normalised to the particle number concentration measured with a CPC. As the aerosol was nearly monodisperse, the particle's surface areas are expected to be approximately the same for all particles and thus it was not necessary to use particle surface area distributions in order to get the mass per particle loadings.

The error bars marked in Fig. 5.6a to Fig. 5.6c correspond to the total propagated errors from the measurement's standard deviation and the applied correction factors. They thus give an estimation of the statistical uncertainty of the absolute value of every experiment. In those cases where the same correction factors had to be applied to different experiments, part of the error is a systematic error with respect to the comparison of such experiments. However, if two experiments needed to be corrected with different factors, the error shown on the graph is purely of random nature with respect to the comparison of such measurements. The error of the instrument calibration was not used in the calculation of the error bars, as the same calibration is applied to several experiments and thus is purely a systematic error. When comparing two experiments one should also have in mind that the reproducibility of the different particle generator table settings, although good, was not perfect. According to these considerations the mathematical determinations of the level of significance for two experiments to be different, for example using the T-test, is impossible. If a difference between two similar experiments is clearly visible, it will be discussed for every case separately.

Examplary Calculation of the Sulphate Mass per Particle

To illustrate the calculation of the mass per particle, the calculation steps are demonstrated on the example of one day of the measurement campaign FROST1. Figure 5.4 shows the mass concentration time series together with the particle number concentration recorded by the CPC. The vertical lines delimit the measurement intervals. During one interval typically 10^6 to 10^7 particles were sampled, depending on the particle number concentration and the sampling time. For interval 1 in this example, the number of particles examined was 10^6 and in interval 2, $\sim 3 \times 10^6$ particles have been analysed. In Fig. 5.4 the trace of the mass concentration has the same shape as the trace of the particle number concentration. However, the signal to noise ratio of the particle concentration is much better than the signal to noise ratio of the mass concentration.

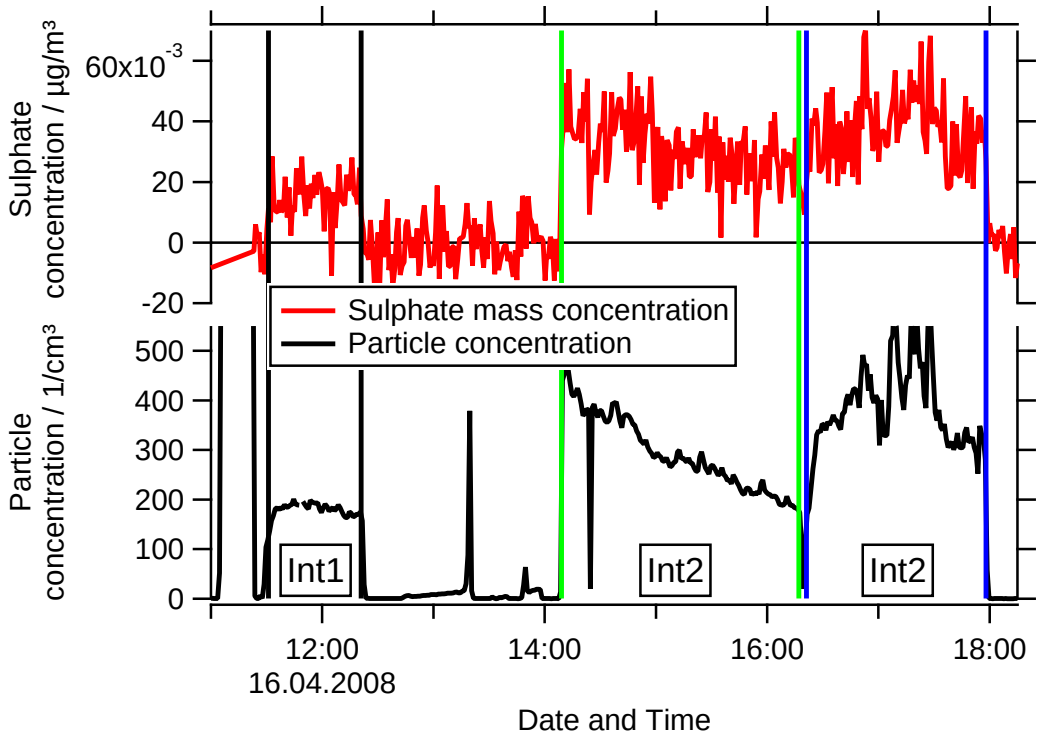

Fig. 5.4: Sulphate mass concentration measured with the AMS together with the particle number concentration from CPC measurements for one day of the FROST1 campaign. The vertical lines indicate the limits of the measurement intervals. Lines with the same colour delimit one interval.

The particle concentration has an original time resolution of 1 s. To calculate the mass per particle, the particle concentration is averaged to the time resolution of the AMS which was set to 1 min during the FROST1 campaign. In Fig. 5.5 the sulphate mass per particle is presented. It was calculated by dividing the mass concentration by the particle number concentration. Although the mass concentrations of the individual intervals differ, the mass per particle is equal for all three intervals. To get the average mass per particle m_{ppraw} for one interval, the time series were averaged. The uncertainty of the average is assumed to be equal to the standard deviation of the mean of the time series. In the case of interval 2, this yields a sulphate mass per particle of 137 ± 4 ag. To determine the correct values, the average of the time series needs to be corrected for the collection efficiency together with the recalibration factor, the lens transmission for 300 nm particles and the relative ionisation efficiency of sulphate. The calculation is summarised in Eq. (5.3) with m_{ppcor} being the corrected mass per particle. To correct for the RIE, the default RIE of sulphate, which is 1.2, needs to be divided by the corrected RIE. The uncertainty of m_{ppcor} (Δm_{ppcor}) was determined by Gaussian error propagation

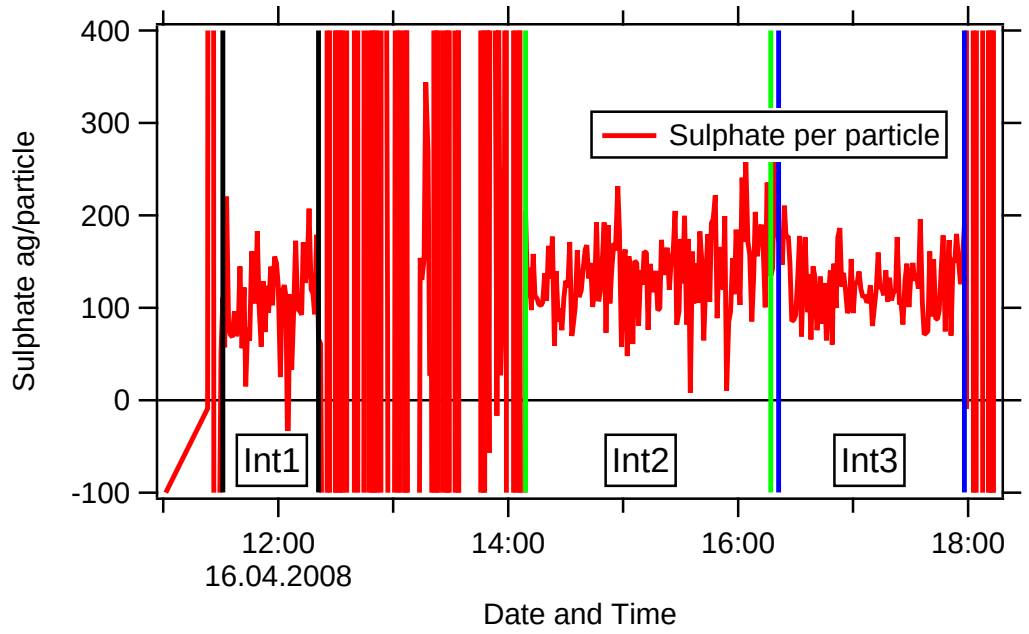

Fig. 5.5: Sulphate mass per particle concentration for the same day as shown in Fig. 5.4. The mass per particle was calculated by normalising the mass concentrations measured with the AMS to the particle number concentrations from CPC measurements. The vertical lines indicate the limits of the measurement intervals. Lines with the same colour delimit one interval.

using Eq. (5.6). The resulting m_{ppcor} is 516 ± 42 ag. To get the values for a certain set of experimental conditions, in this case the intervals Int1 to Int3, the weighted average of the individual intervals was calculated. The corresponding value is shown in Fig. 5.6a as experiment 11.

$$m_{ppcor} = CE^{-1} \cdot k_{comp} \cdot k_{trans} \cdot \frac{RIE(default)}{RIE} \cdot m_{ppraw} \tag{5.3}$$

$$= 0.36^{-1} \cdot 0.46 \cdot 1.5 \cdot \frac{1.2}{0.615} \cdot 137 \text{ ag} \tag{5.4}$$

$$= 516 \text{ ag} \tag{5.5}$$

$$\Delta m_{ppcor} = m_{ppcor} \cdot \sqrt{\left(\frac{\Delta CE}{CE}\right)^2 + \left(\frac{\Delta k_{comp}}{k_{comp}}\right)^2 + \left(\frac{\Delta k_{trans}}{k_{trans}}\right)^2 + \left(\frac{\Delta RIE}{RIE}\right)^2} \tag{5.6}$$

$$= 516 \text{ ag} \cdot \sqrt{\left(\frac{0.02}{0.36}\right)^2 + \left(\frac{0.02}{0.46}\right)^2 + \left(\frac{0.041}{1.5}\right)^2 + \left(\frac{0.011}{0.615}\right)^2 + \left(\frac{4}{137}\right)^2} \tag{5.7}$$

$$= 42 \text{ ag} \tag{5.8}$$

The mass per particle can be translated into a coating thickness d_{coat} using Eq. (5.9). m_{ppcor} is divided by the density $\rho_{H_2SO_4}$ of the coating material, which in this case was assumed to be sulphuric acid. Furthermore, it is divided by the surface area A, which yields a good approximation, as long as the coatings are thin. This was the case for all coatings of the FROST campaigns. The surface area was approximated by the surface area of a sphere with a diameter equal to the mobility diameter of the particles. The assumption of sulphuric acid as coating material is an approximation too. In Sect. 5.2.5 the chemical nature of the coating is discussed and evidence for chemical reactions of the sulphuric acid with the particle surface is given. For the presented example, the coating thickness is estimated to $0.99 \pm 0\ 08$nm. The uncertainty was calculated using Eq. (5.9) with m_{ppcor} substituted by Δm_{ppcor}. Generally speaking, a sulphuric acid coating of 500 ag on a 300 nm particle corresponds to approximately 1 nm.

$$d_{coat} = \frac{m_{ppcor}}{\rho_{H_2SO_4} A} \tag{5.9}$$

$$= \frac{516 \text{ ag}}{1.8356 \times 10^{-3} \text{ ag/nm}^3 \cdot \pi \, (300 \text{ nm})^2} \tag{5.10}$$

$$\cong 1 \text{ nm} \tag{5.11}$$

From the mass per particle, the number of coating molecules N_{coat} can be estimated and compared to the number of molecules N_{ATD} contained in the ATD core material. For simplification, the ATD core is assumed to be composed of pure SiO_2 with a molecular weight M_{SiO_2} of 60 g/mol. For the presented example, the coating is again assumed to be composed of sulphuric acid. Equation (5.12) describes the conversion of mass to number of molecules. "..." is a placeholder for the ATD core or the coating material. N_A is the Avogadro number. The mass is divided by the molar mass and multiplied by N_A to convert moles to molecules.

$$N_{...} = \frac{m_{...}}{M_{...}} \cdot N_A \tag{5.12}$$

An ATD particle of 300 nm contains:

$$\frac{\frac{\pi}{6} (300 \text{ nm})^3 \cdot 2.6 \times 10^{-3} \text{ ag/nm}^3}{60 \text{ g/mol}} \cdot 6.023 \times 10^{23} \text{molec/mol} \cong 4 \times 10^8 \text{ molec} \tag{5.13}$$

compared to:

$$\frac{516 \text{ ag/nm}^3}{98 \text{ g/mol}} \cdot 6.023 \times 10^{23} \text{molec/mol} \cong 3 \times 10^6 \text{ molec} \tag{5.14}$$

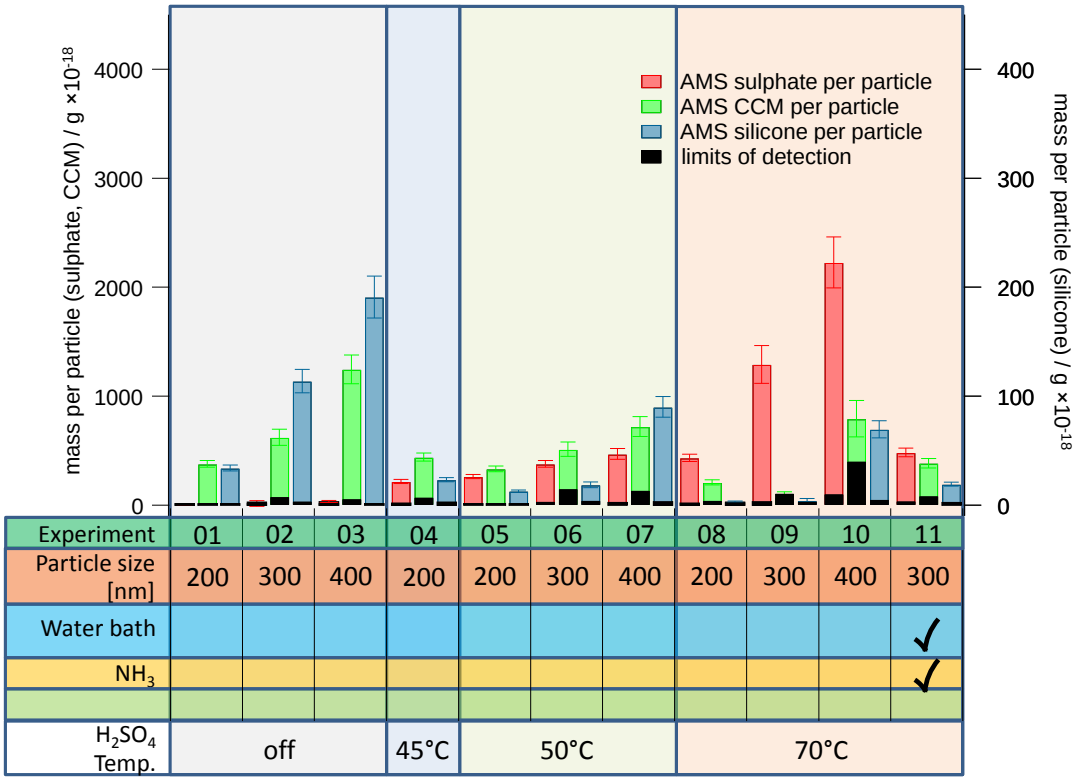

Fig. 5.6a: Summary of the mass per particle for the FROST1 campaign (Experiments 1-11, recorded at 600 °C AMS vaporiser temperature). The left axis refers to sulphate and CCM, the right axis refers to silicone. Note the factor of 10 between the axes. On the horizontal axis, the second line shows the particle size, the third one indicates if the water bath was used, the fourth one if ammonium was added. The last line refers to the temperature of the sulphuric acid coating section.

for the coating. The amount of coating material in this example is thus lower by two orders of magnitude compared to the ATD core material. In the following, the mass per particle is calculated for all experimental settings used during the FROST1 and FROST2 campaigns.

Quantified ATD surface compounds

Figure 5.6a shows a compilation of the average mass per particle calculated for the FROST1 campaign. The AMS vaporiser was set to 600 °C. For all particle preparation settings the AMS species sulphate, CCM and silicone are shown. All other species could not be quantified as they were below the detection limit of the AMS or disturbed by air ions, as was the case for ammonium. The DL were calculated using the new algorithm described in Sect. 3.2.7 and are indicated in black in the graph. The major fragments of ammonium have the mass to charge ratios 15, 16, and 17. Especially m/z 16 caused major problems, as it also includes

the O^+ ions from the air. The signal of the O^+ ions is calculated from the air signal on m/z 14 (N^+) and subtracted from the total signal on m/z 16 in order to obtain the contribution of the other species. It is assumed that the ratio between nitrogen and oxygen in the air is constant (Allan et al., 2004). However, this was not the case during this study. The highest fluctuations of the ratio between oxygen and nitrogen were observed when ammonia was added to the particle flow to neutralise the particles. The ammonia was mixed with nitrogen and its flow seemed to be slightly unstable, thus varying the amount of nitrogen added during the experiments. In the DMA a fraction of this additional nitrogen could diffuse into the air that was sampled by the AMS. The reason for the small fluctuations when no nitrogen was added are unknown. An alternative to the correction via the nitrogen signal at m/z 14 appeared to be the direct use of the signal on m/z 32, which corresponds to O_2^+. This way the influence of the fluctuations of the ratio between the oxygen and the nitrogen concentration is avoided. However when using this correction in situations which were known not to contain ammonium, it nevertheless showed fluctuation around the zero line which were clearly higher than the noise level. Finally it was only possible to use the ammonium signal for experiments during FROST2 with the water bath in use and with a sulphuric acid bath temperature of 85 °C. These experiments yielded the thickest coatings of this study. Only for these measurements, the ammonia uptake was high enough to provide a signal which was clearly above the fluctuations caused by the nitrogen-oxygen-ratio fluctuations.

Mass per particle during FROST1

The first three experiments in Fig. 5.6a show the non-refractory mass loadings for uncoated ATD particles with mobility diameters of 200 nm, 300 nm, and 400 nm. The amount of CCM and silicone is proportional to the squared particle diameters and thus to the particle's surface areas. This indicates that all of the detected material originates from the particle surface and not from the bulk of the particles. The next three temperature groups (experiments 04-11) present measurements for which the particles were coated at 45, 50 and 70 °C. As expected, the amount of sulphate on the particles increases with coating bath temperature as can be seen for example by comparing experiments 04, 05 and 08 with an identical particle size of 200 nm. While the sulphate mass per particle for one particle size increased, the amount of silicone decreased. This can most likely be explained by oxidation of the methyl silicone by the sulphuric acid. If a complete oxidation occurs, the following chemical reaction is proposed:

Table 5.2: Sulphuric acid coating thickness of the FROST1 campaign. Note that the AMS could not detect all of the sulphate material with the vaporiser set to 600 °C. A fraction of the sulphuric acid reacted with the particle surface and formed refractory metal sulphates.

experiment	coating temperature / °C	size	coating thickness / nm
04	45	200	0.94 ± 0.08
05	50	200	1.13 ± 0.08
06	50	300	0.73 ± 0.06
07	50	400	0.51 ± 0.05
08	70	200	1.88 ± 0.14
09	70	300	2.5 ± 0.34
10	70	400	2.4 ± 0.25
11	70(WB)	300	0.93 ± 0.07

WB: For this experiment, the water bath was used and NH_3 was added to the flow.

$$[SiOC_2H_6]_n + 8n\,H_2SO_4 \longrightarrow 2n\,CO_2 + n\,SiO_2 + 11n\,H_2O + 8n\,SO_2$$

n is the number of monomers of the methyl silicone polymer. A smaller, similar effect of the sulphuric acid is observed for the CCM.

The amount of coating increased when the particle size increased, as can be seen for experiments 05 to 07 and 08 to 10 for 50 °C and 70 °C, respectively. However, the increase was not proportional to the particle surface as was found for the CCM and the silicone on the pure dust. The reason for this behaviour is not clear. In the case of those particles coated at 70 °C (experiment 08 to 10), the ratio between the sulphate mass and the squared particle mobility diameter was identical for the 300 nm and 400 nm particles. Table 5.2 shows the coating thicknesses of sulphuric acid, which correspond to the ratio of the coating volume and the particle surface area, for the different FROST1 experiments. The coating thickness at 70 °C sulphuric acid bath temperature, is lower by nearly 25 % for the 200 nm particles compared to the 300 nm and 400 nm particles. For those particles coated at 50 °C (experiment 05 to 07), the ratio between the sulphate mass per particle and the square of the diameter decreased with increasing diameter. As the behaviour is different depending on the coating temperature, it is difficult to explain this effect. A possible explanation could be that the particle coating section did not exactly reproduce the coating thicknesses between different experiments with different particle sizes. A reason for this might be that the particle concentration in the coating section was different for different particle sizes. This was very likely the case for the 400 nm particles, as the impactor was set to a higher cut-off diameter causing a bigger fraction of the particles to pass. However, only for the particles coated at 50 °C the 400 nm

particles (experiment 07) show the expected lower coating thickness while for 70 °C the 300 nm (experiment 09) and 400 nm (experiment 10) particles show the same coating thickness. A comparison of the mass per particle deduced from different intervals of the same aerosol preperation setting (e.g.: Fig. 5.5), shows that the mass per particle varies only slightly between different measurement intervals of the same experiment. The different coating thicknesses are thus not related to bad reproducability of the same experiments. An exception were the 300 nm particles coated with sulphuric acid at a temperature of 70 °C (experiment 09). In this case a very high difference between measurements with similar settings was observed. One measurement interval showed a mass per particle loading of 1290 ag and two showed approximately 680 ag. A detailed analysis of the fragmentation pattern showed that for the two lower values, the sulphuric acid reacted with the particle surface producing partially refractory metal sulphates. The two lower values are thus artefacts and are not included in the average of mass per particle for experiment 09. Particle surface reactions are discussed in more detail in Sect. 5.2.4.

The last experiment in Fig. 5.6a (experiment 11) shows the mass per particle loading for particles with a size of 300 nm which were coated at 70 °C followed by the water bath and the addition of ammonia. The water bath was originally included into the set-up to humidify the particles in order to improve the uptake of ammonia to the particles and achieve a full neutralisation of the coated ATD. In Sect. 5.2.3 to Sect. 5.2.5 it is shown that the use of the water bath did additionally cause the reaction of the sulphuric acid with the particle surface to be accelerated and/or the reaction equilibrium was changed. This caused the formation of partially refractory sulphate compounds and thus the average sulphate mass loading for the last category was much lower than for those particles sized 300 nm which were coated with sulphuric acid at 70 °C without the use of the water bath (experiment 09).

Mass per Particle during FROST2

Untreated ATD

Figure 5.6b shows the mass per particle loadings for experiments recorded during the FROST2 campaign. The presented experiments were conducted without coating or with low coating at a sulphuric acid bath temperature of 45 °C. All experiments during the FROST2 campaign where performed with particles of a mobility diameter of 300 nm. In addition to the water bath the thermodenuder was used during some of the experiments. The AMS vaporiser was set to a temperature of 820 °C, allowing for the evaporation of compounds which are refractory at the standard AMS vaporiser temperature of 600 °C. The first experiment in the graph (experi-

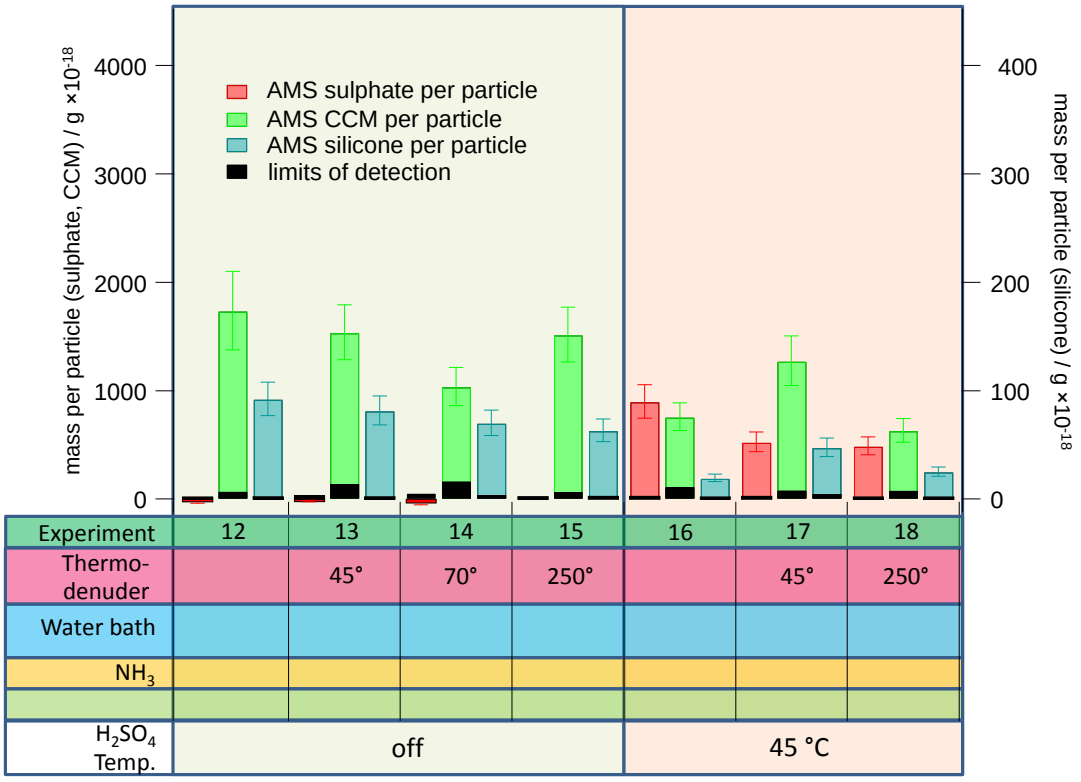

Fig. 5.6b: Summary of the mass per particle for the FROST2 campaign thinnest coating experiments (Experiments 12-18, recorded at 820 °C AMS vaporiser temperature). All particles had a mobility diameter of 300 nm. The left axis refers to sulphate and CCM, the right axis refers to silicone. Note the factor of 10 between the axes. On the horizontal axis, the second line now shows the thermodenuder temperature in contrast to Fig. 5.3a, the third one indicates if the water bath was used, the fourth one if ammonium was added. The last line refers to the temperature of the sulphuric acid coating section.

ment 12) shows the non-refractory composition of uncoated ATD. The amount of silicone was approximately the same for this measurement as for the corresponding measurement during the FROST1 campaign (see Fig. 5.6a). However, the CCM material was much higher for the FROST2 campaign than for the FROST1 campaign. This can be explained by the thermal decomposition of carbonates from the ATD surface on the vaporiser of the AMS (Zhao et al., 2010). For example calcium carbonate, which was detected in the ATD by Vlasenko et al. (2005), could decompose to calcium oxide and carbon dioxide.

Uncoated ATD treated with the thermodenuder

Experiments 13 to 15 show measurements of pure ATD after passing the thermodenuder set to 45 °C, 70 °C and 250 °C. The CCM does not show any clear trend. It is high for a thermodenuder temperature of 45 and 250 °C and lower in experiment

14, where the thermodenuder was set to 70 °C. The silicone is slightly reduced by the thermodenuder. It would be surprising if the silicone present on the particle surface had a volatility which is low enough to remain mainly on the particle surface even at a denuder temperature of 250 °C. It is therefore likely that the main fraction of the silicone was condensing on the particle surface after the aerosol passed the thermodenuder. This could be explained by the assumption that the silicone is present in the compressed air rather than being already present on the ATD surface after the manufacturing of the dust.

ATD coated at 45 °C

During experiments 16 to 18 a low amount of sulphuric acid was condensed on the particle surface with the sulphuric acid coating bath set to 45 °C. The coating thicknesses ranged from 0.95 ± 0.16 nm (491 ag) to 1.7 ± 0.3 nm (901 ag). The first of these three experiments shows the effect of condensing sulphuric acid on the ATD without further processing. Similar to the FROST1 data, the silicone was clearly reduced by the addition of sulphuric acid which reacted with the silicone. The sulphuric acid could consume silicone present on the particle surface or silicone which was condensing on the ATD after the sulphuric acid coating. In experiment 17 and 18, the effect of the thermodenuder on the amount of sulphate was analysed. The denuder was set to temperatures of 45 °C and 250 °C, respectively. The thermodenuder originally was meant to remove the sulphuric acid from the particle surface in order to check if the IN-efficiency of ATD could be restored this way. However, the graph shows that most of the sulphate signal that was present on the non-denuded particles, remained after the denuding. The reason for this is that the thermodenuder, similar to the water bath, accelerates the reactions with the particle surface, resulting in compounds with lower volatility which cannot be removed by the thermodenuder. More details are presented in Sect. 5.2.4. Interestingly, the silicone signal is higher when the thermodenuder is used compared to experiment 16 which was conducted without the thermodenuder. The highest silicone signal for the coated particles was observed at a thermodenuder temperature of 45 °C. This favours the assumption that the silicone was at least partially condensed on the ATD after the particle generation section. After applying the thermodenuder, no unreacted sulphuric acid was left on the particle surface to oxidise newly condensing silicone.

ATD coated at 70 °C *without further processing*

Figure 5.6c shows the mass per particle loadings for those particles which were coated by medium and thick coatings, corresponding to coating bath temperatures

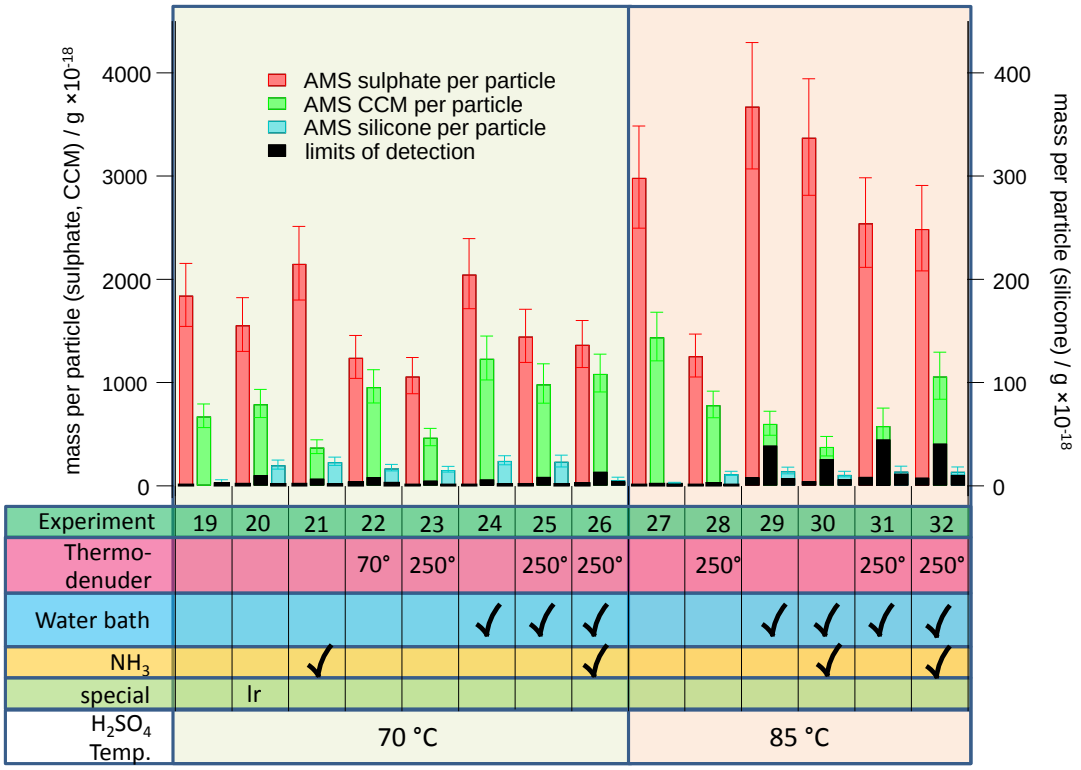

Fig. 5.6c: Summary of the mass per particle for the FROST2 campaign thicker coating experiments (Experiments 19-32, recorded at 820 °C AMS vaporiser temperature). All particles had a mobility diameter of 300 nm. The left axis refers to sulphate and CCM, the right axis refers to silicone. Note the factor of 10 between the axes. On the horizontal axis, the second line shows the thermodenuder temperature, the third one indicates if the water bath was used, the fourth one if ammonium was added. The lr marked in the special line refers to an experiment with an additional residence volume of 10 L after the particle coating. The last line refers to the temperature of the sulphuric acid coating section.

of 70 °C and 85 °C. The resulting coating thicknesses ranged from 2.1 ± 0.3 nm (1065 ag) up to 7.1 ± 1.2 nm (3681 ag). The left part of the graph (experiments 19 to 26) shows the mass loadings of particles coated with the sulphuric acid bath temperature set to 70 °C. For experiments 19 and 20 no treatment was applied except for the coating with sulphuric acid. During experiment 20, the length of the tubing after the coating section was increased to get 10 dm^3 of extra residence volume resulting in an additional residence time of 10 min. The only effect caused by this longer residence time was that the silicone signal was increased while the sulphate signal is not significantly lower. The longer residence time could give the sulphuric acid more time to react with the particle surface or with ammonia present in the air, deactivating the sulphuric acid which could have oxidised the silicone. In Sect. 5.2.4 it is shown that there is only a minor increase of the reaction on the particle

surface for the longer residence experiment. Furthermore Sect. 5.2.5 indicates that particle surface reactions did not result in the formation of refractory substances at 820 °C vaporiser temperature. The second possible effect, which is the reaction with the ammonia present in the air is thus more likely. This assumption is supported by the increase of the ammonium signal for these experiments. However, as mentioned before, the ammonium signal is disturbed and consequently the observed increase of ammonium might be an artefact.

Effect of the water bath and the thermodenuder on particles coated with sulphuric acid at 70 °C

The addition of ammonia to the dry, coated ATD (experiment 21) results in a higher sulphate signal. The signal is slightly higher than for the non-neutralised particles but the difference is not significant. A clear reduction of the sulphate signal can however be seen for experiments 22, 23, 25 and 26 with the thermodenuder in use. Even a denuder temperature of 70 °C is enough to achieve a reduction of the sulphate signal in the same range as with the higher temperature of 250 °C. The use of the water bath prior to the thermodenuder (experiments 25 and 26) resulted in a slightly higher signal for the sulphate. The use of the water bath without the thermodenuder again results in a similar sulphate mass per particle as found when only coating the particles.

Effect of the thermodenuder with and without prior humidification of the ATD coated at 85 °C

On the right side of Fig. 5.6c (experiments 27 to 32) particles coated with the sulphuric acid bath set to 85 °C are shown. Qualitatively the same effects can be seen as for those experiments with thinner coatings for which the coating bath temperature was adjusted to 70 °C. However, the difference in the sulphate mass per particle between those particles which were denuded without prior humidification (experiment 28) and those that passed the water bath before the thermodenuder (experiments 31 and 32) is much clearer. This can be explained by the observation (Sect. 5.2.4) that the water bath accelerated reactions of the particle surface with the sulphuric acid, producing products which cannot be easily evaporated by the thermodenuder. This interpretation is also in accordance with the higher difference between the denuded and humidified particles (experiment 31 and 32) and those that were only denuded (experiment 28), when comparing the thicker coatings to the medium coatings (experiments 22 to 26). When the thermodenuder was used without prior humidification of the particles, more time is necessary for the thicker

coatings to completely react with the particle surface. Consequently more unreacted sulphuric acid was left on these particles, which could be evaporated at 250 °C.

Detection of ammonium on the ATD particles coated at 85 °C

For those particles which were coated at a temperature of 85 °C and processed with the water bath (experiements 29 and 30) the ammonium signal was high enough to be quantified. The ammonium measured for these experiments corresponds to 0.51 ± 0.12 times the concentration necessary for a complete neutralisation of the sulphuric acid. This value was calculated by dividing the ammonium mass per particle by the amount of ammonium necessary to completely neutralise the sulphuric acid. The amount of ammonium per particle was calculated i the same way as the sulphate mass per particle. The uncertainty was calculated using Gaussian error propagation. However, when the thermodenuder was used after the water bath, the ammonium signal was reduced at least by a factor of 2.

Silicone: A useful contaminant

The silicone was present for all categories except when no more processing than coating with sulphuric acid was performed. This matches the assumption that the silicone condensed on the particles after the processing section because all processings led at least to a partial consumption of the sulphuric acid. A longer residence time could also lead to a partial neutralisation of the sulphuric acid as was indicated by the ammonium signal. Thus the unreacted sulphuric acid would also be reduced for experiment 20. This indicates that the elevated ammonium signal for the longer residence is not an artefact. Silicone could only survive on the ATD surface, when the reactivity of the sulphate compounds was reduced. The silicone contamination can therefore be used as a possible proxy for the presence of unreacted sulphuric acid after the particle preparation section.

Generally, the sulphate mass per particle loadings for the different processes show that the sulphuric acid did not only produce a coating on the surface of the ATD but it also reacted with the surface. In the following, stronger evidence for surface reactions is provided and linked to the reduction of the ATD IN-efficiency when subject to sulphuric acid coating.

5.2.3 Comparison of AMS Sulphate Concentrations to the IN-Efficiency of ATD

In this section, the sulphate mass per particle is compared to the IN-fraction calculated from the CFDC data and the LACIS data. For all experiments shown in this

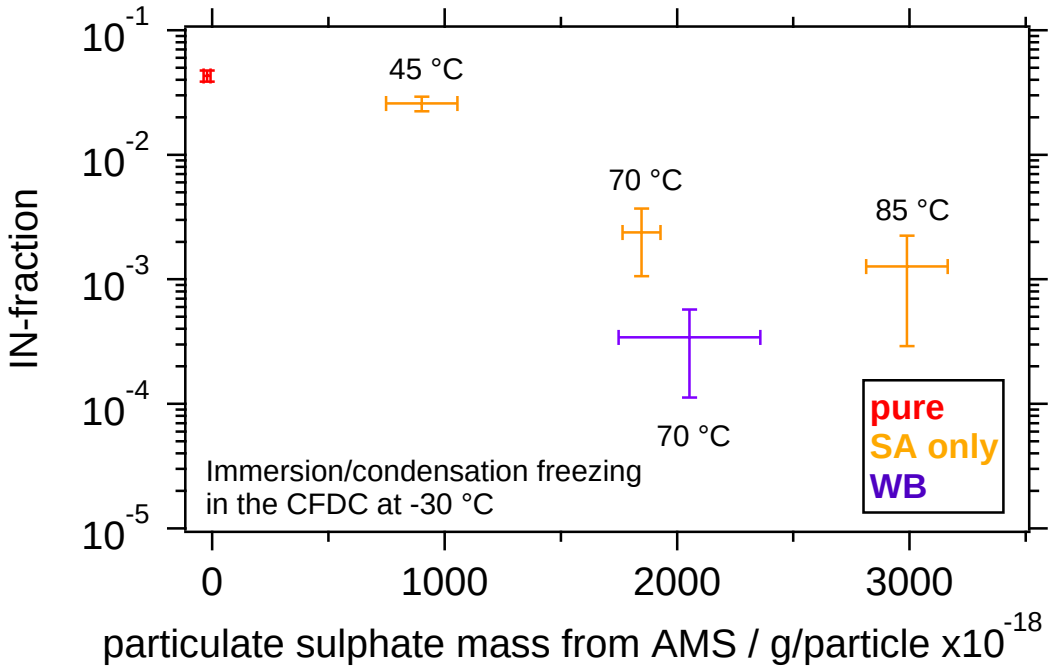

Fig. 5.7: Comparison of AMS sulphate per particle masses to the CFDC ice nuclei counts at −30 °C in the immersion-freezing regime. Different coating temperatures are shown for the different particle classes. The particle class "pure" includes those experiments with no treatment and no sulphuric acid condensation. The particle class "SA only" includes particles which passed the sulphuric acid bath but no further processing was performed and "WB" indicates the additional use of the water bath. The IN-activity of the ATD is reduced if more sulphuric acid is condensed on the particle surface and the use of the water bath decreases the number of IN even further. The error bars of the mass concentrations were determined as described in Sect. 5.2.2.

section, the CFDC and LACIS where operated in a way that the ATD particles were first activated as cloud droplets and only afterwards started to freeze. In the case of the CFDC the freezing mode was thus immersion or condensation freezing (Sullivan et al., 2010b) and for LACIS it is known that the freezing mode is immersion freezing (Niedermeier et al., 2010). This means that for both chambers the ATD particles were immersed in a liquid droplet prior to freezing. After the different processing steps the soluble fraction of the coating was highly dissolved and thus no relevant freezing point depression was expected. Sullivan et al. (2010b) calculated that for the settings of the CFDC used during the campaign, the droplets were big enough for the freezing point depressing to be below 0.1 °C.

Figure 5.7 shows the comparison of the IN-active fraction of the ATD, deduced from the CFDC measurements, to the mass of sulphate per particle calculated from the AMS measurements. The red point is a reference measurement for pure ATD without any processing. It shows the highest IN-efficiency. The orange points orig-

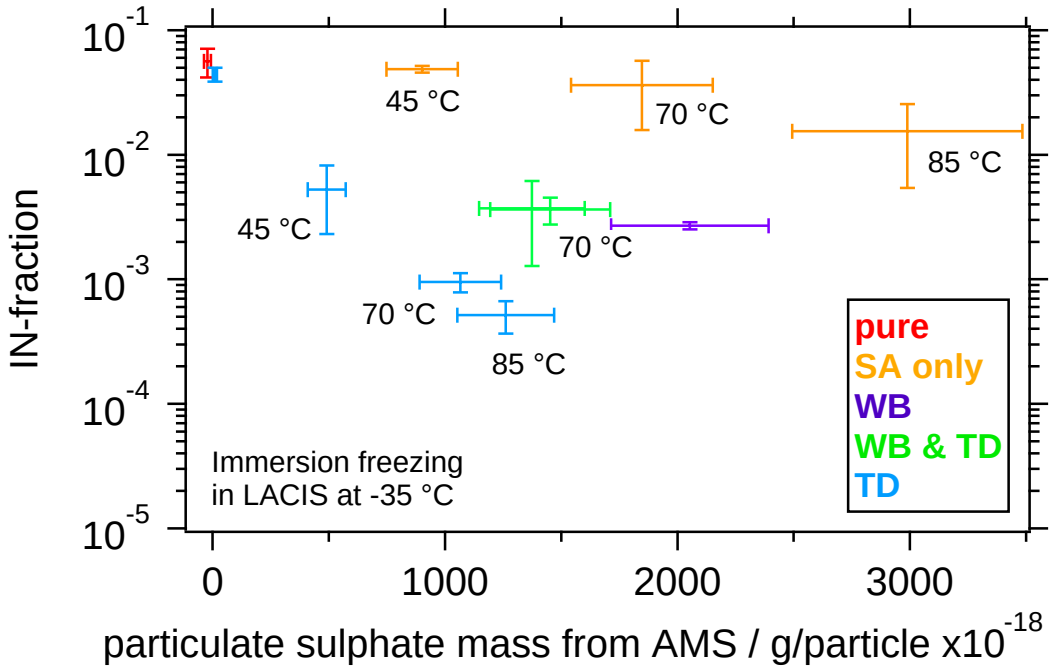

Fig. 5.8: Comparison of AMS sulphate per particle masses to the LACIS ice nucleus counts at −35 °C during FROST2. Different sulphuric acid bath temperatures are shown for every particle class. The particle class "pure" includes those experiments with no treatment and no sulphuric acid condensation. The particle class "SA only" includes particles which passed the sulphuric acid bath but no further processing was performed. "WB" indicates the additional use of the water bath and "TD" the additional use of the thermodenuder after the treatment except for the blue point on the upper left which refers to particles which passed the thermodenuder but were not coated. The error bars of the mass concentrations were determined as described in Sect. 5.2.2.

inate from measurements of sulphuric acid coated particles. The more sulphate is present on the particles' surface the more the IN-efficiency is reduced. Again, the sulphate signal must be interpreted as the sum of all substances that contribute to the mass to charge ratios related to sulphate compounds which include sulphate salts as well as sulphuric acid. Those data points coloured in purple refer to measurements with the water bath in use. For similar amounts of sulphate on the ATD as for the non-humidified particles, these measurements yielded much lower IN-fractions. This is a strong indication that humidification enhances reactions on the particle surface which contribute to the reduction of the ice active surface properties.

Figure 5.8 shows the comparison of the ice active fraction of ATD deduced from LACIS measurements compared to the sulphate mass per particle as found by the AMS. A comparison of LACIS and CFDC is shown in Niedermeier et al. (2011). The red point in Fig. 5.8 corresponds to a measurement of pure ATD and is shown for reference. Similar to the comparison to the CFDC data the orange points show the

effect of coating with sulphuric acid without further processing, which also resulted in a reduction of the ice active fraction of the ATD. The water bath data, marked in purple, show the same effect as in the comparison with the CFDC: the IN-fraction is further reduced. For the comparison of the LACIS data with the AMS sulphate mass fraction, data with the thermodenuder in use were available. Those data points which refer to measurements with the thermodenuder used after the coating and the water bath are coloured in green. They show the same IN-fraction for a given sulphate mass per particle as those data points which refer to coated particles which were only humidified after the coating. This indicates that after the use of the water bath, nearly no sulphuric acid is left, as sulphuric acid would be removed from the surface at a thermodenuder temperature of 250 °C.

The blue points in Fig. 5.8 mark those experiments which a thermodenuder temperature of 250 °C but without prior use of the water bath. The blue point close to the red point was recorded without coating and is used as reference. This point shows that the heating in the thermodenuder alone is not able to reduce the IN-fraction of the ATD. However, when the particles were coated prior to passing the thermodenuder, the IN-fraction is strongly reduced. It appears as if the effect was even stronger than for the water bath only, but it has to be considered that the thermodenuder also removes part of the sulphuric acid and thus shifts the blue points to the left. Therefore, the heat processing effect of the thermodenuder when used after the sulphuric acid coating can be considered to be similar to the effect of the water bath.

In Sullivan et al. (2010b) the strong reduction of the IN-fraction due to the use of the water bath after the sulphuric acid coating was interpreted as an irreversible destruction of ice active sites. The destruction is thought to be irreversible because the particles had been activated as cloud droplets when the freezing occurred. If the sulphuric acid acted as a pure surface covering effect, the activation as a water droplet would have dissolved the sulphuric acid. Thus, the IN-ability of the ATD should have been restored as the freezing point depression effect was negligible. The fact that the IN-efficiency was not restored after the droplet activation is thus a further indication for a reaction on the particle surface which can not be reversed.

The nature of the active sites is still unknown, but it appears that they can be destroyed by etching through sulphuric acid. A possible property of ice active sites could be a structure which is similar to hexagonal ice and which can participate in hydrogen bond like interactions (Pruppacher and Klett, 1997, chapter 9.2) or related to strong local electric fields, as was indicated by Choi et al. (2005). Cubic ice formation appears to be relevant in homogeneous freezing (Murray and Bertram, 2006,

Murray et al., 2005). Therefore it could be expected that cubic-ice-like-structures might also play a role in heterogeneous ice formation (Eastwood et al., 2008). Other properties are also possible. The properties which are crucial for the ATD to act as an ice nucleus cannot be fully explained in this study. However, the possible chemical nature of active sites can be analysed.

5.2.4 Sulphate Fragmentation Pattern: Evidence for ATD Surface Etching

In the preceding sections, it became clear that a reaction of the sulphuric acid with the particle surface is probably taking place but could not be detected directly. In this section, evidence for a reaction of the sulphuric acid with the particle surface is given by showing that after the use of the water bath and/or the thermodenuder, the compounds belonging to the AMS sulphate species are no longer sulphuric acid but must be metal sulphates. First possible reactions are suggested and afterwards they are experimentally verified.

The following model reactions (React. (R5.1) to React. (R5.7)) are suggested to take place on the particle surface, based on the available material. M is a metal with a valency of 3 e.g. aluminium. However, other metals which are present on the ATD surface with different valencies were probabely also involved in the surface reactions. Carbonate is shown as an example for an anion. In Sect. 5.2.5 an analysis is presented to find out which metals were involved in the surface reactions and the possible anions are discussed. The reaction equations are not equilibrated as the relative contribution of the different products is unknown.

Reaction (R5.1) refers to a coating with sulphuric acid followed by a humidification of the particle surface by the water bath. Beside the metal sulphates, mixed sulphates of ammonium and a metal are also possible. Part of the sulphuric acid is also expected to be neutralised to ammonium sulphate. Water and carbondioxide can form in this process and are released to the gas phase as indicated by "g". Reaction (R5.2) describes the evaporation of the compounds formed in React. (R5.1) on the AMS vaporiser. Only those compounds marked with "g" were evaporated and could be detected in the AMS. SO_i with i equal to 1, 2 or 3 as well as H_2SO_4 contributed to the AMS sulphate species signal. H_2O is veiled by the instrument residual gas and NH_3 contributes to the ammonium species signal. However, as mentioned in Sect. 5.2.2, most of the time it was not possible to quantify ammonium.

$$\mathrm{M_2(CO_3)_3 + H_2SO_4 + NH_3 \overset{H_2O}{\rightarrow} M_2(SO_4)_3 + MNH_4(SO_4)_2 + (NH_4)_2SO_4 + CO_2(g) + H_2O(g)} \quad \text{(R5.1)}$$

$$\overset{vaporiser}{\rightarrow} \mathrm{M_2O_3 + NH_3(g) + SO_i(g) + H_2SO_4(g) + H_2O(g)} \quad \text{(R5.2)}$$

In React. (R5.3), the effect of the thermodenuder is shown without using the water bath before. The only chemical effect of the thermodenuder was to enhance the reaction with the particle surface. Since the ammonia uptake without the water bath is expected to be low, only metal sulphates, water and carbon dioxide are produced. As water and carbon dioxide evaporate in the TD, only metal sulphates are left from the reaction. In the AMS evaporation process (React. (R5.4)) the metal sulphates decomposed into metal oxides and sulphure oxides. The sulphure oxides contributed to the AMS sulphate species and no sulphuric acid was present.

$$\mathrm{M_2(CO_3)_3 + H_2SO_4 \overset{250\,^\circ C}{\rightarrow} M_2(SO_4)_3 + CO_2(g) + H_2O(g)} \quad \text{(R5.3)}$$

$$\overset{vaporiser}{\rightarrow} \mathrm{M_2O_3 + SO_i(g)} \quad \text{(R5.4)}$$

Reaction (R5.5) to React. (R5.7) depict the processes which could take place if the coated ATD was first humidified and passed the thermodenuder afterwards. Reaction (R5.5) is identical to React. (R5.1). After the water bath the thermodenuder could not enhance the reaction of the sulphuric acid, as it reacted already due to the humidification. It only removed part of the material from the particle surface. Those compound which contained ammonium mainly decomposed at a temperature of 250 °C. For the vaporisation step (React. (R5.7)) only metal sulphates and bisulphates were left. When decomposed on the vaporiser, they produced metal oxides, water and sulphure oxides.

$$\mathrm{M_2(CO_3)_3 + H_2SO_4 + NH_3 \overset{H_2O}{\rightarrow} M_2(SO_4)_3 + MNH_4(SO_4)_2 + (NH_4)_2SO_4 + CO_2(g) + H_2O(g)} \quad \text{(R5.5)}$$

$$\overset{250\,^\circ C}{\rightarrow} \mathrm{M_2(SO_4)_3 + M(HSO_4)_3 + NH_3(g) + H_2O(g) + SO_i(g)} \quad \text{(R5.6)}$$

$$\overset{vaporiser}{\rightarrow} \mathrm{M_2O_3 + H_2O(g) + SO_i(g)} \quad \text{(R5.7)}$$

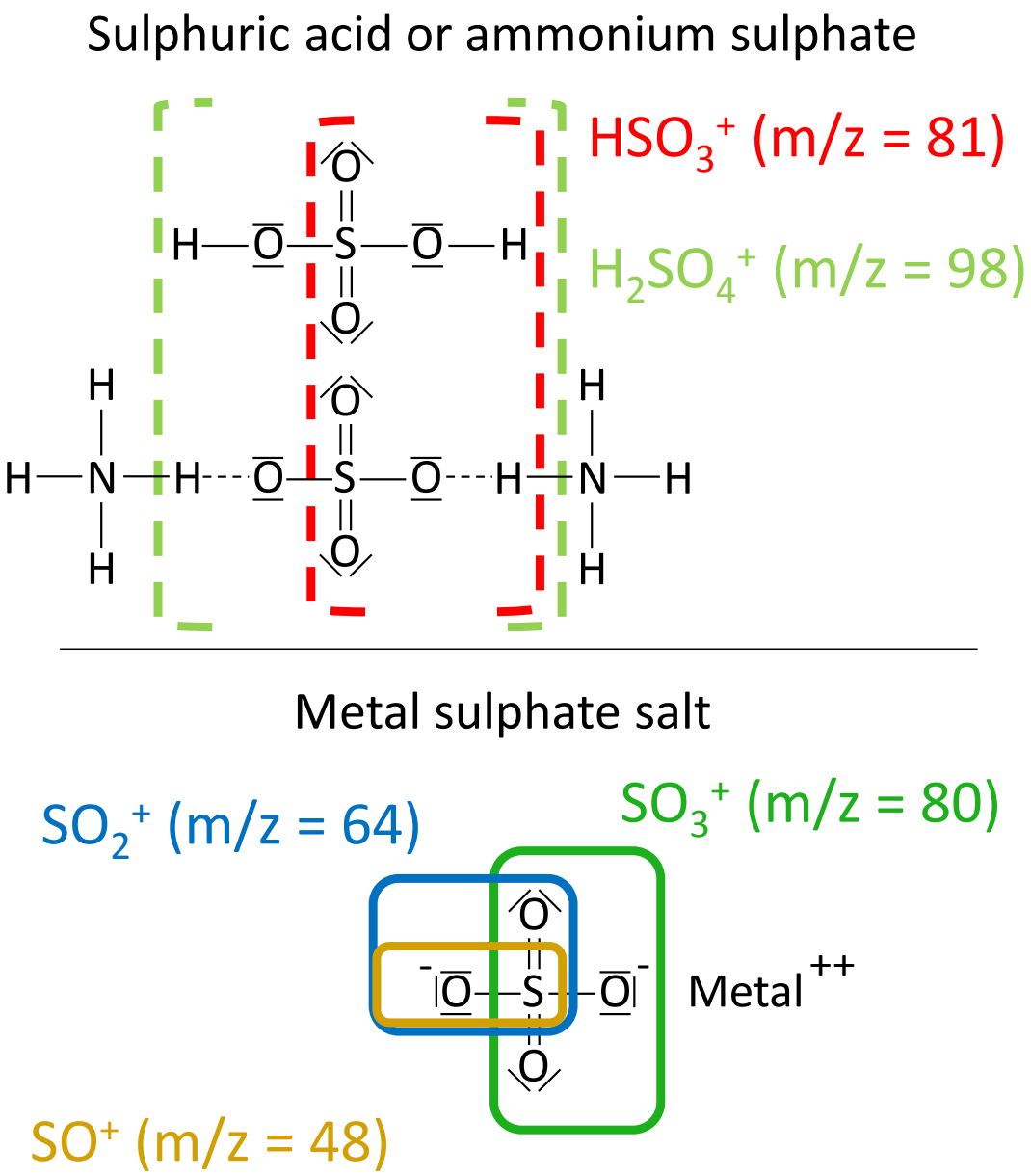

Fig. 5.9: Comparison of the possible fragments attributed to sulphate depending on the sulphate compound. For ammonium sulphate and sulphuric acid, hydrogen containing fragments are produced in the vaporisation and ionisation process while metal sulphate salts cannot produce such fragments. Typical examples for metals could be aluminium, iron or calcium.

The following paragraph describe, how it is possible to distinguish if SO_i or H_2SO_4 mainly contributed to the AMS sulphate species. When SO_i was to the dominant

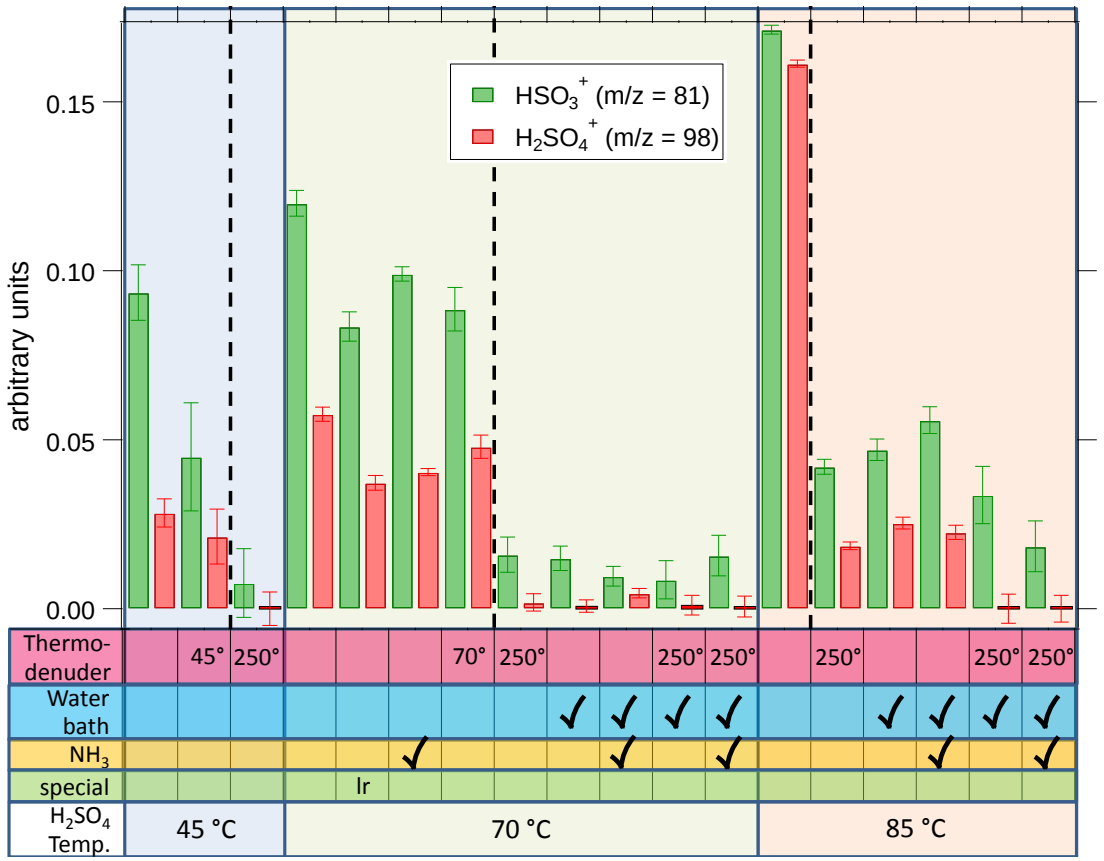

Fig. 5.10: Intensity of the fragments HSO_3^+ ($m/z = 81$) and $H_2SO_4^+$ ($m/z = 98$) normalised to the intensity of the fragment SO_2^+ ($m/z = 64$) for the FROST2 campaign. The first line on the horizontal axis shows the thermodenuder temperature, the second one indicates if the water bath was used and the third one if ammonium was added. The lr marked in the special line refers to an experiment with an additional residence volume of 10 L after the particle coating. The last line refers to the temperature of the sulphuric acid coating section.

substance, the sulphuric acid must have reacted with the particle surface. Figure 5.9 depicts the possible fragmentation patterns of sulphuric acid, ammonium sulphate and metal sulphates within the AMS detection process. The upper part of the figure shows the chemical structure of sulphuric acid and ammonium sulphate. The two fragments, HSO_3^+ and $H_2SO_4^+$, which are shown in this figure, are proxies for the presence of one of these compounds. Both of these fragments include at least one hydrogen atom and thus can not occur if a metal sulphate was measured as shown in the lower part of Fig. 5.9. There are a lot more fragments which can be produced in the evaporation/decomposition and ionisation process of these compounds, but the fragments shown are the most prominent.

If the sulphuric acid really reacted with the particle surface when the water bath and/or the thermodenuder were used, the fragmentation pattern of these exper-

iments should show clearly reduced signals at the fragments HSO_3^+ and $H_2SO_4^+$. Figure 5.10 shows these fragments for those experiments of the FROST2 campaign, for which the ATD was coated with sulphuric acid. The first three categories with the blue background refer to a sulphuric acid bath temperature of 45 °C. The categories with the green and the red background refer to coating temperatures of 70 °C and 85 °C respectively. The categories on the left of the dashed line of each coating temperature area correspond to measurements for which the particles were only coated with sulphuric acid and the thermodenuder was not used at a higher temperature as was used for the coating itself. No water bath was used in these experiments but ammonia was added to the dry particles for one experiment. On the right side of the dashed lines, those experiments for which the water bath and/or the thermodenuder were used after the coating are shown.

For all coating temperatures the intensity of the hydrogen-containing fragments was clearly reduced when the water bath and/or the thermodenuder were used. This is in accordance to what could be expected when comparing to the previous section, where these experiments also showed the highest reduction of the IN-active fraction.

The intensity of the hydrogenated fragments was highest when the coating was thickest. This also supports the assumption that the sulphuric acid reacted with the particle surface and that humidification and heating of the particles accelerate these reactions. For the thin coatings, a higher fraction of the sulphuric acid could react in the same time compared to thicker coatings, where more sulphuric acid needed to be consumed. In the case of the thick coatings it was also important to consider the partial neutralisation of the aerosol due to the omnipresent ammonia. The neutralisation of parts of the sulphuric acid prior to reaction with the particle surface led to the formation of ammonium sulphate or bisulphate. These compounds also produce hydrogenated fragments as has been shown in Fig. 5.9. After neutralisation, the sulphuric acid could no longer etch the particle surface. The last two experimental settings shown in Fig. 5.10 refer to particles which were humidified before they passed the thermodenuder. Interestingly, these experiments showed no fragments on m/z 98 but nevertheless a clear signal on m/z 81. It is expected that the m/z 81 fragments originate from metal bisulphates which produced HSO_3 in the flash vaporisation process (React. (R5.7)). This is in accordance the the suggested production of ammonium metal sulphates which decompose to bisulphates in the TD.

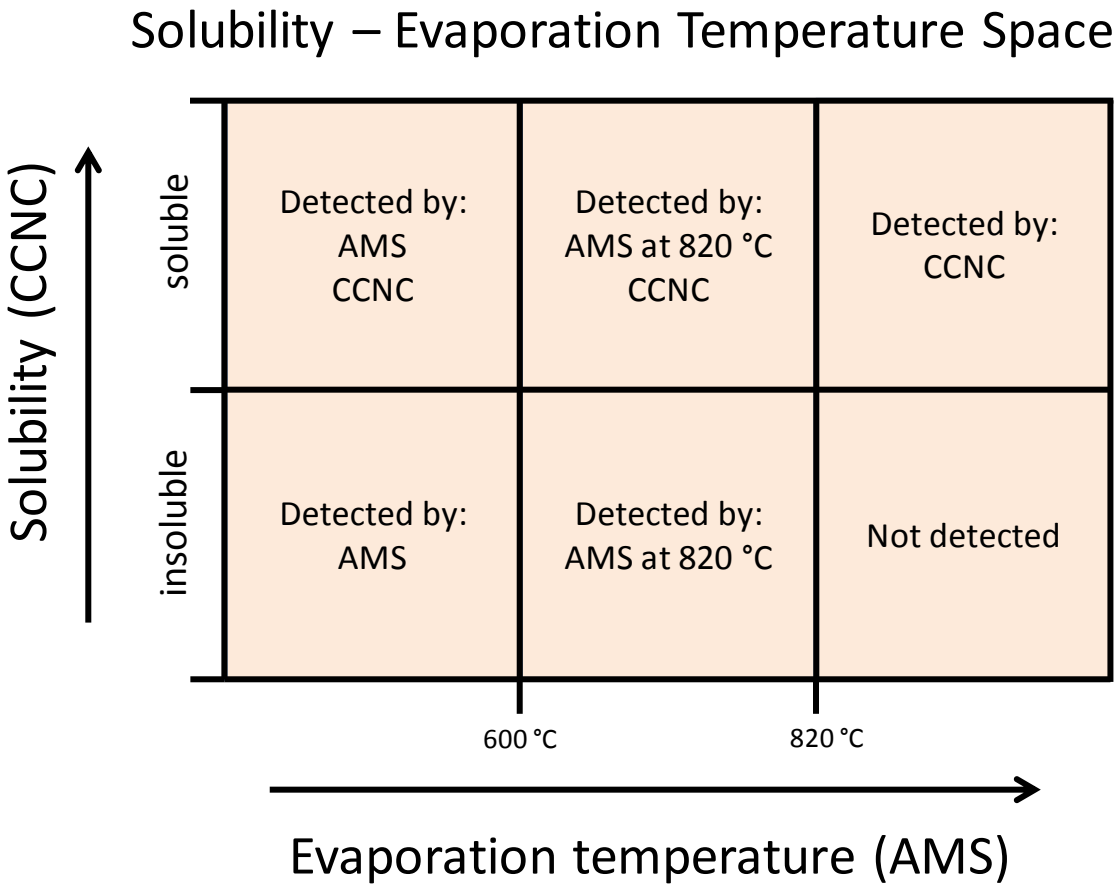

Fig. 5.11: Scheme of the solubility-evaporation temperature space. The left axis indicates increasing solubility and the bottom axis refers to increasing evaporation temperature. The space is roughly divided into six areas. The text in each area indicates whether the AMS and the CCNC are able to detect material situated in the respective region.

5.2.5 Comparison of AMS Sulphate Concentrations to Soluble Mass Concentrations

From Fig. 5.10 it is only possible to conclude that the sulphuric acid must have reacted with the particle surface and that metal sulphates must have been produced. The reaction appears to be faster when the aerosol is humidified or heated. However, no information on the metals involved in these reactions can be deduced from the AMS spectra, as metal sulphates decomposed into sulphur oxides and refractory metal oxides. In this section, the possible reactants and products of the ATD surface reactions will be restricted by comparing the soluble mass fraction of the processed ATD to the non-refractory mass fraction.

Using Köhler theory it is possible to determine the soluble mass per particle if a surface substance is assumed. The method was described in Sect. 2.2.1. Figure 5.12

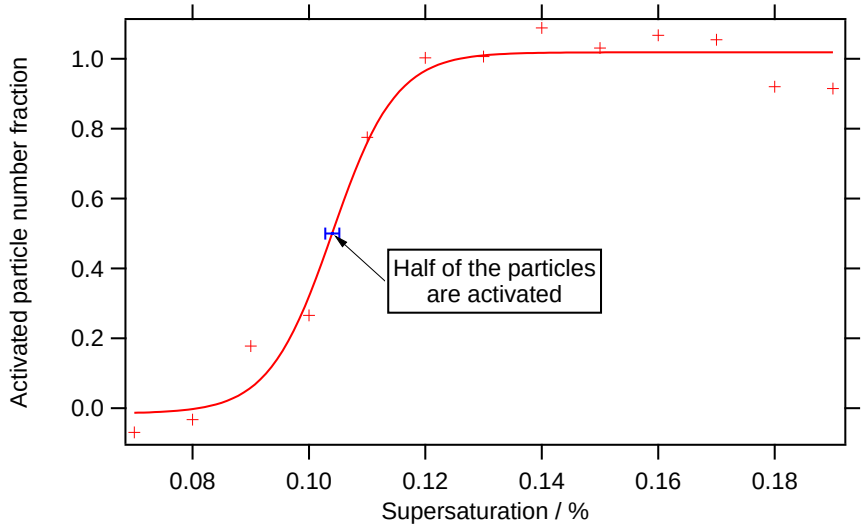

Fig. 5.12: Fictive example of a CCNC activation curve. At ~ 0.103 % supersaturation, half of the particles activated as cloud droplets. This supersaturation is considered to be the critical supersaturation and thus corresponds to the maximum of the Köhler curve (Eq. (2.2)).

shows a fictive example of an activation curve of the CCNC. The supersaturation at which 50 % of the particles are activated as cloud droplets is considered the critical supersaturation. This supersaturation is the maximum of the Köhler curve (Eq. (2.2)) and can be used to determine the parameter κ_{app}. The uncertainty of the determination of the critical supersaturation determines the uncertainty of κ_{app}. The soluble mass fraction was deduced using Eq. (2.5).

Figure 5.11 illustrates the solubility-evaporation temperature space (SETS) as it can be deduced from AMS and CCNC measurements. The CCNC is only sensitive to those substances that are hygroscopic and soluble. Sulphates always have some hygroscopicity, but some of them are insoluble. The rough information of the CCNC concerning whether the coating is soluble or insoluble is shown on the y-axis. It was combined with the information if the coating is refractory or non-refractory at a given AMS vaporiser temperature. As the vaporiser of the AMS was set to 600 °C or 820 °C respectively for the different campaigns, it is possible to distinguish three evaporation temperature regions which are shown on the x-axis. The region on the left includes those compounds which can be evaporated by the AMS at a vaporiser temperature of 600 °C. The centre region includes those substances which cannot yet be evaporated at 600 °C but can be evaporated at 820 °C. All substances which cannot be evaporated by the AMS belong to the region on the right. All three

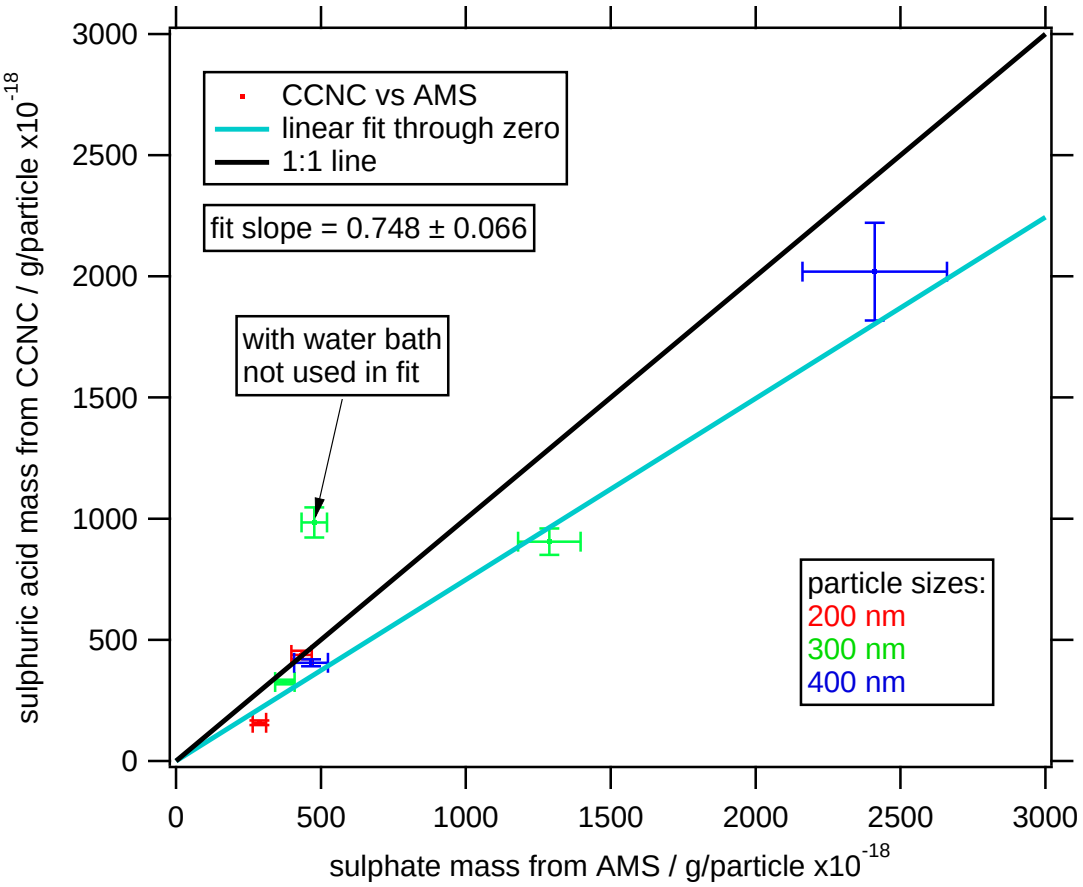

Fig. 5.13: Comparison of AMS sulphate per particle masses to CCNC soluble mass per particle for the FROST1 campaign. The point strongly deviating from the linear fit was recorded with the water bath in use. All other points refer to experiments during which the particles were coated with sulphuric acid without further processing.

regions are split into two areas, one including the soluble and one the insoluble compounds.

As the compounds produced on the particle surface are always present as a mixture, it is not possible to get absolute information on the position of different substances in the SETS. However, it was possible to detect changes of the amount of material which is present in the different regions of the SETS.

Figure 5.13 shows the soluble coating mass per particle deduced from the CCNC, under the assumption that the soluble mass is composed of sulphuric acid. It is compared to the non-refractory sulphate species mass deduced from the AMS measurements with a vaporiser temperature of 600 °C. The colour of the data points refers to the size of the particles. All but one of the points shown are located approximately on the line of an orthogonal least distance fit through zero. This means that the ratio between the soluble material and the non-refractory material is constant.

It can therefore be expected that the chemical composition of the coating for these experiments is approximately the same. It was not expected that the data points lie on the one-to-one line, as the quantities compared are not the same. Furthermore, assuming sulphuric acid in the calculation of the soluble mass is certainly not completely correct. The important information of the graph is the linearity between soluble and non-refractory material and not the absolute values.

One point in Fig. 5.13 is situated completely apart from the rest of the points. This indicates that the chemical composition of the coating material for this point is different. The major difference between this point and the rest of the graph is that it was recorded during measurements with the water bath in use. The amount of sulphuric acid condensed on the particle surface was similar to those measurements performed without the water bath, which resulted in the green point on the right of the point with the water bath in use. This means that with the use of the water bath, the chemical composition of the surface material of the ATD must have changed. The newly formed material appears to be soluble, as it is detected in the CCNC but a significant fraction is no longer detected by the AMS at a vaporisation temperature of 600 °C. Referring to the SETS in Fig. 5.11 parts of the newly formed substances should therefore be located in the upper centre and right areas.

The same comparison of the soluble material to the non-refractory material as shown in Fig. 5.13 for an evaporation temperature of 600 °C is shown in Fig. 5.14 for an AMS vaporiser temperature of 820 °C. Only 300 nm sized particles were used in these experiments. The colour code indicates the different treatments of the particles. The red points correspond to particles which had only been coated with sulphuric acid at different temperatures and the blue and the orange points correspond to experiments with the thermodenuder or the water bath in use. All points are located on the fit line. This indicatesthat the material which was produced when the water bath was in use and which could not completely be evaporated at 600 °C vaporiser temperature, was fully evaporated in the AMS at 820 °C. With respect to the SETS shown in Fig. 5.11, this means that the newly formed substances are located in the upper centre area. They are soluble and can be evaporated at 820 °C while this was not yet possible at 600 °C.

In order to find possible candidates for the newly formed substances, the chemical composition of ATD as given by Vlasenko et al. (2005) was checked for substances which could possibly be formed by the sulphuric acid with the particle surface. Table 5.3 gives a compilation of the material present on the particle surface and the possible compounds that can be formed from these substances by reaction with sulphuric acid. For all of these compounds the decomposition temperature and the

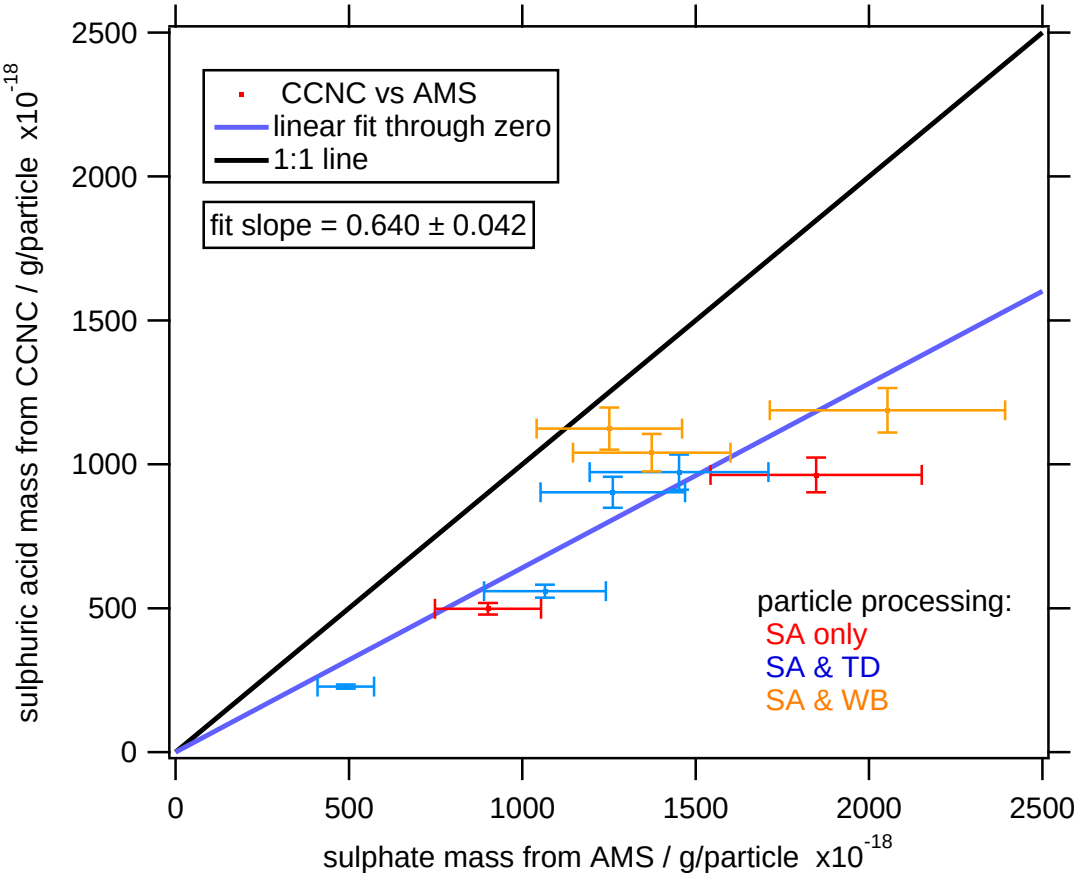

Fig. 5.14: Comparison of AMS sulphate per particle masses to CCNC soluble mass per particle for the FROST2 campaign. All data points refer to a particle size of 300 nm.

solubility are given. For some compounds the melting temperature is indicated, as this temperature is close to the evaporation temperature under high vacuum. The first restriction for the possible reaction products with the sulphuric acid was that the substance needs to be soluble. According to Petters and Kreidenweis (2008) all substances that have a solubility higher than 200 g/L are soluble enough to be completely detected by the CCNC. $CaSO_4$ can therefore be ruled out as an explanation for the observed effect, as it would not have been detected by the CCNC. Also, $AlNH_4(SO_4)_2$ and K_2SO_4 are unlikely candidates. These substances might have been formed but they cannot be responsible for the observed effect. The second constraint was that the newly formed substances evaporate between 600 °C and 820 °C. This is only the case for $Al_2(SO_4)_3$ and $CaSO_4$. As $CaSO_4$ is hardly soluble, the newly formed substance which can explain best the observed difference is $Al_2(SO_4)_3$. It is therefore likely that this compound was formed when the water

Table 5.3: ATD surface elemental composition from XPS as found by Vlasenko et al. (2005) and possible compounds formed with these substances. Mg is expected to be on the particle surface as it is found in the bulk material, but the XPS data was recorded with an Mg anticathode, masking the Mg of the sample. The list shown below is only a suggestion for possible reaction products based on the availability of the respective material. It was not possible to directly identify these compounds. The numbers in the two last columns indicate the decomposition temperature T_d in °C and the solubility S_{20} at 20 °C in g/l (IFA, 2010).

element	fraction at ATD surface [%]	possible compounds	T_d	S_{20}
Na	2	Na_2SO_4	890	170
		$NaHSO_4$	315	1080
Mg	-	$MgSO_4$	1124	300
Al	24	$Al_2(SO_4)_3$	770	364
		$AlNH_4(SO_4)_2$	190[1]	150
Si	63	no information	-	-
K	3	K_2SO_4	1069[1]	111.1
		$KHSO_4$	195	490
Fe	3	$Fe(II)SO_4$	400	256
		$Fe(III)_2(SO_4)_3$	480	4400
		$NH_4Fe(III)(SO_4)_2$	41[1,2]	1240[3]
Ca	5	$CaSO_4$	700	2

[1]Melting temperature, [2]source: AlfaAeser (2010), [3]source: Sitzmann (2004) at 25 °C.

bath was used. There were no measurements available with the thermodenuder in use and the AMS vaporiser set to 600 °C. However, a similar effect is expected.

To determine which substances are possible reactants of the etching process, the chemical composition of ATD was analysed for possible mineral anions which can react with sulphuric acid. Vlasenko et al. (2005) found that the soluble anions of the composing minerals of ATD are mainly sulphate, phosphate and chloride. From the binding energy of calcium Vlasenko et al. (2005) concluded that calcium is mainly present as carbonates, which are inhomogeneously distributed over the different ATD particles. Other anions which were found in low amounts were fluoride and nitrate. Only those anions whose respective acids have a lower dissociation constant than sulphuric acid can be displaced by the latter.

Those surface compounds that are already sulphates prior to the reaction with sulphuric acid could be chemically changed if they are part of a mixed compound with other anions or if their oxidation state changes (e.g.: Fe(II) to Fe(III)). Table 5.4

Table 5.4: Compilation of the dissociation constants of the acids corresponding to the anions found in ATD. Those anions which are located below the sulphate ion, can be displaced by sulphuric acid. Source: Jander et al. (2002)

		pk_a by dissociation level		
anion	abundance in ATD [a.u.]	1	2	3
Cl^-	0.7	-7		
SO_4^{2-}	41	-3	1.92	
NO_3^-	0.2	-1.32		
PO_4^{3-}	3	2.13	7.20	12.36
F^-	0.1	3.14		
CO_3^{2-}	NA[1]	6.52	10.40	
SiO_4^{4-}		9.51[2]	11.74[2]	NA

[1]Not quantified by Vlasenko et al. (2005) but their XPS data showed that Ca was associated with carbonates on the particle surface.

[2]Source: Widberg and Fischer (2007)

shows the anions found by Vlasenko et al. (2005) with their respective concentration. The mass fractions these concentrations correspond to are not given. Except for chloride, all anions shown in this table can be displaced from their salts by sulphuric acid as their acid dissociation constants pk_a are higher than the pk_a of sulphuric acid in the first dissociation step. In its second dissociation level, sulphuric acid can no longer displace nitrate from its salts but is still strong enough to displace phosphates, fluorides, and carbonates. It can therefore be concluded that most of the anions present in the particle which are not part of the silicate structure can be etched by sulphuric acid. The silicate structure itself may also be etched considering the pk_a of silicic acid, of which SiO_2 is the anhydride form. However, the solubility of silicic acid is very low. The condensation of water on the aerosol surface could nevertheless solve a minor fraction of potentially formed silicic acid and thus the alumino-silicates are a potential source for aluminium that can form $Al_2(SO_4)_3$.

Kaolinite is a mineral which is known to act as IN ((e.g.: Lüönd et al., 2010, Murray et al., 2011, Salam et al., 2006, Welti et al., 2009)). Colina et al. (2002) reported that the alumino silicate kaolin, which is mainly constituted of kaolinite reacts with sulphuric acid when heated. If at least parts of the alumino-silicates of the ATD are present in the crystalline form of kaolinite, it is possible that these are responsible for the ATD ice nucleus efficiency. The heating with the thermodenuder could increase the reaction of the sulphuric acid with this mineral and therefore reduce the ATD ability to act as an IN. The study by Colina et al. (2002) showed that $Al_2(SO_4)_3$ is

formed in the reaction as was found in this thesis. Whether the humidification of the coated ATD can have a similar effect could not be determined from literature. Simulations by Croteau et al. (2010) showed that in kaolinite trenches, water molecules can be ferroelectrically ordered. This might be the reason for kaolinite to act as ice nuclei and sulphuric acid could destroy such trenches. Salam et al. (2006) and Welti et al. (2009) report that montmorillonite, as well as illite (Welti et al., 2009), which are both constituted of alumino-silicates, act as ice nuclei. These minerals or similar structures can be present on the ATD surface and are thus candidates for being etched by sulphuric acid coatings, producing $Al_2(SO_4)_3$.

Calcium carbonate, although not responsible for the effect of the shift in the SETS, is a candidate for being involved in the ice active sites. It is etched by sulphuric acid and earlier studies already suggested it could be responsible for the ice nucleation ability of aerosol particles (Klein et al., 2010, Manson, 1957, Mason and Maybank, 1958, Zimmermann et al., 2008).

The collected information allows for a restriction of the possible compounds formed on the particle surface. However, it is not possible to directly link the formation of certain substances to the destruction of ice active sites on the ATD surface. The proposed reactions should be considered as indications on the chemical nature of the ice active sites. In future studies these compounds could be analysed in more detail.

6

Aerosol Cloud Interaction Experiments at the AIDA

This chapter describes experiments performed at the AIDA facility at the KIT in Karslruhe. Since the evaluation of the data showed weaknesses in the experimental method with respect to the use of an AMS, the goal of this chapter is to show how the experiments can be improved in order to adjust the experimental conditions to the measurement capacities of the AMS.

6.1 Effect of Cloud Processing on Aerosol Composition

During the laboratory measurement campaign ACI-03 (Aerosol Cloud Interaction) experiments were performed with ambient air in the AIDA chamber (see Sect. 2.2.4). Filling the AIDA with ambient aerosol produces a realistic starting composition of the aerosol. In the experiment described in the following, the ambient aerosol particles in the chamber were sampled with an AMS before and after an expansion of the air in the chamber.

During the expansion, the pressure in the chamber was reduced from 1008 mbar to approximately 780 mbar. The starting temperature was 264 K. Thus, when refilling the chamber to ambient pressure with filtered air, the aerosol was diluted by a factor of 0.77. Additionally the particle number concentration is reduced by a factor of 2 in the AIDA chamber in the time between two expansions. However, the mass concentration measured with the AMS was constant during the time the AMS was measuring between the expansions, as shown in Fig. 6.1. During the expansion, the humidity in the chamber reached saturation with respect to water after ~ 40 s and a supersaturation of 10 % was reached ~ 25 s later. At a supersaturation of 10 % all particles larger than ~ 30 nm are activated with respect to the Kelvin effect alone (Eq. (1.1)). Therefore all particles which are transmitted into the AMS should have become activated as CCN at this supersaturation. The maximum supersaturation reached is 40 %. As the supersaturation lasted for more than a quarter of an hour, some of the droplets probably sedimented and removed the aerosol within. Figure 6.2

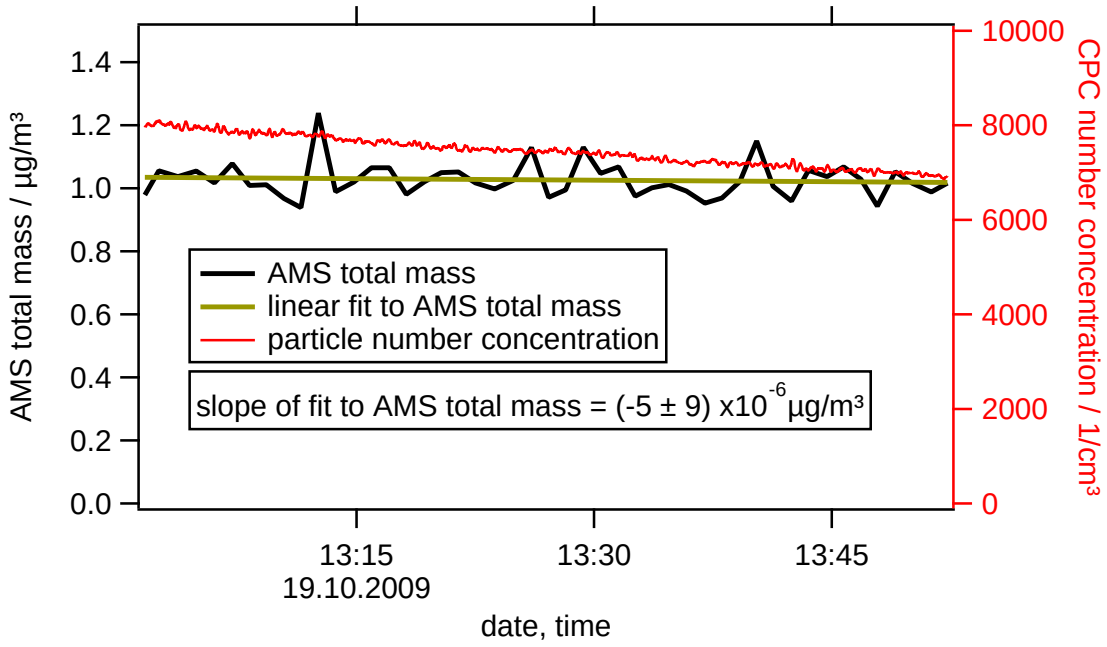

Fig. 6.1: Aerosol particle mass and number concentration in the AIDA between the expansions shown in Fig. 6.2 measured with the AMS and a CPC, respectively.

shows the aerosol particle composition before and after the activation experiment. The total mass was reduced from 0.940 µg/m^3 to 0.378 µg/m^3, which corresponds to a factor of 0.40 compared to a dilution factor of 0.77 from the pumping. As the mass concentration did not appear to be reduced during the time between two expansions (Fig. 6.1), the particle mass concentration must have been reduced by a factor of 2 during the expansion. Probably parts of the droplets sedimented. This is plausible as the initial particle number concentration was 1000 cm^{-3} at a pressure of 1000 hPa and a temperature of 264 K. Assuming a supersaturation of 10 % and an initial aerosol diameter of 200 nm, the particles would grow to a size of 10 µm within 3 s. This value was calculated using the solution of the coupled growth equations (Pruppacher and Klett, 1997) including latent heat release and transport back to the droplets. Assuming that the droplets sediment according to Eq. 3.36 in Hinds (1999) for stirred settling, the particles would need approximately half an hour for the concentration to be reduced by a factor of 2. Since the supersaturration in the AIDA was high for a quarter of an hour, the particles could grow further and the settling velocity increased. Accordingly, the time for half of the particles to sediment is further reduced. Figure 6.2 shows that the relative chemical composition was not changed by the sedimentation. However, because of the high supersaturation, all particles were activated as CCN and no selective sedimentation of efficient CCN could be expected.

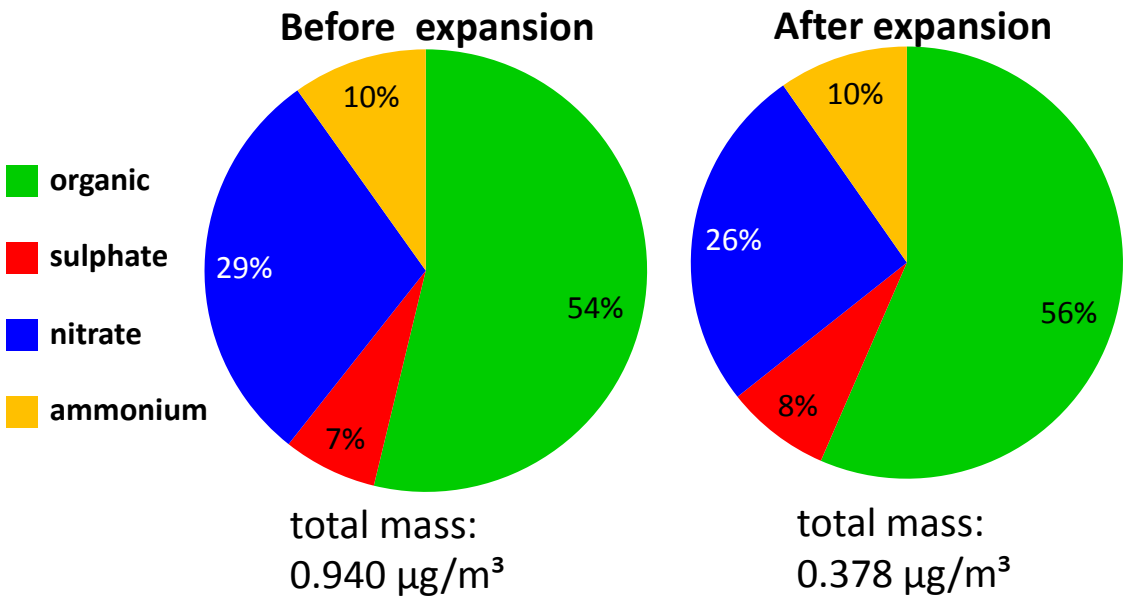

Fig. 6.2: Aerosol particle composition in the AIDA before and after the expansion. The total mass is reduced by a factor of 0.40. The pressure was reduced from 1008 mbar to 780 mbar. The initial temperature was 264 K.

To study the effect of selective activation of ambient aerosol in a chamber, a similar experiment with a lower supersaturation could be performed. If the droplets grew to a size of 10 µm, they would sediment with a velocity of approximately 0.003 m/s (Hinds, 1999, Tab. 3.1) and thus half of the aerosol particles within droplets would be washed out within half an hour. The AMS could sample size resolved chemical compositions before and after the experiment. These size distributions could be used to validate the statement of Dusek et al. (2006) that the size of the particles is more important than their chemical composition for their ability to act as CCN. However, the AIDA is not suitable for this experiment, as a supersaturation below 1 % cannot be maintained in the AIDA for several minutes.

An interesting feature of Fig. 6.2 is the molar ratio between ammonium on the one hand and sulphate and nitrate on the other hand. It shows that the aerosol is slightly acidic with respect to these species (acidity coefficient: 1.12). The acidity coefficient is calculated as $NO3/M_{NO3} + 2 \cdot SO4/M_{SO4})/(NH4/M_{NH4})$ with $NO3$, $SO4$ and $NH4$ being the fractions of nitrate sulphate and ammonium, respectively and $M_{...}$ the corresponding molar masses. If the standard RIE values of the evaluation tool SQUIRREL were used instead of the corrected RIEs from Sect. 4.1.3 (Fig. 6.3), the aerosol would appear slightly basic (acidity coefficient 0.88). Although both values are close to neutral, they differ by a factor of 1.28. The effect would even be much more pronounced for the RIEs of the FROST campaigns, where the RIE of sulphate

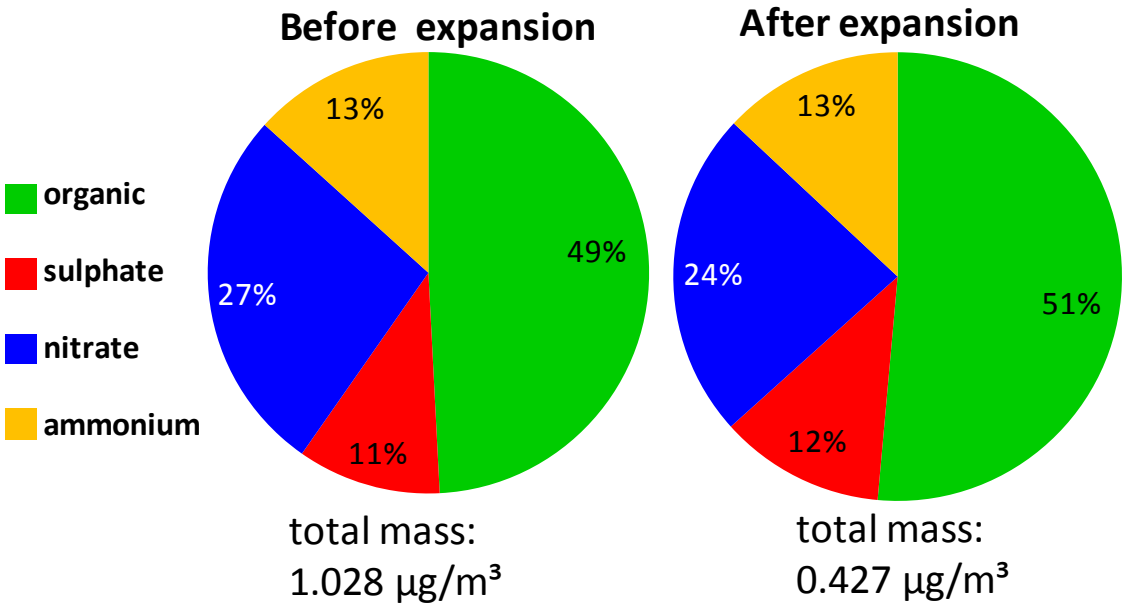

Fig. 6.3: Data shown in Fig. 6.2 without the application of the correction factors for the RIE.

was reduced and the RIE of ammonium was increased. This should be kept in mind when calculating acidity ratios for ambient aerosol and the RIE should be published along with the results.

6.2 Detection of Coating on Mineral Dust During Cloud Activation Experiments

One of the objectives of the AMS measurements during the ACI-03 campaign was to quantify the amount of coating on mineral dust particles. This was possible under some assumptions for the FROST campaigns (Chapt. 5) during which monodisperse aerosol was used. During ACI-03, the probed mineral dust was polydisperse. This caused major fractions of the dust to be outside the transmission range of the AMS aerodynamic inlet lens for all experiments. In contrast to the FROST campaigns, it was not possible to correct for these transmission losses as no size distributions for monodisperse particles relevant for the aerosol inside the AIDA chamber were available for the AMS. Due to losses and coagulation inside the chamber, the aerosol size distribution was changing gradually and thus it would have been necessary to monitor it continuously. Scanning mobility particle sizer (SMPS) measurements are not optimal for such a monitoring, as they monitor the number size distribution of the aerosol and not the surface size distribution. The count rate for bigger particles,

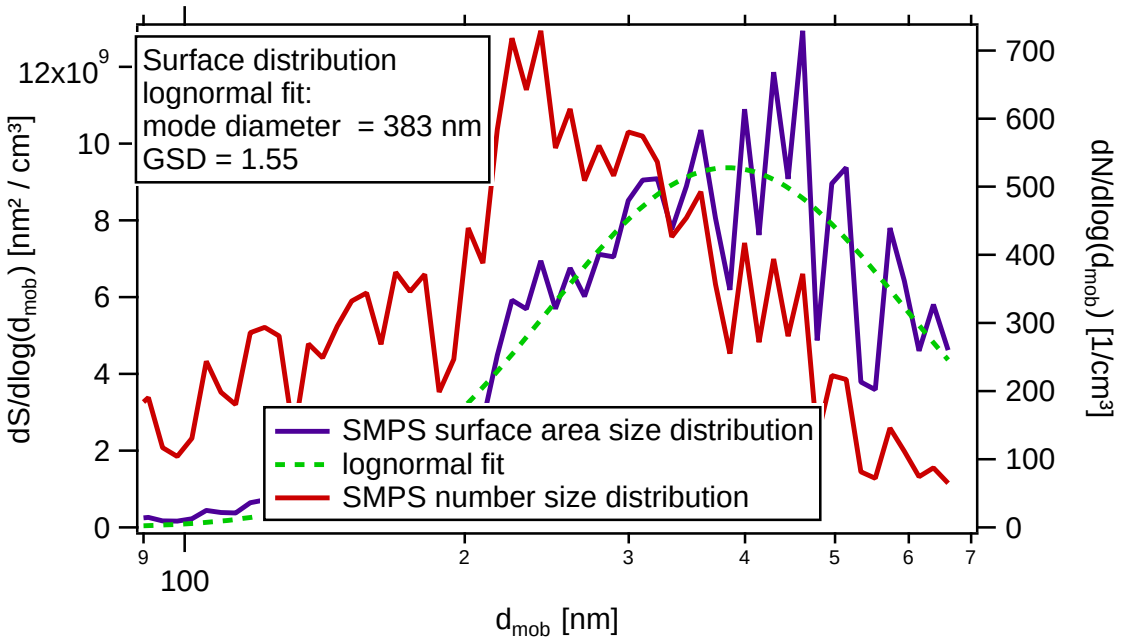

Fig. 6.4: Number size distribution measured with an SMPS and surface size distribution calculated from the number size distribution. Note the low signal to noise ratio at high diameters due to low counting rates. The total particle concentration in the AIDA was ~ 350 1/cm^3. The size distribution of this figure was averaged for close to two hours.

which are relevant for the surface size distribution was low and thus the uncertainty was high.

Figure 6.4 shows the number size ditribution measured with an SMPS of the Asian Dust samples (AD2) used during ACI-03 together with the surface size distribution. The surface size distribution is an approximation of the mass size distribution as measured by the AMS for the case of thin coatings. As no size distribution of the dust from the AMS was available, several parameters had to be approximated. In the size range of the maximum surface, the SMPS measurement only provided low counting rates, resulting in a very noisy signal and thus a very uncertain fit maximum, ranging between 350 and 450 nm (Fig 6.4). This uncertainty had to be considered when calculating the transmission of the instrument. Additionally, as no AMS size distributions for the aerosol in the chamber were available, it was impossible to exactly determine the Jayne shape factor (see Eq. (4.1)). This introduces an additional error in the determination of the mode diameter of the aerosol in the AIDA. As the Jayne shape factor is not identical for all particles but shows a distribution, the size distribution of the aerosol is broadened by an unknown factor.

To estimate the range of the correction factors, a density of 2.6 g/cm^3, a Jayne shape factor between 0.77 and 1, as well as a Jayne shape factor distribution width

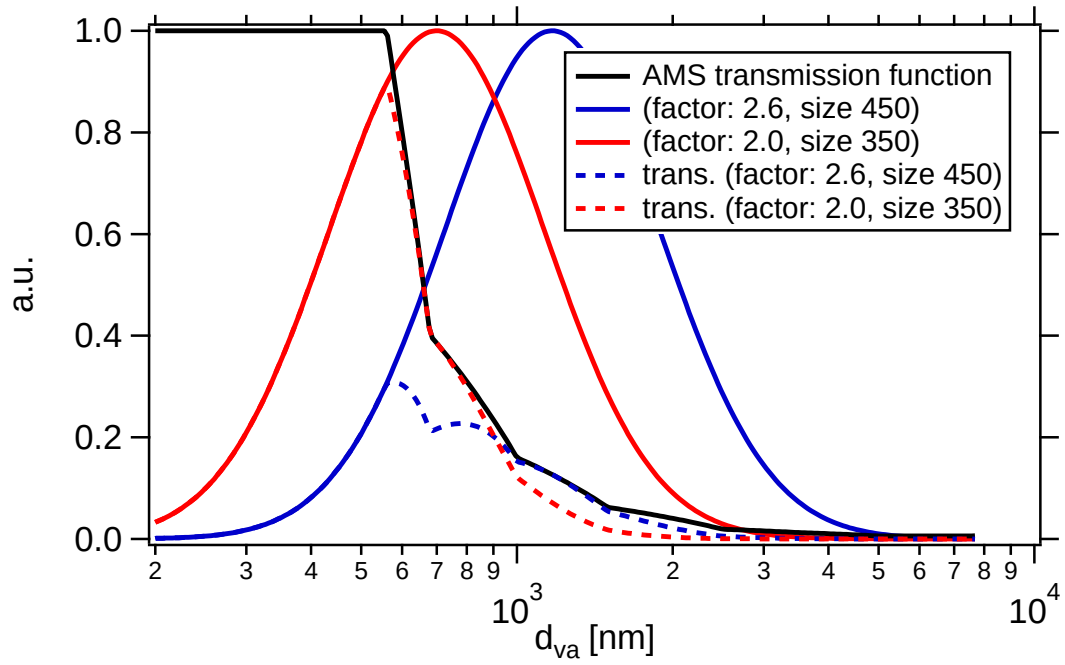

Fig. 6.5: Estimation of the range for the transmission correction factor for the ACI-03 AD2 measurements. The black line shows the transmission function of the AMS. The red line shows the mass size distribution as estimated from the SMPS data under the assumption of a factor of 2.0 between the mobility and the vacuum aerodynamic diameter. The blue line shows a similar estimation for a factor of 2.6. The dashed lines refer to the mass which could really pass the AMS lens.

of 0.25 were used. The transmission was calculated in the same way as described in Sect. 4.1.1. Figure 6.5 shows the estimated mass size distributions by scaling the SMPS surface size distributions. The black curve shows the transmission function of the AMS aerodynamic lens. It was determined by sampling PSL standards size particles. The blue curves refer to the vacuum aerodynamic size distribution of the aerosol assuming a Jayne shape factor of 1 and an SMPS size of 450 nm. The dashed curve is the size distribution which really entered the AMS. The red curves show the same distributions but for a Jayne shape factor of 0.77 and an SMPS size of 350 nm. The correction factor resulting from the blue curves is 4.5 and the red curves yield a correction factor of 1.85. This means that only from the uncertainty of the size distributions a range of approximately a factor of 2.4 is possible. Potentially the error could be even higher, as the use of the surface size distribution is only an approximation. The thicker the coatings are, the more the size distributions converge to volume size distributions. This would correspond to an additional shift of the mass size distributions to higher diameters, further increasing the correction factor for the lens transmission.

The goal of the AMS measurements was to quantify the surface coating thickness of the dust in the AIDA chamber. To do so, it would have been necessary to normalise the mass concentrations to the particle's total surface area. This again would have involved the calculation of surface size distributions from particle counts, which again would have introduced a big uncertainty. Additionally, the uncertainties of the correction factors described in Sect. 4.1 add to the above presented uncertainties. Finally, the calibration error of the AMS is assumed to be 30 %. With all these uncertainties, it is impossible to give any reliable quantification of the aersol coatings in the AIDA chamber.

In future studies these obstacles could be overcome by the use of a new aerodynamic lens which operates at higher pressures and can therefore focus particles in a higher size range. This type of lens is still being characterised but it can potentially focus particles of up to 3 µm. In addition, experiments with size selected particles should be performed with every type of dust used in the chamber in order to better access the Jayne shape factor of the aerosol as well as its distribution. With these modifications the experiments would be more suitable for the application of an AMS and the quantification of coatings on mineral dust particles would be possible for the experimental situation at the AIDA.

7

Conclusions and Outlook

In this study the AMS was used during three laboratory measurement campaigns, FROST1 and FROST2 at the LACIS facility at the IfT in Leipzig and the ACI-03 campaign at the AIDA facility at the KIT in Karlsruhe. In all three campaigns, the effect of coatings on mineral dust ice nuclei was investigated. For the FROST1 and FROST2 the characterisation of thin sulphuric acid coatings on ATD particles was successfully performed.

As the instrument was operated with very low signals, the mathematical tools to analyse the detection limits of the AMS were improved. Different methods have been tested to obtain satisfactory results. It is now possible to calculate detection limits of the AMS under operation conditions, without losing precious time by sampling through a particle filter, and without being restricted to periods with a constant closed signal.

The characterisation of the instrument was improved to enable correct quantification of the sulphate loadings on the ATD particle surfaces. Correction factors for the instrument inlet transmission, the collection efficiency, and the relative ionisation efficiency have been determined. Using these corrections, the mass per particle loadings of the ATD after the condensation of sulphuric acid on its surface could be calculated.

Combining AMS results to ice nucleus counter results revealed that the IN-efficiency of ATD is reduced by the condensation of sulphuric acid on the particle's surfaces. The reason for this reduction was not the covering of the particle's surface but a chemical reaction of sulphuric acid with the particle's surface. This reactions were accelerated when the aerosol was humidified or heated after the coating with sulphuric acid. Evidence for the stronger reaction of the sulphuric acid with the ATD surface when heated or humidified was given by the reduction of the hydrogen containing fragments, which were identified as proxies for sulphuric acid and

ammonium sulphate, and which are missing if the sulphate originates from metal sulphates.

A further indication for the production of new chemical compounds was the change of the position of the sulphate containing compounds in the solubility-evaporation temperature space. This information was retrieved by comparing the soluble mass per particle deduced from CCNC measurement with the non-refractory mass per particle deduced from the AMS data recorded at 600 °C and 820 °C. The newly formed substance which is responsible for the shift in the SETS is most likely $Al_2(SO_4)_3$. However, it was not possible to determine whether the formation of this substance is responsible for the loss of the IN-ability of ATD. A further compound of interest is $CaCO_3$ as it is contained in the ATD and is also likely to react with sulphuric acid.

Future Work

A direct identification of the reactions that took place on the ATD surface was not possible but further explorations of the SETS could restrict the possible compounds. The soluble mass could be measured with a particle into liquid sampler (PILS) or a similar instrument which can directly access the soluble mass fraction of the aerosol. An instrument that could potentially directly detect the surface compounds is the single particle laser ablation instrument SPLAT2 (Zelenyuk et al., 2009). Due to the two step ablation and ionisation it can be used to selectively evaporate the surface of particles.

The main result of this study, namely that sulphuric acid reduces ATD ice nucleation ability through surface etching, can be used in theoretical studies on the nature of ice nuclei. The structure studied need to be sensitive to sulphuric acid etching and the addition of water must increase the reaction kinetics.

Croteau et al. (2010) showed in simulations that water can start freezing in trenches in kaolinite. Based on these simulations it is feasible to analyse kaolinite particles for trenches on their surface using transmission electron microscopy. These particles could be used afterwards for immersion freezing experiments on a cold stage as described by Murray et al. (2011). The idea is to determine whether those particles with the more pronounced trenches are also the best ice nuclei. The same effect could be expected for other clay mineral particles which are known to be good ice nuclei, like e.g. montmorillonite and illite. Both of these minerals are alumino silicates and could, regarding to the chemical composition of ATD, be present on the ATD surface.

The same evaluation applied on the ATD can also be applied to other mineral dust systems. The interesting question is whether the reduction of the IN-ability can always be connected to particle surface reactions.

To improve the atmospheric relevance of this type of experiments, the aerosol preparation at the LACIS facility will be modified in a way to produce the sulphuric acid from gas phase SO_2 which is oxidised and humidified to form sulphuric acid in the carrier air of the particles. This avoids exposing the particles to atmospherically unrealistic high temperature over the sulphuric acid bath. Similar studies are also planned with nitric acid.

The data collected with the AMS at the AIDA facility could not be evaluated reliably due to very high uncertainties in the necessary instrument inlet transmission correction factors. This can be avoided in future studies by the use of a new aerodynamic inlet lens which is optimised for the transmission of larger particles.

In order to verify the predominance of the size effect over the chemistry effect in the CCN activation behaviour, the following cloud activation experiment is proposed: An AIDA-like expansion chamber could be filled with ambient air to get an atmospherically relevant aerosol. An expansion experiment is performed with a low expansion rate to get only low, atmospherically relevant supersaturations to selectively activate the most efficient CCN. The AMS could measure before and after the expansion, increasing its sampling time compared to measurements of the activated fraction during an expansion experiment and allowing to get chemically resolved size distributions before and after the expansion. These chemically resolved size distributions could be compared to see which size fraction and which chemical fraction of the aerosol sedimented and must therefore have been activated. The challenge of this experiment is to achieve low supersaturations in an expansion chamber for several minutes. The advantage of such a measurement is that the competition of the droplets for water vapour is simulated on a realistic time scale. Furthermore the AMS can measure for a long period before and after the experiment. This way it can sample long enough to retrieve size distributions which are clearly above the detection limit.

List of Figures

List of Tables

List of Symbols and Abbreviations

Abbrevations

	Explantion
ACI-03	Aerosol Cloud Interaction-03
AD2	Asian Dust sample 2
AIDA	Aerosol Interaction and Dynamics in the Atmosphere
AMS	Aerosol Mass Spectrometer
ATD	Arizona Test Dust
BCR	BCR-66 quartz size standards; Acronym significance is not known.
BFSP	Brute Force Single Particle
C-TOF-AMS	Compact Time Of Flight Aerosol Mass Spectrometer
CAD	Computer-Aided Design
CCM	Carbon Containing Material
CCN	Cloud Condensation Nucleus
CCNC	Cloud Condensation Nucleus Counter
CE	Collection Efficiency
CFDC	Continuous Flow Diffusion Chamber
CPC	Condensation Particle Counter
DL	Detection Limit
DMA	Differential Mobility Analyser
FFT	Fast Fourier Transformation
FROST	FReezing Of duST
GSD	Geometric Standard Deviation
HR-TOF-AMS	High Resolution Time Of Flight Aerosol Mass Spectrometer
IN	Ice Nucleus

KIT	Karlsruhe Institute of Technology
LACIS	Leipzig Aerosol Cloud Interaction Simulator
MCP	Multi Channel Plate
MS	Mass Spectrum
PILS	Particle Into Liquid Sampler
POLARCAT	POLar study using Aircraft, Remote sensing, surface measurements and modelling of Climate, chemistry, Aerosols and Transport
PSL	PolyStyrol Latex
PTOF	Particle Time Of Flight
Q-AMS	Quadrupole Aerosol Mass Spectrometer
RIE	Relative Ionisation Efficiency
SETS	Solubility-Evaporation-Temperature Space
SIS	Single Ion Signal
SQUIRREL	SeQUential Igor data RetRiEvaL
TEM	Transmission Electron Microscope
XPS	X-ray Photoelectron Spectroscopy

Symbols

	Explantion	**unit**
α	Parameter of the Cunningham slip correction factor calculation	
α	Random noise	
A	Factor of the Kelvin term	m
A	Particle surface area	nm^2
A_i	Fitting parameter of the H_i at location i	
a_i	Fitting parameter of the h_i at location i	
A_{duty}	Factor of the duty cycle correction	$u^{0.5}\,eV^{-0.5}$
B_i	Fitting parameter of the of H_i at location i	
b_i	Fitting parameter of the of h_i at location i	
C_i	Fitting parameter of the H_i at location i	
c_i	Fitting parameter of the h_i at location i	
D_i	Fitting parameter of the H_i at location i	
d_i	Fitting parameter of the h_i at location i	
β	Parameter of the Cunningham slip correction factor calculation	

B	Factor of the Raoult term	m^3
$B_{i,n}$	Bernstein polynomials	
CE	Collection efficiency	
C_c	Cunningham slip correction factor	
C_j	Complex intensities of the Fourier spectrum frequencies	
C_S	Mass Concentration	$\mu\mathrm{g}\,\mathrm{m}^{-3}$
$C_{DL\text{-}cubic}$	Computational complexity of the *DL-cubic*-algorithm	
C_{Bezier}	Computational complexity of the Bezier detrending method	
D	Diameter of the wet particle	nm
d_a	Aerodynamic diameter	nm
D_p	Particle diameter	nm
D_{ATD}	Projected mass size distribution	
d_{coat}	Coating thickness	nm
D_{crit}	Critical diameter for cloud activation	nm
D_{dry}	Diameter of the dry particle	nm
d_{ic}	Effective diameter of the insoluble core in the modified Köhler equation	nm
d_{mob}	Mobility diameter	nm
d_{mod}	Modal diameter	nm
d_{ve}	Volume equivalent diameter	nm
d_{va}	Vacuum aerodynamic diameter	nm
ϵ	Gaussian noise	
ϵ_i	Volume fraction of soluble material	
E	Detrended signal using the *DL-cubic*-algorithm	
ΔF	Activation energy for crossing the liquid water/ice boundary	J
$\overline{f_{AB}}$	Average airbeam correction factor	
F	Signal with noise	
f	Ideal signal without noise	
f_{AB}	Airbeam correction factor	
F_{puls}	Number of pulses of the mass spectrometer per second	s^{-1}
f_{trans}	Transmission function of the AMS aerodynamic lens	
ΔG_{het}	Gibbs free energy for the formation of a critical ice embryo	J
γ	Amplitude of the electronic noise	

γ	Parameter of the Cunningham slip correction factor calculation	
H	Third order local polynomial fitting functions to F	
h	Planck constant	J s
h	Third order local polynomial fitting functions to f	
ΔI	Modelled counts noise level of the AMS	ion
ΔI_{diff}	Counting statistics error	ion
IE	Ionisation efficiency	ion molec^{-1}
I	Counts signal of the AMS	ion
i	Index	
I_S	Ion count rate	s^{-1}
I_{closed}	Ion counts in closed mode	ion
I_{open}	Ion counts in open mode	ion
j	Factor indicating how many standard deviations the *DL-cubic*-output is over or underestimating the real value	
j	Index	
j_{het}	Heterogenous freezing rate	molec s^{-1} m^{-3}
ϵ_{coat}	Volume fraction of the particle coating material	
ϵ_{core}	Volume fraction of the particle core material	
κ_i	Apparent hygroscopicity parameters	
κ_{app}	Apparent hygroscopicity parameter	
κ_{coat}	Apparent hygroscopicity of the particle coating	
κ_{core}	Apparent hygroscopicity of the particle core	
k	Boltzmann constant	J K^{-1}
k	Iteration step of the de Casteljau-algorithm	
k	Number of SIS	
k	Number of active sites per surface and differential temperature interval	m^{-2} K^{-1}
k_{comp}	Correction factors needed to compare the FROST campaigns, determined by a recalibration of the AMS-CPC-dilution-stage-system to the CCNC	
k_{trans}	Correction factor for the AMS lens transmission	
λ	Mean free path of air	nm
l	Length of a generated signal	
Δm_{ppcor}	Uncertainty of the AMS mass per particle including all correction factors	ag

MW_{NO_3}	Molecular weight of nitrate	$\mathrm{g\,mol^{-1}}$
μ	Mean value of a distribution	
m/z	Mass to charge ratio	$\mathrm{u\,eV^{-1}}$
$M_{\mathrm{SiO_2}}$	Molecular weight of silicon oxide	$\mathrm{g\,mol^{-1}}$
M_w	Molecular weight of water	$\mathrm{g\,mol^{-1}}$
m_{ppcor}	AMS mass per particle including all correction factors	ag
m_{ppraw}	AMS mass per particle prior to the application of the correction factors	ag
$m_{soluble}$	Soluble mass per particle loading	ag
N	Number of points of an AMS signal	
N	Number of time bins	
N'	Number of points of a Fourier transformed AMS signal	
N_A	Avogadro number	$\mathrm{molec\,mol^{-1}}$
n_a	Surface density of ice active sites	$\mathrm{m^{-2}}$
n_s	Number density of water molecules at the ice nucleus/water interface	$\mathrm{molec\,m^{-2}}$
n_s	Number of solute moles	mol
N_{ATD}	Number of molecules contained in the ATD core material	molec
N_{coat}	Number of coating molecules	molec
N_{crit}	Critical value for the the number of points of a signal for which the *DL-cubic*-algorithm can be applied with a desired precision of j standard deviations.	
ω_j	Frequencies of the Fourier transformed spectrum	$\mathrm{s^{-1}}$
O	Order function of the computational complexity	
$\vec{P}_i$	Defining polygon of a Bezier curve (in this thesis: the AMS closed signal)	
$p(k,N)$	Probability that in a time series with N time bins, the k^{th} SIS is recorded in a time bin which did not include an SIS before	
p°	Water saturation vapour pressure over a flat water surface	Pa
p_w	Saturation vapour pressure over a droplet	Pa
$\overline{Q_{in}}$	Average AMS inlet flow rate	
Q_{in}	Inlet flow rate	$\mathrm{cm^3\,s^{-1}}$
RIE	Relative ionisation efficiency	
ρ_0	Unit density: 1 g/cm^3	$\mathrm{g\,cm^{-3}}$

$\rho_{H_2SO_4}$	Density of sulphuric acid: 1.8356×10^{-3} ag/nm^3	$\mathrm{ag\,nm^{-3}}$
ρ_p	Particle density	$\mathrm{g\,cm^{-3}}$
ρ_w	Density of water	$\mathrm{kg\,m^{-3}}$
ρ_{coat}	Density of the coating	$\mathrm{g\,cm^{-3}}$
$\vec{r}$	Bernstein-Bezier-curve	
R	Standard deviation of the *DL-cubic* detrended signal E	
R	Universal gas constant	$\mathrm{J\,mol^{-1}\,K^{-1}}$
$\Delta\sigma_{...}$	Abbrevation for $\Delta\sigma_{base}$ and $\Delta\sigma_{algo}$	
$\Delta\sigma_{algo}$	Estimate of $\Delta\sigma_{base}$ from σ_{algo} using Eq. (3.25)	
$\Delta\sigma_{base,rel}$	Ratio of the standard deviation of the algorithm outputs $\Delta\sigma_{base}$ to the real standard deviation of the input noise σ_{base}	
$\Delta\sigma_{base}$	Standard deviation of the algorithm outputs	
$\Delta\sigma_{rel}$	Relative difference between σ_{input} and σ_{est}	
σ	Factor of the broadening of the counting statistics error due to variations of the intensity between different SISs	
σ	Standard deviation of the noise of an AMS closed signal	$\mu\mathrm{g\,m^{-3}}$
σ_w	Surface tension of water	$\mathrm{N\,m^{-1}}$
$\sigma_{...}$	Abbrevation for σ_{base} and $\Delta\sigma_{algo}$	
σ_{algo}	Output of the *DL-cubic*-algorithm for one signal	
σ_{base}	Standard deviation of the basic population of the random numbers used to test the *DL-cubic*-algorithm	
σ_{cnt}	Counts noise level	
σ_{est}	Standard deviation of the estimated pure noise using a Bezier curve	
σ_{filter}	Standard deviation of a filter measurement	
σ_{input}	Standard deviation of the noise added to a generated signal	
σ_{mc}	Mass concentration noise level	$\mu\mathrm{g\,m^{-3}}$
S	Jayne shape factor	
S	Scaling factor which accounts for the difference between T_{int} and the real width of a time bin	
S_{20}	Solubility at 20 °C	$\mathrm{g\,l^{-1}}$
S_{crit}	Critical saturation ratio for cloud activation	
S	Saturation ratio	
$d\theta$	Differential temperature interval	K
T	Temperature	K

T	Time spend averaging one m/z during a DL determination period	s
t_i	Location i on the time axis	
T_{closed}	Time spent in AMS closed mode	s
T_{int}	Time integrating the signal which is attributed to one m/z during one pulse of the mass spectrometer	ns
t_{meas}	Total time spent measuring with the AMS during one DL determination period	s
T_{open}	Time spent in AMS open mode	s
U_{ion}	Voltage of the ion chamber	V
V_{coat}	Volume of the particle coating	nm^3
V_{SI}	Unit conversion factor equal to the area below a single ion signal	bit ns
V_{total}	Total volume of the particle	nm^3
χ	Dynamic shape factor	
x_{pulser}	Open length of the pulser electrode of the mass spectrometer	mm
z	Parameter referring to the position on a Bezier curve. $z \in [0, 1]$	

Publications Originating from this Thesis

Niedermeier, D., Hartmann, S., Shaw, R. A., Covert, D., Mentel, T. F., Schneider, J., Poulain, L., Reitz, P., Spindler, C., Clauss, T., Kiselev, A., Hallbauer, E., Wex, H., Mildenberger, K., and Stratmann, F.: Heterogeneous freezing of droplets with immersed mineral dust particles - measurements and parameterization, Atmospheric Chemistry and Physics, 10, 3601–3614, 2010.

Niedermeier, D., Hartmann, S., Clauss, T., Wex, H., Kiselev, A., Sullivan, R. C., DeMott, P. J., Petters, M. D., Reitz, P., Schneider, J., Mikhailov, E., Sierau, B., Stetzer, O., Reimann, B., Bundke, U., Shaw, R. A., Buchholz, A., Mentel, T. F., and Stratmann, F.: Experimental study of the role of physicochemical surface processing on the IN ability of mineral dust particles, Atmos. Chem. Phys. Discuss., 11, 18 557–18 588, doi:10.5194/acpd-11-18557-2011, 2011.

Reitz, P., Schneider, J., Wex, H., Stratmann, F., Niedermeier, D., Mildenberger, K., Covert, D., Mentel, T. F., Spindler, C., Poulain, L., and Borrmann, S.: Detection of thin coatings on refractory particles with an Aerosol Mass Spectrometer: Application in laboratory studies of hygroscopic growth, CCN and IN activation, in: European Aerosol Conference, poster presentation, 2009a.

Reitz, P., Schneider, J., Wex, H., Stratmann, F., Niedermeier, D., Mildenberger, K., Covert, D., Mentel, T. F., Spindler, C., Poulain, L., and Borrmann, S.: Thin Coatings On Refractory Particles: Detection With Mass Spectrometry And Implications For Studies Of Hygroscopic Growth, CCN And IN Activation, in: International Conference on Nucleation and Atmospheric Aerosol, talk, 2009b.

Reitz, P., Schneider, J., Wex, H., Stratmann, F., Niedermeier, D., Mildenberger, K., Hartmann, S., Kiselev, A., Shaw, R., Covert, D., Buchholz, A., Spindler, C., Mentel, T. F., Poulain, L., Sullivan, R. C., DeMott, P. J., Petters, M. D., and Borrmann, S.: Surface modification of mineral dust particles by thin coatings: Im-

plications for CCN and IN abilities, in: International Aerosol Conference, poster presentation which received a **Best Poster Prize**, 2010.

Reitz, P., Spindler, C., Mentel, T. F., Poulain, L., Wex, H., Mildenberger, K., Niedermeier, D., Hartmann, S., Clauss, T., Stratmann, F., Sullivan, R. C., DeMott, P. J., Petters, M. D., Sierau, B., and Schneider, J.: Surface modification of mineral dust particles by sulphuric acid processing: implications for CCN and IN abilities, Atmos. Chem. Phys. Discuss., 11, 7235–7289, doi:10.5194/acpd-11-7235-2011, 2011.

Sullivan, R. C., Petters, M. D., DeMott, P. J., Kreidenweis, S. M., Wex, H., Niedermeier, D., Hartmann, S., Clauss, T., Stratmann, F., Reitz, P., Schneider, J., and Sierau, B.: Irreversible loss of ice nucleation active sites in mineral dust particles caused by sulphuric acid condensation, Atmospheric Chemistry and Physics, 10, 11 471–11 487, doi:10.5194/acp-10-11471-2010, 2010.

References

Abbatt, J. P. D., Benz, S., Cziczo, D. J., Kanji, Z., Lohmann, U., and Möhler, O.: Solid ammonium sulfate aerosols as ice nuclei: A pathway for cirrus cloud formation, Science, 313, 1770–1773, doi:10.1126/science.1129726, 2006.

Albrecht, B. A.: Aerosols, cloud microphysics, and fractional cloudiness, Science, 245, 1227–1230, 1989.

AlfaAeser: data sheet ammonium iron(III) sulphate, 2010.

Alfarra, M. R., Coe, H., Allan, J. D., Bower, K. N., Boudries, H., Canagaratna, M. R., Jimenez, J. L., Jayne, J. T., Garforth, A. A., Li, S. M., and Worsnop, D. R.: Characterization of urban and rural organic particulate in the lower Fraser valley using two aerodyne aerosol mass spectrometers, Atmospheric Environment, 38, 5745–5758, doi:10.1016/j.atmosenv.2004.01.054, 2004.

Allan, J. D.: Error Calculation for AMS Analysis (talk AMS user meeting 2010), URL http://cires.colorado.edu/jimenez-group/UsrMtgs/UsersMtg11/JDAerrorpresentation.pdf, 2010.

Allan, J. D., Jimenez, J. L., Williams, P. I., Alfarra, M. R., Bower, K. N., Jayne, J. T., Coe, H., and Worsnop, D. R.: Quantitative sampling using an Aerodyne aerosol mass spectrometer. 1. Techniques of data interpretation and error analysis, Journal of Geophysical Research, 108, AAC1–1–AAC1–10, doi:10.1029/2002jd002358, 2003.

Allan, J. D., Delia, A. E., Coe, H., Bower, K. N., Alfarra, M. R., Jimenez, J. L., Middlebrook, A. M., Drewnick, F., Onasch, T. B., Canagaratna, M. R., Jayne, J. T., and Worsnop, D. R.: A generalised method for the extraction of chemically resolved mass spectra from aerodyne aerosol mass spectrometer data, Journal of Aerosol Science, 35, 909–922, doi:10.1016/j.jaerosci.2004.02.007, 2004.

Bahreini, R., Jimenez, J. L., Jian, W., Flagan, R. C., Seinfeld, J. H., Jayne, J. T., and Worsnop, D. R.: Aircraft-based aerosol size and composition measurements during ACE-Asia using an Aerodyne aerosol mass spectrometer, Journal of Geophysical Research, 108, ACE13–1–ACE13–ACE13–22, doi:10.1029/2002jd003226, 2003.

Barnett, V. and Lewis, T.: Outliers in statistical data, Wiley Series in Probability & Statistics, John Wiley and Sons, Chichester New York Brisbane Toronto Singapore, 3rd edn., 1994.

Bronstein, I., Semendjajew, K., Musiol, G., and Mühlig, H.: Taschenbuch der Mathematik, Wissenschaftlicher Verlag Harri Deutsch GmbH, Frankfurt am Main, 2008.

Canagaratna, M. R., Jayne, J. T., Jimenez, J. L., Allan, J. D., Alfarra, M. R., Zhang, Q., Onasch, T. B., Drewnick, F., Coe, H., Middlebrook, A., Delia, A., Williams, L. R., Trimborn, A. M., Northway, M. J., DeCarlo, P. F., Kolb, C. E., Davidovits, P., and Worsnop, D. R.: Chemical and microphysical characterization of ambient aerosols with the aerodyne aerosol mass spectrometer, Mass Spectrometry Reviews, 26, 185–222, doi:10.1002/mas.20115, 2007.

Carslaw, K. S., Wirth, M., Tsias, A., Luo, B. P., Dornbrack, A., Leutbecher, M., Volkert, H., Renger, W., Bacmeister, J. T., and Peter, T.: Particle microphysics and chemistry in remotely observed mountain polar stratospheric clouds, Journal of Geophysical Research-Atmospheres, 103, 5785–5796, 1998.

Chen, Y., Kreidenweis, S. M., McInnes, L. M., Rogers, D. C., and DeMott, P. J.: Single particle analyses of ice nucleating aerosols in the upper troposphere and lower stratosphere, Geophys. Res. Lett., 25, 1391–1394, doi:10.1029/97gl03261, 1998.

Choi, E. M., Yoon, Y. H., Lee, S., and Kang, H.: Freezing transition of interfacial water at room temperature under electric fields, Physical Review Letters, 95, doi:08570110.1103/PhysRevLett.95.085701, 2005.

Christner, B. C., Morris, C. E., Foreman, C. M., Cai, R. M., and Sands, D. C.: Ubiquity of biological ice nucleators in snowfall, Science, 319, 1214–1214, doi:10.1126/science.1149757, 2008.

Colina, F. G., Esplugas, S., and Costa, J.: High-Temperature Reaction of Kaolin with Sulfuric Acid, Industrial & Engineering Chemistry Research, 41, 4168–4173,

doi:10.1021/ie010886v, 2002.

Crosier, J., Jimenez, J. L., Allan, J. D., Bower, K. N., Williams, P. I., Alfarra, M. R., Canagaratna, M. R., Jayne, J. T., Worsnop, D. R., and Coe, H.: Technical note: Description and use of the new jump mass spectrum mode of operation for the aerodyne quadrupole aerosol mass spectrometers (Q-AMS), Aerosol Science and Technology, 41, 865–872, doi:10.1080/02786820701501899, 2007.

Croteau, T., Bertram, A. K., and Patey, G. N.: Observations of High-Density Ferroelectric Ordered Water in Kaolinite Trenches using Monte Carlo Simulations, Journal of Physical Chemistry A, 114, 8396–8405, doi:10.1021/jp104643p, 2010.

Cziczo, D. J., Murphy, D. M., Hudson, P. K., and Thomson, D. S.: Single particle measurements of the chemical composition of cirrus ice residue during CRYSTAL-FACE, Journal of Geophysical Research-Atmospheres, 109, 13, doi: D0420110.1029/2003jd004032, 2004.

Cziczo, D. J., Stetzer, O., Worringen, A., Ebert, M., Weinbruch, S., Kamphus, M., Gallavardin, S. J., Curtius, J., Borrmann, S., Froyd, K. D., Mertes, S., Möhler, O., and Lohmann, U.: Inadvertent climate modification due to anthropogenic lead, Nature Geoscience, 2, 333–336, doi:10.1038/ngeo499, 2009.

de Casteljau, P.: Courbes à pôles, (document was not available), 1959.

DeCarlo, P. F., Slowik, J. G., Worsnop, D. R., Davidovits, P., and Jimenez, J. L.: Particle morphology and density characterization by combined mobility and aerodynamic diameter measurements. Part 1: Theory, Aerosol Science and Technology, 38, 1185–1205, doi:10.1080/027868290903907, 2004.

DeCarlo, P. F., Kimmel, J. R., Trimborn, A., Northway, M. J., Jayne, J. T., Aiken, A. C., Gonin, M., Fuhrer, K., Horvath, T., Docherty, K. S., Worsnop, D. R., and Jimenez, J. L.: Field-deployable, high-resolution, time-of-flight aerosol mass spectrometer, Analytical Chemistry, 78, 8281–8289, doi:10.1021/ac061249n, 2006.

DeMott, P. J., Chen, Y., Kreidenweis, S. M., Rogers, D. C., and Sherman, D. E.: Ice formation by black carbon particles, Geophysical Research Letters, 26, 2429–2432, 1999.

DeMott, P. J., Sassen, K., Poellot, M. R., Baumgardner, D., Rogers, D. C., Brooks, S. D., Prenni, A. J., and Kreidenweis, S. M.: African dust aerosols as atmospheric ice nuclei, Geophysical Research Letters, 30, 4, doi:173210.1029/2003gl017410, 2003.

DeMott, P. J., Prenni, A. J., Liu, X., Kreidenweis, S. M., Petters, M. D., Twohy, C. H., Richardson, M. S., Eidhammer, T., and Rogers, D. C.: Predicting global atmospheric ice nuclei distributions and their impacts on climate, Proceedings of the National Academy of Sciences of the United States of America, 107, 11 217–11 222, doi:10.1073/pnas.0910818107, 2010.

Diehl, K., Quick, C., Matthias-Maser, S., Mitra, S. K., and Jaenicke, R.: The ice nucleating ability of pollen - Part I: Laboratory studies in deposition and condensation freezing modes, Atmospheric Research, 58, 75–87, 2001.

Diehl, K., Matthias-Maser, S., Jaenicke, R., and Mitra, S. K.: The ice nucleating ability of pollen: Part II. Laboratory studies in immersion and contact freezing modes, Atmospheric Research, 61, 125–133, 2002.

Drewnick, F., Hings, S. S., DeCarlo, P., Jayne, J. T., Gonin, M., Fuhrer, K., Weimer, S., Jimenez, J. L., Demerjian, K. L., Borrmann, S., and Worsnop, D. R.: A new time-of-flight aerosol mass spectrometer (TOF-AMS) - Instrument description and first field deployment, Aerosol Science and Technology, 39, 637–658, doi: 10.1080/02786820500182040, 2005.

Drewnick, F., Hings, S. S., Alfarra, M. R., Prevot, A. S. H., and Borrmann, S.: Aerosol quantification with the Aerodyne Aerosol Mass Spectrometer: detection limits and ionizer background effects, Atmospheric Measurement Techniques, 2, 33–46, 2009.

Dusek, U., Frank, G. P., Hildebrandt, L., Curtius, J., Schneider, J., Walter, S., Chand, D., Drewnick, F., Hings, S., Jung, D., Borrmann, S., and Andreae, M. O.: Size matters more than chemistry for cloud-nucleating ability of aerosol particles, Science, 312, 1375–1378, doi:10.1126/science.1125261, 2006.

Eastwood, M. L., Cremel, S., Gehrke, C., Girard, E., and Bertram, A. K.: Ice nucleation on mineral dust particles: Onset conditions, nucleation rates and contact angles, Journal of Geophysical Research-Atmospheres, 113, doi: D2220310.1029/2008jd010639, 2008.

Falkovich, A. H., Ganor, E., Levin, Z., Formenti, P., and Rudich, Y.: Chemical and mineralogical analysis of individual mineral dust particles, Journal of Geophysical Research, 106, 18 029–18 036, doi:10.1029/2000jd900430, 2001.

Findeisen, W.: Die kolloidmeteorologischen Vorgänge bei der Niederschlagsbildung, Meteorologische Zeitung, 55, 121–133, 1938.

Gallavardin, S. J., Froyd, K. D., Lohmann, U., Möhler, O., Murphy, D. M., and Cziczo, D. J.: Single Particle Laser Mass Spectrometry Applied to Differential Ice Nucleation Experiments at the AIDA Chamber, Aerosol Science and Technology, 42, 773–791, doi:10.1080/02786820802339538, 2008.

Hartmann, S., Niedermeier, D., Voigtlander, J., Clauss, T., Shaw, R. A., Wex, H., Kiselev, A., and Stratmann, F.: Homogeneous and heterogeneous ice nucleation at LACIS: operating principle and theoretical studies, Atmospheric Chemistry and Physics, 11, 1753–1767, doi:10.5194/acp-11-1753-2011, 2011.

Haynes, W. M.: "Properties of solids" in CRC Handbook of chemistry and Physics, CRC Press/Taylor and Francis, Boca Raton, FL, 91st edition (internet version 2011) edn., 2011.

Heymsfield, A. J. and Miloshevich, L. M.: Homogeneous ice nucleation and supercooled liquid water in orographic wave clouds, Journal of the Atmospheric Sciences, 50, 2335–2353, 1993.

Hinds, W. C.: Aerosol technology, John Wiley & Sons, Inc., New York, Chichester, Weinheim, Brisbane, Singapore, Toronto, 2nd edn., 1999.

Hings, S.: Characterisation and Field Deployment of a Novel Quantitative Time-of-Flight Aerosol Mass Spectrometer (ToF-AMS), MPI-Chemie, IMPRS, Mainz, 2007.

Hinz, K. P., Trimborn, A., Weingartner, E., Henning, S., Baltensperger, U., and Spengler, B.: Aerosol single particle composition at the Jungfraujoch, Journal of Aerosol Science, 36, 123–145, doi:10.1016/j.jaerosci.2004.08.001, 2005.

Hoose, C., Kristjansson, J. E., and Burrows, S. M.: How important is biological ice nucleation in clouds on a global scale?, Environmental Research Letters, 5, doi:02400910.1088/1748-9326/5/2/024009, 2010.

Huffman, J. A., Jayne, J. T., Drewnick, F., Aiken, A. C., Onasch, T., Worsnop, D. R., and Jimenez, J. L.: Design, modeling, optimization, and experimental tests of a particle beam width probe for the aerodyne aerosol mass spectrometer, Aerosol Science and Technology, 39, 1143–1163, doi:10.1080/02786820500423782, 2005.

IFA: GESTIS-material-database„ URL http://www.dguv.de/ifa/de/gestis/stoffdb/index.jsp, 2010.

Jander, G., Jahr, K. F., Schulze, G., and Simon, J.: Maßanalyse, vol. 16, Walter de Gruyter, Berlin, 2002.

Jayne, J. T., Leard, D. C., Zhang, X. F., Davidovits, P., Smith, K. A., Kolb, C. E., and Worsnop, D. R.: Development of an aerosol mass spectrometer for size and composition analysis of submicron particles, Aerosol Science and Technology, 33, 49–70, 2000.

Jennings, S. G.: The mean free path in air, Journal of Aerosol Science, 19, 159–166, doi:Doi:10.1016/0021-8502(88)90219-4, 1988.

Jensen, E. J., Toon, O. B., and Hamill, P.: Homogeneous freezing nucleation of stratospheric solution droplets, Geophysical Research Letters, 18, 1857–1860, 1991.

Jensen, E. J., Toon, O. B., Tabazadeh, A., Sachse, G. W., Anderson, B. E., Chan, K. R., Twohy, C. W., Gandrud, B., Aulenbach, S. M., Heymsfield, A., Hallett, J., and Gary, B.: Ice nucleation processes in upper tropospheric wave-clouds observed during SUCCESS, Geophysical Research Letters, 25, 1363–1366, 1998.

Kamphus, M., Ettner-Mahl, M., Klimach, T., Drewnick, F., Keller, L., Cziczo, D. J., Mertes, S., Borrmann, S., and Curtius, J.: Chemical composition of ambient aerosol, ice residues and cloud droplet residues in mixed-phase clouds: single particle analysis during the Cloud and Aerosol Characterization Experiment (CLACE 6), Atmospheric Chemistry and Physics, 10, 8077–8095, doi: 10.5194/acp-10-8077-2010, 2010.

Kellner, R., Mermet, J.-M., Otto, M., Valcarcel, M., and Widmer, H. M. E.: Analytical chemistry - A modern approach to analytical science, WILEY-VCH Verlag GmbH & Co. KgaA, Weinheim, Germany, 2nd edn., 2004.

Klein, H., Nickovic, S., Haunold, W., Bundke, U., Nillius, B., Ebert, M., Weinbruch, S., Schuetz, L., Levin, Z., Barrie, L. A., and Bingemer, H.: Saharan dust and ice nuclei over Central Europe, Atmospheric Chemistry and Physics, 10, 10 211–10 221, doi:10.5194/acp-10-10211-2010, 2010.

Köhler, H.: The nucleus in and the growth of hygroscopic droplets, Transactions of the Faraday Society, 32, 1152–1161, 1936.

Lohmann, U. and Diehl, K.: Sensitivity studies of the importance of dust ice nuclei for the indirect aerosol effect on stratiform mixed-phase clouds, Journal of the Atmospheric Sciences, 63, 968–982, 2006.

Lohmann, U. and Feichter, J.: Global indirect aerosol effects: a review, Atmospheric Chemistry and Physics, 5, 715–737, 2005.

Lüönd, F., Stetzer, O., Welti, A., and Lohmann, U.: Experimental study on the ice nucleation ability of size-selected kaolinite particles in the immersion mode, Journal of Geophysical Research-Atmospheres, 115, doi:D1420110.1029/2009jd012959, 2010.

Manson, J. E.: Calcium carbonate as an ice nucleus, Journal of Meteorology, 14, 85–86, 1957.

Mason, B. J. and Maybank, J.: Ice-nucleating properties of some natural mineral dusts, Quarterly Journal of the Royal Meteorological Society, 84, 235–241, 1958.

Matsumoto, M., Saito, S., and Ohmine, I.: Molecular dynamics simulation of the ice nucleation and growth process leading to water freezing, Nature, 416, 409–413, 2002.

Matthew, B. M., Middlebrook, A. M., and Onasch, T. B.: Collection efficiencies in an Aerodyne Aerosol Mass Spectrometer as a function of particle phase for laboratory generated aerosols, Aerosol Science and Technology, 42, 884–898, doi: 10.1080/02786820802356797, 2008.

Mauritsen, T., Sedlar, J., Tjernstrom, M., Leck, C., Martin, M., Shupe, M., Sjogren, S., Sierau, B., Persson, P. O. G., Brooks, I. M., and Swietlicki, E.: An Arctic CCN-limited cloud-aerosol regime, Atmospheric Chemistry and Physics, 11, 165–173, doi:10.5194/acp-11-165-2011, 2011.

Mertes, S., Verheggen, B., Walter, S., Connolly, P., Ebert, M., Schneider, J., Bower, K. N., Cozic, J., Weinbruch, S., Baltensperger, U., and Weingartner, E.: Counterflow virtual impactor based collection of small ice particles in mixed-phase clouds for the physico-chemical characterization of tropospheric ice nuclei : Sampler description and first case study, Aerosol Science and Technology, 41, 848–864, doi:10.1080/02786820701501881, 2007.

Möhler, O., Nink, A., Saathoff, H., Schaefers, S., Schnaiter, M., Schock, W., and Schurath, U.: The Karlsruhe aerosol chamber facility AIDA: Technical description and first results of homogeneous and heterogeneous ice nucleation experiments, vol. 2001 of *C E R N Reports*, pp. 163–168, C E R N, Geneva, 2001.

Möhler, O., Buttner, S., Linke, C., Schnaiter, M., Saathoff, H., Stetzer, O., Wagner, R., Krämer, M., Mangold, A., Ebert, V., and Schurath, U.: Effect of sulfuric

acid coating on heterogeneous ice nucleation by soot aerosol particles, Journal of Geophysical Research-Atmospheres, 110, 12, doi:D1121010.1029/2004jd005169, 2005.

Möhler, O., DeMott, P. J., Vali, G., and Levin, Z.: Microbiology and atmospheric processes: the role of biological particles in cloud physics, Biogeosciences, 4, 1059–1071, 2007.

Möhler, O., Benz, S., Saathoff, H., Schnaiter, M., Wagner, R., Schneider, J., Walter, S., Ebert, V., and Wagner, S.: The effect of organic coating on the heterogeneous ice nucleation efficiency of mineral dust aerosols, Environmental Research Letters, 3, 8, doi:02500710.1088/1748-9326/3/2/025007, 2008.

Morris, C. E., Georgakopoulos, D. G., and Sands, D. C.: Ice nucleation active bacteria and their potential role in precipitation, Journal De Physique Iv, 121, 87–103, doi:10.1051/jp4:2004121004, 2004.

Murray, B. J. and Bertram, A. K.: Formation and stability of cubic ice in water droplets, Physical Chemistry Chemical Physics, 8, 186–192, doi:10.1039/b513480c, 2006.

Murray, B. J., Knopf, D. A., and Bertram, A. K.: The formation of cubic ice under conditions relevant to Earth's atmosphere, Nature, 434, 202–205, doi:10.1038/nature03403, 2005.

Murray, B. J., Wilson, T. W., Dobbie, S., Cui, Z. Q., Al-Jumur, S., Möhler, O., Schnaiter, M., Wagner, R., Benz, S., Niemand, M., Saathoff, H., Ebert, V., Wagner, S., and Kärcher, B.: Heterogeneous nucleation of ice particles on glassy aerosols under cirrus conditions, Nature Geoscience, 3, 233–237, doi:10.1038/ngeo817, 2010.

Murray, B. J., Broadley, S. L., Wilson, T. W., Atkinson, J. D., and Wills, R. H.: Heterogeneous freezing of water droplets containing kaolinite particles, Atmospheric Chemistry and Physics, 11, 4191–4207, doi:10.5194/acp-11-4191-2011, 2011.

Niedermeier, D., Hartmann, S., Shaw, R. A., Covert, D., Mentel, T. F., Schneider, J., Poulain, L., Reitz, P., Spindler, C., Clauss, T., Kiselev, A., Hallbauer, E., Wex, H., Mildenberger, K., and Stratmann, F.: Heterogeneous freezing of droplets with immersed mineral dust particles - measurements and parameterization, Atmospheric Chemistry and Physics, 10, 3601–3614, 2010.

Niedermeier, D., Hartmann, S., Clauss, T., Wex, H., Kiselev, A., Sullivan, R. C., DeMott, P. J., Petters, M. D., Reitz, P., Schneider, J., Mikhailov, E., Sierau, B., Stetzer, O., Reimann, B., Bundke, U., Shaw, R. A., Buchholz, A., Mentel, T. F., and Stratmann, F.: Experimental study of the role of physicochemical surface processing on the IN ability of mineral dust particles, Atmos. Chem. Phys. Discuss., 11, 18 557–18 588, doi:10.5194/acpd-11-18557-2011, 2011.

Nink, A., Saathoff, H., Schnaiter, M., and Möhler, O.: Laboratory investigation of the impact of aircraft particulate emissions on cirrus cloud formation, pp. 149–153, EUR19428, Seeheim, 2000.

Peter, T.: Microphysics and heterogeneous chemistry of polar stratospheric clouds, Annual Review of Physical Chemistry, 48, 785–822, 1997.

Petters, M. D. and Kreidenweis, S. M.: A single parameter representation of hygroscopic growth and cloud condensation nucleus activity, Atmospheric Chemistry and Physics, 7, 1961–1971, 2007.

Petters, M. D. and Kreidenweis, S. M.: A single parameter representation of hygroscopic growth and cloud condensation nucleus activity - Part 2: Including solubility, Atmospheric Chemistry and Physics, 8, 6273–6279, 2008.

Pincus, R. and Baker, M. B.: Effect of precipitation on the albedo susceptibility of clouds in the marine boundary layer, Nature, 372, 250–252, 1994.

Press, W. H.: ran2, p. 994 pp, Cambridge University Press, New York, 2nd edn., 1992.

Pruppacher, H. and Klett, J.: Microphysics of clouds and precipitation, Kluwer Academic Publishers, Netherlands, 2nd edn., new corrected version available since 2010, 1997.

Reitz, P., Spindler, C., Mentel, T. F., Poulain, L., Wex, H., Mildenberger, K., Niedermeier, D., Hartmann, S., Clauss, T., Stratmann, F., Sullivan, R. C., DeMott, P. J., Petters, M. D., Sierau, B., and Schneider, J.: Surface modification of mineral dust particles by sulphuric acid processing: implications for CCN and IN abilities, Atmos. Chem. Phys. Discuss., 11, 7235–7289, doi:10.5194/acpd-11-7235-2011, 2011.

Richardson, M. S., DeMott, P. J., Kreidenweis, S. M., Cziczo, D. J., Dunlea, E. J., Jimenez, J. L., Thomson, D. S., Ashbaugh, L. L., Borys, R. D., Westphal, D. L., Casuccio, G. S., and Lersch, T. L.: Measurements of heteroge-

neous ice nuclei in the western United States in springtime and their relation to aerosol characteristics, Journal of Geophysical Research-Atmospheres, 112, 16, doi:D0220910.1029/2006jd007500, 2007.

Roberts, G. C. and Nenes, A.: A continuous-flow streamwise thermal-gradient CCN chamber for atmospheric measurements, Aerosol Science and Technology, 39, 206 – 221, 2005.

Roedel, W.: Physik unserer Umwelt: die Atmosphäre, Springer-Verlag Berlin Heidelberg New York, 3rd edn., 2000.

Rogers, D. C., DeMott, P. J., Kreidenweis, S. M., and Chen, Y.: A Continuous-Flow Diffusion Chamber for airborne measurements of ice nuclei, Journal of Atmospheric and Oceanic Technology, 18, 725–741, doi:10.1175/1520-0426(2001)018<0725:ACFDCF>2.0.CO;2, 2001.

Salam, A., Lohmann, U., Crenna, B., Lesins, G., Klages, P., Rogers, D., Irani, R., MacGillivray, A., and Coffin, M.: Ice Nucleation Studies of Mineral Dust Particles with a New Continuous Flow Diffusion Chamber, Aerosol Science & Technology, 40, 134–143, doi:10.1080/02786820500444853, 2006.

Salcedo, D., Onasch, T. B., Dzepina, K., Canagaratna, M. R., Zhang, Q., Huffman, J. A., DeCarlo, P. F., Jayne, J. T., Mortimer, P., Worsnop, D. R., Kolb, C. E., Johnson, K. S., Zuberi, B., Marr, L. C., Volkamer, R., Molina, L. T., Molina, M. J., Cardenas, B., Bernabe, R. M., Marquez, C., Gaffney, J. S., Marley, N. A., Laskin, A., Shutthanandan, V., Xie, Y., Brune, W., Lesher, R., Shirley, T., and Jimenez, J. L.: Characterization of ambient aerosols in Mexico City during the MCMA-2003 campaign with Aerosol Mass Spectrometry: results from the CENICA Supersite, Atmospheric Chemistry and Physics, 6, 925–946, 2006.

Schmale, J., Schneider, J., Jurkat, T., Voigt, C., Kalesse, H., Rautenhaus, M., Lichtenstern, M., Schlager, H., Ancellet, G., Arnold, F., Gerding, M., Mattis, I., Wendisch, M., and Borrmann, S.: Aerosol layers from the 2008 eruptions of Mount Okmok and Mount Kasatochi: In situ upper troposphere and lower stratosphere measurements of sulfate and organics over Europe, Journal of Geophysical Research-Atmospheres, 115, doi:D00l0710.1029/2009jd013628, 2010.

Schneider, J., Weimer, S., Drewnick, F., Borrmann, S., Helas, G., Gwaze, P., Schmid, O., Andreae, M. O., and Kirchner, U.: Mass spectrometric analysis and aerodynamic properties of various types of combustion-related aerosol particles, International Journal of Mass Spectrometry, 258, 37–49, doi:10.1016/j.ijms.2006.

07.008, 2006.

Schwarz, H. R. and Köckler, N.: Numerische Mathematik, B. G. Teubner Verlag / GWV Fachverlage GmbH, Wiesbaden, 6 edn., 2006.

Seinfeld, J. H. and Pandis, S. N.: Atmospheric chemistry and physics: From air pollution to climate change, John Wiley & sons, Inc., New York, Chichester, Weinheim, Brisbane, Singapore, Toronto, 1998.

Sitzmann, H.: Roempp Online - Version 3.5, URL http://www.roempp.com, 2004.

Solomon, S., Qin, D., Manning, M., Chen, Z., Marquis, M., Averyt, K., Tignor, M., and Miller, H.: Climate change 2007: The physical science basis, Tech. rep., 2007.

Storelvmo, T., Hoose, C., and Eriksson, P.: Global modeling of mixed-phase clouds: The albedo and lifetime effects of aerosols, Journal of Geophysical Research-Atmospheres, 116, doi:D0520710.1029/2010jd014724, 2011.

Stratmann, F., Kiselev, A., Wurzler, S., Wendisch, M., Heintzenberg, J., Charlson, R. J., Diehl, K., Wex, H., and Schmidt, S.: Laboratory studies and numerical simulations of cloud droplet formation under realistic supersaturation conditions, Journal of Atmospheric and Oceanic Technology, 21, 876–887, 2004.

Stull, R. B.: An Introduction to Boundary Layer Meteorology, Kluwer Academic Publishers, Dordrecht, 1988.

Sullivan, R. C. and Prather, K. A.: Investigations of the diurnal cycle and mixing state of oxalic acid in individual particles in Asian aerosol outflow, Environmental Science & Technology, 41, 8062–8069, doi:10.1021/es071134g, 2007.

Sullivan, R. C., Guazzotti, S. A., Sodeman, D. A., and Prather, K. A.: Direct observations of the atmospheric processing of Asian mineral dust, Atmospheric Chemistry and Physics, 7, 1213–1236, 2007.

Sullivan, R. C., Moore, M. J. K., Petters, M. D., Kreidenweis, S. M., Roberts, G. C., and Prather, K. A.: Timescale for hygroscopic conversion of calcite mineral particles through heterogeneous reaction with nitric acid, Physical Chemistry Chemical Physics, 11, 7826–7837, 2009.

Sullivan, R. C., Miñambres, L., DeMott, P. J., Prenni, A. J., Carrico, C. M., Levin, E. J. T., and Kreidenweis, S. M.: Chemical processing does not always impair heterogeneous ice nucleation of mineral dust particles, Geophys. Res. Lett., 37, L24805, doi:10.1029/2010gl045540, 2010a.

Sullivan, R. C., Petters, M. D., DeMott, P. J., Kreidenweis, S. M., Wex, H., Niedermeier, D., Hartmann, S., Clauss, T., Stratmann, F., Reitz, P., Schneider, J., and Sierau, B.: Irreversible loss of ice nucleation active sites in mineral dust particles caused by sulphuric acid condensation, Atmospheric Chemistry and Physics, 10, 11 471–11 487, doi:10.5194/acp-10-11471-2010, 2010b.

Svane, M., Hagstrom, M., and Pettersson, J. B. C.: Chemical analysis of individual alkali-containing aerosol particles: Design and performance of a surface ionization particle beam mass spectrometer, Aerosol Science and Technology, 38, 655–663, doi:10.1080/02786820490485944, 2004.

Svane, M., Hagstrom, M., and Pettersson, J. B. C.: Online measurements of individual alkali-containing particles formed in biomass and coal combustion: Demonstration of an instrument based on surface ionization technique, Energy & Fuels, 19, 411–417, doi:10.1021/ef049925g, 2005.

Szyrmer, W. and Zawadzki, I.: Biogenic and anthropogenic sources of ice-forming nuclei: A review, Bulletin of the American Meteorological Society, 78, 209–228, 1997.

Tabazadeh, A., Toon, O. B., and Jensen, E. J.: Formation and implications of ice particle nucleation in the stratosphere, Geophysical Research Letters, 24, 2007–2010, 1997.

Takegawa, N., Miyazaki, Y., Kondo, Y., Komazaki, Y., Miyakawa, T., Jimenez, J. L., Jayne, J. T., Worsnop, D. R., Allan, J. D., and Weber, R. J.: Characterization of an Aerodyne Aerosol Mass Spectrometer (AMS): Intercomparison with other aerosol instruments, Aerosol Science and Technology, 39, 760–770, doi:10.1080/02786820500243404, 2005.

Timko, M. T., Yu, Z. H., Kroll, J. H., Jayne, J. T., Worsnop, D. R., Miake-Lye, R. C., Onasch, T. B., Liscinsky, D., Kirchstetter, T. W., Destaillats, H., Holder, A. L., Smith, J. D., and Wilson, K. R.: Sampling artifacts from conductive silicone tubing, Aerosol Science and Technology, 43, 855–865, doi:10.1080/02786820902984811, 2009.

Trimborn, A.: Personal communication: AMS tuning, 2009.

Twomey, S.: Influence of pollution on shortwave albedo of clouds, Journal of the Atmospheric Sciences, 34, 1149–1152, 1977.

Vlasenko, A., Sjogren, S., Weingartner, E., Gaggeler, H. W., and Ammann, M.: Generation of submicron Arizona test dust aerosol: Chemical and hygroscopic properties, Aerosol Science and Technology, 39, 452–460, doi:10.1080/027868290959870, 2005.

von Blohn, N., Mitra, S. K., Diehl, K., and Borrmann, S.: The ice nucleating ability of pollen: Part III: New laboratory studies in immersion and contact freezing modes including more pollen types, Atmospheric Research, 78, 182–189, doi:10.1016/j.atmosres.2005.03.008, 2005.

Walter, S.: Personal communication: AMS lens transmission function, 2008.

Warren, S. G., Hahn, C. H., London, J., Chervin, R. M., and Jenne, R. L.: Global distribution of total cloud cover and cloud type amounts over land, URL http://nldr.library.ucar.edu/repository/technotes/TECH-NOTE-000-000-000-628, 1986.

Warren, S. G., Hahn, C. H., London, J., Chervin, R. M., and Jenne, R. L.: Global distribution of total cloud cover and cloud type amounts over the ocean, URL http://nldr.library.ucar.edu/repository/technotes/TECH-NOTE-000-000-000-467, 1988.

Welti, A., Lüönd, F., Stetzer, O., and Lohmann, U.: Influence of particle size on the ice nucleating ability of mineral dusts, Atmospheric Chemistry and Physics, 9, 6705–6715, 2009.

Wex, H., Hennig, T., Salma, I., Ocskay, R., Kiselev, A., Henning, S., Massling, A., Wiedensohler, A., and Stratmann, F.: Hygroscopic growth and measured and modeled critical super-saturations of an atmospheric HULIS sample, Geophysical Research Letters, 34, 5, doi:L0281810.1029/2006gl028260, 2007.

Wiacek, A. and Peter, T.: On the availability of uncoated mineral dust ice nuclei in cold cloud regions, Geophysical Research Letters, 36, 5, doi:L1780110.1029/2009gl039429, 2009.

Widberg, N. and Fischer, G.: Lehrbuch der anorganischen Chemie, Walter de Gruyter & Co, Berlin, 102 edn., 2007.

Wikipedia: De-Casteljau-Algorithmus, URL http://de.wikipedia.org/wiki/De-Casteljau-Algorithmus, 2011.

Wood, S. N.: Generalized Additive Models, Texts in statistical science, Chapman & Hall/CRC Taylor & Francis group, Boca Raton, 2006.

Yu, Y., Alexander, M. L., Perraud, V., Bruns, E. A., Johnson, S. N., Ezell, M. J., and Finlayson-Pitts, B. J.: Contamination from electrically conductive silicone tubing during aerosol chemical analysis, Atmospheric Environment, 43, 2836–2839, doi:10.1016/j.atmosenv.2009.02.014, 2009.

Zelenyuk, A., Yang, J., Choi, E., and Imre, D.: SPLAT II: An aircraft compatible, ultra-sensitive, high precision instrument for in-situ characterization of the size and composition of fine and ultrafine particles, Aerosol Science and Technology, 43, 411–424, doi:10.1080/02786820802709243, 2009.

Zhang, Q., Canagaratna, M. R., Jayne, J. T., Worsnop, D. R., and Jimenez, J. L.: Time- and size-resolved chemical composition of submicron particles in Pittsburgh: Implications for aerosol sources and processes, Journal of Geophysical Research-Atmospheres, 110, doi:D07s0910.1029/2004jd004649, 2005.

Zhao, D. F., Buchholz, A., Mentel, T. F., Müller, K. P., Borchardt, J., Kiendler-Scharr, A., Spindler, C., Tillmann, R., Trimborn, A., Zhu, T., and Wahner, A.: Novel method of generation of $Ca(HCO_3)_2$ and $CaCO_3$ aerosols and first determination of hygroscopic and cloud condensation nuclei activation properties, Atmospheric Chemistry and Physics, 10, 8601–8616, doi:10.5194/acp-10-8601-2010, 2010.

Zimmermann, F., Weinbruch, S., Schütz, L., Hofmann, H., Ebert, M., Kandler, K., and Worringen, A.: Ice nucleation properties of the most abundant mineral dust phases, Journal of Geophysical Research, 113, D23 204, doi:10.1029/2008jd010655, 2008.

(Acknowledgements cleared)